ABSTRACT

Title of Dissertation:	CHROMOPHORIC DISSOLVED ORGANIC MATTER (CDOM) IN THE OPEN OCEAN: OPTICAL AND CHEMICAL PROPERTIES AND THEIR RELATION TO CDOM STRUCTURE AND SOURCES.
	Carmen Marie Cartisano, Doctor of Philosophy, 2019
Dissertation directed by:	Professor Neil V. Blough, Department of Chemistry and Biochemistry

The carbon contained as dissolved organic matter (DOM) in the Earth's oceans is an important factor in the global carbon cycle, but studying and tracking DOM in the aquatic environment can be challenging. However, the light-absorbing and emitting subcomponents of DOM, called chromophoric dissolved organic matter (CDOM) and fluorescent dissolved organic matter (FDOM) can be directly probed using absorption and fluorescence spectroscopy, respectively.

Detailed studies on CDOM from the open oceans are limited with many of the existing studies having very limited data sets (only select wavelengths or indices). To address this, the optical properties of CDOM from a variety of geographic locations (North Pacific Ocean: NPO, Equatorial Atlantic Ocean: EAO, Middle Atlantic Bight: MAB, Delaware River and Delaware Bay) were compared, and chemical tests performed (sodium

borohydride ($NaBH_4$) reductions and pH titrations). The responses to the chemical tests along with similarities and differences in the optical properties were examined to compare the structures present in terrestrial, coastal and open ocean samples.

A long-pathlength capillary waveguide spectrometer was used to characterize open ocean CDOM samples, with the need for a calibration and validated protocol addressed prior to use. The optical properties of the NPO samples did not vary significantly at depths from ~300-4500 meters with only the surface samples showing significant differences. Solid phase extraction of the natural waters did remove unique absorbing and emitting bands in the UV region that could be marine in origin, while enriching the "humic like" fraction.

The open ocean samples showed similarities to the coastal and riverine samples including: 1) monotonically decreasing and unstructured absorbance with increasing wavelength; 2) loss of absorption upon $NaBH_4$ reduction at all wavelength, with the largest percent loss in the visible; 3) enhanced absorption with increasing pH with spectral changes that occurred over the same pH ranges as the pKas of carboxylic acids and phenols; 4) attenuation of absorption enhancement with increasing pH following reduction at most wavelengths. These similarities not only suggest that there are structural similarities throughout all samples, but also indicate that there may be a terrestrial source of CDOM in the open ocean.

CHROMOPHORIC DISSOLVED ORGANIC MATTER (CDOM) IN THE OPEN OCEAN: OPTICAL AND CHEMICAL PROPERTIES AND THEIR RELATION TO CDOM STRUCTURE AND SOURCES.

By

Carmen Marie Cartisano

Dissertation submitted to the Faculty of the Graduate School of the
University of Maryland, College Park, in partial fulfillment
of the requirements for the degree of
Doctor of Philosophy
2019

Advisory Committee:
Professor Neil V. Blough, Chair
Professor Alice C. Mignerey
Professor Russell R. Dickerson
Professor Amy S. Mullin
Professor Sujay S. Kaushal

Acknowledgements

There are many people who have supported and mentored me throughout my graduate career, and many others who have helped me get to this point in my life. I am deeply grateful to all of them. I would like to thank Dr. Neil Bough for allowing me to work in his research lab, and for mentoring and advising me throughout my graduate career. I would also like to thank Dr. Rossana Del Vecchio, who helped me grow in my ability to conduct lab work as well as improve my analytical and critical thinking skills. Rossana aided in my understanding of this field and was always a great mentor.

I would also like to thank the members of my committee, Alice C. Mignerey, Russell R. Dickerson, Amy S. Mullin and Sujay S. Kaushal for your time and support throughout this process.

Thank you to Natalia White who is a great mentor and support. TAing for you was always a great learning experience and you really helped to shape me as an educator. You always made time to listen to me and I have always valued your advice and opinion and will continue to do so. I really would not have made it through without you!

Thank you to Dr. Lenea Stocker, you made my first TAing experience not only manageable but enjoyable and I think successful. I could not have had a better introduction to TAing. I had the pleasure of working with Dr. Stocker again during my GAANN fellowship, and I learned so much from her mentorship.

I would also like to thank all of the professors who helped prepare me for graduate school by allowing me to conduct undergraduate research Dr. Isiah Warner, Dr. Robert Cook, Dr. Thomas Douglas, and Dr. Liesbet Lagae. I did not fully understand at the time

just how valuable the skills I learned would be, and I would like to thank you for giving me the time and support I needed to learn.

I would also like to thank all of the staff of the LA-STEM program. One goal of the program was to help prepare us for graduate school and you did that and more. Dr. Melissa Crawford you were always there with advice and support; I had an amazing undergraduate experience and I owe a lot of that to you.

All my lab mates, especially Marla Bianca and Danielle Le Roux thank you, thank you, thank you. You not only helped me in my professional life (with lab work, analysis and writing) you also helped me stay sane, by chatting about life during lunch or letting me vent when needed.

To all my friends who were always there to listen and have fun thank you. Marla, Taylor and Siobhan you advice and support was priceless and weekly dinners always gave me something to look forward to, so thank you!

Thank you to my parents Mark and Su Cartisano, and to my sisters Tia and Faith who were also there to listen, when I was excited because an experiment worked and when I was frustrated because one did not. Also thank you for all your guidance and teaching me to be a strong and independent women. The life lessons that you taught me were invaluable.

Gregory thank you for all your support and being there with me every step of the way. Moving to Maryland from Louisiana was a big change for you but it means the world to me. Last but not least thanks to Foxy my pup, and constant companion who has spent most days with me in the office, she really does deserve her own Ph.D. I know that everyone in the lab is more relaxed and happy after some snuggles so thanks for keeping the stress levels down.

Table of Contents

List of Tables

List of Figures

List of Abbreviations

Chromophoric Dissolved Organic Matter (CDOM)

Dissolved Organic Matter (DOM)

Organic Matter (OM)

Dissolved Organic Carbon (DOC)

Fluorescent Dissolved Organic Matter (FDOM)

Total organic carbon (TOC)

Ultra-Violet (UV)

Suwannee River natural organic matter (SRNOM)

Suwannee River fulvic acid (SRFA)

Pony Lake fulvic acid (PLFA)

North Pacific Ocean (NPO)

Equatorial Atlantic Ocean (EAO)

Middle Atlantic Bight (MAB)

North Pacific Sub-Tropical Water (NPSTW)

Sub-tropical Mode Water (STMW)

North Pacific Intermediate Water (NPIW)

Antarctic Intermediate Water (AAIW)

North Pacific Deep Water (NPDW)

Lower Circumpolar Water (LCPW)

National Institute of Standards and Technology (NIST)

World Precision Instrument (WPI)

Multi-pathlength liquid capillary waveguide absorption spectrometer (MPLCW)

Quinine sulfate equivalents (QSE),

C18 organic matter extracts (C18-OM)

Combined extraction and elution efficiencies (CEE)

Extraction efficiency (EE)

Humification Index (HIX)

Fluorescence Index (FI)

Biological Index (BIX)

Specific UV absorbance (SUVA)

Solid Phase Extraction (SPE)

Charge transfer (CT)

Chapter 1: Chromophoric Dissolved Organic Matter (CDOM): What it is and why we have been researching it for decades.

1.1 What is CDOM:

Chromophoric dissolved organic matter (CDOM), has been studied for decades; it was previously referred to by many other names including yellow substance, gilvin, Gelbstoff and humic substance. However, none of these names clearly indicated the nature of the material being studied. CDOM on the other hand is a very descriptive name; "chromophoric" comes from the fact that it can absorb visible and ultraviolet (UV) radiation. Thus, CDOM is the light absorbing subset of dissolved organic matter (DOM), while "dissolved" typically means that it can pass through a 0.2 µm filter. CDOM is comprised of a complex mixture of organic compounds, thus the "organic matter" portion of its name. The organic matter that comprises CDOM can come from many sources including plant and animal matter and their waste products.[1-3] CDOM is an important natural component found ubiquitously in aquatic environments and plays a substantial role in determining the aquatic light field, with its absorption at short wavelengths (< 440 nm) usually dominating total absorption in the upper water column of the open oceans.[1–6]

Solid phase extraction (SPE) is often used to isolate DOM from natural waters because the natural levels of DOM or CDOM are too low for most analytical techniques. DOM isolated with SPE columns provides a more concentrated sample. Extracts, however, are only a fraction of the total DOM due to the fact that certain components are not retained on the column and others are not eluted, and thus only the fraction that is retained by and then eluted from the column is present in the extract. Common SPE columns include silica-based octadecyl bonded phase (C18) and styrene divinyl benzene polymer (PPL) which

have been shown to provide extracted samples that are fairly representative of the natural water.[7,8] The material isolated from SPE is often referred to as extracted DOM or humic substances (HS). If particular extraction processes are utilized, particular fractions of the HS can be isolated including humic and fulvic acids; humic acid is soluble at pHs above 2 while fulvic acid is soluble at all pHs.[9]

1.2 Why are we still studying CDOM:

Although CDOM is a descriptive name it does not indicate why it has been the focus of so many studies for so many years. That comes from the role CDOM plays in the aquatic environment. With the current interest in global climate change, DOM in the oceans has drawn significant attention because of its immense size and dynamics of this carbon pool (Fig. 1.1). There is ~700 $x10^{15}$ g of carbon contained in the DOM present in the world's oceans that is only slightly less than the amount of carbon contained in atmospheric CO_2 (~750 $x10^{15}$ g). This makes DOM a very significant carbon pool, but one that is not particularly well understood.[10] Many studies have focused on tracking DOM and better defining its sources and sinks, because understanding the distribution and dynamics of DOM in the aquatic environments, both now and in the future is critical. Thus, methods must be developed that will allow for the rapid and unequivocal assessment of DOM in terms of its source and structure. Even though CDOM is only a subset of DOM, it is of particular interest because of its optical properties that allow for fast and relatively easy monitoring with absorption and emission spectroscopy. Researchers have thus tried to correlate changes in the optical properties to changes in the larger DOM pool, such as average molecular size or aromaticity using nuclear magnetic resonance spectroscopy and mass spectrometry.[11–15]

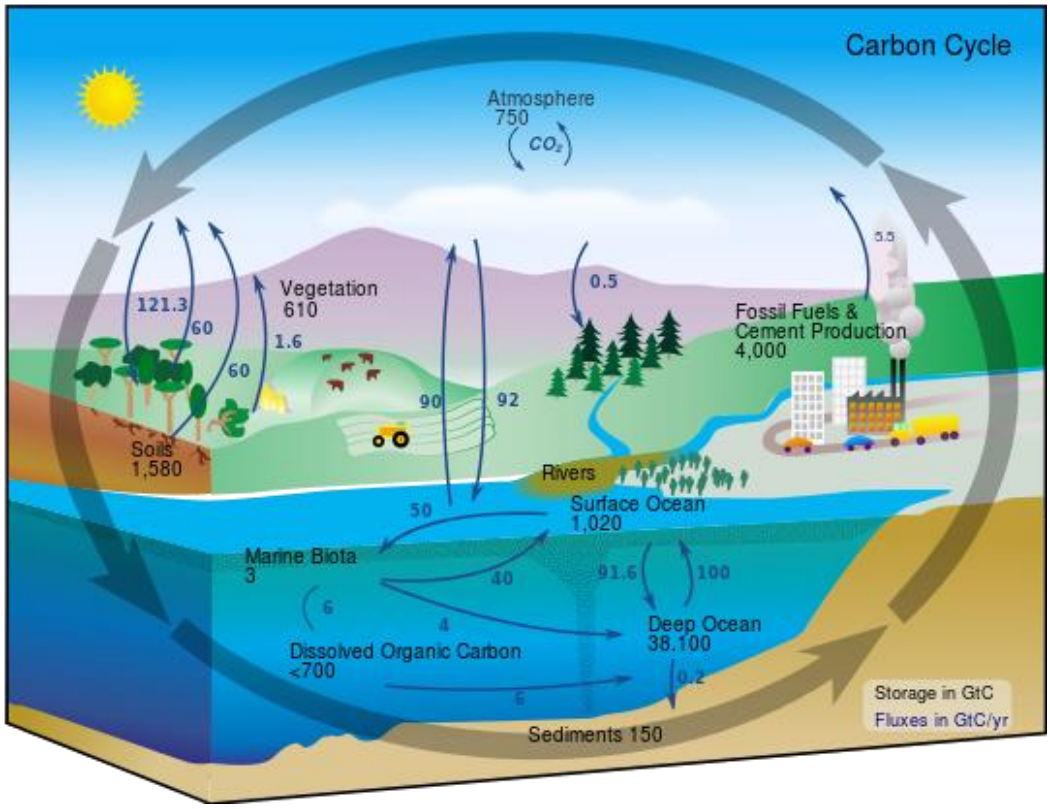

Figure 1.1: Diagram of the carbon cycle giving the storage and exchange of carbon. Adapted from geoteach2017.

CDOM on its own is an influential component to natural waters. It absorbs solar radiation and influences photochemical and photobiology processes that can occur at the surface of the ocean and throughout the euphotic zone. CDOM's absorption of light not only limits the penetration of damaging UV radiation into the water, but also can limit the light available for photosynthesis under some circumstances.[1,2,16,17] Further, CDOM can undergo photochemistry to form reactive oxygen species such as hydrogen peroxide (H_2O_2), hydroxyl radical ($\bullet OH$) and superoxide (O_2^-).[18–20] These species can play a critical role in the aquatic environment by influencing the bioavailability of trace metals and nutrients.[4-6] In some fresh waters and waste waters CDOM can cause aesthetic problems, including an unpleasant odor, taste and a yellow to brown color. (Fig. 1.2) Further, CDOM can be transformed into potentially harmful disinfection byproducts during water treatment

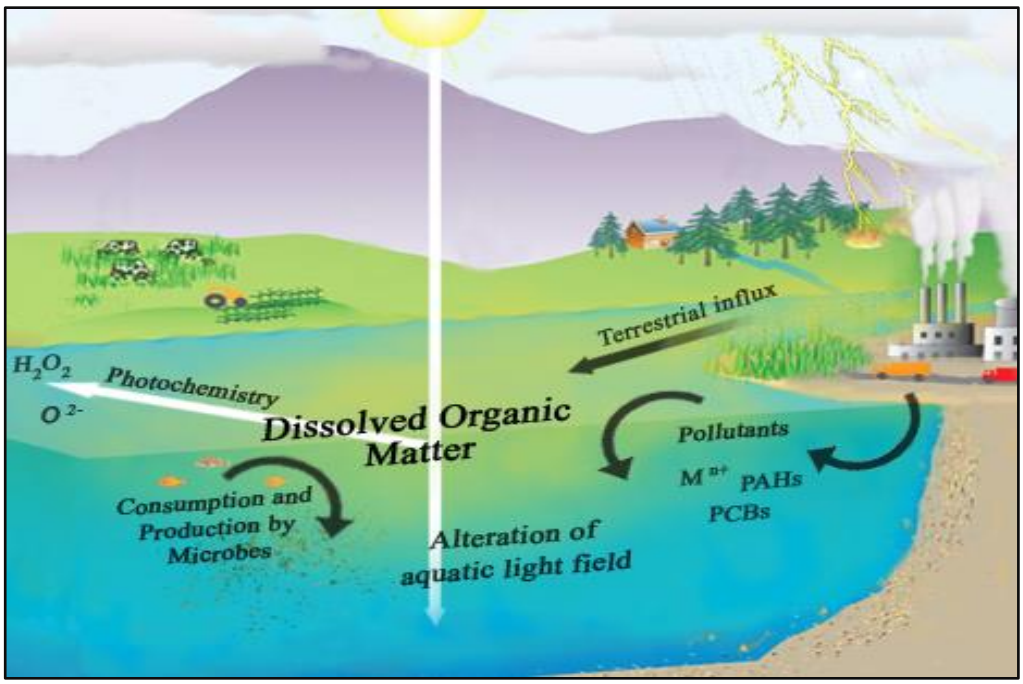

Figure 1.2: DOM/CDOM in the aquatic environment. Adapted image from visionlearning.com

processes.[7-9] The solubility and transport of pollutants including agricultural chemicals, such as pesticides, are also affected by DOM/CDOM.[10]

1.3 Optical properties of CDOM:

1.3.1 Absorbance and Fluorescence

The optical properties of natural waters and extracted materials, including absorbance and fluorescence emission, have been extensively investigated [1,3,5,16,21–24] (and references therein) (Fig. 1.3). Due to the fact that CDOM absorbs light in the UV and visible region, absorption spectroscopy can be used to investigate its optical properties. CDOM absorption spectra are typically broad and featureless with the absorbance decreasing in an approximately exponential fashion with increasing wavelength[25,26]; (Fig.

1.4c) therefore the spectra can often be fit to an exponential model [25] using a nonlinear least squares fitting routine:

$$a(\lambda) = a(\lambda_0)e^{-S(\lambda-\lambda_0)} \qquad \textbf{Eq. 1.1}$$

where a is the absorbance, λ_0 is a reference wavelength and S is the spectral slope [1]. Modeling the wavelength dependence of the absorption of CDOM has been conducted over many different wavelength ranges including 275-298 nm and 350-400 nm,[27–34] but the ~300-700 nm range is commonly used.[1,16,35]

The magnitude of the absorption and the rate at which it decreases with increasing wavelength (spectral slope) have proven to be useful indicators of changes in CDOM with time and in different geographical locations. Fresh water such as rivers and coastal areas like bays and estuaries generally have much higher absorbance and smaller spectral slopes compared to open ocean waters. This difference is due to the large input of terrestrial material that is highly aromatic and complex, which allows for more and longer wavelength absorbance. However, it is critical to examine how well the model fits the data because

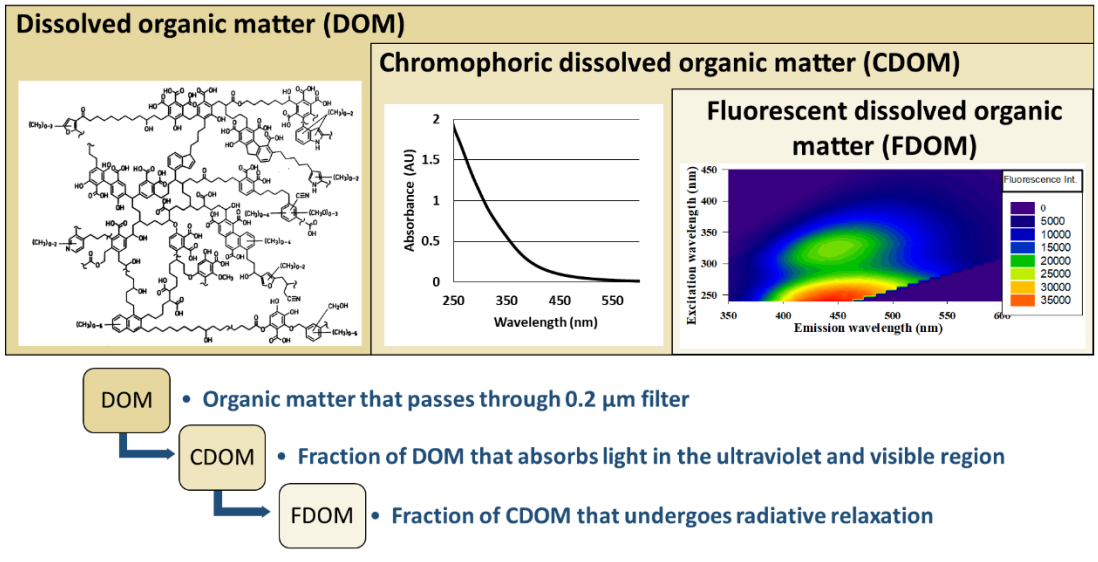

Figure 1.3: Diagram of the chromophoric and fluorescent fractions of dissolved organic matter (DOM).

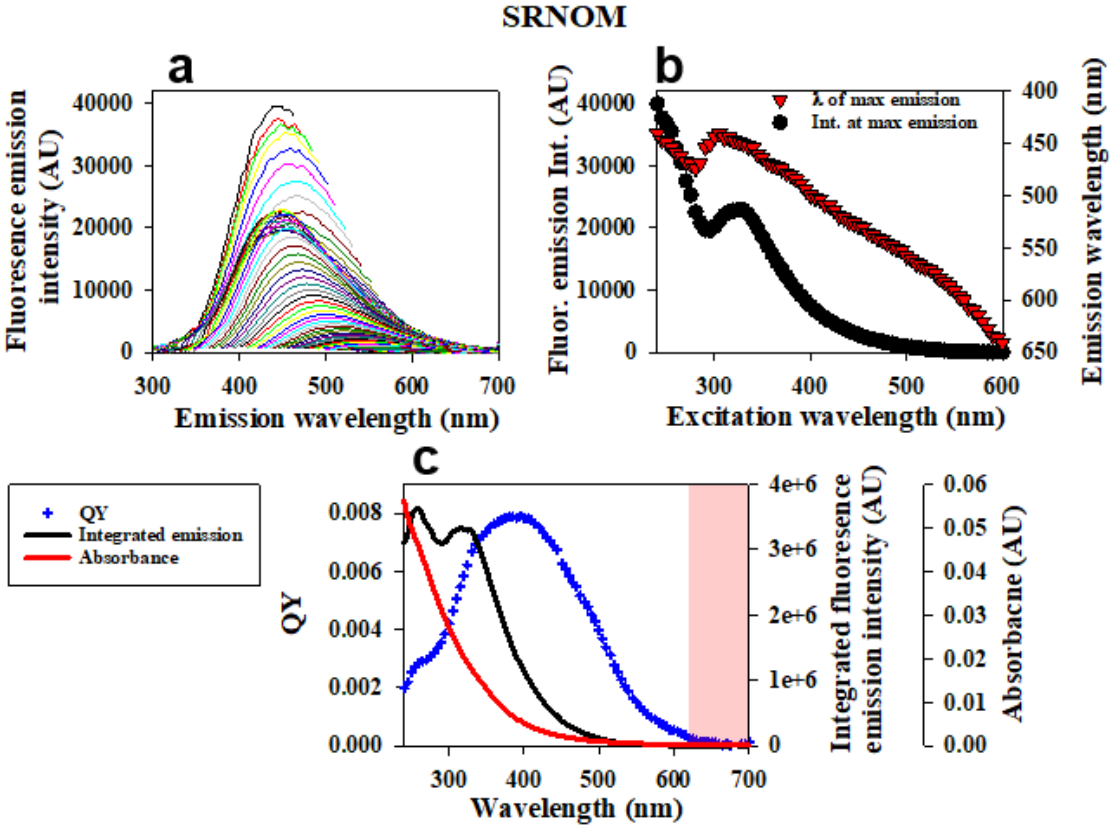

Figure 1.4: Optical properties of Suwannee River natural organic matter (SRNOM) (a) fluorescence emission intensity λex: 240-600 nm every 5 nm and, λem: 290-700 nm every 1 nm, (b) Peak fluorescence emission intensity and the emission wavelength of peak fluorescence emission for each excitation wavelength, (**c**) absorbance (**red**), integrated fluorescence emission intensity for each excitation wavelength (**black**), and apparent fluorescence quantum yields (Eq. 1.2) (**blue**).

shoulders and bands can influence spectral slope calculations. Thus examining the difference between the spectra and the fit (the residuals) can be informative.

Several other parameters have also gained popularity in the field because they appear to be correlated to the source and/or structure of CDOM in natural waters. One such parameter is the specific UV absorbance (SUVA). SUVA is the absorbance of a water sample at a given wavelength normalized to dissolved organic carbon (DOC) concentration (L mg-C^{-1} m^{-1}). $SUVA_{254}$, which utilizes the absorbance of the sample at 254 nm, has been correlated with the percent aromaticity of the DOM as determined by ^{13}C NMR.[11] Another

popular parameter to measure is the ratio of the absorbance at 250 and 365 nm often referred to as E2:E3 or E2/E3. This parameter is thought to correlate with the molecular size and aromaticity of the DOM sample.[36,37] As molecular size increases, E2/E3 has been shown to decreased because of more absorption at 365 nm due to higher molecular weight CDOM.[33,36]

However, despite the correlations that have been drawn between these optical parameters and CDOM structure, the $SUVA_{254}$ and E2:E3 values can be significantly impacted by shoulders or bands in the absorption spectrum[35]. Thus, it is critical to conduct a more complete examination of the CDOM by examining not only the full wavelength dependence of the absorbance, but also examine the fluoresces and the optical changes following chemical tests such as sodium borohydride reduction and pH titration (discussed in section 1.5) and not base conclusions solely off of these parameters. As mentioned, one way of gaining more information about the structure of CDOM is to examine the fluorescence emission.

A fraction of CDOM not only absorbs UV and visible radiation, but following excitation, undergoes radiative relaxation and can emit light in the UV and visible regions (Fig. 1.3 and 1.4). This fraction is referred to as fluorescent dissolved organic matter (FDOM). Because of this emission, fluorescence spectroscopy can also be utilized to further investigate the optical properties. Due to the complexity of CDOM/FDOM, the emission spectra, much like the absorption spectra, are also broad and unstructured. Also, for most samples at excitation wavelengths $\gtrsim$280 nm the emission spectra continuously red-shift in emission maxima with increasing excitation wavelength; this is often referred to "humic like" emission. Additionally, the emission intensity also decreases with

increasing excitation wavelength to the point where each emission spectra at successive excitation wavelengths falls under the envelope of the prior excitation wavelength. (Fig. 1.4a-b) Because of this relationship between excitation and emission for CDOM it is often important to collect three dimensional spectra called excitation emission matrix spectra (EEMs), which provide a more complete view of CDOM by showing the fluorescence emission intensity as a function of excitation wavelength. Just like with the absorbance select parameters, used to gain structural and source information, have gained popularity in the field. The three main parameters, referred to as index, that are often reported are: 1) Fluorescence index (FI), which has been correlated to the microbial contribution[38,39], 2) Humification index (HIX), which has been correlated to the humic substance content[40,41], and 3) Biological index (BIX), which has also been correlated to the contribution of autochthonous or microbially derived DOM[40]. However, just like with the absorbance, relying solely on these parameters can be misleading. Examining the full EEMs can provide more information about the source and structure of CDOM, as well as changes in the composition in time and space, by identifying various fluorescing components. EEMs of natural water samples often display a "humic like" region as well as discrete bands that fall mostly in the UV, while extracted CDOM mainly displays the "humic like" region.[7,16,35]

1.3.2 Apparent fluorescence quantum yields

Apparent fluorescence quantum yields (QY or ϕ) are a way of comparing the number of photons absorbed to the number emitted, with a fluorescence quantum yield of 1.0 indicating that all photons absorbed are re-emitted as fluorescence. Calculation of ϕ s is

accomplished by taking the ratio of the fluorescence emission with the absorbance and then comparing the ratio to a known standard, which in most cases in quinine sulfate (QS).

$$\phi(\lambda_{ex}) = \left(\frac{F_{S(int)}(\lambda_{ex})}{F_{QS(int)}(\lambda ex_{350nm})} * \frac{A_{QS}(\lambda ex_{350nm})}{A_S(\lambda_{ex})}\right) 0.51 \qquad \textbf{Eq. 1.2}$$

where $F_{S(int)}$ and $F_{QS(int)}$ are the integrated emission intensities of the sample and quinine sulfate, respectively, at the excitation wavelength (λ_{ex}); A_S and A_{QS} are the absorbance of samples and quinine sulfate standard respectively, at λ_{ex}; 0.51 is the published quantum yield of the quinine sulfate [26].

QYs for CDOM samples are wavelength dependent and thus can be calculated for each excitation wavelength. (Fig. 1.4c) Like absorbance and fluorescence emission, QYs can be used to help determine the source and structure of CDOM. Typically CDOM has relatively low QY values around 0.001-0.03, however peaks in the QYs with wavelength can indicate discrete components with different structure from the bulk "humic-like" material.[16,21,22,26,35]

In the environment, the absorbance and fluorescence of CDOM can be impacted by many factors, including physical mixing, biological or photodegradation, as well as possible biological production.[2,34,42–45] All of these processes could alter the optical properties of CDOM as it is transported or produced in the environment. Thus, CDOM from the same source may have different optical properties depending on the extent to which it was modified by these factors.

1.4 Electronic interaction model:

The optical properties of CDOM cannot be fully explained by a simple superposition of non-interacting absorbing and emitting species[21,22,46–49]. Instead, a more complex

model, the electronic interaction model or the charge transfer (CT) model has been proposed. This model requires molecular interactions among chromophores and better explains the optical properties of CDOM [21,22,24]. According to this model: 1) the long wavelength optical properties arise in part through electronic interactions between donors and acceptors within CDOM leading to a spectrum that is *not* the simple sum of the isolated chromophores, and 2) the majority of short-wavelength absorbance (< 350 nm) arises from individual chromophores (electron donor and acceptor molecules). (Fig. 1.5) Within this model, aromatic or substituted phenols and carboxylic moieties are proposed to represent the principle electron donors, while carbonyl-containing molecules (aromatic ketones, aldehydes, and quinones) account for the principal electron acceptors. Terrestrially derived CDOM and reference humic substances are thought to be primarily comprised of the

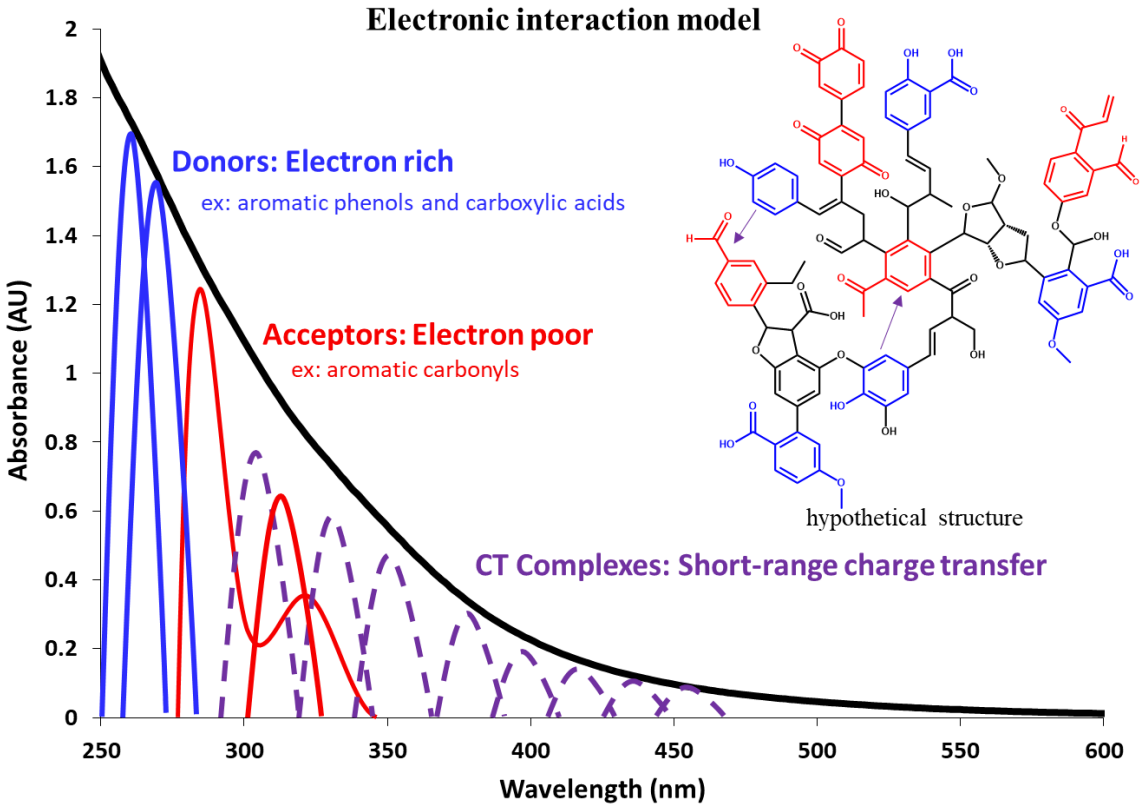

Figure 1.5: Visual representation of the electronic interaction model.

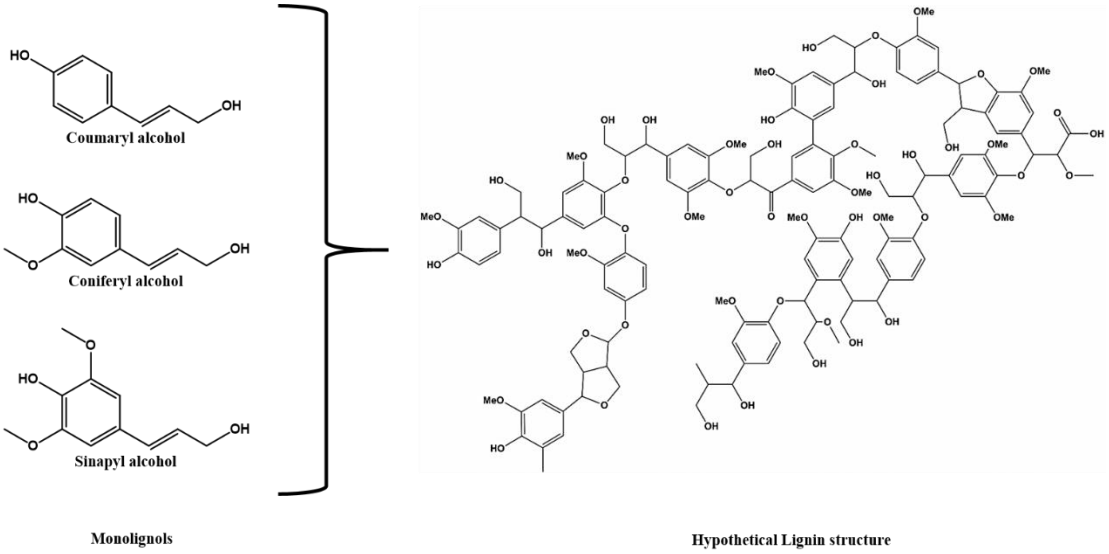

Figure 1.6: (left) Monolignols that form lignin in plant cells as well as a (right) hypothetical lignin structure. Modified from Derkacheva, O. & Sukhov, D. (2008).

degradation products from lignins and possibly tannins [12,23,24,50–54] and have been shown to contain functional groups such as ketones, aldehydes, quinones, phenols and carboxylic acids [21,22,24,55]. (Fig. 1.6)

To further test this model sodium borohydride ($NaBH_4$) reductions and pH titrations have been performed on humic and fulvic acid reference material, as well as natural waters and extracts. Both of these chemical tests can probe for the presence of functional groups involved in the electronic interactions, thus testing the validity of the model and at the same time providing further information about the structure of CDOM. [16,46,56–59] $NaBH_4$ reductions (discussed in detail in section 1.5.1) can selectively reduce carbonyl-containing compounds including ketones, aldehydes and quinones (electron acceptors)[46,60]. Addition of $NaBH_4$ to CDOM has been shown to alter the optical properties at both short and long wavelengths due to reduction of carbonyl containing groups, and the elimination of electronic interactions arising from the carbonyl containing groups, respectively. In contrast, pH titrations (discussed in detail in section 1.5.2) probe possible electron

donors[58,59,61,62]. With increasing pH the short and long wavelength absorption have been shown to increase and this increase has been attributed to the deprotonation of carboxylic and phenolic groups, as well as increased charge-transfer interactions caused by the presence of better electron donors. Both of these tests suggest that there are interactions between chromophores within HS and CDOM samples and thus support the charge transfer model.

Recently, work done by McKay *et al.* (2018) suggested that charge transfer interactions do not contribute significantly to the optical properties of DOM. They came to this conclusion based on the lack of optical changes in HS and DOM samples following change in solvent temperature, viscosity, and polarity.[63] However, as previously noted, HS and DOM samples have complex structures and it is questionable if the solvents used and the temperature range was sufficient to disrupt CT interactions. DOM samples, especially those with high average molecular weight, are thought to form aggregates and be organized into structures were an inner core is surrounded by an outer core comprised of charged groups.[64–67] Consequently, donors and acceptors could be in contact with one another and surrounded by charged moieties making them more stable and hard to access, causing changes in solvent to have little impact on the CT interactions.[58,68,69]

1.5 Probing the origins and structure of CDOM using chemical tests:

1.5.1 $NaBH_4$ Reduction

The addition of sodium borohydride to samples, including humic and fulvic acid reference materials, natural waters, and extracts, can selectively reduce carbonyl-containing compounds including ketones, aldehydes and quinones through a nucleophilic addition reaction. The reduction with $NaBH_4$ occurs in two steps. First, a hydrogen anion is

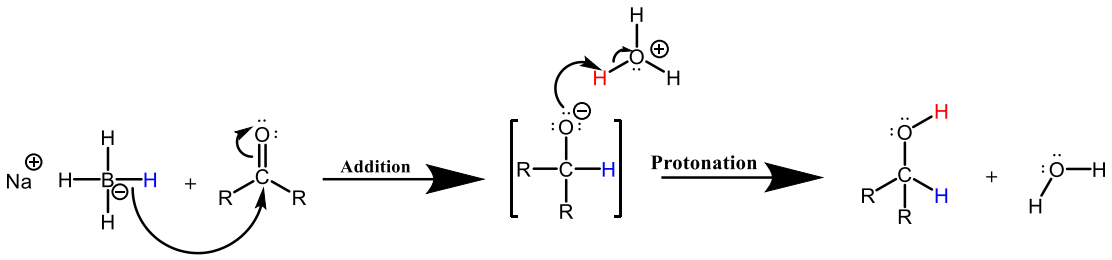

Figure 1.7: Borohydride reduction mechanism

transferred from the nucleophilic borohydride to the electrophilic carbonyl carbon forming an alkoxide/phenoxide intermediate. Then, the intermediate is protonated with an acid (H_3O^+) to form the alcohol. (Fig. 1.7)

The reduction of Suwannee River natural organic matter (SRNOM) and other reference materials from the International Humic Substance Society (IHSS) shows a loss in absorbance with the addition of sodium borohydride. (Fig. 1.8) As the amount of $NaBH_4$ used to reduce a sample increases, the absorbance loss also increases until eventually asymptoting.

The amount of $NaBH_4$ needed to reach this asymptote has been shown to be ~25 fold mass excess, however the exact amount is sample dependent.[56,57] The rate at which the absorbance is lost during reduction has also been investigated for humic and fulvic acid reference materials and indicates that there are several different pools of reducible carbonyls within these samples: one pool that is rapidly (< 3 h) and irreversibly reduced, a second that slower (24-48 h) to reduce but is still irreversible and a third that is reduced, but is reversible under aerobic conditions. The extent to which these groups impact the optics can provide information about the structure of the CDOM sample.[57,68]

When comparing the reduced absorbance to the initial absorbance of the sample, the percent loss is greatest over the long wavelengths (>450 nm) while short wavelengths

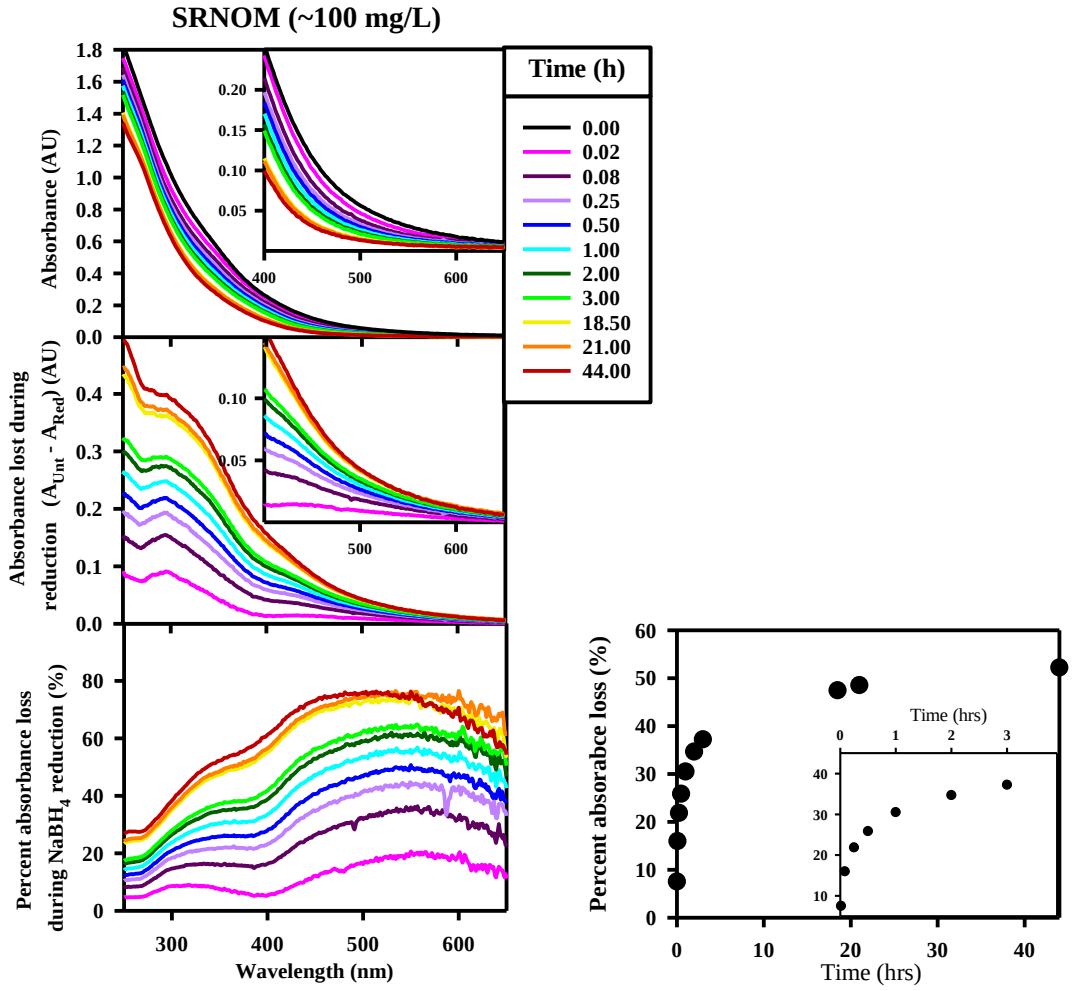

Figure 1.8: Time dependence of absorbance changes with reduction for SRNOM solution reduced with 25 fold mass excess NaBH4. (**Top**) absorbance (**middle**) absorbance lost during reduction (ΔA = Auntreated – Areduced) (**bottom**) percent absorbance loss during reduction $\left(\%\ \text{reduced} = \frac{A_{unt}-A_{red}}{A_{unt}}\right)$ and, (**right**) average percent absorbance loss from 250-650 nm.

(<300 nm) exhibit significantly smaller changes. (Fig. 1.8) These trends have been seen not only in reference materials but also in natural water samples acquired from rivers and the ocean.[16,30,35,46,56,57,68] This preferential loss of long wavelength absorbance following reduction indicates that the reduction significantly impacts the CT interaction. Despite significant losses observed in the long wavelength absorbance following reduction there has always been some absorbance remaining in the visible region, even with very large

amounts of borohydride added to the sample.[56,57] The remaining absorbance could be attributed to a combination of possible factors. First, due to the complexity of CDOM, there may be reducible groups that are not accessible. This is supported by the fact that humic substances (HS) with a larger average molecular size exhibit less absorbance loss following $NaBH_4$ reduction compared to those with a smaller average molecular size.[57,58] Another explanation is the presence of quinones which are reversibly reduced, thus could still participate in CT interactions. However, studies that have investigated the contribution of quinones have suggested that they alone would not account for all the remaining absorbance because their contribution to the long wavelength absorbance is small.[68] The final possibility is that there are chromophores that absorb in the visible region that are not impacted by reduction. However, this would require the presence of extended aromatic, heteroaromatic or conjugated compounds that absorb in the visible and near-IR and currently there is no evidence that there are structures that fit this criteria within HS or CDOM samples.

Following reduction with $NaBH_4$, there is also a significant change in the fluorescence emission. Unlike the loss seen in absorbance following reduction, the majority of fluorescence emission shows enhancement in intensity as well as a slight blue shift. Only at long excitation wavelengths was there a slight loss of emission following reduction. Studies have shown that following reduction the majority of the emission can be enhanced as much as two fold. However, there was often small losses in the visible (emission wavelengths $\gtrsim 500$ nm) at longer excitation wavelengths ($\gtrsim 400$ nm).[16,46,68] (Fig. 1.9)

The changes seen in the optics following reduction are consistent with the electronic interaction model. Sodium borohydride irreversibly reduces ketones and

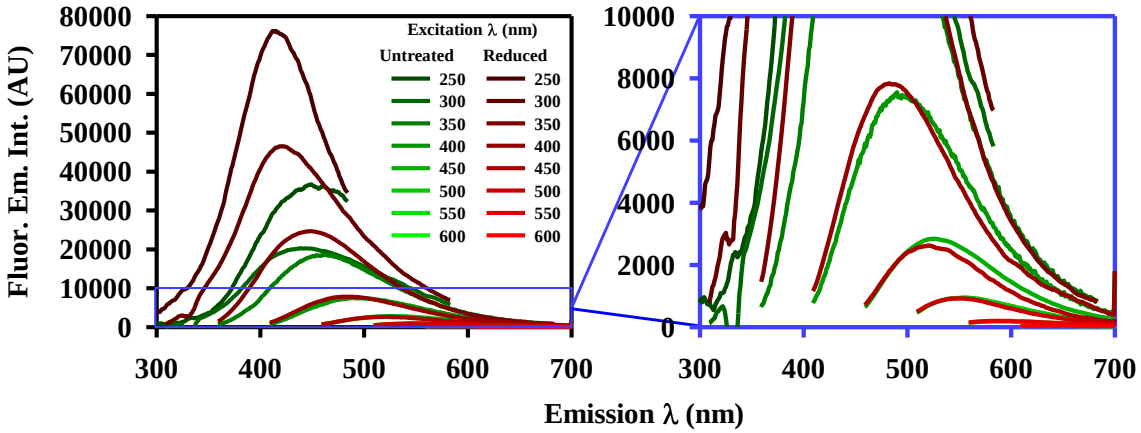

Figure 1.9: Fluorescence emission intensity for untreated (**green**) and $NaBH_4$ reduced (**red**) SRNOM.

aldehydes; with these molecules reduced to alcohols, they no longer participate in charge transfer interaction. This loss of acceptor moieties and subsequent loss in charge transfer (CT) interactions causes the long wavelength absorbance to significantly decrease because the model asserts this absorbance is caused primarily by CT interactions.[10,15] The majority of the emission spectra is enhanced and blue shifted possibly due to discrete donor species that are no longer quenched by acceptors because some acceptors are now reduced.[16]

1.5.2 pH titration

The optical properties of CDOM have also been shown to be pH dependent with both the absorption and fluorescence emission changing with increasing pH.[56,59,62] Absorption spectra of reference materials from the IHSS are significantly enhanced at all wavelengths with increasing pH (pH ~2-12) (Fig. 1.10), while the fluorescence emission was enhanced at all excitation wavelengths when comparing pH 3 to pH 7, but only long excitation wavelengths show an increase in emission when comparing pH 7 to pH 10 (Fig. S1.1).[58] The fact that the optics are pH dependent is critical when comparing samples as the pH at which the measurements were taken would become important. As mentioned

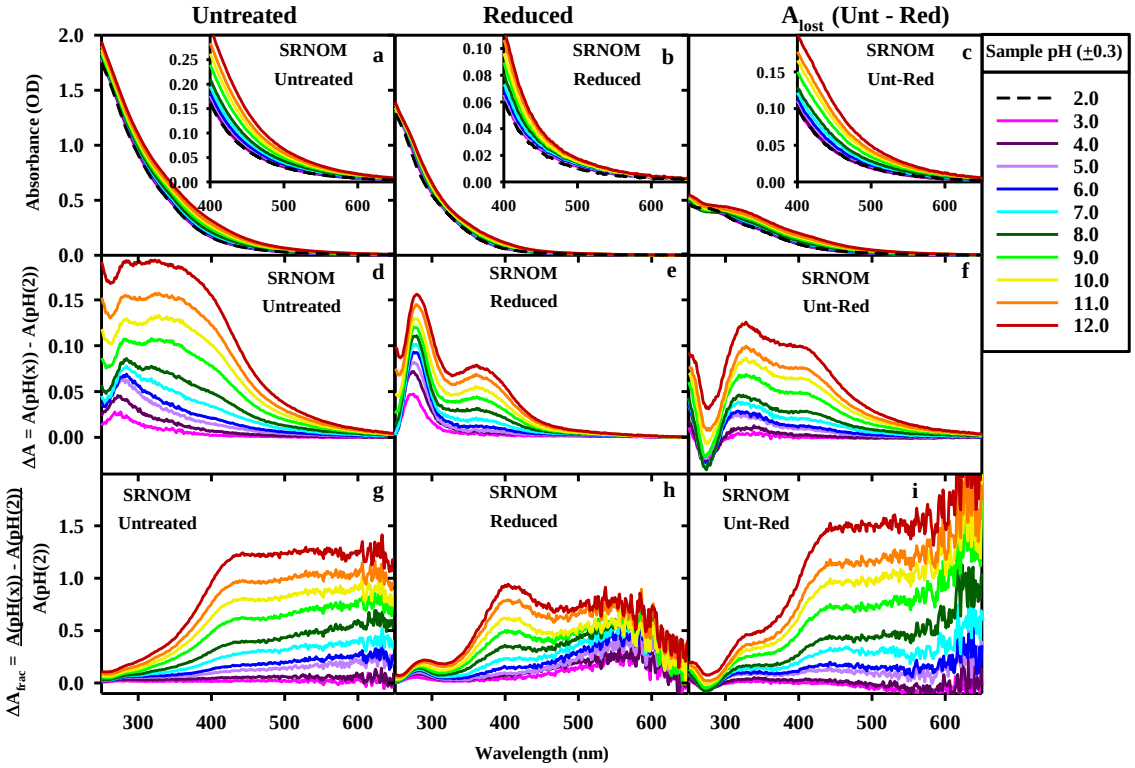

Figure 1.10: pH titration of SRNOM, (**top**) normalized absorbance at increasing pHs (**middle**) difference spectra, and (**bottom**) fractional difference spectra. (**Left**) untreated sample, (**center**) reduced sample and (**right**) untreated – reduced (A_{lost}).

earlier, there are many correlations drawn between different optical parameters and CDOM structure, but many of these parameters do not specify a pH and often the pH of the samples is not reported, making comparisons between data sets challenging. Understanding that the optics change with pH is not only important because it could affect comparisons, but because the pH dependence itself can provide information about the molecular moieties contributing to the absorption of the sample.

The effect of pH on the optical properties of reference materials including humic and fulvic acid from the IHSS has previously been conducted in detail.[56] This work shows that the absorption is enhanced with increasing pH (Fig. 1.10), and that there are distinct optical changes over different pH ranges. Using difference spectra, which are generated by

subtracting the absorbance at pH ~2 from the absorbance at higher pHs (3-12), the contribution of specific moieties can be seen. Three major regions were found in all the reference materials tested: 1) short wavelength band ~280 nm that increases at low pHs in the pKa range for carboxylic acids (3-6), 2) band around 300-450 nm that increases predominantly at high pHs in the pKa range for phenolic groups (>8), and 3) long wavelength region (>450 nm) that is enhanced at all pHs. This indicates that phenols and carboxylic acids may contribute to short wavelength optical properties with their individual absorbance and to long wavelength optical properties through electronic interactions.[17]

Phenols and substituted aromatic carboxylic acids are of interest because they are thought to act as donors in the electronic interaction model and examining the changes in the optics upon deprotonation would better illuminate the structure of CDOM present in a given sample. The study done on reference materials from the IHSS showed that there were some clear difference between the samples from different sources.[56,58] Thus applying this technique to CDOM samples from different geographical locals will not only provide information about the molecular groups present in the sample and how they influence the optics but should also provide information about the source of the material.

1.6 Possible sources of CDOM in open oceans:

Although CDOM in riverine and coastal regions is believed to be mostly terrestrial in origin, the source and chemical structure of CDOM in the open ocean is more controversial. Past research, using single wavelength optical measurements combined with properties such as chlorophyll concentration or apparent oxygen utilization (AOU), has led some researchers to conclude that the majority of CDOM in open oceans is produced in situ from marine source material [2,5,70–73]. In contrast, other studies based on detailed optical

and chemical measurements have concluded that the long wavelength or "humic like" optical properties arise primarily from a terrestrial source. [1,16,45,74–76] However, many samples also have discrete absorbing and emitting bands predominantly in the UV region that vary based on location. These more unique features indicate a marine source or possible modification of terrestrial material [16].

Although the optical properties of CDOM are often studied, mass spectrometry (MS) and isotope analysis are other popular tools for examining the structure and source of DOM/CDOM. These techniques have been employed on samples from a variety of locations including the open ocean. One study using ultrahigh-resolution mass spectrometry found that there are a core group of molecular formulae (184 formulae) that are characteristic of riverine systems and can be tracked to the open ocean DOM. [77] This high molecular similarity between terrigenous and marine DOM has also been noted by Koch *et al*. (2005). They state that it could indicate a larger terrestrially-derived component of DOM present in the ocean than previously thought. However, they concluded that the similarities are due to general chemical structures in DOM that are refractory and are thus "inaccessible or energetically unattractive for microbial utilization" and these general structures are independent of the source of the organic matter.[78] Another MS study found that the molecular signature of DOM samples in the deep ocean is fairly uniform, but the same uniformity is not seen in the microbial communities, which are highly variable. This discrepancy suggests that there may be a terrestrial source of CDOM that is causing the intense similarities and that the microbial contribution is not as significant.[79] This uniformity was also seen by Sleighter and Hatcher (2008) who noted that there is significant overlap of peaks on Van Krevelen diagrams (plots of atomic O/C versus H/C

ratios) in the lignin region, which is indicative of terrestrial sourced material and suggests that lignin could be a significant source of DOM in the ocean. [54]

Analysis of $\delta^{13}C$ has also indicated that there may be a fraction of terrestrial DOM in open ocean. Terrestrial sourced material tends to be more depleted in ^{13}C with stable isotope values that range from ~ -28 to -26 ‰ compared to that of marine material with values ranging from ~ -20 to -22 ‰. Thus the isotope values can provide information about the source of DOM in the aquatic environment.[80] Research conducted in the North Pacific Ocean by Zigah et al. (2017) indicates that DOC present in the open ocean could be derived from terrestrial and hydrothermal sources based on concentration and isotopic profiles.[81]

1.7 Importance and overview of research:

Due to the many roles that DOM/CDOM plays in the aquatic environment, an understanding of its fate and transport, as well as the structural basis of its optical properties, is needed to obtain valuable information about this significant carbon pool.

Prior work in the Equatorial Atlantic Ocean (EAO) provided evidence of a major terrestrial "humic-like" component of the CDOM[16] in the open ocean. Part of the research presented herein is an expansion of this prior research to a depth profile in the North Pacific Ocean (NPO) at Station ALOHA, by monitoring the optical properties before and after sodium borohydride reduction (**Chapter: 3**). The majority of Chapter 3 was published in Marine Chemistry in 2018 (reference 35). The optical properties of both NPO and EAO samples were also compared to the Delaware River, Delaware Bay, and Middle Atlantic Bight (MAB) (**Chapter: 5**). Reference materials from the International Humic Substance Society (IHSS) were also evaluated and used to test the impact that sodium borohydride reduction and pH titration has on the optical properties of samples from different sources

both before and after exposure to solar radiation. (**Chapter: 4**). pH titrations were also performed on samples from multiple geographic locals which is also included in **Chapter 5**. The detailed optical measurements acquired for samples from these different geographic locales allowed for comparisons between samples from rivers to open oceans. Reduction and pH titration provided more details as to the structures responsible for the optical properties including ketones, aldehydes, phenols and carboxylic acids. Comparison of the samples' response to these chemical tests indicated high degrees of similarity between samples from all locals indicating that there is a component of terrestrial CDOM that is transported throughout the aquatic environment.

However, there were some notable changes moving from riverine samples to offshore and open ocean samples including larger spectral slopes which indicates a decrease in the average molecular size of the CDOM which could be due to photo or microbial degradation. Samples from the deep open ocean were highly comparable no matter if they were from the Atlantic or Pacific suggesting that there is a component of CDOM that is not easily degraded and is transported throughout the deep ocean (**Chapter: 5**).

This research helped to develop a set of tests that could be applied to any CDOM sample in order to investigate its source and structure. These more well defined and informative protocols can now be used to investigate CDOM from a wide ranges of sources, and will provide a more effective and uniform way of comparing CDOM samples. To show the versatility of these tests, they were also applied to CDOM collected from more discreet sources such as exudate from mangrove leaves (**Supplemental: S5b**).

Because natural waters from the open ocean exhibit very low absorption, a long pathlength spectrometer was used for absorbance measurements. However, due to the lack of a standard calibration/validations procedure, results obtained from these types of instruments were not always comparable. To improve reproducibility and inter-laboratory comparability, a detailed protocol was developed (**Chapter: 2**). The majority of Chapter 2 was previously published in Limnology and Oceanography: Methods in 2018 (reference 127). This protocol included suggested methods for: 1) pathlength determination, 2) cell cleaning, 3) sample preparation 4) precision and accuracy measurements and, 5) acquiring a salinity reference. Following this newly developed method, more reproducible measurements of natural water absorbencies were acquired.

Chapter 6 is a critical evaluation of a popular tool used in this field, to evaluate Excitation Emission Matrixes (EEMs), called parallel factor analysis (PARAFAC). PARAFAC is a method of decomposing multi-way data arrays such as a set of EEMs into their underlying signals. PARAFAC has gained in popularity due to its ease of use and because it can handle large datasets. However, when using PARAFAC for environmental samples, the usefulness of the results is often limited due to some of the assumptions that the model requires. Thus because PARAFAC has gained in popularity it is important to evaluate its usefulness and limitations so that it does not add confusion to the field.

Chapter 2: A calibration/validation protocol for long/multi-pathlength capillary waveguide spectrometers.

The majority of this chapter has been published in reference 127:

Cartisano, C. M., Del Vecchio, R. & Blough, N. V. A calibration/validation protocol for long/multi-pathlength capillary waveguide spectrometers. *Limnol. Oceanogr. Methods* (2018). doi:10.1002/lom3.10282

2.1 Abstract:

Long/multi-pathlength spectrometers are being employed increasingly in ocean science, but detailed calibration/validation protocols for these instruments remain unavailable. The lack of such protocols has led to the collection of absorption data from different instruments that is not always comparable. The goal of this work was to develop procedures that improve inter-laboratory data reproducibility and accuracy. A World Precision Instrument (WPI) multi-pathlength liquid capillary waveguide spectrometer along with a Shimadzu dual-beam spectrometer were employed to evaluate the proposed protocols, which address the following issues: 1) sample cross-contamination due to improper cell cleaning, 2) non-standardized sample preparation, 3) errors in effective pathlength determination, and 4) offsets due to refractive index effects (ex. high salinity samples). Effective pathlength calculation is critical given that the measured and manufacturer-provided pathlengths can differ significantly, with the provided pathlengths resulting in data with large variation (up to 21 %) and percent error (up to 33 %) when employing different pathlengths. When these proposed protocols were applied, we found that the WPI spectrometer's precision (measured as a coefficient of variation) was < 0.6 % for intra-day measurements and < 1.5 % for inter-day measurements, and there was < 2 % error in absorbance measurements. These procedures allowed for the correction of the significant baseline offsets caused by differences in refractive index between reference and

sample, by either subtracting a collected or a generated reference spectrum that matches the offset. Our results indicate that employing the procedures described herein will provide accurate, reproducible and pathlength-independent absorption data.

2.2 Introduction:

Long pathlength liquid core capillary waveguide spectrometers are extremely valuable instruments for measuring very weakly absorbing samples and have therefore gained popularity in the ocean sciences owing to their ability to measure the low levels of chromophoric dissolved organic matter (CDOM) in oligotrophic seawaters [16,28,35,82–84] as well as in trace analysis[85–88]. CDOM, which absorbs light over the UV and visible wavelengths, is an important natural component found ubiquitously in aquatic environments and is a subset of the dissolved organic matter (DOM) pool. CDOM plays a substantial role in determining the aquatic light field, with its absorption at short wavelengths (< 440 nm) usually dominating total absorption in the upper water column of the open oceans [1–5]. Because of its importance, optical spectroscopy as well as satellite ocean color measurements have been employed to examine its distribution and dynamics [1,5,21,89–92]. However, the very low levels of CDOM absorption observed in the open ocean are difficult to determine accurately by standard benchtop spectrometers, which are generally limited to short pathlengths (≤ 10 cm). Thus, instrumentation capable of measuring these low signals are required. These instruments usually employ longer pathlengths such as those used in the UltraPath manufactured by World Precision Instruments (WPI). The UltraPath and other liquid core waveguide instruments are used, not only because of the longer pathlengths available, but also because they are typically

more portable and fairly simple to setup in the field, and usually use smaller sample volumes.

Two types of liquid core waveguide cells are commonly used, one with Teflon AF tubing (used in the UltraPath and focus of this work) and a second with fused silica capillary tubing and an outer coating of Teflon AF. Comparisons of these cell types have been conducted previously [93], along with measurements of linearity, precision, accuracy and effective pathlength [28,88,90,94,95]. However, consistent results among instruments are still not always achieved [96].

The variability in the determined absorption coefficient among samples acquired with different instruments[96], indicates that better calibration/validation protocols are needed. To generate reproducible and intercomparable data, we developed a standard protocol that addressed the following issues: 1) instrument cleaning, 2) sample preparation, 3) effective pathlength determination, 4) evaluation of instrument accuracy and precision, and 5) appropriate correction for refractive index effects using calibration curves (i.e. salinity matching NaCl solutions). After applying these procedures, the data collected with the WPI UltraPath spectrometer was highly reproducible, accurate and pathlength-independent.

2.3 Methods:

2.3.1 Materials

Standard reference material 935a (potassium dichromate, $K_2Cr_2O_7$) was obtained from National Institute of Standards and Technology (NIST). Tris-(hydroxymethyl)aminomethane (THAM, molecular biology grade), and perchloric acid ($HClO_4$, 70%, ACS grade) were obtained from Fisher BioReagents/chemicals. Phenol red

($C_{19}H_{14}O_5S$, ACS grade; Lot # MKBX8070V) was obtained from Sigma-Aldrich, while sodium chloride crystals (NaCl, ACS grade) were obtained from EMD Inc. Purified water was obtained from a Milli-Q Plus purification system by Millipore. Nylon syringe filters (pore size of 0.2 µm) and hydrochloric acid (HCl, 36.5-38%, ACS grade) were obtained from VWR chemicals. Methanol (MeOH, >99.9%, gradient grade) was obtained from Honeywell Burdick and Jackson. The concentrated non-foaming liquid cleanser (Contrad NF) was obtained from Decon Labs, Inc.

Two natural water samples were collected from a surface water pumping system at a depth of 2 meters during a research cruise onboard the R/V Hugh R. Sharp in July 2016: a Delaware Bay sample (38°49'07.2"N, 75°05'07.2"W) and an offshore sample (38°09'31.8"N, 74°44'54.6"W) with salinities of 31.43 and 31.60 PSU, respectively. Samples were immediately filtered through 0.2 µm nylon syringe filters pre-washed with purified water (see *Optical measurements* below) obtained from VWR, and stored at 4 °C in amber glass vials (~2 months).

2.3.2 Equipment

A World Precision Instrument (WPI) multi-pathlength liquid capillary waveguide absorption spectrometer (MPLCW, UltraPath) (Fig. 2.1 and S2.1), having a capillary with light collection at nominal pathlengths of ~ 2, 10, 50 and 200 cm (Table 1), was employed for the absorption measurements. Absorption measurements were also acquired with a Shimadzu dual-beam UVPC 2401 benchtop spectrophotometer employing 1 and 10 cm pathlength quartz cuvettes (Uvonic Instruments inc.) (Table 2.1).

A Thermo-Scientific micro pH electrode coupled to an Orion 4 Star pH ISE benchtop meter was employed for pH measurements. A Mettler AT261 Delta Range

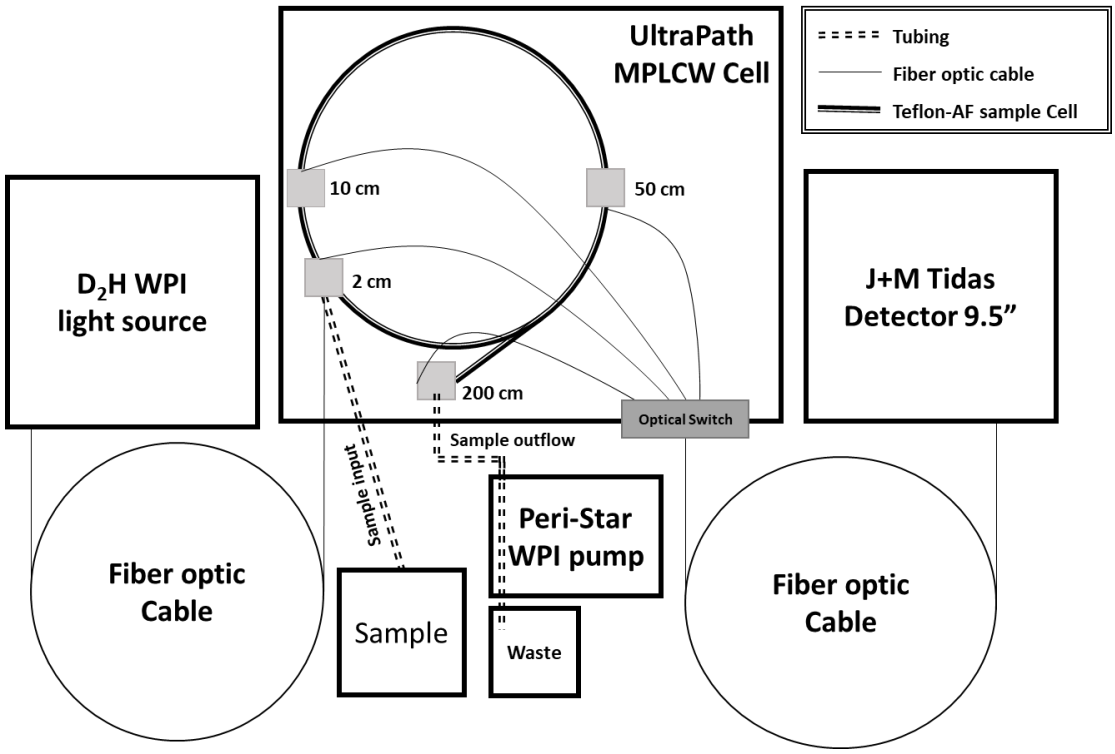

Figure 2.1: Schematic diagram of the WPI MPLCW (UltraPath) modified from Miller et al. (Miller et al., 2002). System components and nominal pathlengths are reported.

($1x10^{-5}$ gram sensitivity) and a Mettler PJ400 ($1x10^{-2}$ gram sensitivity) balances were used for mass measurements. A Stabil-Therm OV-12A oven from Blue M Electric Co. was employed for baking the sodium chloride.

Volumetric flasks from Pyrex and Kimax were used to prepare solutions, with flask volume verified using purified water (density at ~23°C: 0.997 g/cm^3) and the Mettler PJ400 balance. Micropipettes from Fisherbrand and Eppendorf Research were employed for small volume measurements; these pipettes were calibrated every 6 to 12 months by PetteCal.

Table 2.1: Instruments and optical cells examined during this study.

cell	Manufacturer	Instrument	cell type	Nominal pathlength (cm)	Manufacturer Provided pathlength (cm)	*Effective pathlength (cm)	Deviation from provided pathlength (%)
I	Uvonic Instruments inc.	Shimadzu UVPC 2401	Rectangular quartz	1	1.00 ± 0.01	0.99 ± 0.01	1.0
II	Uvonic Instruments inc.	Shimadzu UVPC 2401	Cylindrical quartz	10	10.00 ± 0.1	9.99 ± 0.1	0.1
III	World Precision Instruments	UltraPath MPLCW	Solid Teflon AF tubing (inner diameter ~2 mm)	2	2.05 ± 0.1	2.72 ± 0.06	32.7
IV	World Precision Instruments	UltraPath MPLCW	Solid Teflon AF tubing (inner diameter ~2 mm)	10	9.99 ± 0.1	10.5 ± 0.2	4.8
V	World Precision Instruments	UltraPath MPLCW	Solid Teflon AF tubing (inner diameter ~2 mm)	50	50.07 ± 0.5	49.7 ± 1	0.7
VI	World Precision Instruments	UltraPath MPLCW	Solid Teflon AF tubing (inner diameter ~2 mm)	200	208.01 ± 1	199 ± 2	4.3

*Determined using the protocols described in the text

2.3.3 Solutions

Phenol red and $K_2Cr_2O_7$ solutions were prepared following the protocols described by Belz et al. (2006), Burke and Mavrodineanu, (1977), and May and Trahey, (2000), but employing differing concentrations.

The phenol red stock solution (16 μM) was prepared by adding $1.10x10^{-3}$ g of phenol red (354.38 g/mol), weighed on the Mettler AT261 balance, to a small amount (< 100 mL) of THAM stock solution (0.05 M) in a 200 mL volumetric flask. Following dissolution of the phenol red, the volumetric flask was filled to 200 ± 0.2 mL using the same THAM stock solution. The THAM solution (50 mM) was prepared by adding 6.06 grams of THAM (121.14 g/mol), weighed on the Mettler PJ400 balance, to $1.0x10^3$ ± 0.6 mL of purified water. Once the phenol red solution was prepared, its pH was recorded (~10.4) using the Thermo-Scientific micro pH electrode.

The $K_2Cr_2O_7$ solution ($2.0x10^2$ ppm) was prepared by adding 200.0 mg of $K_2Cr_2O_7$ (294.18 g/mol), weighed on the Mettler AT261 balance, to $1.0x10^3$ g of dilute $HClO_4$ (1.0

mM) in a volumetric flask. The $HClO_4$ solution (1.0 mM) was prepared by diluting 85.5 ± 0.5 µL of concentrated $HClO_4$ (11.7 M) in $1.0x10^3$ ± 0.6 mL of purified water.

Sodium chloride solutions, ranging from 5 to 45 ppt, in 5 ppt increments, were prepared with NaCl previously baked at 180 °C for 24 hrs. The NaCl was weighed on the Mettler PJ400 balance and dissolved in purified water within volumetric flasks.

2.3.4 Optical measurements

Absorption spectra were collected from 188 to 725 nm employing the WPI UltraPath spectrometer, but results are presented over smaller ranges based on the WPI suggested operational wavelength range (250-730 nm; World Precision Instruments, 2007) and the wavelength ranges of the standard / reference materials. Both the light source (WPI D2H UV-VIS-NIR light source) and detector (J&M TIDAS) were switched on and allowed to stabilize prior to any measurements (typically lamp stabilization took ~2-3 hours (Fig. 2.2a and b)). The instrument parameters were set using the WPI provided software (TIDAS Spectralys) following the WPI manual as follows: a) selecting the pathlength by adjusting the fiber optic cable; b) setting the integration time to achieve an intensity of ~70 % of the maximum; c) selecting the scan range (188-725 nm) and wavelength interval (1 nm); d) selecting the number of absorbance scans averaged per output by adjusting the accumulations number (3 scans). Before collecting a spectrum, the instrument was baselined to purified water which was drawn into the cell using a peristaltic pump at a flow rate of ~ 18.4 mL/min. The flow was then stopped and a dark spectrum was acquired with the internal shutter of the light source closed. The shutter was then opened and a reference scan was acquired with purified water in the cell. Once the spectrometer was baselined, sample spectra were collected by pumping sample into the cell at the same flow rate,

stopping the flow and acquiring the spectrum. All sample spectra were thus referenced to purified water. All measurements were conducted at room temperature (23 °C ± 1) to minimize changes in refractive index due to temperature [82], as well as to changes in water

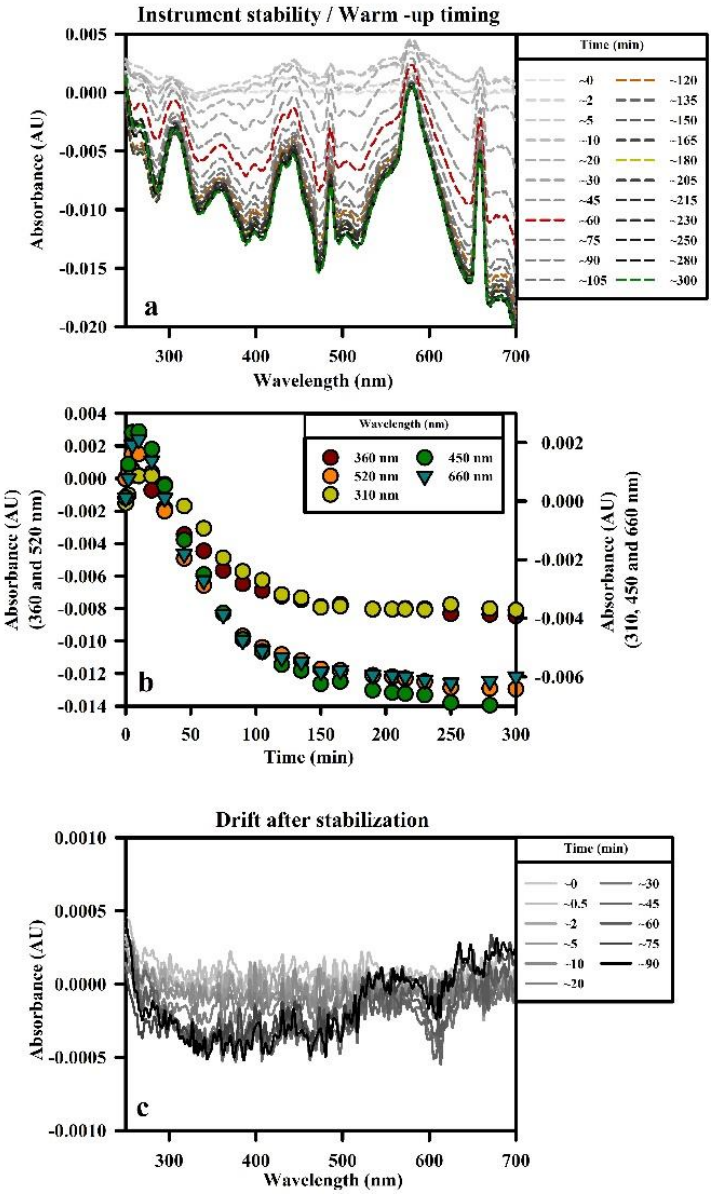

Figure 2.2: (**a**) Consecutive water scans taken after turning on the instrument and immediately acquiring a dark and reference scan with purified water in the cell. The time in minutes is the time since the reference scan was acquired (and the lamps turned on), scans at 60, 120, 180 and 300 min are highlighted for comparison. **(b)** Absorbance (AU) at select wavelengths plotted against time from last reference. **(c)** Consecutive water scans taken after the instrument was turned on and allowed to stabilize (~ 3 hrs.) before taking a dark and reference scan of water.

absorption coefficients [100,101]. Because the WPI UltraPath cells are highly sensitive to light scattering by particles, a syringe was employed to pass the samples through a 0.2 µm nylon syringe filter prior to being pumped into the WPI UltraPath cell; these filters were rinsed with at least 100 mL of purified water to remove any absorbing residue prior to coming in contact with samples, with the absorbance of the filtered purified water monitored to ensure that the filters were clean prior to use (Fig. 2.3).

Absorption spectra were also collected from 190 to 820 nm employing the Shimadzu UVPC 2401 benchtop spectrophotometer. The dual-beam spectrometer was baselined against air in both sample and reference beam paths. Spectra of all samples were then recorded versus an air reference. An absorption scan of purified water referenced to air was employed as the blank and subtracted from the sample spectra during data processing. Referencing to air and recording scans of water allows for close monitoring of any variation in the water and/or the cells, thus allowing for a better control of the quality of the blank.

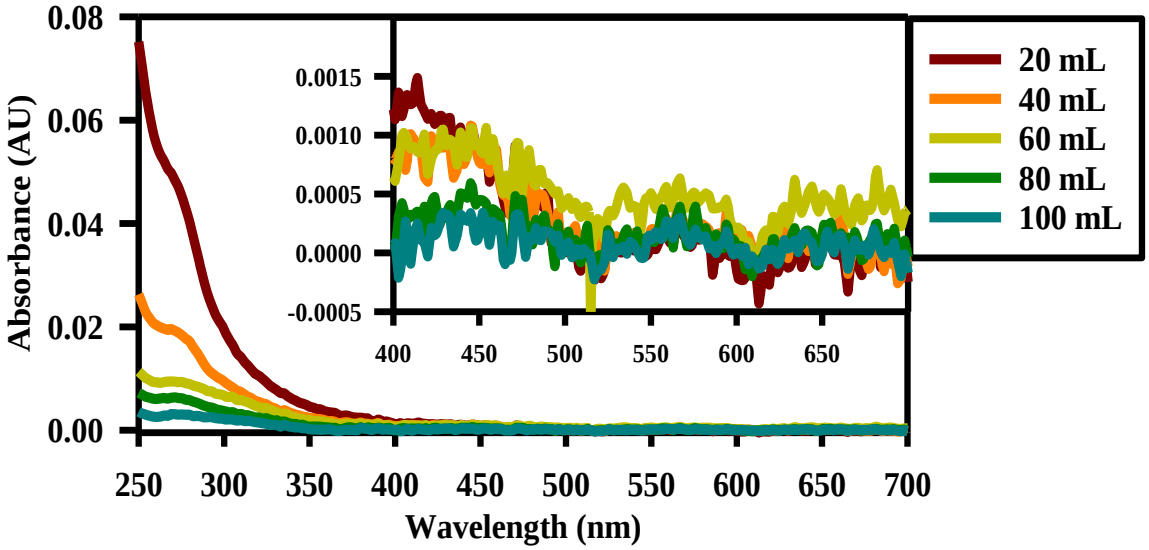

Figure 2.3: Absorption spectra of purified water passed through VWR nylon filters as function of volume of water passed through the filter, referenced to unfiltered purified water. Absorption spectra recorded with the UltraPath employing cell VI (~200 cm, Table 1). Inset is a magnification of the long wavelength region (400-700 nm).

2.3.5 Cleaning of quartz cuvettes and the WPI UltraPath cells

Cleaning of standard 1 cm and 10 cm quartz cuvettes (cell I and II) was accomplished by rinsing with dilute acid, purified water, and small amounts of the sample by hand. To clean the UltraPath cells prior to measurements, the instrument parameters were first set for cell VI (~200 cm), with dark and reference scans then recorded with purified water in the cell. The cell was then refilled with water and a water absorbance spectrum was recorded ("pre-cleaning scan"). Twenty milliliters each of the Contrad NF cleaning solution (10% v/v in purified water), methanol, and HCl (10% v/v in purified

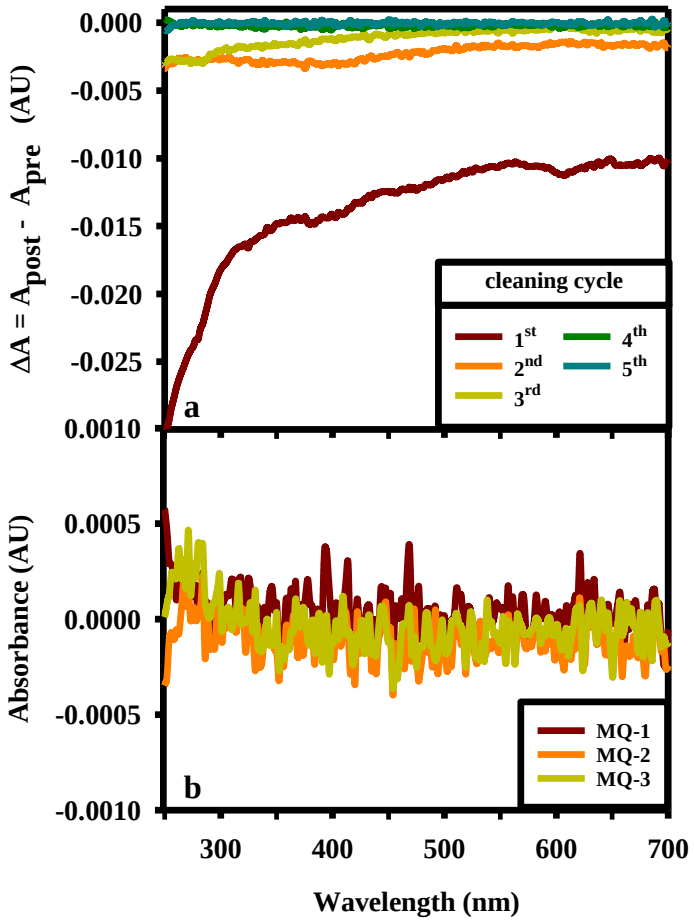

Figure 2.4: (**a**) Difference spectra ($\Delta A = A_{post} - A_{pre}$) for purified water following 5 consecutive cleaning cycles. (**b**) Three consecutive scans of water recorded following the final cleaning cycle and the acquisition of new dark and reference scans, with the cell re-filled with water.

water) were passed consecutively through the cell at a flow rate of ~18.4 mL/min. The cell was subsequently flushed with purified water for ~5 minutes. A new water absorbance spectrum was then recorded ("post-cleaning scan"). The "post-cleaning scan" (A_{post}) was subtracted from the "pre-cleaning scan" (A_{pre}), thus providing ΔA ($\Delta A = A_{post} - A_{pre}$); if ΔA was significantly different from zero (> ± 0.0005 AU) over the 250-700 nm range, this cleaning cycle was repeated, with the old "post-cleaning scan" becoming the new "pre-cleaning" scan. This cleaning procedure was repeated until there was no significant difference between the pre- and post-cleaning water spectra ($\Delta A \simeq 0.0$) (Fig. 2.4a). Once the cell was clean, new dark and reference scans were acquired along with three consecutive water scans, with the cell flushed with fresh purified water between each scan (MQ 1-3 in Fig. 2.4b).

2.3.6 Determination of cell pathlength

The effective pathlength (l_{eff}) was acquired experimentally for cells I-VI (Table 1) employing both a standard material (phenol red) and NIST reference material 935a (potassium dichromate; $K_2Cr_2O_7$) following three different protocols (Eqs. 2.1-2.3, below). The first protocol employed the method from Belz et al. (2006),

$$l_{eff} = \frac{A(peak)_{cells\ (II-VI)} - A(700)_{cells\ (II-VI)}}{A(peak)_{cell\ (I)} - A(700)_{cell\ (I)}} * l_{cell\ (I)} * \frac{C_{cell\ (I)}}{C_{cells\ (II-VI)}}. \qquad \textbf{Eq. 2.1}$$

where A(peak) is the absorbance (in absorbance units, AU) of the standard or reference material at the peak maxima (Table 2), A(700) is the sample absorbance at 700 nm, $l_{cell\ (I)}$ is the pathlength of cell I (1.00 cm), and C is the concentration of the sample being measured.

A second protocol employed the molar absorption/specific absorption coefficient of the standard/reference material [94,98,102] (Table 2.2) to calculate the pathlength through Beer's Law ($A_\lambda = \varepsilon_\lambda \cdot b \cdot C$) (Eq. 2.2),

$$l_{eff} = \frac{A_b(peak)}{\varepsilon_{(peak)} * C} \qquad \textbf{Eq. 2.2}$$

where C is the concentration of the standard/reference material, A_b(peak) is the baseline-corrected absorbance at the peak maxima, and ε_{peak} is the molar absorption coefficient/specific absorption coefficient of the standard/reference material at the peak maximum (Table 2). The absorbance spectrum was baseline-corrected by subtracting the average absorbance from 700-715 nm from the entire spectrum; this baseline correction was always less than 0.001 AU while the peak absorbance ranged from 0.06 – 2.9 AU for these samples.

Because commercially-available phenol red is known to contain impurities and its absorption spectrum is dependent on both pH and temperature [103], the molar absorption coefficient was determined under well-defined conditions (pH 10.4 and 23 °C) for our particular lot of phenol red employing the duel beam Shimadzu spectrophotometer and the 1 cm cell. Eight independently prepared solutions were employed to generate an absorbance versus concentration curve, with the molar absorption coefficient then determined from the slope acquired from the linear regression (Table 2.2).

The third protocol employed the molar absorption coefficients/specific absorption coefficients along with the slope of absorbance versus concentration curve generated from the standard/reference materials (Eq. 2.3),

$$l_{eff} = \frac{Slope_b(peak\ \lambda)}{\varepsilon_{(peak\ \lambda)}} \qquad \textbf{Eq. 2.3}$$

where $Slope_b$ (peak λ) is the slope of the absorbance vs. concentration at the peak wavelength, and $\varepsilon_{peak\lambda}$ is the molar absorption coefficient/specific absorption coefficient at the same wavelength (Table 2.2).

For all pathlength calculations, absorbance measurements of five-independently prepared phenol red solutions and five-independently prepared dichromate solutions were collected at the peak wavelengths of the phenol red (558 nm) and the dichromate (257, 350 nm). These solutions were prepared at differing concentrations for each cell in order to generate absorbance values between ~0.2 and 1.0. For the first and second protocols (Eq. 2.1-2.2), the values determined for l_{eff} at each peak wavelength were averaged to obtain the pathlength of each cell (n =5). For the third protocol, the slope at each peak wavelength was obtained from a linear regression of the data. For all pathlength calculations, only absorbance values within the linear range of the instrument were employed (see Instrument linear range below).

Table 2.2: Peak wavelengths and molar absorption coefficients/specific absorption coefficients for phenol red and K_2Cr_2O7 solutions.

Standard/reference solution	Peak Wavelength (nm)	molar absorption coefficient/specific absorption coefficient	Reference
Phenol red in THAM (0.05 M)	558	$6.36 \times 10^4 \pm 0.05 (M^{-1}\ cm^{-1})$	This paper [a]
Phenol red in sodium carbonate (25 mM)	558	$6.2 \times 10^4 (M^{-1}\ cm^{-1})$	Belz et al., 1999 [b]
$K_2Cr_2O_7$ in HClO4 (1.0 mM)	257	$14.3 (kg\ g^{-1}\ cm^{-1})$	Burke and Mavrodineanu, 1977
$K_2Cr_2O_7$ in HClO4 (1.0 mM)	350	$10.7 (kg\ g^{-1}\ cm^{-1})$	Burke and Mavrodineanu, 1977

[a] Note that the molar absorption coefficient for phenol red (Sigma-Aldrich, Lot # MKBX8070V) is likely to be lot specific due to impurities and is pH and temperature dependent (Lai et al. 2016)
[b] Calculated from absorption data provided from Belz et al. 1999

2.3.7 Methodological precision and accuracy

The methodological precision was examined by recording three scans each of six dichromate solutions and eight phenol red solutions each day over a period of three days employing both spectrometers (Shimadzu and WPI UltraPath). For the Shimadzu benchtop instrument, each cell (I and II) was filled with a solution, the spectrum recorded relative to an air reference and the sample discarded. This step was repeated two additional times employing the same stock solution. A purified water spectrum referenced to air was also measured and then subtracted from the sample spectra during the data processing. For the WPI UltraPath, the solution was drawn into the cell (III-VI) at a flow rate of ~18.4 mL/min and the absorbance recorded in stopped-flow mode relative to purified water. This procedure was repeated two additional times to gather triplicate measurements of the same stock solution. Because the UltraPath is a single beam instrument, drift of the reference over time can be a significant source of error. Examination of the instrument drift after the lamp was allowed to stabilize indicated that acquiring a new dark and reference scan every ~30 min was sufficient to account for drift (Fig. 2.2). These measurements were repeated with both spectrometers over three separate days employing the same stock solutions.

Within each day, the triplicate scans were averaged and the standard deviation calculated to determine intra-day variation (n=3) as a percentage (Eq 2.4). Similarly, the triplicate scans across the three days were averaged, the standard deviation calculated and used to determine the inter-day variation (n=9) (Eq. 2.4).

$$\text{coefficient of variation } (\%) = \left(\frac{\text{standard deviation}}{\text{average}}\right) * 100 \qquad \textbf{Eq. 2.4}$$

To examine the variation with respect to absolute absorbance, the standard deviations of the six $K_2Cr_2O_7$ solutions for each pathlength were averaged at matching

absorbance to calculate intra-day deviation; similarly the standard deviations for the solutions taken across three days were also averaged to examine inter-day deviation.

The six dichromate solutions and eight phenol red solutions were also employed to examine the linear response of the instrument by plotting the absorbance of the samples at their peak maxima versus the concentration of the solutions to evaluate where the absorbance deviated from linearity.

2.3.8 Instrument accuracy

New stock solutions of both phenol red and $K_2Cr_2O_7$ were prepared for the determination of accuracy; thus the pathlengths were determined using one set of solutions while accuracy was determined using independently prepared solutions. The theoretical absorbance (A_{theor}) was calculated for each solution employing the effective pathlengths (determined as described above), the molar absorption coefficient/specific absorption coefficient and Beer's law. For each cell, a total of nine solutions of each standard were tested; three solutions with peak absorbance in each of three absorbance ranges (0.2 ± 0.1 AU, 0.4 ± 0.1 AU and 0.8 ± 0.2 AU). The accuracies were calculated as percent error by comparing the experimental (A_{exp}) and theoretical (A_{theor}) absorbance (Eq. 2.5) of the three solutions in each range, and were averaged and reported for each pathlength.

$$\text{Percent error in accuracy} = \left(\frac{|A_{exp} - A_{theor}|}{A_{theor}}\right) * 100 \qquad \textbf{Eq. 2.5}$$

The accuracy of the effective pathlengths was also evaluated by comparing the absorption coefficient (m^{-1}) of natural waters acquired using each of the cells III-VI in the WPI UltraPath, as follows (Eq. 2.6),

$$a(\lambda) = \frac{2.303\ A(\lambda)}{l_{eff}} \qquad \textbf{Eq. 2.6}$$

where A(λ) is the absorbance of the sample at a given wavelength and l_{eff} is the effective pathlength of cells III-VI.

2.3.9 Salinity reference spectra

The absorption of a pure water sample can change with salinity [29], but at the wavelengths examined in this study (250/300-700 nm), these changes are minimal. However, because the liquid core capillary waveguide measurements rely on total internal reflection, changes in the refractive index of the inner core (liquid sample) can substantially alter light throughput to the detector. This results in spectra of higher refractive index media such as saline solutions ($n \approx 1.339$, seawater) being considerably offset when referenced to a lower refractive index medium such as purified water ($n = 1.333$) [84]. To acquire spectra in high salinity waters, this offset must be corrected appropriately [16,28,82,90,96].

To address this issue, and to evaluate the magnitude of the cell-dependent offset produced by the increase in refractive index with increasing salt concentration, salinity reference spectra were acquired relative to a purified water baseline for NaCl solutions ranging from 5 to 45 ppt in cells III-VI of the WPI UltraPath instrument. The cell-dependent offsets at each wavelength across the spectrum were plotted against NaCl concentration to generate calibration curves for each wavelength. The slopes of these calibration curves were then employed to generate a salt reference spectrum for any given salinity (Eq. 2.7),

$$\text{salt reference spectrum } (\lambda) = \Big(\big(\text{slope}(\lambda)\big) * (\text{salinity})\Big) \qquad \textbf{Eq. 2.7}$$

In principle, higher salinity samples whose spectra are recorded relative to purified water can then be corrected by subtracting the appropriate salt reference spectrum. This approach is similar to that described by Nelson et al. (2007), except that they employed

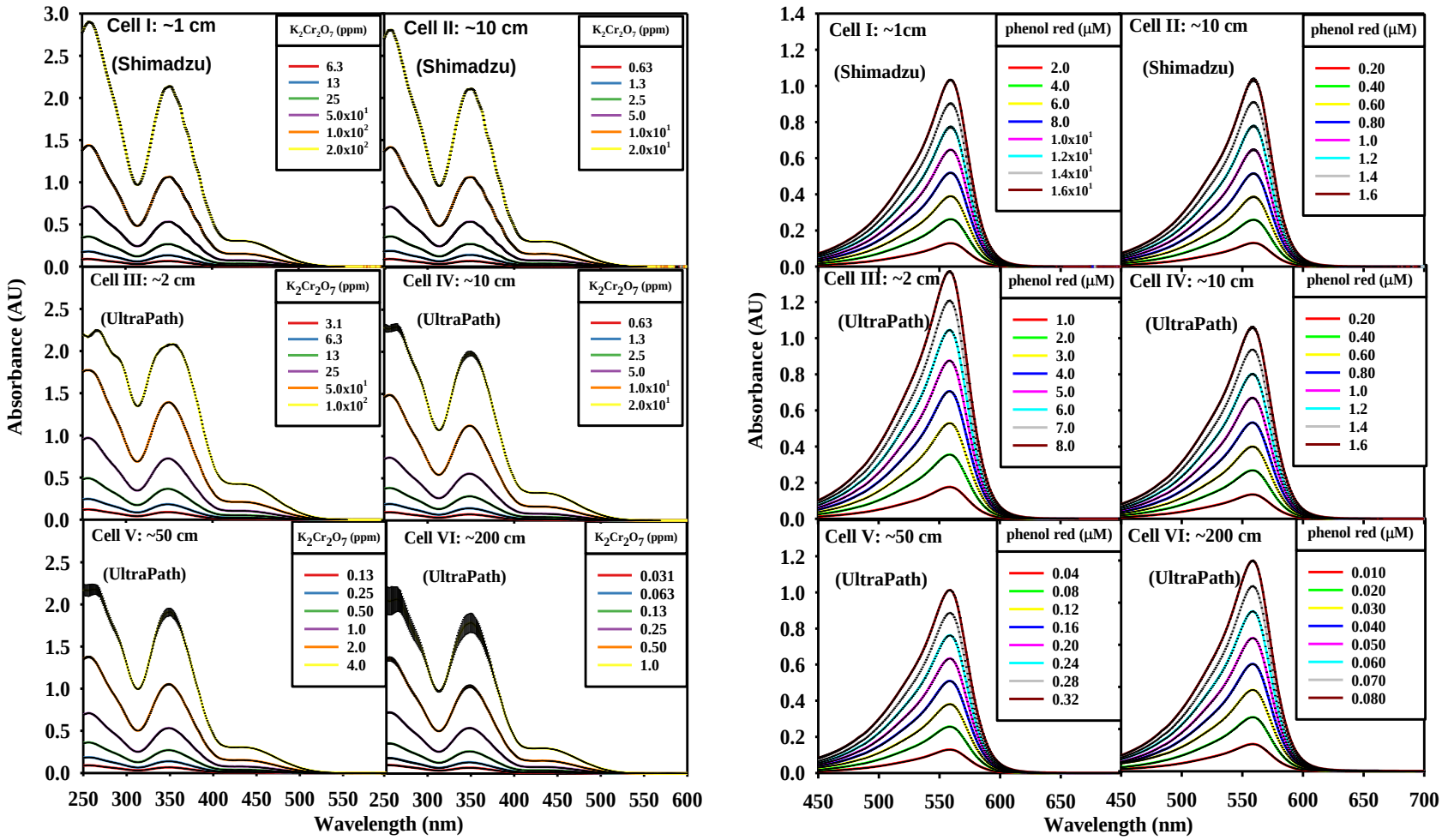

Figure 2.5: Absorption spectra, (left K_2Cr_2O7); (right phenol red) at various concentrations employing different cells as indicated in each plot. Error bars (calculated from three scans) are shown in black and mostly fall within the thickness of each line.

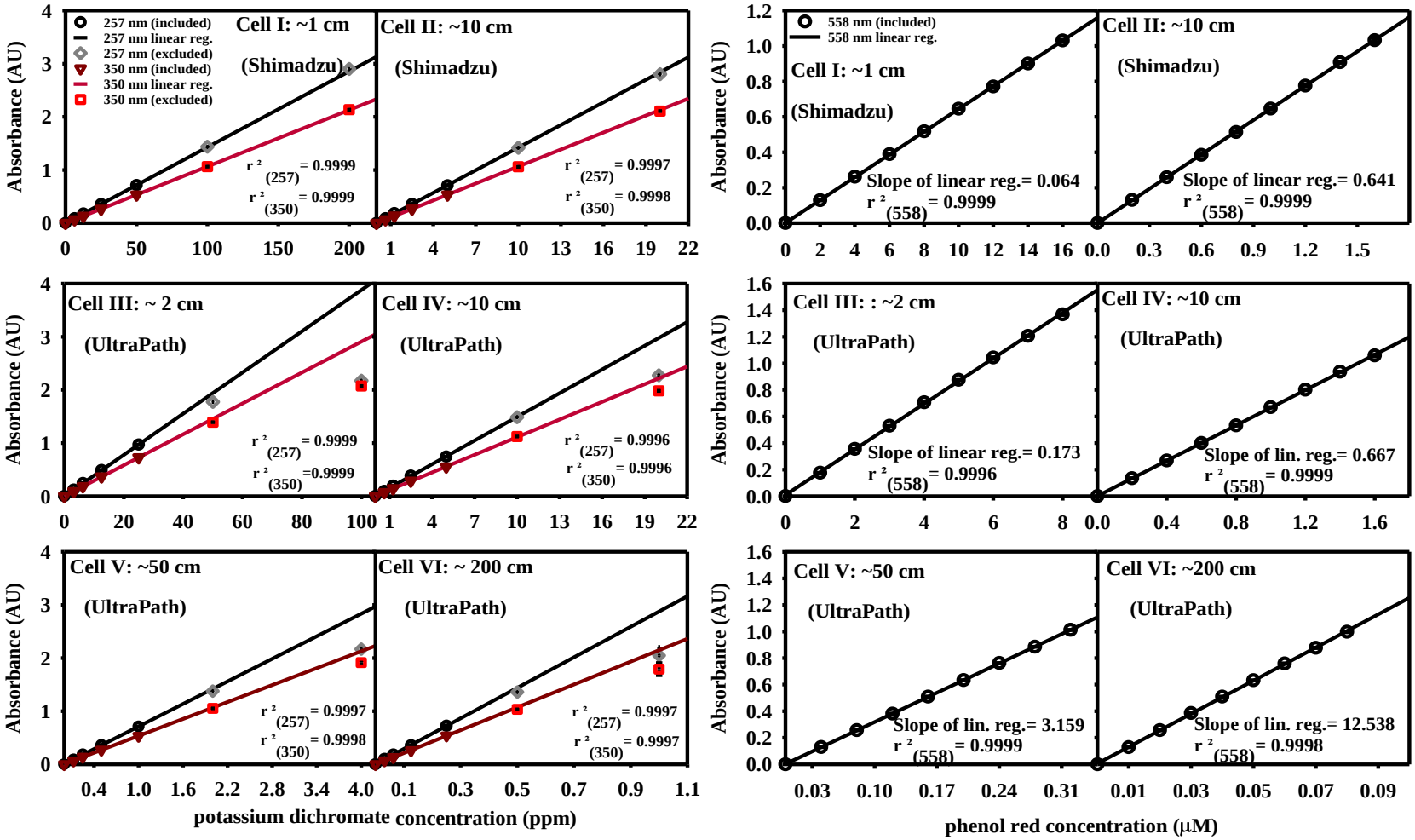

Figure 2.6: Absorption vs. concentration for materials at peak wavelengths: (**left**) absorption at 257 nm (**black**) and 350 nm (**red**) for $K_2Cr_2O_7$ solutions (the grey and light red points are not included in the linear regression and are displayed only to show the loss of linear response); (**right**) absorption at 558 nm for phenol red solutions.

artificial seawater media [82]. These calculations can be easily carried out in Excel using the built in Slope function or with a MATLAB algorithm.

2.4 Assessment/discussion:

2.4.1 Instrument linear range

The linear range of long pathlength spectrometers has been previously reported by Belz et al. (1999) and Miller et al. (2002), but were re-examined here following the application of the cleaning and sampling protocols described above. The WPI UltraPath spectrometer was linear up to ~ 1.2 AU, which is slightly less than that reported by Belz et al. (1999) (1.7 AU), while the Shimadzu double-beam spectrometer was linear to ~ 2.7 AU

Table 2.3: Measured effective pathlength for all cells (I-VI), employing both K_2Cr_2O7 and phenol red as well as Eqs. 2.1, 2.2, and 2.3. Average effective pathlength (in bold) along with the standard deviation is listed for each cell and protocol.

cell	l_{eff} (cm)									
	First protocol (Eq: 1)[a]			Second protocol (Eq: 2)[a]			Third protocol (Eq: 3)[b]			Avg.
	$K_2Cr_2O_7$		Phenol Red	$K_2Cr_2O_7$		Phenol Red	$K_2Cr_2O_7$		Phenol Red	
	257 nm	350 nm	558 nm	257 nm	350 nm	558 nm	257 nm	350 nm	558 nm	
I (~ 1 cm) [c]	**0.99** ± 0.002	**1.00** ± 0.005	**1.00** ± 0.006	**1.00** ± 0.005	**0.99** ± 0.005	**1.00** ± 0.006	**1.00** ± 0.001	**0.99** ± 0.001	**0.99** ± 0.002	**0.99** ± 0.01
II (~ 10 cm)	**9.96** ± 0.05	**9.90** ± 0.05	**10.0** ± 0.05	**10.1** ± 0.2	**10.0** ± 0.2	**10.1** ± 0.05	**9.90** ± 0.08	**9.96** ± 0.07	**10.0** ± 0.02	**9.99** ± 0.1
III (~ 2 cm)	**2.73** ± 0.02	**2.72** ± 0.01	**2.73** ± 0.04	**2.74** ± 0.02	**2.73** ± 0.01	**2.74** ± 0.04	**2.71** ± 0.01	**2.72** ± 0.06	**2.74** ± 0.02	**2.72** ± 0.06
IV (~ 10 cm)	**10.6** ± 0.3	**10.4** ± 0.2	**10.4** ± 0.06	**10.7** ± 0.2	**10.5** ± 0.2	**10.4** ± 0.05	**10.4** ± 0.1	**10.3** ± 0.1	**10.4** ± 0.03	**10.5** ± 0.2
V (~ 50 cm)	**50.0** ± 1	**50.1** ± 0.9	**49.1** ± 0.4	**50.0** ± 1	**50.0** ± 0.9	**49.5** ± 0.4	**49.5** ± 0.4	**49.7** ± 0.4	**49.4** ± 0.1	**49.7** ± 1
VI (~ 200 cm)	**201** ± 2	**199** ± 1	**198** ± 1	**200** ± 2	**199** ± 2	**198** ± 1	**198** ± 1	**201** ± 2	**196** ± 2	**199** ± 2

[a] Average and standard deviation of five independent solutions.
[b] Slope calculated employing nine phenol red and five dichromate solutions. Standard deviation based on the uncertainty in the slope value.
[c] Note that cell I, with an expected pathlength of 1.00 cm, was used to calculate the molar absorption coefficient of phenol red; thus the pathlengths determined using phenol red and the second and third protocols would be expected to agree with this value.

(Figs. 2.5, 2.6). Only values falling within the linear range were used to determine the cell pathlength and to calculate the instrument precision and accuracy.

2.4.2 Effective pathlength

The determined effective pathlengths (l_{eff}) were independent of the standard solution employed ($K_2Cr_2O_7$ or phenol red) and of the protocol used (Eqs 2.1-2.3) (Table 2.3). However, deviations were observed, between the pathlengths that we determined and those provided by the manufacturer; these differences were most pronounced in cells III, IV, and VI (Table 1). The most significant difference was observed for the shortest WPI UltraPath cell (cell III: ~2 cm), where the determined pathlength was 32.7% greater than the manufacturer-provided pathlength. Cells IV and VI also exhibited significant deviations from the provided value (> 4%), while cell V showed an insignificant deviation (~ 0.7 %). Because the discrepancies between our effective pathlengths and those provided by the manufacturer were not consistently high or low across the different cells, these deviations could not have arisen from some systematic bias in the measurements.

2.4.3 Instrument precision

For all cells, the intra-day coefficient of variation (Eq. 2.4), calculated using $K_2Cr_2O_7$ standards, was < 0.6% at all wavelengths investigated (250-500 nm) (Fig. 2.7a). The inter-day coefficient of variation was larger, but still < 1.5 % (Fig. 2.7a) The standard deviation with respect to the absolute absorbance values were also examined (Fig. 2.7b), and similar uncertainties were observed. In both cases, the precision was lower for the longer pathlengths.

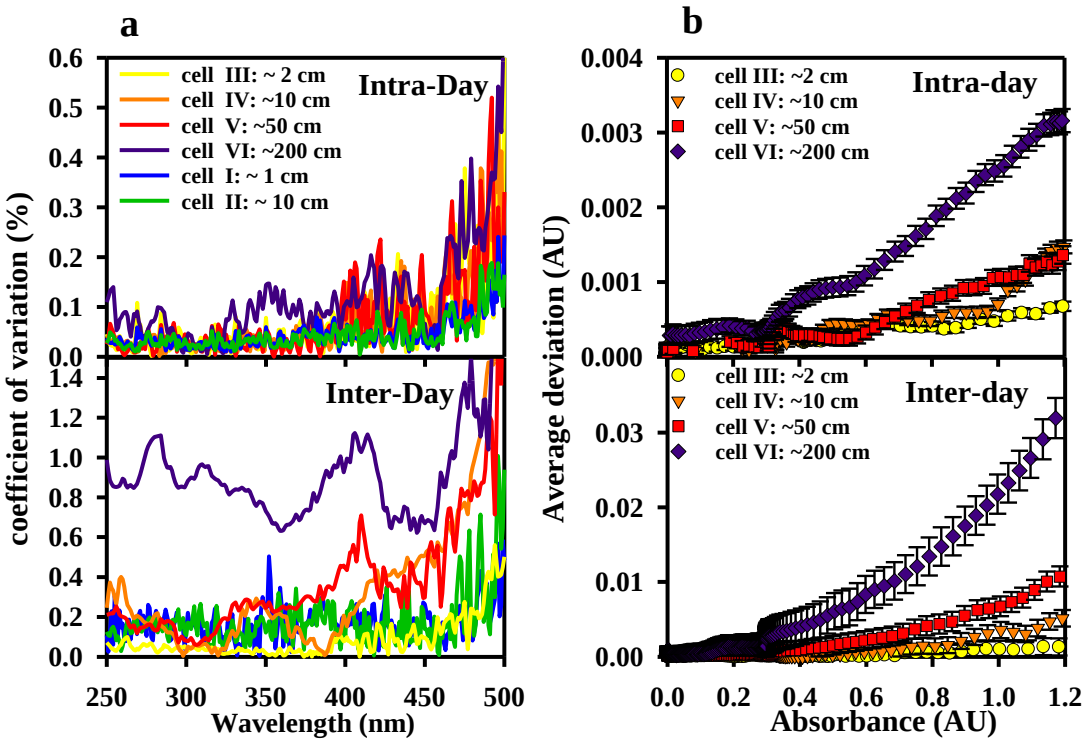

Figure 2.7: (**a**) **top**) Intra- day and (**bottom**) Inter-day coefficient of variation for all cells (I-VI) calculated from 250-500 nm employing Eq. 4 and absorbance spectra of $K_2Cr_2O_7$. (**b**) (**top**) Intra- day and (**bottom**) Inter-day average deviation in absorbance units for cells III-VI calculated as describe above (*Methodological precision and accuracy*) error bars indicate one standard deviation.

2.4.4 Instrument accuracy

The measured pathlengths were employed to determine the accuracy of the instrument using Beer's law and independently prepared solutions of phenol red and $K_2Cr_2O_7$. The percent error (Eq. 2.5) was < 2 % for each cell (III-VI) at absorbance values ranging from ~0.2-0.8 AU (Table 2.4). Due to the linear relationship between pathlength and absorbance, the error in accuracy increased proportionally when employing the manufacturer provided pathlengths, from ~1.2 to 5.7 % for cell VI, and from ~1.1 to 33.5% for cell III.

To test further the accuracy of the measured pathlengths, the absorption spectra were recorded for two natural water samples employing cells III-VI of the UltraPath

Table 2.4: Accuracy based on $K_2Cr_2O_7$ and phenol red solutions for absorbance values ranging from ~ 0.1-1.0 AU. (**Top**) The percent error based on the measured effective pathlength for three independent solutions was averaged for each absorbance range (value in bold) with the standard deviation provided directly below. (**Bottom**) Average percent error for all absorbance ranges based on both measured and manufacturer provided pathlengths for cells III and VI.

cell	Average percent error (%) using $K_2Cr_2O_7$			Average percent error (%) using phenol red		
	~ 0.2 (AU)	**~ 0.4 (AU)**	**~ 0.8 (AU)**	**~ 0.2 (AU)**	**~ 0.4 (AU)**	**~ 0.8 (AU)**
cell III: ~2 cm	**1.1** ± 0.6	**1.1** ± 0.2	**0.7** ± 0.5	**1.2** ± 0.4	**1.5** ± 0.4	**0.8** ± 0.5
cell IV: ~10 cm	**1.8** ± 0.4	**1.6** ± 0.9	**1.3** ± 0.7	**1.4** ± 0.4	**0.8** ± 0.3	**1.2** ± 0.5
cell V: ~50 cm	**1.4** ± 0.5	**0.9** ± 0.4	**1.0** ± 0.6	**0.9** ± 0.3	**0.6** ± 0.2	**1.0** ± 0.4
cell VI: ~200 cm	**0.8** ± 0.7	**1.0** ± 0.6	**1.5** ± 0.4	**0.9** ± 0.4	**1.6** ± 0.4	**1.3** ± 0.5

	Average percent error (%) using $K_2Cr_2O_7$ and phenol red (~ 0.2- 0.8 AU)	
	Measured effective pathlength	**Manufacturer provided pathlength**
cell III: ~ 2 cm	**1.1** ± 0.5	**33.5** ± 4
cell VI: ~200 cm	**1.2** ± 0.5	**5.7** ± 0.6

spectrometer. These spectra were referenced to NaCl solutions that matched the observed salinity to account for the refractive index differences. When the determined pathlengths were employed, the absorption coefficients (m^{-1}) were independent of cell used (Eq. 2.6; Fig. 2.8a-b) and both Bay and Shelf samples displayed high reproducibility, with an average coefficient of variation ranging from 4.27 % for cell III to 0.78 % for cell VI from 300 to 700 nm (n=3). The variation among the absorption coefficients was < 5 % for wavelengths from 300 to 400 nm and < 11% at the longer wavelengths (Fig. 2.9, red line). This variation was significantly larger when employing the manufacturer provided

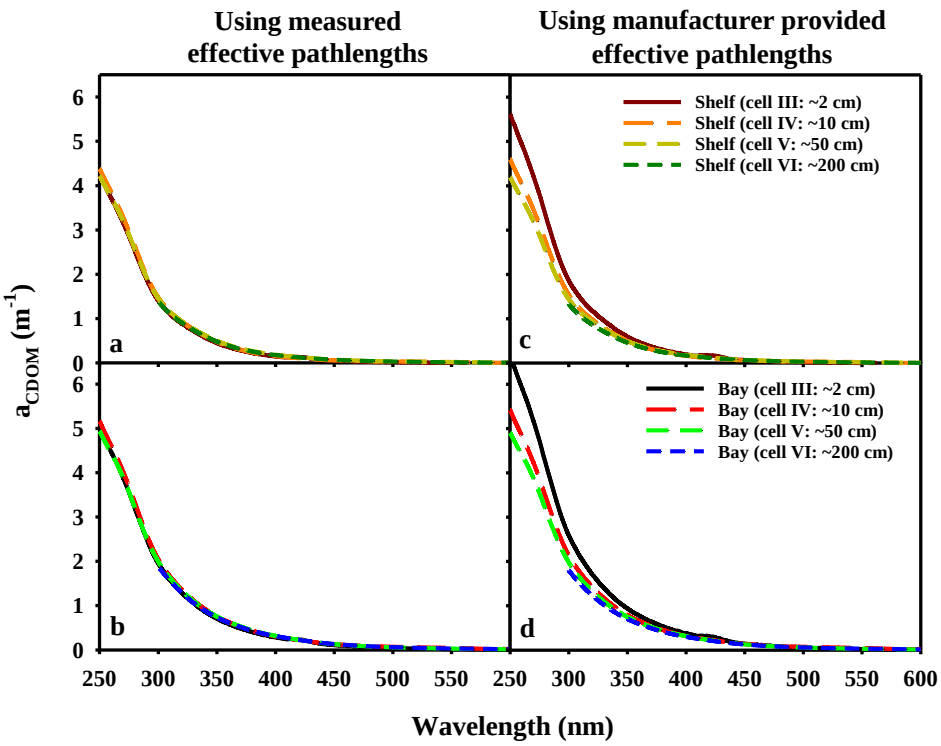

Figure 2.8: Absorption coefficients of shelf (**a and c**) and bay (**b and d**) samples acquired employing the measured (**a and b**) and manufacturer provided (**c and d**) effective pathlength of cells III-VI. Data acquired with cell VI ends at 300 nm because the sample absorbance exceeded the linear range.

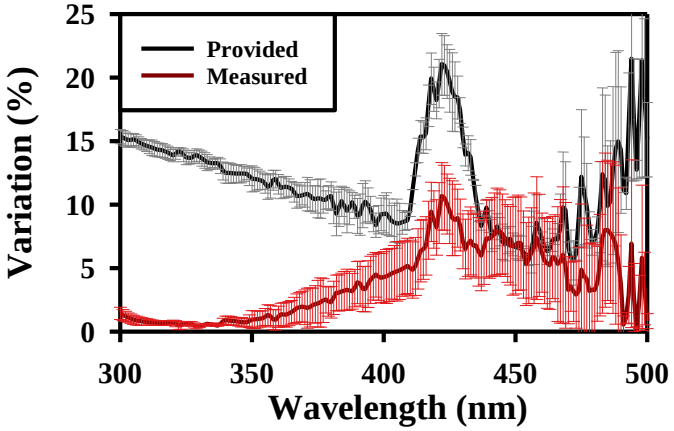

Figure 2.9: Variation in the absorption coefficients (300-500 nm) for the Bay and Shelf natural water samples when employing all cells III-VI and the manufacturer provided (**black**) and determined (**red**) pathlengths. Variation for the Shelf and Bay samples were calculated separately using Eq. 2.4 and then averaged (**solid lines**) with the deviation indicated by the error bars.

pathlengths (Fig. 2.9, black line). The larger variation at wavelengths > 400 nm for both the manufacturer provided and measured pathlengths is due in part to the low absorption

of the natural water samples that approaches the instrument detection limit, especially when employing cell III. The shoulder seen at ~ 420 nm is due to an artifact present in the data from cell III that results from an incomplete reference subtraction, producing a small shoulder in the data. The cause of this poor subtraction is discussed in the following section.

2.4.5 Salinity reference spectra

Due to the differing optical configurations, the dual-beam and WPI UltraPath spectrophotometers exhibited very different spectral responses to the NaCl solutions (Figs. 2.10-2.12). Absorption spectra acquired with the Shimadzu double-beam instrument relative to air did not display any detectable changes with increasing NaCl concentrations over the 300-700nm wavelength range (Fig. 2.10). Because the dual-beam spectrometer employs a single, broad-area detector (photomultiplier tube), slight differences in focusing resulting from changes in refractive index are unimportant, unlike that previously observed for a diode-array detector [26]. Further, as previously noted (Green and Blough, 1994), the amount of incident light lost due to reflection at the interface changes only slightly between quartz-water (0.53%) and quartz-seawater (0.50%). Due to the negligible effects of both refractive index differences and of light absorption by the salt itself over this spectral range (300-700 nm), matching the salinity of the reference to that of the sample is not critical for the duel-beam spectrophotometer.

As previously reported for the WPI UltraPath and other liquid core waveguide cells [28,82,94,95], the WPI UltraPath utilized in this study exhibits increasingly significant offsets relative to a pure water reference with increasing NaCl concentration owing to the increase in the refractive index of the solutions. The spectral response of each cell with increasing

NaCl concentration was unique, but was reproducible on a daily basis with < 4% variation for each cell examined (Eq. 2.4). The offsets exhibited a linear dependence on NaCl concentration from 0 to 45 ppt over the 300-700 nm range for all but cell IV (~10 cm) (Figs. 2.11-2.12); in this case absorption was linearly related to NaCl concentration at short wavelengths (~300-450 nm), but not at long wavelengths (Figs. 2.11-2.12). In principle, the offsets in this cell at long wavelengths could be modeled using a non-linear fitting function. Interestingly, while the offsets of cells IV-VI were negative with respect to the water reference, those of cell III were positive (Fig. 2.11).

Because the offset in absorption changed linearly with increasing NaCl concentration for both V and VI (Fig. 2.11-2.12) and the offsets were reproducible, calibration curves can be generated (Eq. 2.7) and used to compute a salinity reference spectrum for any given salinity (Fig. 2.12) as previously reported by Nelson et al. (2007). Although cell III also exhibited linear response to increasing NaCl concentration, a

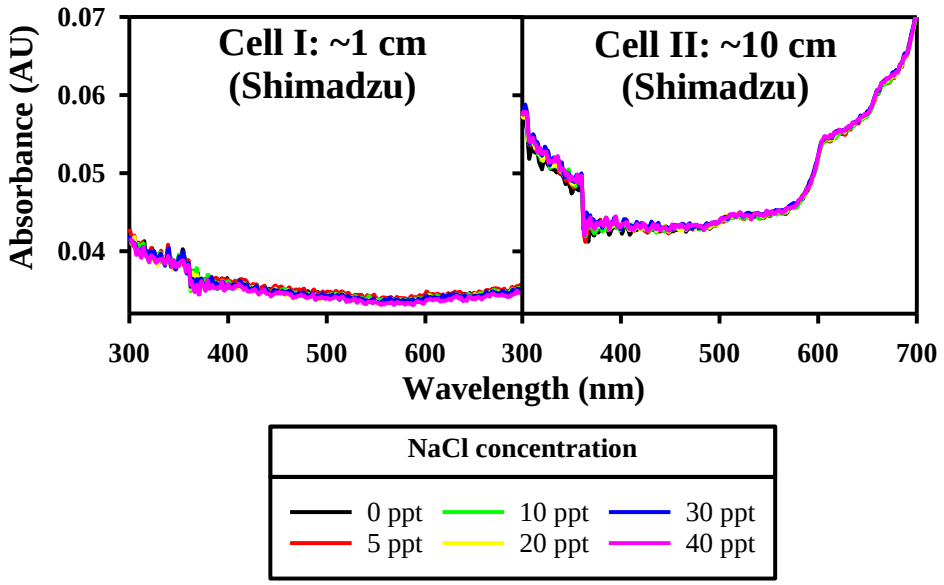

Figure 2.10: Absorption spectra of aqueous NaCl solutions relative to air at various concentrations (from 0-40 ppt), acquired with the Shimadzu double beam spectrometer employing cells I and II.

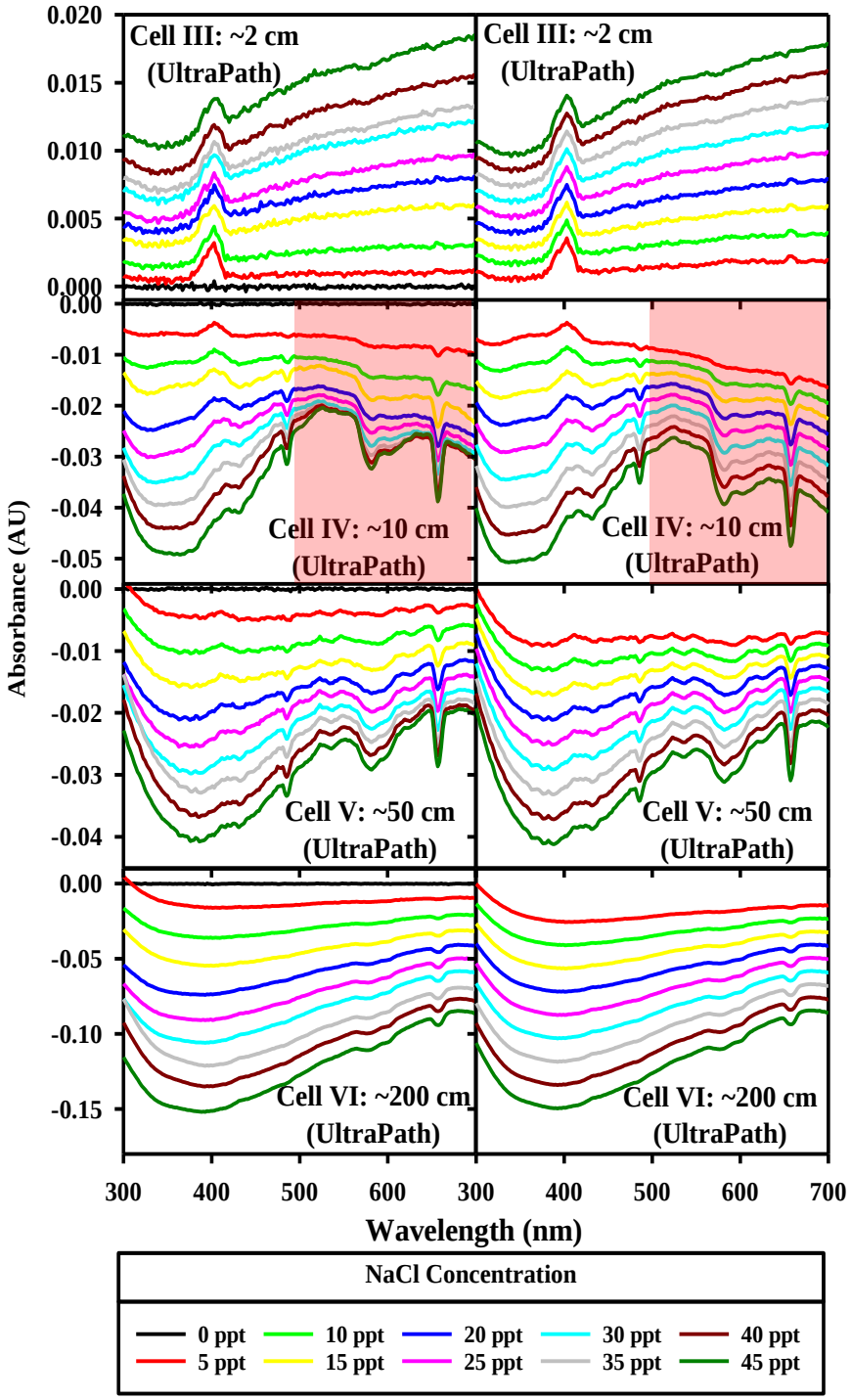

Figure 2.11: Salinity reference spectra of salt solutions measured **(left)** and calculated using Eq. 2.7 (**right**) employing cells III-VI. Highlighted sections display the region of nonlinear response to increasing NaCl concentration.

prominent band in the reference spectra at ~ 420 nm was not always completely subtracted from the sample spectrum (Fig. 2.8), producing a shoulder in the data. Although

incomplete subtraction was only observed for cell III, prominent bands were observed in all of the NaCl reference spectra acquired with the UltraPath (Fig. 2.12), demonstrating the need to compare reference spectra to sample spectra to ensure that features in the reference spectra are completely removed.

In many cases, the strong bands in the NaCl reference spectra appear to match the spectral output of the light source (Fig. S1). Due to increased light throughput with increasing NaCl concentration (cells IV, V, and VI), there remains the possibility that the transmitted light exceeded the linear range of the detector when the integration time was set to obtain a maximum intensity of 70% of the full scale relative to pure water. To test

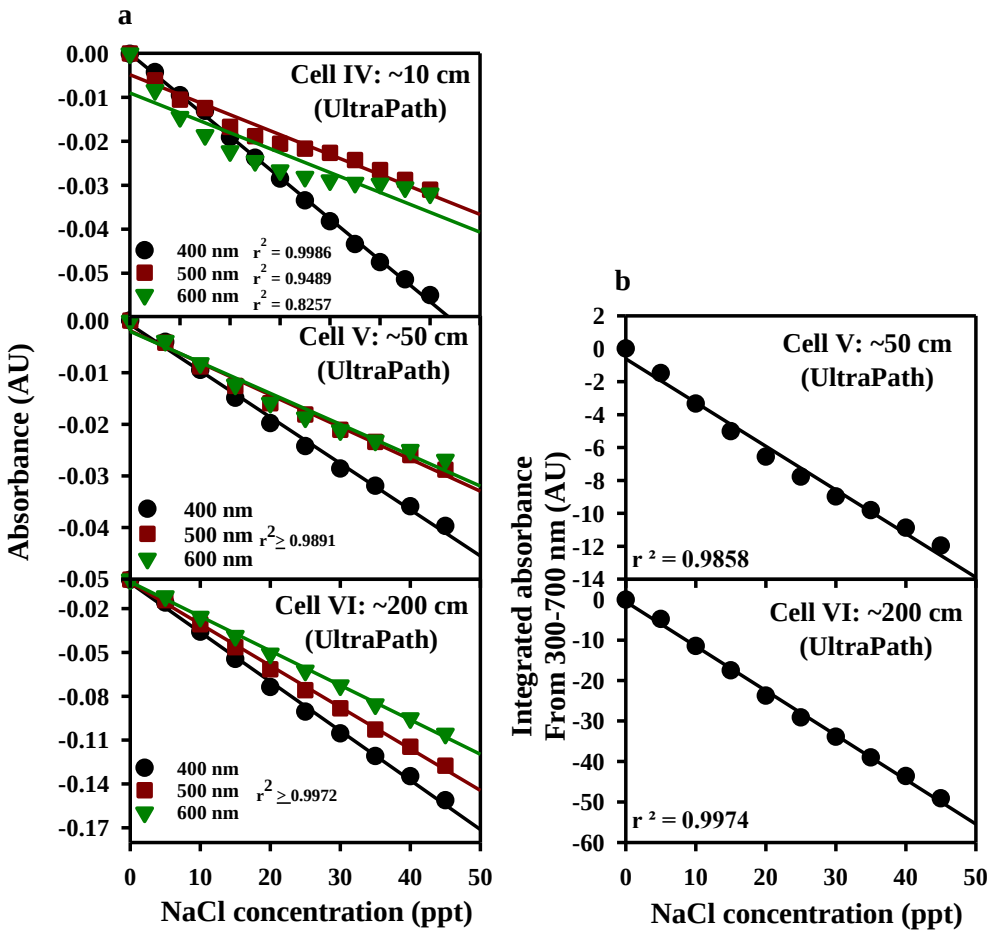

Figure 2.12: Dependence of absorbance on NaCl concentration, **a)** at three selected wavelengths (400, 500 and 600 nm) for cells IV-VI, and **b)** for the integrated absorbance (300-700nm). r^2 values for linear regression lines are displayed for each data set.

this possibility integration times were set to obtain a maximum intensity of 70% and 50% of the full scale relative to water. However, the NaCl reference spectra were unchanged between these two settings (Fig. S1). This result indicates that the bands seen in these spectra were not affected by a loss of linearity caused by higher light transmission observed for the NaCl solutions (Fig. S2.1).

These results are consistent with past work where theoretical reference spectra were generated for cells that showed a linear response to salt concentration [82]. However, the exact response is likely to be both instrument and cell dependent and thus each instrument/cell should be independently tested, with calibration curves specific for that instrument/cell generated.

2.5 Discussion and recommendations:

We have provided a protocol for the calibration/validation of the WPI UltraPath spectrometer that, when followed, provides accurate and reproducible data that is independent of the pathlength employed. Based on our results, we recommend the following:

- The spectrometer should be cleaned at the beginning of each day as reported in the methods (*Cleaning of WPI UltraPath cells*). Due to drift, it is recommended that a new reference scan be taken approximately every 30-60 minutes if the instrument has stabilized, more frequently if not (see Fig. 2.2). Drift over this time period (~30-60 min) was found to be < 0.0005 AU for our instrument (Fig. 2.2c); if the water scan deviates by more than this value, the cell is most likely contaminated, and a cleaning cycle is recommended before acquiring a new reference. Because referencing to a contaminated cell impacts all future sample measurements with the

effects not easily accounted for, it is essential that the cell be clean, particularly when running samples having very different absorption coefficients.

- Samples should be passed through pre-cleaned filters, free of any absorbing residue (*Optical measurements*). The appropriate pathlength or sample concentration should be chosen to ensure that the absorbance remains within the linear range of the instrument. Sample spectra should be acquired at the same temperature as that employed to determine the effective pathlength to avoid discrepancies caused by temperature [100,101].
- Effective pathlengths should be determined using a NIST standard and/or a well-characterized reference material prior to the collection of data to confirm that the pathlengths provided by the manufacturer are correct (*Determination of cell pathlength*). A NIST standard is preferred, as these standards have been developed specifically for this purpose. If phenol red (or another dye) is chosen as the reference material for use in the second and third protocols (Table 2.3), the molar absorption coefficients for that particular lot (or better yet, the purified material) should be determined under well-defined and reported solution conditions using a research grade spectrophotometer. If the first protocol is employed, constant solution conditions must be maintained under dilution. The effective pathlengths should also be checked on a regular basis, especially if the instrument has been used extensively or deployed in the field.
- The intra/inter day precision and accuracy should be acquired for each instrument/cell using a standard and/or reference material and be reported

(*Methodological precision and accuracy*), thus allowing for better comparisons among instruments from different laboratories.

- Salinity reference spectra should be recorded for each instrument/cell based on calibration curves (Eq. 2.7) and used as a blank to account for the absorbance offset relative to pure water caused by differences in the refractive index (*Salinity reference spectra*). Once determined, a few salinity reference spectra should recorded regularly to ensure that these offsets have not changed; if significant deviations are observed, new calibration curves should be acquired.

These proposed procedures can easily be adopted and employed with minimal work and expense. We believe this calibration/validation protocol will substantially improve inter-laboratory comparisons of data acquired with long/multi-pathlength capillary waveguide spectrometers and will further improve the quality of the absorption data acquired from weakly absorbing offshore marine waters.

Chapter 3: Investigating the sources and structure of chromophoric dissolved organic matter (CDOM) in the north pacific ocean (NPO) utilizing optical spectroscopy combined with solid phase extraction and borohydride reduction.

The majority of this chapter has been published in reference 35:

Cartisano, C. M., Del Vecchio, R., Bianca, M. R. & Blough, N. V. Investigating the sources and structure of chromophoric dissolved organic matter (CDOM) in the North Pacific Ocean (NPO) utilizing optical spectroscopy combined with solid phase extraction and borohydride reduction. *Mar. Chem.* **204,** 20–35 (2018).

3.1 Abstract:

Prior optical measurements of waters in the Equatorial Atlantic Ocean (EAO) provided evidence of a major terrestrial "humic-like" component of the CDOM that absorbed in the ultraviolet (UV) and visible and emitted across the visible, along with a marine component that primarily absorbed and emitted in the UV. Here we extend these measurements to the North Pacific Ocean (NPO) at Station Aloha (22° 45' N, 158° 00' W). Detailed optical measurements of both the natural waters (CDOM) and C18 organic matter extracts of these waters (C18-OM) were acquired before and after sodium borohydride ($NaBH_4$) reduction of samples obtained throughout the water column. Optical properties of the "humic-like" component were relatively uniform with depth below the ~600 m [$a_{CDOM}(350)$ ~ 0.08 (m^{-1}), a^*_{CDOM} (350) ~ 0.2 (m^{-1} mg^{-1} C L), $SUVA_{254}$ ~ 0.55 (m^{-1} mg^{-1} C L), E_2:E_3 ~ 10, $S_{300\text{-}700}$ ~ 0.02 (nm^{-1}), $S_{350\text{-}400}$ ~ 0.012 (nm^{-1}), S_R ~1.7, F(350/450) ~ 0.009 (QSE), and ϕ_{360} ~ 0.026], but were significantly different in surface waters, likely due to photobleaching and biological activity [$a_{CDOM}(350)$ ~ 0.026 (m^{-1}), a^*_{CDOM} (350) ~ 0.027 (m^{-1} mg^{-1} C L), $SUVA_{254}$ ~ 0.36 (m^{-1} mg^{-1} C L), E_2:E_3 ~ 45, $S_{300\text{-}700}$ ~ 0.03 (nm^{-1}), $S_{350\text{-}400}$ ~ 0.003 (nm^{-1}), S_R ~6.8, F(350/450) ~ 0.003 (QSE), and ϕ_{350} ~ 0.024]. Optical properties of the short-wavelength components (UV bands) were more variable with depth. Response

to solid phase extraction was also relatively uniform with depth, with preferential extraction of the long-wavelength absorbing/emitting "humic-like" component (~30-50 % extraction efficiency at λ <300 nm and ~50-80% at λ >400 nm) and virtually no extraction of the UV absorbing/emitting bands. Response to $NaBH_4$ reduction was also similar down the water column with preferential loss of absorption in the visible region, and enhanced, blue-shifted fluorescence emission.

As in the EAO the 'humic-like" component exhibited very similar, although not identical, properties to those observed for terrestrially-dominated estuarine and coastal environments, providing evidence that this component originates from a terrestrial source. Although this component dominated the absorption, marine contributions (i.e. UV bands) similar to those observed in the EAO were also observed. However, these components were found to absorb and emit primarily in the UV and were not efficiently extracted by the C18 columns, clearly showing that they are structurally distinct from the "humic-like" component.

3.2 Introduction:

The importance of chromophoric dissolved organic matter (CDOM) to a variety of environmental and biogeochemical processes is now widely recognized. CDOM can affect the underwater light field by absorbing UV and visible light [1,2,4], while the photoproduction of reactive oxygen species by CDOM can influence the speciation of trace metals and its photobleaching [1,4,18,23,49,89,104]. CDOM controls light absorption at short wavelengths (< 440 nm) in the upper layers of the open oceans [5] and thus in situ optical spectroscopy and satellite ocean color measurements have been employed to examine its distribution and dynamics, providing information relevant to carbon cycling, the mixing of surface water

masses and basin-scale biogeochemical processes [1,5,89]. The recognition of its importance has led to a very large number of studies of its optical absorption and emission properties over a broad spectrum of aquatic environments over the last 20 years [3,5,23,45,105], as well as to studies examining possible relationships between the optical and photochemical properties [18,21,48,49], and their dependence on CDOM structure and source [5,16,21,24]. Certain CDOM optical signals have further been suggested to serve as a proxy for the "quality" of the dissolved organic matter (DOM) pool [23,31,33,106], as an indicator of DOM source [16,33,106,107], and as measure of biological and (photo)chemical processing [1,3,107,108].

The source of CDOM in offshore marine waters and the structural basis of its optical properties remain as open questions. A number of studies have concluded that CDOM is created *in situ* from marine dissolved or particulate organic matter based on correlations between measurements of either absorption or fluorescence and apparent oxygen utilization (AOU) [2,5,71,73,109,110]. In contrast, other studies have suggested offshore marine waters contain a significant "humic-like" terrestrial component [16,74,75]. Most of the studies that have proposed a solely marine source of CDOM were based on either absorption or fluorescence measurements alone, often at only a few wavelengths, with no additional chemical tests of source or structure. Similarly, incubation studies have suggested that "humic like" CDOM can be produced biologically via marine source materials [5,111–117], but few, if any, secondary tests are performed to examine whether this material exhibits the same properties as the CDOM observed in the natural waters.

Prior work in the Equatorial Atlantic Ocean (EAO; [16]), which combined acquisition of complete absorption and emission spectra with additional chemical tests (C18 extraction and borohydride reduction), provided strong evidence for a major terrestrial component

that absorbs in the UV and visible but emits in the visible, along with marine CDOM component that absorb and emit primarily in the UV. In this study, we extended this work to the North Pacific Ocean (Station ALOHA) to examine both the spectral dependence of the optical absorption and emission properties of the natural waters alone, as well as the effects of solid phase extraction [7,8] and $NaBH_4$ reduction [7,16,46,57] on these properties. This particular site was chosen for three reasons. First, we wished to compare the results previously acquired in the Atlantic to those in the Pacific. Second, vertical profiles of the water column at this site would allow us to probe very different water masses and thus examine how the CDOM might vary with water mass origin. Third, it enabled us to sample North Pacific Intermediate Waters, where past studies have provided potentially conflicting evidence concerning a possible terrestrial source of the CDOM, [74,76] as opposed to marine *in situ* production [5,70]. As in the EAO, our results suggest the presence of a substantial terrestrial "humic-like" component throughout the water column, along with structurally-dissimilar marine CDOM components that primarily absorb and emit in the UV.

3.3 Methods:

3.3.1 Samples

North Pacific Ocean (NPO) samples were collected at Station ALOHA (22° 45' N, 158° 00' W) in December 2014 onboard the RV Kilo Moana. Water samples were collected from the surface to 4500 meters encompassing different water masses including 1) North Pacific Sub-Tropical Water (NPSTW: 0-200 m); 2) Sub-tropical Mode Water (STMW: 200-500 m); 3) North Pacific Intermediate Water (NPIW: 500-800 m); 4) Antarctic

Intermediate Water (AAIW: 800-2000 m); 5) North Pacific Deep Water (NPDW: 2000-3000 m); 6) Lower Circumpolar Water (LCPW: 3000-4500 m) [76,118–125].

Natural waters and C18 extracts were collected as previously described [24,45] (Fig.3.1). Briefly, samples were collected using a CTD rosette with Niskin bottles and immediately transferred into acid rinsed carboys (20 L). Samples were then filtered through a 0.2 µm double layer HT Tuffryn hydrophilic polysulfone filters (maxi capsule- Pall Corporation) which was previously rinsed with Milli-Q water and then for each sample a small volume of the natural water (~ 1 L) was passed though the filter and discarded to further rinse the filter. An aliquot (250 mL) of the filtered water was stored at 4°C in the dark for later analysis ("CDOM"). In order to optimize CDOM extraction onto the non-polar C18 columns, the remaining filtered waters were acidified to pH 2 with ~100 mL of HCl (2 M). An aliquot (250 mL) of the acidified water was collected and stored at 4 °C in the dark until later analysis ("pre-extraction water"). The remaining acidified natural water (~20 L) was passed through C18 columns (United Chemical Technologies, Inc.) at a flow rate of ~50 mL min^{-1} to extract DOM, using the method previously described [24,126]. C18 extraction columns were preconditioned with 100 mL of MeOH and 50 mL of acidified Milli-Q water at pH 2. Two extractions were collected at each depth (20 L each). An aliquot of the extracted water (250 mL) was collected ("post-extraction water") stored in the dark at 4 °C. The columns were then rinsed with acidified Milli-Q water (100 mL, pH 2) to remove salts, and stored in the dark at 4 °C (~2 months).

Prior to DOM elution, the cartridges were rinsed with an aqueous solution of formic acid (0.1 % by volume) to remove any remaining HCl, and gently dried with N_2 gas to remove as much water as possible. DOM was eluted with 50 mL of high purity MeOH.

The first ~ 5 mL of eluent were discarded to remove the small amounts of water still contained in the dead volume; the remaining eluent (45 mL) from the two extractions at each depth were combined and roto-evaporated at ~ 35 °C until dry. The dried DOM was dissolved in Milli-Q water (~2 mL) and adjusted to neutral pH with NH_4OH. This concentrated extracted material (referred to as "extracts" or "C18-OM") was stored frozen in the dark (up to 1 year).

To provide a procedural blank, two C18 columns were treated following this protocol employing 20 L of acidified Milli-Q water in place of natural waters. Pre and post extraction waters as well as the extracted material from these procedural blank columns were tested for their optical properties (absorption and fluorescence), which were nearly indistinguishable from zero.

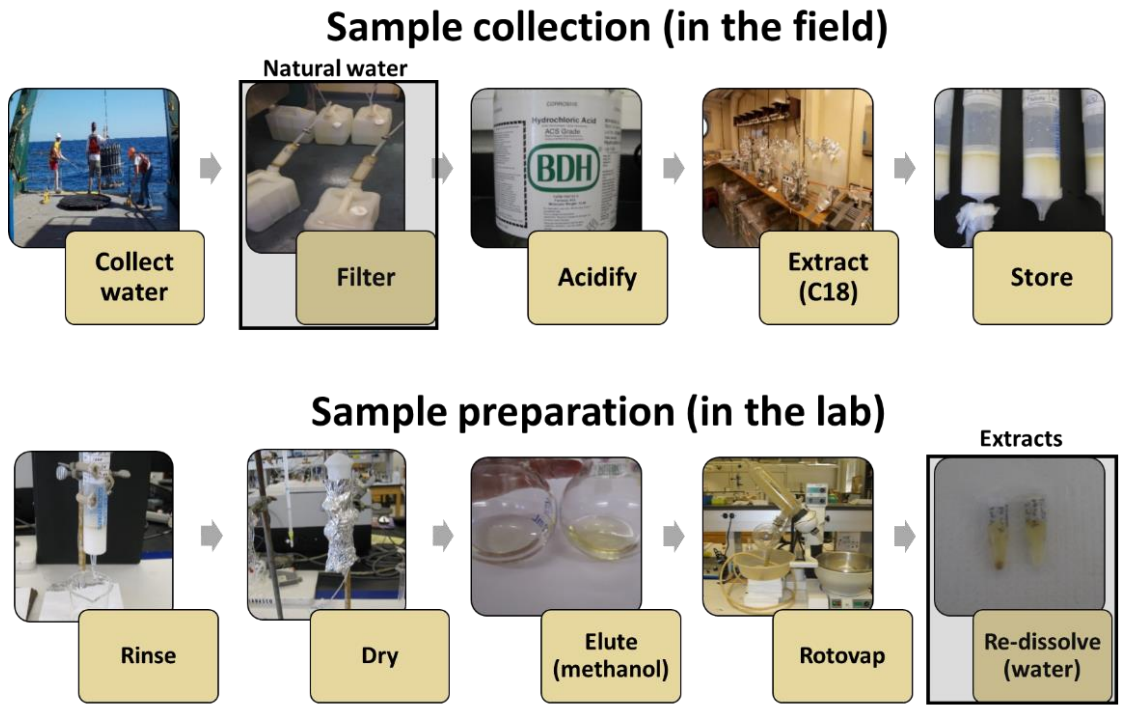

Figure 3.1: Flow diagram for sample collection and preparation.

3.3.2 Optical measurements

Absorption measurements were collected using both a World Precision Instrument (WPI) multi-pathlength absorption spectrometer (~200 cm pathlength)[127] and a Shimadzu UVPC 2401 benchtop spectrophotometer (1 cm pathlength). The WPI spectrometer, employing a 200 cm pathlength, was used to measure the CDOM absorption of the seawaters, to obtain more accurate absorbance values over the visible range. The WPI spectrometer was blanked with Milli-Q [28,94] and a NaCl solution matching the ionic strength of the natural water sample was used as a reference to account for changes in refractive index [82]. The Shimadzu spectrometer was employed to measure the absorption of the C18-OM employing a 1 cm cell; this instrument was blanked with air while Milli-Q water was used as the reference.

Absorption spectra were collected over the 190-820 nm range. Absorption from both instruments were converted into (Naperian) absorption coefficients, a (λ), or specific absorption coefficients, a*(λ), using the following equations,

$$a(\lambda) = \frac{2.303 \cdot A(\lambda)}{b} \qquad \textbf{Eq. 3.1}$$

$$a^*(\lambda) = \frac{2.303\ A(\lambda)}{b \cdot C} \qquad \textbf{Eq. 3.2}$$

where A is the absorbance at a given wavelength (λ), b is the pathlength (in meters) and C is the carbon concentration in mg C L^{-1}. Other optical indices were calculated, for comparison to other studies including $SUVA_{254}$ (Eq. 3.3)[11] and, E_2:E_3 (Eq. 3.4)[36]

$$\mathrm{SUVA_{254}} = \frac{\mathrm{A(254)}}{\mathrm{b \cdot C}} \qquad \textbf{Eq. 3.3}$$

$$\mathrm{E_2 : E_3} = \frac{\mathrm{A(250)}}{\mathrm{A(365)}} \qquad \textbf{Eq. 3.4}$$

The absorption spectra were plotted on a natural log scale to visualize differences in spectral line shape, but were also fitted to an exponential model [25] over a 300-700 nm range using a nonlinear least squares fitting routine,

$$a(\lambda) = a(\lambda_0)e^{-S(\lambda-\lambda_0)} \quad \textbf{Eq. 3.5}$$

where λ_0 is a reference wavelength and S is the spectral slope [1]. Residuals (differences between the fit and the actual absorption values) were examined to determine how closely the fits matched the spectra and to discern the wavelength ranges where the absorption spectra deviated from the exponential fit. For comparison to other studies, the non-linear least squares fitting routine was also run over two other regions (275-295 nm and 350-400 nm), to calculate the spectral slope ratio (S_R), defined as the ratio of $S_{275\text{-}295}$ to $S_{350\text{-}400}$ [33].

$$S_R = \frac{S_{275-295}}{S_{350-400}} \quad \textbf{Eq. 3.6}$$

Fluorescence measurements were acquired with a Horiba Fluoromax-4 luminescence spectrometer. Three dimensional excitation-emission matrixes (EEMs) were collected, with the excitation wavelengths varied from 240-600 nm in 10 nm steps, and the emission spectra scanned from 290-700 nm in 1 nm steps. Excitation and emission bandpasses were each set to 4 nm, while first- and second-order Rayleigh scattering were masked. To optimize the signal-to-noise ratios, integration times were set at 0.2 s for extracts and 1.0 s for the natural waters. Spectra were corrected using instrument correction factors supplied by Horiba. A Matlab 5 point running average smoothing program was used to minimize the noise while a Raman correction program from the decomposition routines for Excitation Emission Matrices (drEEM) toolbox was run to remove Raman scattering [128]. Quinine sulfate (QS) was employed as a standard (10 ppb in 0.1 N H_2SO_4) that was run daily (excitation at 350 nm and emission from 290-700 nm).

The emission intensities of the corrected fluorescence emission spectra ($F_{s(int)}(\lambda_{ex})$) were converted into quinine sulfate equivalents (F_{QSE}) as follows,

$$F_{QSE} = \frac{F_{s(int)}(\lambda_{ex})}{\left(\frac{F_{QS(int)}}{10}\right)} \quad \textbf{Eq. 3.7}$$

where $F_{QS(int)}$ is the integrated emission intensity of the quinine sulfate standard (10 ppb) at λ_{ex} 350 nm. All emission intensities are displayed in QSE. Apparent quantum yields (ϕ) were calculated as described previously [26] using the equation below:

$$\phi_s(\lambda_{ex}) = \left(\frac{F_{s(int)}(\lambda_{ex})}{F_{QS(int)}(\lambda ex_{350nm})} * \frac{A_{QS}(\lambda ex_{350nm})}{A_s(\lambda_{ex})}\right) 0.51 \quad \textbf{Eq. 3.8}$$

where $F_{S(int)}$ and $F_{QS(int)}$ are the integrated emission intensities of the sample and quinine sulfate, respectively, at the excitation wavelength (λ_{ex}); A_S and A_{QS} are the absorbance of samples and quinine sulfate standard respectively, at λ_{ex}; 0.51 is the published quantum yield of the quinine sulfate [26].

Fluorescence emission indices were also calculated to compare our results to other studies: the humification index (HIX), calculated employing a slightly modified method from Ohno (2002)(Eq. 3.9)

$$HIX = \frac{\sum F_{S_{435-480}}}{(\sum F_{S_{300-345}} + \sum F_{S_{435-480}})} \quad (\lambda_{ex}\ 250\ \text{nm}) \quad \textbf{Eq. 3.9}$$

where $\sum F_{S\ 435\text{-}480}$, and $\sum F_{S\ 300\text{-}345}$ is the sum of the emission intensity from 435-480 nm and 300-345 nm, at excitation 250 nm. HIX is generally calculated at excitation 254 nm, but because this data was not available, the λ_{ex} 250 nm was employed. The fluorescence index (FI) was calculated following the method of Cory and Mcknight (2005),

$$FI = \frac{F_s(470)}{F_s(520)} \quad (\lambda_{ex}\ 370\ \text{nm}) \quad \textbf{Eq. 3.10}$$

where $F_S(470)$ and $F_S(520)$ are the emission intensities of the sample at 470 nm and 520 nm with excitation 370 nm respectively. The biological index (BIX) was also calculated following the method of Huguet et al. (2009),

$$BIX = \frac{F_S(380)}{F_S(430)} \quad (\lambda_{ex}\ 310\ \text{nm}) \qquad \textbf{Eq. 3.11}$$

where $F_S(380)$ and $F_S(430)$ are the emission intensities of the sample at 380 nm and 430 nm with excitation 310 nm.

3.3.3 Extraction efficiencies

The efficiency of the C18 columns to extract CDOM from natural waters provides further insights into the structure of this material. Compounds efficiently extracted exhibit a higher affinity for the column than compounds not extracted; because the C18 column is non-polar, non-polar and uncharged (at pH 2) compounds will be preferentially extracted. The extraction efficiency (EE) was determined by absorption as follows:

$$\text{EE} = \left(1 - \frac{a_{\text{CDOM}}(\text{post extraction water, pH 2})}{a_{\text{CDOM}}(\text{pre extraction water, pH 2})}\right) * 100 \qquad \textbf{Eq. 3.12}$$

thus providing the percent absorption removed by the C18 column at each wavelength. EE thus represents an estimate of the CDOM retained onto the column during the extraction process. The combined extraction and elution efficiencies (CEE) were calculated as follows:

$$CEE = \left(\frac{a^c{}_{C18-OM}}{a_{CDOM}}\right) * 100 \qquad \textbf{Eq. 3.13}$$

where $a^C{}_{C18\text{-}OM}$ is

$$a^c{}_{C18-OM} = (a_{C18-OM})\left(\frac{\text{Final vol.of extracted material (}\sim\text{0.002 L)}}{\text{Total vol.of Natural water extracted(}\sim\text{ 40 L)}}\right) \qquad \textbf{Eq. 3.14}$$

and the ratio of volumes represents the dilution factor, which is based on the volume of the extract for which the absorption was measured (aC18-OM). This calculation provides an estimate of what is retained on the column and then successfully eluted.

3.3.4 TOC measurements

Total organic carbon measurements were acquired using a Shimadzu TOC- L analyzer equipped with an auto-sampler (ASI-L). Unfiltered samples and standards were acidified with H_3PO_4 (50 %) (5 µL per 1 mL of sample). Prior to measurements the samples were sparged with ultra-pure air for three minutes to remove inorganic carbon. Samples were injected until the standard deviation of three measurements was < 3%, usually 3 to 5 times. A calibration curve was generated with potassium hydrogen phthalate solutions ranging in concentration from 0.1 – 1.0 ppm carbon.

3.3.5 Sodium borohydride reductions

Past studies have shown that sodium borohydride selectively reduces carbonyl containing moieties, principally ketones and aldehydes, in humic and fulvic acid reference materials [46,56,68] as well as CDOM and C18-OM seawater samples [16], producing significant changes in the optical properties. This process can thus be employed to examine the contribution of these functional groups to the samples' optical properties.

Natural waters (15 mL) were transferred to glass vials with 15 mg of $NaBH_4$ (Fisher) then added to each vial. Samples were allowed to reduce for 48 h. in the dark under aerobic conditions [57] and filtered thereafter through a 0.2 µm nylon filter. Due to the increase in pH upon reduction, absorbance was recorded twice, once at pH 10 and again after the pH was readjusted to ~8 using $HClO_4$.

Depending on the sample availability, C18-OM samples were diluted to match the absorbance of either an ~80 or 30 mg/L Suwannee river fulvic acid (SRFA) reference solution at 350 nm. Three mL of diluted C18-OM was used for each reduction with 6 or 2.25 mg of $NaBH_4$ added, depending on the C18-OM concentration (~80 or 30 mg/L, respectively). Samples were allowed to reduce for 48 h., with the pH then adjusted and optical measurements recorded.

Milli-Q water was also treated with $NaBH_4$ following the same protocol, with the optical properties (absorbance and fluorescence) examined following reduction and pH adjustment with $HClO_4$. Changes in the absorption and emission of Milli-Q water following this reduction procedure were negligible.

3.4 Results/Discussion:

3.4.1 Vertical profile of physical, chemical and selected optical properties

Each of the distinct water masses at Station ALOHA, compiled by Hernes and Benner (2002) from multiple previous studies, were sampled, providing vertical profiles of the physical, chemical and optical properties (Fig. 3.2a-e). Salinity exhibited a distinct decrease with depth, ranging from ~35.2 at the surface to a minimum of ~34.1 at ~530 m, indicative an input of fresher water possibly from the Sea of Okhotsk [76,130]; salinity then increased with depth before leveling off at value of ~34.7 at ~2000 m. While oxygen was relatively uniform with depth from the surface to ~350 m, it also showed a distinct decrease below this depth, reaching a broad minimum at ~770 m, approximately 200 m deeper than the salinity minimum; thereafter, the oxygen slowly increased with increasing depth.

In contrast, $a_{CDOM}(350)$ was lowest at the surface (~0.03 m^{-1}) and increased rapidly with increasing depth, reaching a maximum at ~600 m (~0.11 m^{-1}) and decreased only

slightly with depth thereafter, reaching a value of ~0.08 m^{-1} at 4500 m. The $a_{CDOM}(350)$ maximum fell between the minimum values of salinity and oxygen, although this maximum was closer to the salinity minimum than the oxygen minimum, suggesting a freshwater (i.e. terrestrial) source of CDOM as opposed to its *in situ* production within the oxygen minimum zone [70,76,110]. However, because these minima are so close to the $a_{CDOM}(350)$ maximum, a clear distinction in source cannot be made on the basis of these data alone. The low values of $a_{CDOM}(350)$ in the upper water column are consistent with photobleaching of CDOM in the surface waters [1,22,109,110,131]. Fluorescence emission observed at 450 nm with excitation at 350 nm (F(350/450)) exhibited a very similar pattern with depth to $a_{CDOM}(350)$, although F(350/450) did not appear to decrease to the same extent as $a_{CDOM}(350)$ at depths below the maximum (~600 m).

As with $a_{CDOM}(350)$, values of $a_{CDOM}(280)$ were lower in surface waters (~0.37 m^{-1}), but only increased to ~0.45 m^{-1} at the maximum (~600 to 1000 m). Unlike $a_{CDOM}(350)$, $a_{CDOM}(280)$ decreased at depths below 1000 m to values comparable with those of surface waters, clearly suggesting a change in absorption spectral line shape with depth. This conclusion is supported by the depth-dependence of the spectral slope parameter, $S_{300\text{-}700}$, E_2:E_3, and S_R (Fig 3.2c and 3.3c), where the highest value was observed in surface waters (~0.029 nm^{-1}), the lowest values at intermediate depths (~0.017 to 0.020 nm^{-1} from 500 to 1500 m), and slightly higher values at the lowest depths (~0.021 to 0.022 at 2500 m and deeper). Unlike F(350/450), F(280/305) did not always follow the same pattern as $a_{CDOM}(280)$, indicating a variable input of UV absorbing and fluorescing material (see section *Fluorescence emission* below).

Table 3.1: Specific absorption coefficients for CDOM (a*CDOM (350), and a*CDOM (325)), from the NPO, Northern Atlantic, MAB, and Orinoco river, and for extracted CDOM (a*C18-OM (350)), for Delaware Bay and MAB, as well as reference materials.

		[L (mg org. C) m-1]		
	Salinity (PSU)	**$a^*_{CDOM}(350)$**	**$a^*_{CDOM}(325)$**	**Reference**
NPO (Station ALOHA)				
15 m	35.21	0.03	0.06	This paper
298 m	34.44	0.08	0.14	
496 m	34.06	0.14	0.25	
595 m	34.15	0.23	0.37	
695 m	34.27	0.20	0.34	
794 m	34.35	0.21	0.36	
991 m	34.48	0.20	0.35	
1486 m	34.56	0.21	0.36	
2470 m	34.65	0.17	0.31	
3449 m	34.68	0.16	0.29	
4425 m	34.69	0.16	0.29	
Northern Atlantic (~52°W 30°N)				
Surface (0-500 m)			~0.05 - 0.13	Nelson et al., 2007
Intermediate (500-1000 m)			~0.13 - 0.25	
Deep (1000-5000 m)			~0.20 - 0.35	
MAB				
Upper DE Bay (surface)	~0-15	~1.08 - 1.25		Del Vecchio and Blough, 2004b
Lower DE Bay (Surface)	~15-30	~0.67 - 1.00		
Shelf (below mixed layer)	~30-34	~0.08 - 0.42		
Open Ocean (below mixed layer)	~34-35	~0.08 - 0.33		
Orinoco River				
Orinoco River CDOM		2.33	3.34	Blough et al., 1993
Gulf of Paria				
Gulf of Paria CDOM		0.90	0.93	Blough et al., 1993
MAB		**$a^*_{C18\text{-}OM}(350)$**		
Upper DE bay (Surface)		3.39		Golanoski et al., 2012
Lower DE Bay (Surface)		1.37		
Shelf (MAB) (below mixed layer)		0.49		
Reference materials		**$a^*_{extract}(350)$**		
SRFA		3.42		Golanoski et al., 2012
SRHA		7.46		
LAC		4.48		

The absorbance at 254 nm ($A_{CDOM}(254)$) was fairly uniform with depth with just slightly higher values at the surface (~0.35 m^{-1}) compared to those at depth (~ 0.26 m^{-1}) (Fig. 3.3d). Similarly to $a^*_{CDOM}(280$ and $350)$ (Fig. 3.2), $SUVA_{254}$ was low at surface increasing with depth to ~ 600 m then leveling off for the remainder of the profile (Fig. 3.3d). Because $SUVA_{254}$ is often used as a general indicator of aromaticity [11], the low values at the surface suggests that the DOM in the mixed layer is less aromatic. This result likely arises from both a greater contribution of non-colored carbon produced biologically in surface waters, and a lower absorption contribution due to photobleaching.

The total organic carbon concentration (TOC) was highest at the surface, ~79 µM, and decreased with depth to ~ 39 µM by ~700 m, remaining approximately constant below this depth (Fig. 3.2c). Because of this decrease in TOC with depth, the increase in specific absorption coefficients with depth (a^*_{CDOM}; Fig. 3.2d-e) was significantly larger than the increase in absorption coefficient; for $a^*_{CDOM}(350)$, the values increased by about an order of magnitude, from ~0.03 m^{-1} mg^{-1} C L at the surface to ~0.23 m^{-1} mg^{-1} C L by 600 m, and decreased only slightly at depths below 2000 m. These specific absorption coefficients at depth are comparable to those found previously in offshore marine waters in the Northern Atlantic at depths of 500-1000 m (Table 3.1) [82], in the Middle Atlantic Bight (MAB) and other coastal regions (Table 3.1) [45,132], but are ~10- to 20-fold lower than those observed for isolated humic substances of terrestrial origin (Suwannee River humic and fulvic acids) or for C-18 extracts of estuarine or coastal waters [18]. This result implies either that 1) the CDOM in the deep waters is more weakly absorbing than the terrestrial materials, or 2) the CDOM remains as strongly absorbing as terrestrial materials but represents only a small

Table 3.2: Spectral slope ratio (SR) and absorbance ratio (E2:E3) for CDOM and C18-OM from several locations.

	S_R ($S_{275-295}$:$S_{350-400}$)		E_2:E_3 (A_{250}:A_{365})		
	CDOM	**C18-OM**	**CDOM**	**C18-OM**	**Reference**
North Pacific Ocean					
St. ALOHA (15 m)	6.80	0.80	45.3	15.23	This paper
Pacific Ocean (21 m)*		1.57		14.19	Kellerman et al., 2018
Pacific Ocean (240 m)*		1.27		10.78	Kellerman et al., 2018
St. ALOHA (298 m)	1.29	0.81	15.3	8.31	This paper
St. ALOHA (496 m)	2.02	0.91	11.0	6.62	This paper
St. ALOHA (595 m)	1.77	0.91	8.0	6.11	This paper
Pacific Ocean (674 m)*		1.74		4.86	Kellerman et al., 2018
St. ALOHA (695 m)	2.01	0.96	8.8	6.30	This paper
St. ALOHA (794 m)	1.45	0.95	9.4	5.74	This paper
St. ALOHA (991 m)	1.13	1.03	10.2	6.72	This paper
St. ALOHA (1486 m)	1.57	1.02	8.9	6.20	This paper
St. ALOHA (2470 m)	1.83	1.13	10.2	7.11	This paper
St. ALOHA (3449 m)	1.76	0.95	10.5	7.27	This paper
St. ALOHA (4425 m)	1.82	0.92	11.7	7.94	This paper
Equatorial Atlantic					
St. 26 (2 m)	1.28	1.29	26.97	18.97	Andrew et al., 2013
St. 51 (2 m)	5.28	0.78	23.86	16.15	
St. 73 (2 m)	1.65	0.87	24.11	17.88	
St. 75 (2 m)	0.79	0.94	24.29	18.26	
St. 26 (1000 m)	0.61	1.38	8.77	8.17	
St. 51 (1000 m)	0.95	1.42	7.66	7.84	
St. 73 (1000 m)	0.44	1.10	10.25	7.80	
St. 75 (1000 m)	0.12	1.23	7.42	7.49	
MAB (Aug./ Sept.)					
Upper Bay (2 m)	0.29	0.33	6.69	5.23	Boyle et al., 2009
Shelf (2 m)	1.82	0.47	18.64	13.73	
Shelf (45 m)	0.61	0.46	9.43	6.49	
Gulf Stream(2 m)	0.38	1.06	28.28	21.00	
Gulf Stream (1000 m)	1.89	1.39	11.77	8.26	
Reference materials		**extracts**		**extracts**	
SRFA		0.75		4.61	Schendorf et al., 2016
SRHA		0.35		3.34	

fraction of the total TOC (~5 to 10%), or 3) some combination of both factors are at play (Table 3.1).

$S_{275-295}$ and $S_{350-400}$ (Fig. 3.3b black and red, respectively) varied only slightly with depth except for the surface waters which exhibited the lowest values of $S_{350-400}$ (Fig. 3.3b). The low $S_{350-400}$ values impacted the S_R values which are highest at the surface declining to values between 1.2 and 2.9 down the water column (Fig. 3.3c). Similarly, the E_2:E_3 ratio follows the same trend with the largest value at the surface (~ 45) decreasing to about constant values (~10) with depth (Fig. 3.3c). Larger values of S_R and E_2:E_3 at the surface have been associated with low molecular weight DOM [33,36]. However, shoulders and bands in the absorbance spectrum can also affect both of these parameters, as observed for the 15 m samples which both exhibit a distinct absorbance shoulder at ~250-280 nm. CDOM from other regions has shown similar trends of S_R and E_2:E_3 with the surface waters exhibiting significantly higher values than deep waters (Table 3.2).

Extracted CDOM (C18-OM) exhibited a more uniform vertical distribution of S_R and E_2:E_3 for (Table 3.2) indicating that these parameters are indeed impacted by discrete bands/shoulders not extracted by C18 columns (see section *Extraction efficiencies* below).

HIX values were lowest in the top 300 meters (~0.44) increasing to ~0.7 at ~500 m, and remaining fairly constant thereafter, except at ~ 4500 m; here HIX decreased again to ~ 0.4 due to a highly fluorescing discrete UV band that significantly altered the integrated emission intensity from 300-345 nm at excitation 250 nm. BIX values were highest (~1.1) at the surface slightly decreasing to ~0.9 at depth. Likewise, FI values were highest (~ 1.77) at the surface slightly decreasing (~1.65) at depth. These indices (HIX, BIX, and FI) have been proposed to provide information about the source and nature of

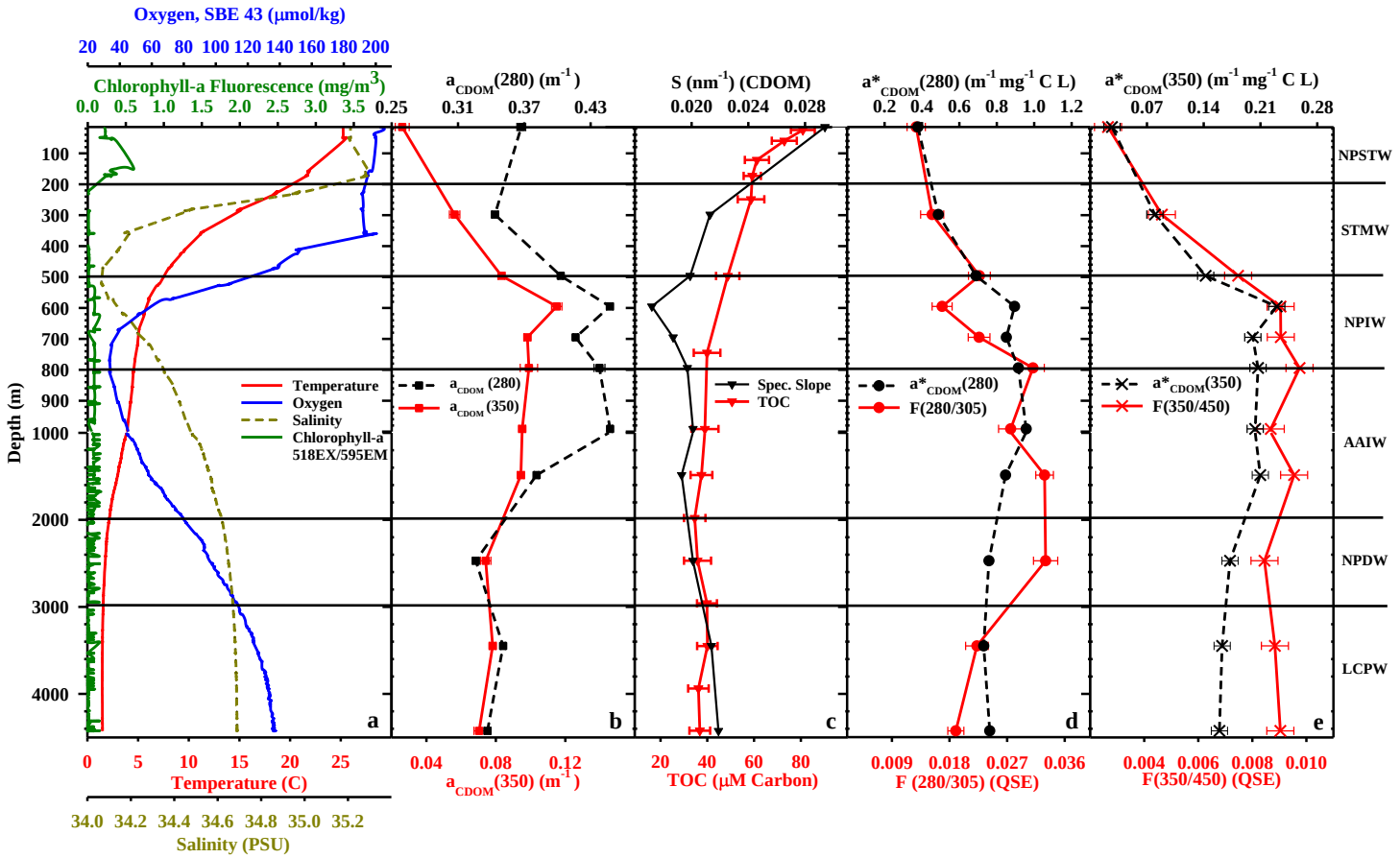

Figure 3.2: Vertical profile of: **(a)** in-situ physical properties, **(b)** absorption coefficients ($a_{CDOM}(280)$ and $a_{CDOM}(350)$), **(c)** total organic carbon (TOC), and spectral slopes ($S_{300\text{-}700}$), **(d)** specific absorption coefficient ($a^*_{CDOM}(280)$), and fluorescence emission (F(280/305)), **(e)** specific absorption coefficient ($a^*_{CDOM}(350)$) as well as fluorescence emission (F(350/450)) for natural water samples. The assignment of each water mass as defined by Hernes and Benner (2002) are shown on the right. North Pacific Sub-Tropical Water (NPSTW), Sub-tropical Mode Water (STMW), North Pacific Intermediate Water (NPIW), Antarctic Intermediate Water (AAIW), North Pacific Deep Water (NPDW), Lower Circumpolar Water (LCPW).

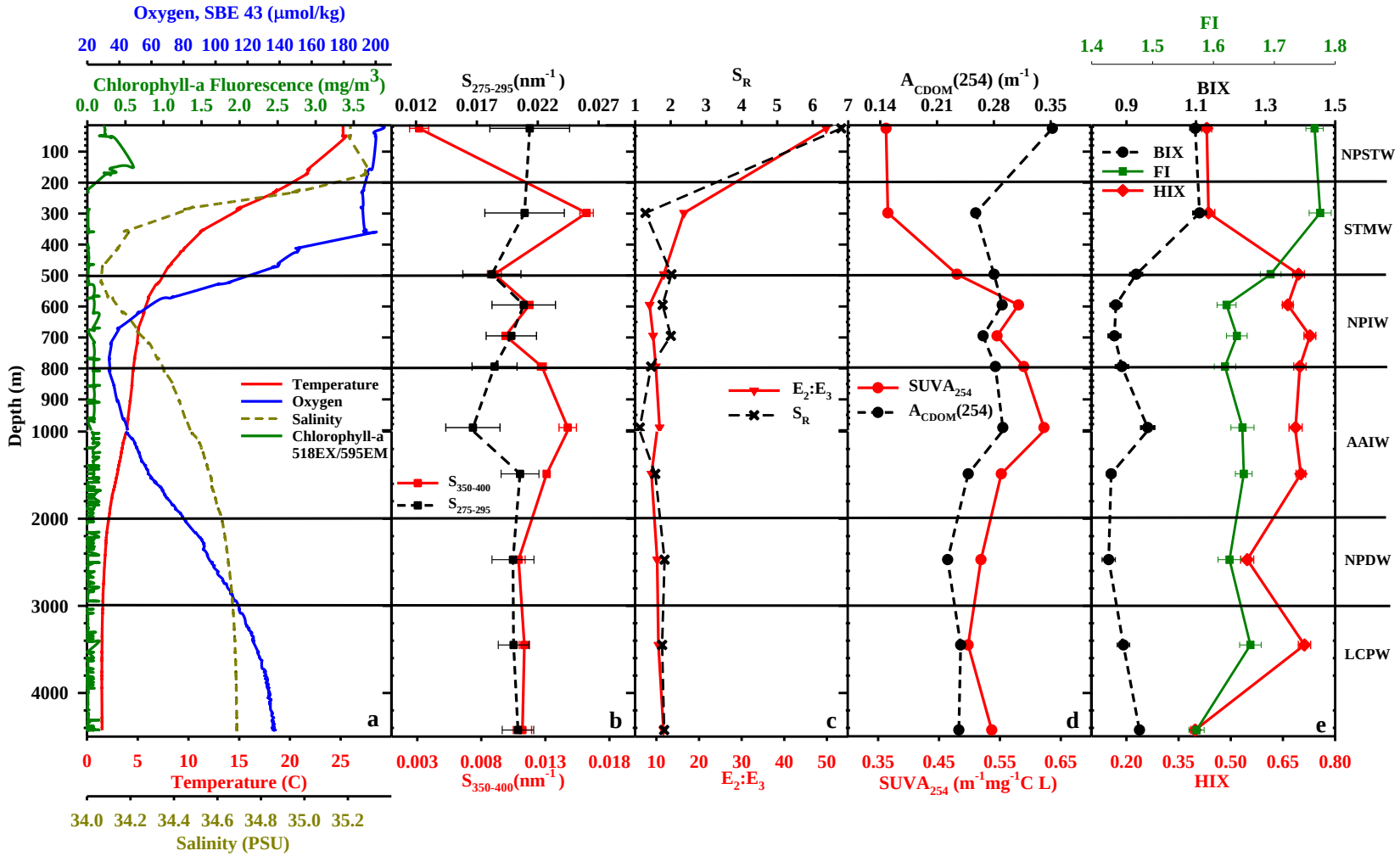

Figure 3.3: Vertical profile of: **(a)** in-situ physical properties, **(b)** spectral slopes ($S275_{-295}$ and $S_{350-400}$), **(c)** spectral slope ratio (S_R) and E_2:E_3, **(d)** A_{CDOM} (254) and $SUVA_{254}$ **(e)** Humification Index (HIX), Fluorescence Index (FI), and Biological Index (BIX).

CDOM and DOM based on correlations of optical parameters with the "degree of humification" (HIX), or within situ production (BIX and FI). Larger values of HIX have been suggested to correlate with a larger "degree of humification" [129], while larger BIX values (> 1) and larger FI values (~1.8) have been suggested to indicate the production of fresh or autochthonous CDOM [39,40]. Because these indices did not vary significantly along

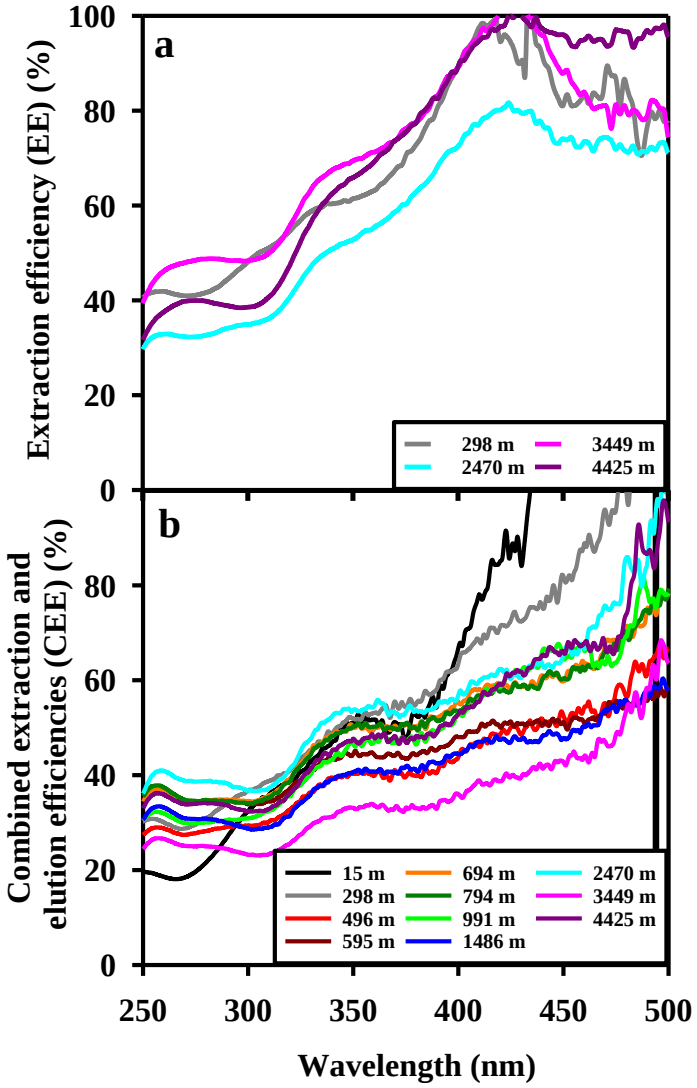

Figure 3.4: (a) Wavelength dependence of extraction efficiencies (EE) of absorption for select samples at various depths, **(b)** wavelength dependence of combined extraction and elution efficiencies (CEE) of absorption for the entire vertical profile.

the water column at Station ALOHA and their values fell within the middle of previously identified ranges, our data indicates that these indices cannot be used to distinguish source(s) of CDOM or DOM in these differing water masses.

Below, the depth dependence of the spectral variations in absorption and fluorescence for both the natural waters and C18-OM extracts are examined in detail, along with effects of borohydride reduction on these optical properties.

3.4.2 Comparison of natural waters (CDOM) and extracts (C18-OM)

Extraction efficiencies

Consistent with prior work [7,24,26,108,133], extraction efficiencies of absorption by C18 SPE increased at longer wavelengths for all depths (Fig. 3.4a and S3.1), ranging from ~40% at λ<300 nm, to ~80% or more at λ > 400 nm. Combined extraction and elution efficiencies were somewhat more variable and were lower, ranging from ~30% at λ<300 to ~50-60% at λ>400 nm, but exhibited a similar spectral dependence (Fig. 3.4b). This preferential extraction and elution produced higher relative absorption over the visible wavelengths for the C18-OM (Fig. 3.5), and concomitantly lower values of the spectral slope parameter, $S_{300\text{-}700}$ (Fig. 3.5, 3.6) as previously reported for other coastal and offshore marine waters[7].

As observed in past studies, absorption of both natural waters and the C18-OM decreases with increasing wavelength in an approximately exponential fashion [1,25] (Fig. 3.5). However, the exponential model provided much poorer fits to the absorption spectra for the natural waters than those for the C18-OM at all depths, but particularly for surface waters. This result was primarily due to weak shoulders in the spectra at ~420 nm, 320 nm and 280 nm that were evident to differing degrees in all of the natural water samples (Fig. 3.5). These shoulders in the spectra were far less evident in the absorption spectra of the

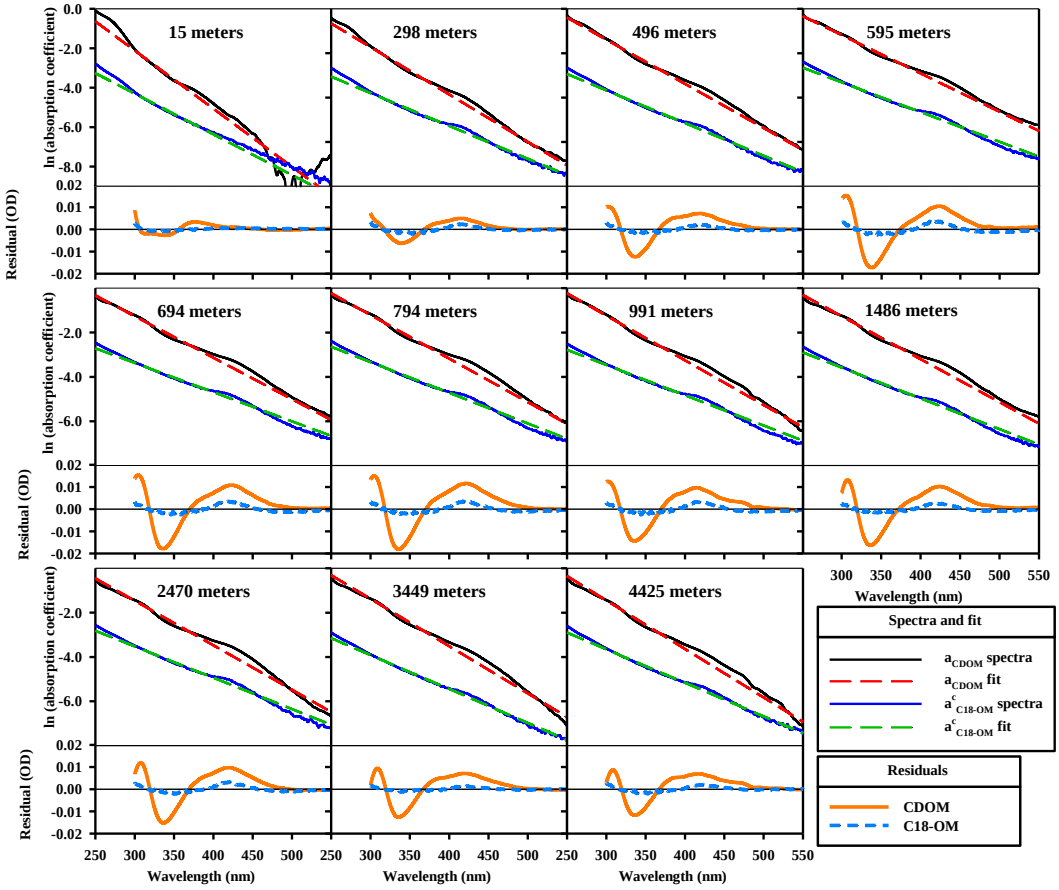

Figure 3.5: (top panels) Natural log of a_{CDOM} and $a^{C}_{C18\text{-}OM}$ (offset by -1 ln unit for clarity) from 250-550 nm along with the nonlinear least squares fit calculated from 300-700 nm (Eq. 5) then extrapolated to 250 nm for all depths, **(bottom panels)** Residuals (defined as 'spectra – fit') for both CDOM and C18-OM spectra from 300-550 nm for all depths**)**.

C18-OM (Fig. 3.5), suggesting that the species associated with these bands were extracted and/or eluted with far lower efficiency than the "humic-like" component. The lack of extraction and/or elution of these bands further indicates that these components are structurally different from the "humic –like" component.

Similar to prior results from the MAB, [45] and the EAO [16], both the CDOM and the C18-OM exhibited broad emission spectra characteristic of "humic-like" materials, with emission maxima systematically shifting to the red at excitation wavelengths beyond ~ 325

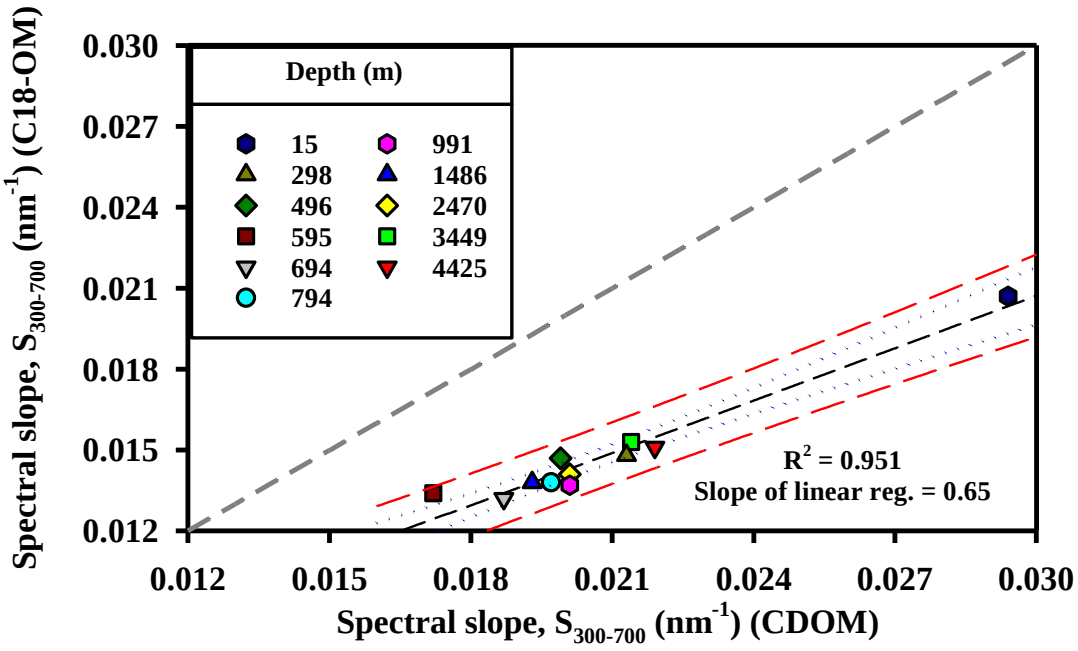

Figure 3.6: Spectra slopes ($S_{300\text{-}700}$) values for CDOM and C18-OM samples. (**---**) linear regression, (---) 1:1 line, (**...**) 95% confidence intervals, and (**---**) 95% prediction band.

nm (Fig. 3.7 and S3.2). Also similar to the results from the EAO, the CDOM exhibited discrete emission bands in the ultraviolet and near-visible that were not observed in the C18-OM (Fig. 3.7), see section *Fluorescence emission* below), indicating that these species were either not extracted or were extracted but not eluted, and thus have a fundamentally different structure from the "humic-like" materials as previously indicated by the absorbance. Thus, both absorption and emission measurements provide evidence that discrete absorbing and emitting components are lost by C18 extraction, while the "humic-like" component is preferentially enriched particularly for absorption at the longer wavelengths in the visible. Further, while these discrete components provide only small contributions to the total absorption (Figs. 3.5, and 3.9), they do contribute significantly to the emission in the UV (Fig. 3.7) owing to their high fluorescence quantum yields (Fig. 3.9).

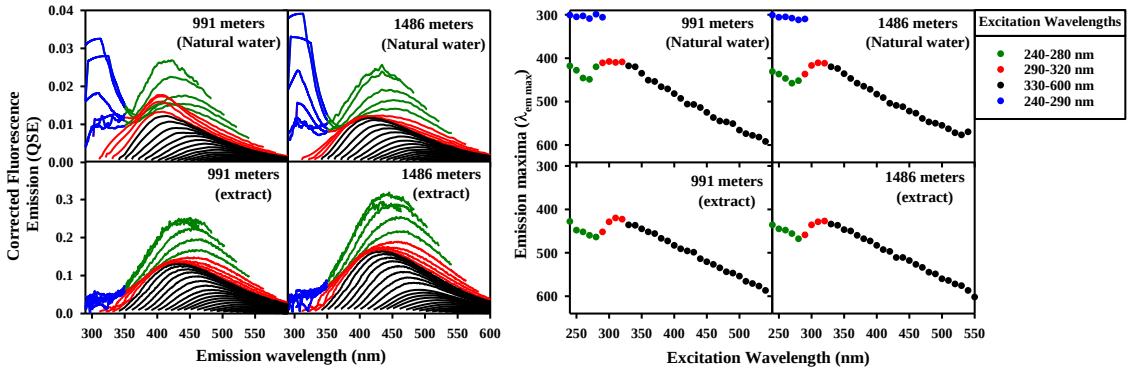

Figure 3. 8: Fluorescence emission spectra for natural waters (**top**) and C18-OM extracts (**bottom**), for 991 and 1486 m samples: EEMs (**left**), emission maxima, $\lambda_{em\ max}$ (λ_{ex} 240-550 nm) (**right**). Several regions are colored for ease of comparison (excitation wavelengths for each color shown in legend).

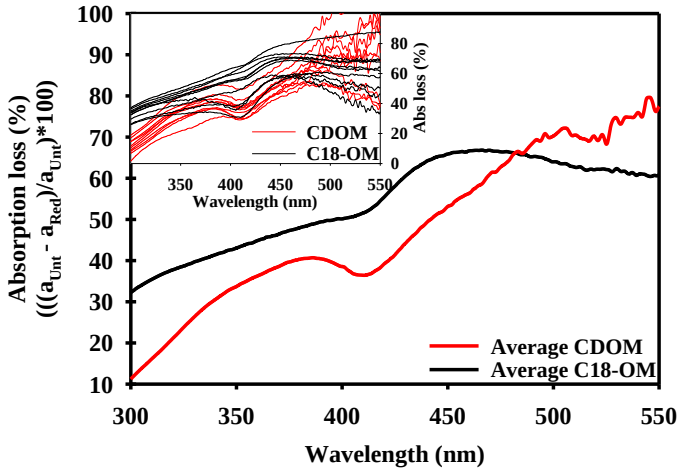

Figure 3.7: Average percent absorption loss after $NaBH_4$ reduction (24 h.) for natural waters (CDOM) (**red**) and extracts (C18-OM) (**black**). **Inset**: Spectra for individual depths.

3.4.3 Depth dependence of the optical properties of CDOM and C18-OM and the effect of sodium borohydride reduction on the optical properties

From the surface to ~600 m, absorption by CDOM increased while S decreased (Figs. 3.2, 3.4, 3.5). Below this depth, absorption and S did not vary substantially, although a very slight increase in S appears evident at depths below 2000 m along with slight decreases in $a_{CDOM}(350)$ and $a_{CDOM}(350)^{*}$(Fig.3.2, 3.5, 3.6). As noted above, fits of the CDOM absorption to an exponential model were poor in most cases (Fig. 3.5) due to clear

shoulders in the absorption spectra at ~415-420 nm, ~320 nm and ~260-280 nm. Previous work by Röttgers and Koch (2012), Catalá et al. (2016) and Andrew et al. (2013) also provided evidence for a band at ~415-420 nm in offshore marine waters, although this band was only observed occasionally in the waters of the EAO [16]. While changes with depth of absorption and S of the C18-OM largely mirrored those of the CDOM (Figs. 3.4, 3.5), fits of the C18-OM absorption to an exponential model were far better (Fig. 3.5), owing to the incomplete extraction of the species giving rise to these shoulders in the CDOM. Nevertheless, a small contribution from the 420 nm shoulder was still evident in the C18-OM (Figs. 3.5, 3.9).

As observed previously for waters in the EAO [16], borohydride reduction of both CDOM and C18-OM produced significant irreversible losses of absorption with the largest percent loss occurring in the visible region (Figs. 3.8, 3.9), consistent with the reduction of ketones/aldehydes to alcohols [46,57] and the charge transfer model of the optical properties of humic substances and CDOM [21,22]. This model proposes that the visible absorption is due primarily to charge-transfer transitions arising among hydroxy-(methoxy) aromatic donors and carbonyl-containing acceptors; by eliminating the acceptors via reduction these interactions are also eliminated producing the preferential loss of visible absorption [21,46,68]. These losses were observed at all depths but were larger at depths below 300 m (Fig. 3.9). As observed previously for the Delaware Bay, the MAB, the EAO and humic substances [16,46,57] the percent loss was greatest over the visible wavelengths (> 400 nm, > 50%), with much smaller losses observed at shorter wavelengths (< 350 nm , < 10-30 %). Larger absorption losses were observed for the C18-OM (Figs. 3.8, 3.9), although the spectral dependence of this loss was similar. There was also some absorption recovered after the

reduced sample was allowed to stabilize in the dark open to air (Fig. S3.3). This reversible loss of absorbance could indicate the presence of quinones which would easily reoxidize when exposed to air.[46,68] However, the percent of the absorbance recovered, is minimal compared to the absorbance that is irreversibly lost.

The preferential loss of long wavelength absorption was also manifested by an increase of $S_{300\text{-}700}$ for both CDOM and C18-OM upon reduction (Figs. 3.9, 3.10), with S increasing by 29 ± 6% on average for CDOM and by 15 ± 7% for C18-OM. The higher percent increase for CDOM may be explained by the presence of short wavelength absorbing species that are not present in the C18-OM due to incomplete extraction; because these species are not as significantly impacted by reduction (compare CDOM and C18-OM in Fig. 3.9), the loss of long wavelength absorbance has a greater influence on the spectral slopes of the CDOM.

Both CDOM and the C18-OM exhibited a dip in the absorption loss at ~420 nm (Fig. 3.8), suggesting that the 420 nm shoulder was unaffected by borohydride reduction. This result suggests that this shoulder is not part of the "humic-like" absorption, and is a distinct species. The observation that this absorption shoulder appears to be less efficiently extracted (Figs. 3.4, 3.5) is consistent with this idea. Because this band was unaffected by borohydride reduction, was incompletely removed by the extraction, but was not emissive, a small dip in the apparent fluorescence quantum yields was observed at ~ 420 nm for the C18-OM at a number of depths due to the absorption by this band (Fig. 3.9). This decrease was particularly evident in the borohydride reduced samples due to the greater absorption contribution of this band following reduction.

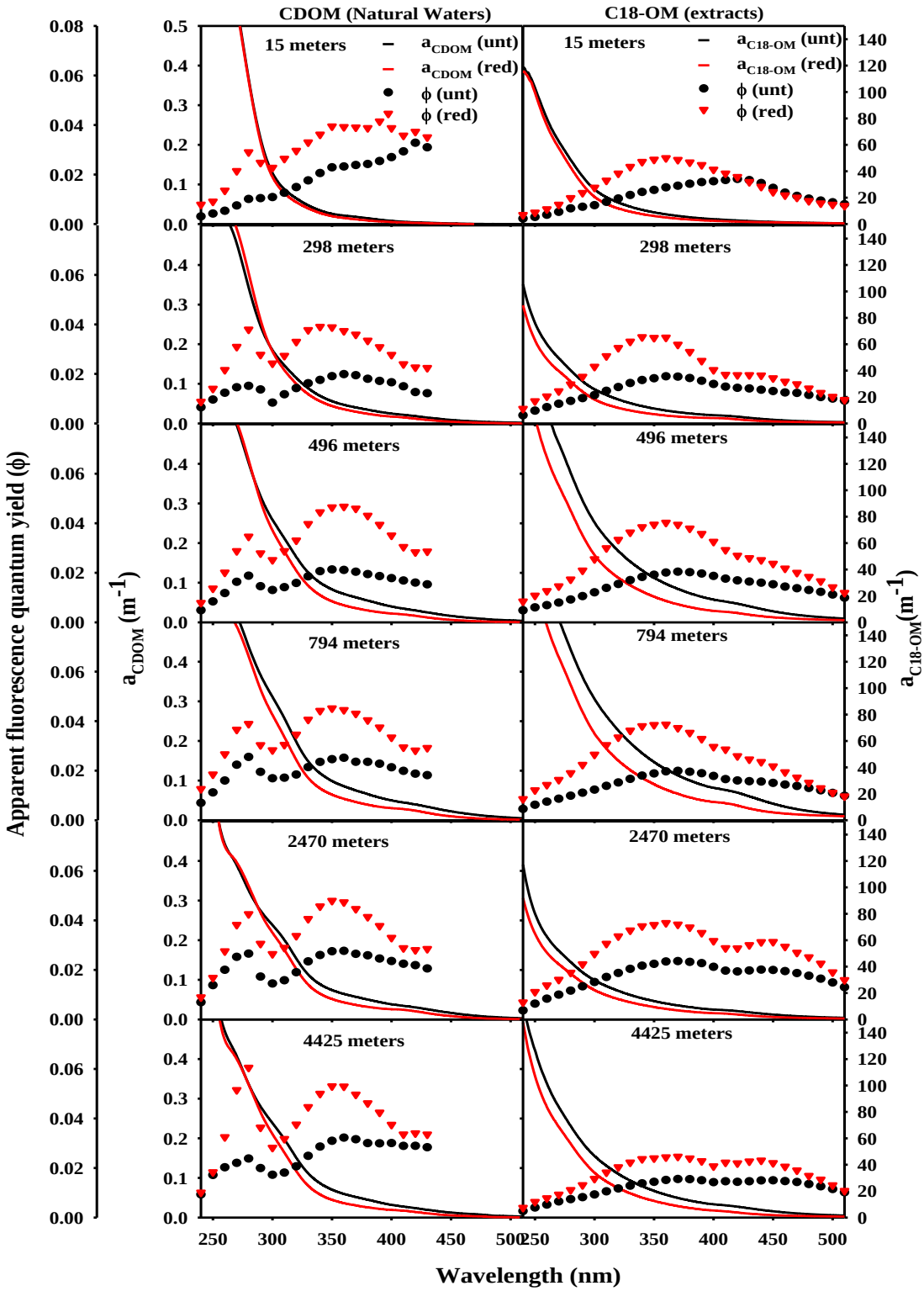

Figure 3.9: Absorption spectra and apparent fluorescence quantum yields (ϕ) for CDOM (**left**) and C18-OM (**right**), untreated (black) and reduced (red) samples.

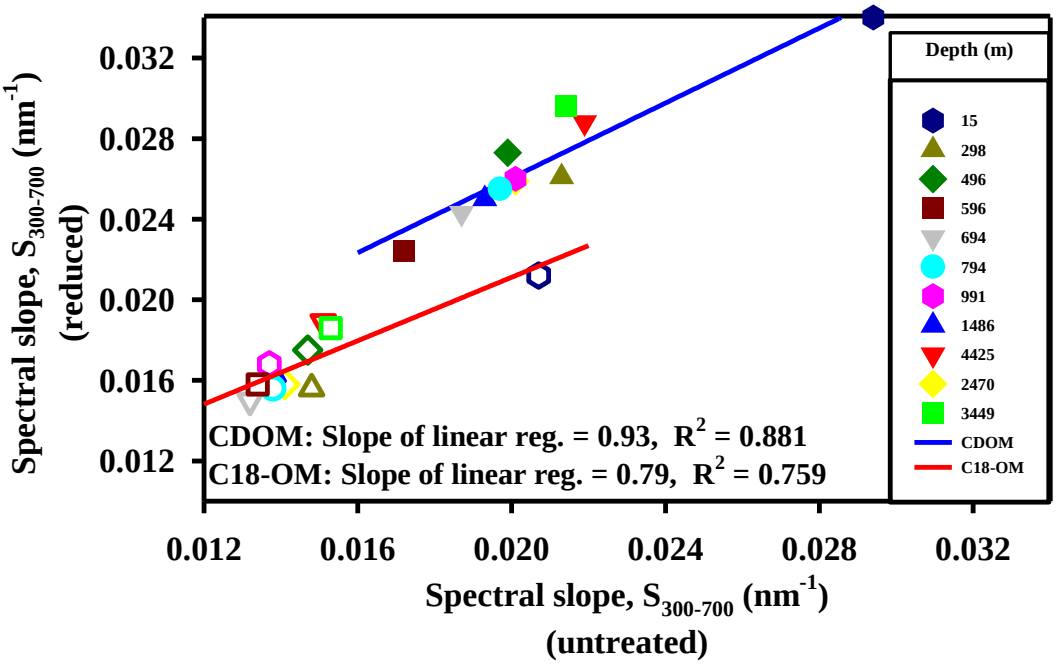

Figure 3.10: Comparison of spectra slope ($S_{300-700}$) values for untreated and reduced CDOM (solid) and C18-OM (outlined) samples. Linear regression lines for CDOM (—) and C18-OM (—).

EEMs spectra of the natural waters (CDOM) (Figs. 3.7, 3.11 and S3.2) reveal the presence of both short-wavelength emitting species in the UV as well as long-wavelength "humic-like" emission in the visible. Several distinct short-wavelength emission bands exhibited substantial emission, including one with the peak excitation(λ_{ex})/emission(λ_{em}) at ~270/305 nm that was observed at all depths, and another with $\lambda_{ex}/\lambda_{em}$ ~240/340 nm that was present only at select depths (298, 2470, and 4425 m). A third distinct band with $\lambda_{ex}/\lambda_{em}$ at ~300/410 nm appears to overlap the "humic like" fluorescence and was only observed at some depths (15, 496, 794, 991 and 4425 m). Andrew et al [16] also found several discrete bands in waters from the EAO, two of which are very similar to bands seen in the NPO,

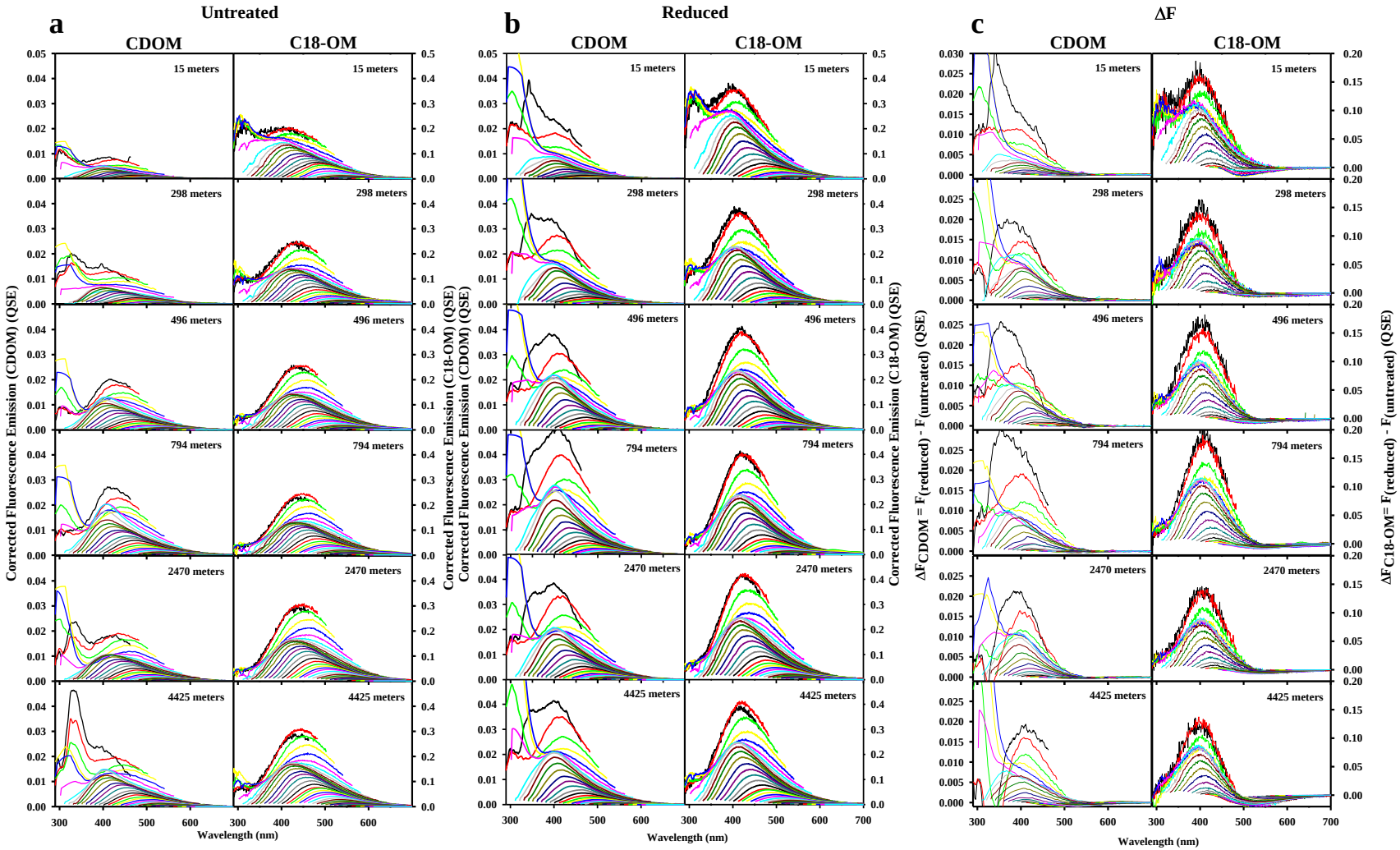

Figure 3.11: Depth dependence of EEMs for CDOM and C18-OM samples collected at Station ALOHA: **(a)** Untreated EEMs; **(b)** sodium borohydride reduced EEMs, **(c)** ΔF (reduced- untreated spectra).

one at $\lambda_{ex}/\lambda_{em}$ ~300/405 nm and one at ~280/310 nm. For the EAO samples, the EEMS scans did not include excitation wavelengths between 240 and 270 nm, and thus the band at $\lambda_{ex}/\lambda_{em}$ ~240/340 nm seen in the NPO could not have been detected in the EAO. With the exception of the surface 15 m sample (Fig. 3.11), these unique emission bands were only seen in the natural waters, and were not present in the C18-OM extracts (Figs. 3.7, 3.11), just as observed in the EAO [16]. These distinct bands exhibited the largest variability with depth (Fig. 3.11). No evidence was acquired for emission from the absorption shoulder at 420 nm.

The variation in intensity of the fluorescence down the water column can be compared by examining EEMS of the natural water samples (Fig. 3.11a, left column; see also Fig. 3.2d-e). For the "humic-like" component emitting in the visible, there are only small changes with depth after the initial increase from the surface to ~600 m; only the discrete bands in the UV exhibit variable contributions down the water column. The overall lower emission that is observed in surface waters can be attributed to photobleaching.

Because the C18-OM fluorescence was not normalized for dilution and concentration processes, its emission intensity cannot be quantitatively compared down the profile or to the natural waters, only the spectral shape and relative intensities can be examined. Because the discrete bands were not extracted, the EEMs of the C18-OM were exclusively "humic-like", exhibiting the characteristic red shift in λ_{em} with increasing λ_{ex} (Figs. 3.7, 3.11). Further, the spectral dependence and magnitude of the apparent fluorescence quantum yields were also very similar to those previously observed on the shelf of the MAB, and in the EAO (~ 0.02 at maximum) (Fig. 3.9, Table 3.3), but were generally higher than terrestrially impacted estuarine waters and humic substances (~ 0.01

Table 3.3: Maximum apparent quantum yield (ϕ), and their excitation wavelength ($\lambda_{ex\ max}$), for NPO, EAO, MAB samples (CDOM and C18-OM) as well as reference materials.

	Max ϕ / λ_{ex} (nm)		
	CDOM	**C18-OM**	**Reference**
NPO (Station ALOHA)			
15 m	0.024 / 350	0.018 / 420	This paper
298 m	0.021 / 360	0.019 / 360	
496 m	0.022 / 350	0.020 / 370	
595 m	0.020 / 350	0.018 / 370	
695 m	0.023 / 350	0.024 / 370	
794 m	0.025 / 360	0.020 / 370	
991 m	0.023 / 360	0.022 / 370	
1486 m	0.026 / 360	0.024 / 370	
2470 m	0.029 / 360	0.024 / 370	
3449 m	0.028 / 360	0.025 / 370	
4425 m	0.034 / 360	0.016 / 370	
EAO			
EAO open ocean (5 m) average[a]	0.023 ± 0.004 / 375	0.014 ± 0.002 / 370	Andrew et al., 2016, 2013
EAO open ocean (1000 m) average[a]	0.022 ± 0.003 / 370	0.023 ± 0.002 / 370	
EAO: St. 96 Congo plume (2 m)	0.0125 / 370	0.008 / 370	
EAO: St. 96 (1000 m)	0.024 / 360	0.026 / 370	
Sargasso Sea			
Sargasso Sea 50 m [b]		0.022 / 355	Green and Blough, 1994
Sargasso Sea 850 m [b]		0.016 / 355	
Sargasso Sea 1500 m [b]		0.021 / 355	
Sargasso Sea 3200 m [b]		0.021 / 355	
MAB			
MAB offshore 2 m	0.028 / 370	0.021 / 370	Andrew et al., 2016
Delaware Bay 2 m	0.018 / 360	0.015 / 370	
Delaware River 2 m	0.015 / 370	0.012 / 370	
Gulf Stream 2 m		0.019 / 370	Boyle et al., 2009
Gulf Stream 1000 m		0.023 / 370	
MAB Shelf 2 m		0.024 / 370	
Reference materials			
SRFA [c]		0.01 / 370	Boyle et al., 2009
SRHA [c]		0.005 / 370	
LAC [d]		0.004 / 370	

[a] Average of samples ± standard deviation

[b] Quantum yields only provided at 355 nm

[c] Isolated humic substances, form the international humic substance society (IHSS)

[d] Lignin, alkali extracted and carboxylated, from Sigma Aldrich

at maximum) [7,16,24,26]. Except for the surface waters, which were blue shifted due to photobleaching, the EEMS of the C18-OM were indistinguishable with depth (Fig. 3.11).

These results suggest that common structures are present throughout the water column, further implying a common source for the CDOM.

As in past studies [7,16,46,57,68], reduction of CDOM and C18-OM with borohydride produced enhanced, blue-shifted emission from the "humic-like" components (Fig. 3.11b-c and S3.4). Because reduction also decreased absorption, apparent quantum yields of fluorescence were also enhanced, predominantly at the shorter wavelengths (Fig. 3.9 and S3.5). Interestingly, some of the discrete bands observed in the CDOM, particularly the band at excitation(λ_{ex})/emission(λ_{em}) ~270/305 nm, also showed evidence of enhanced emission following reduction, suggesting that these species may have also been partially quenched prior to reduction. Because of the enhanced emission from some of the discrete bands in the CDOM, apparent fluorescence quantum yields were also significantly elevated at excitation wavelengths in the UV (Fig. 3.9). Although there was some hint of this behavior in samples from the EAO (see Figs 13, 14 in Andrew et al. 2013), it is more clearly evident in this data set. Thus the change in fluorescence (ΔF) following borohydride reduction was variable for the discrete compounds emitting in the UV, but was quite uniform with depth for the "humic-like" component (Fig. 3.11c).

3.5 Synthesis with past results:

As observed in the EAO, we find that the "humic-like" component in the waters of the NPO exhibits very similar properties to those observed for terrestrially-dominated estuarine and coastal environments such as the MAB, providing strong evidence that this component originates from a terrestrial source. These properties include: 1) emission maxima that systematically red-shift with increasing excitation wavelengths across the UVA and visible; 2) similar spectral dependencies of the emission maxima and

fluorescence quantum yields; 3) preferential C18 extraction of this component, particularly for the longer-wavelength, visible absorbing and emitting material, but not the UV emitting material; 4) preferential loss of visible absorption and enhanced blue-shifted emission following borohydride reduction of both the natural waters and C18-OM from these waters.

Although the "humic-like" component in the deep waters of the EAO and the NPO exhibits very similar properties to each other and to terrestrially-dominated estuarine and coastal waters, they do not appear to be identical. First, spectral slopes of the deep waters in the NPO ranged from ~0.0185 to 0.0215 nm (Fig. 3.5, 3.6), generally higher than those observed in riverine, estuarine and deep coastal waters where they range from ~0.014-0.018 nm^{-1} [7,45,135]. Interestingly, spectral slopes for deep waters in the EAO appear to fall between these values, ranging from ~0.016 to 0.020 nm^{-1} [7,16]. Second, the maximum apparent fluorescence quantum yields for the NPO and EAO appear larger (Fig. 3.9, Table 3.3) [16] than those observed for most riverine, estuarine and coastal waters (~0.02 vs.~0.01, respectively) [7,16,24,26]. Both the higher spectral slopes and fluorescence quantum yields are consistent with the presence of a lower average molecular weight, modified terrestrial material [1,33,37,136]. The higher spectral slopes ($S_{300-700}$), S_R, E_2:E_3, and blue-shifted fluorescence emission spectra observed in the upper water column are also suggestive of a further decrease in the average molecular size via photobleaching [1,17,33,109,110,131].

While the lower values of absorption and emission observed in the upper water column can be readily attributed to the photobleaching of surface waters, the vertical profiles reveal no clear evidence that the "humic-like" component is being created *in situ* at depth within the oxygen minimum zone, as opposed to its injection from a fresher water source (Figs. 3.2,3.2,3.5,3.9,3.11) [70,76,82,137], possibly from the Sea of Okhotsk as

previously suggested [76,130]. The spectral dependence and magnitude of the optical properties of the "humic-like" component did not vary greatly at depths below 600 nm particularly for the C18-OM. These results are inconsistent with a strong biological source of this component within the oxygen minimum zone or in the deep waters below 2000 m. Indeed, this pattern is more consistent with the water column distribution of lignin phenols as previously measured by Hernes and Benner [76].

Although we did not observe a distinct absorption maximum in the NPIW as did Hernes and Benner for the lignin phenols (750 m), CDOM absorption reached its maximum value in the NPIW at ~600 m and exhibited only small decreases with increasing depth, similar to the pattern observed with the lignin phenols. Further, we observed a strong correlation between lignin phenol content as reported by Hernes and Benner (2002) and $a_{CDOM}(285)$ and $a_{CDOM}(350)$ measured by this study (Fig. 3.12), supporting a terrestrial source of CDOM at St. Aloha as previously observed for other regions [43,138]. Moreover, Opsal and Benner (1997) reported a 2.6 fold higher lignin phenol content in the Atlantic compared to the Pacific Deep Ocean strikingly consistent with the ~ 3 fold greater a_{CDOM} (350) in the Atlantic (~ 0.2 -0.35 m^{-1}) [16] as compared to the Pacific (~ 0.07 - 0.11 m^{-1}) (this work). Hernes and Benner, (2002) further found that the size distribution of the lignin phenols was shifted to lower molecular weight in the NPO, relative to terrestrial river end-members, consistent with our observations concerning the optical properties (see results above) and our past proposal that an ensemble of partially oxidized lignins (and possibly other partially oxidized hydroxy-aromatics) could produce the "humic-like" optical properties [21,22].

The high spectral slopes, high fluorescence quantum yields and low $a^*_{CDOM}(350)$ measured in the deep waters from NPO (LCPW and NPDW) suggest a diagenetically-aged "humic-like" component. As the North Atlantic surface water sinks, it is transported southward in the deep Atlantic Ocean as the North Atlantic Deep Water (NADW), eventually upwelling in the Southern Ocean, and sinking again into the deep Pacific Ocean as the Lower Circumpolar Water (LCPW). The LCPW then flows northward in the deep Pacific Ocean until it rises to shallower depths flowing again southward as the North Pacific Deep Water (NPDW). Both the LCPW and the NPDW thus represent the oldest water masses in this study, consistent with the most aged CDOM with high values of $S_{300-700}$, high fluorescence quantum yields and low specific absorption coefficients.

In contrast to the "humic-like" component, the UV absorbing and emitting components exhibited a high degree of variability down the water column, suggesting biological production as a strong local source of these components within the water column. The components exhibiting absorption shoulders at ~280, 320 and 420 nm do not contribute strongly to the overall absorption (Fig. 3.5, 3.9), which is largely dominated by the "humic-like" component. However, the discrete component(s) absorbing at ~280 nm do contribute strongly to the emission as observed by the enhanced fluorescence quantum yields at this excitation wavelength (Fig. 3.9). This result clearly demonstrates that reliance on fluorescence measurements alone can produce a highly distorted picture of the importance of these highly fluorescing species to the CDOM and DOM. The observation that these discrete UV components are not largely extracted while the "humic-like" component is (Fig. 3.5, 3.7), further demonstrates that these species have a fundamentally different structure from the "humic-like" material, which is also reflected in the optical

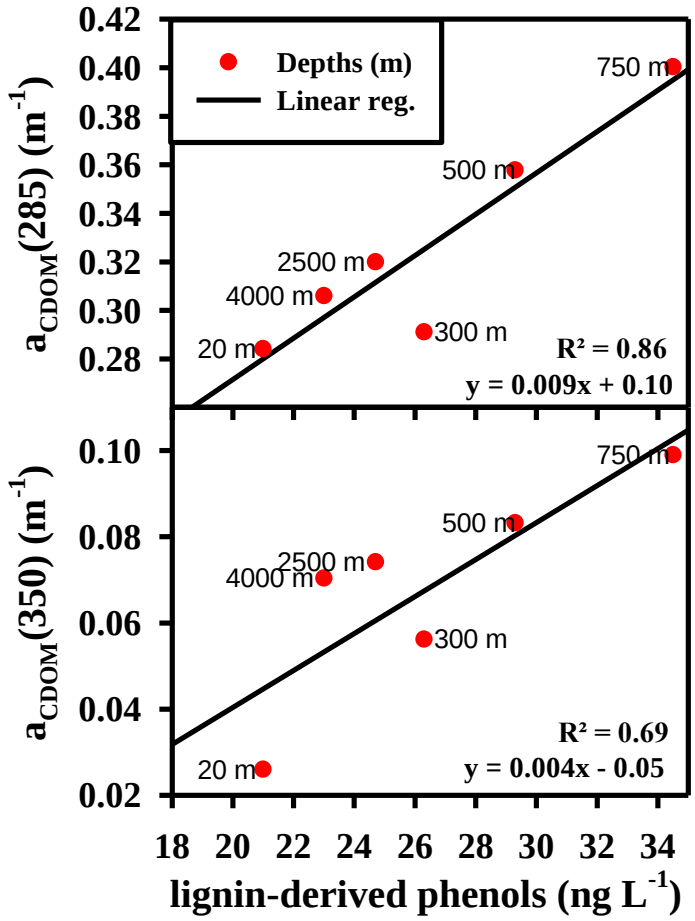

Figure 3.12: Dependence of absorption coefficients (this study) to lignin-derived phenols concentrations (ng L^{-1}) [76]. For selected depths along the profile as available from Hernes and Benner (2002).

properties. Overall, our results suggest a significant terrestrial "humic-like" CDOM contribution throughout the water column of the NPO, along with structurally dissimilar marine components that primarily absorb and emit in the ultraviolet.

As pointed out previously [16], we know of no diagenetic pathway(s) that have yet been demonstrated to produce from marine source materials a "humic-like" component having these same distinct optical and chemical properties. Although a number of incubation studies have suggested the production of "humic like" CDOM and FDOM from marine source materials [5,111–116], to our knowledge, none of these studies performed

detailed optical absorption and emission measurements combined with secondary chemical tests to demonstrate that this material exhibits the same properties as that found in the natural waters. Unlike many of the proposed optical indices (HIX, BIX, FI and others) the responses to these chemical tests are directly related to functional groups/ moieties involved in producing the optical properties. In contrast, most of the proposed optical indices are either based on correlations between the optical properties and presumed sources of the CDOM, or do not account for processes such as photobleaching that could alter these indices.

In addition to C18 extraction and borohydride reduction, other tests of the source and structure of this "humic-like" component in natural waters include measurements of the pH dependence of the spectral absorption, both for untreated samples and those reduced with borohydride [56,57,59,61], measurements of the content and impact of quinones on the optical properties [68], and mass spectrometry combined with Borodeuteride labeling [139]. By examining the combined optical properties and responses to these chemical tests, a far clearer picture of the molecular moieties producing the optical properties of CDOM can be acquired and compared across locations. Having a better understanding of the molecular moieties present within CDOM across location can provide useful information about the carbon cycle, by suggesting the fate of certain sources of CDOM. Some components appear to be more susceptible to degradation (photo or microbial) while others such as the "humic like" component derived from degraded plant tissue are more recalcitrant.

Chapter 4: Effect of pH, borohydride reduction and irradiation on the absorbance of SRNOM, SRFA and PLFA.

4.1 Abstract:

To examine the structures and possible interactions that produce the "humic like" optical properties of CDOM samples, pH titrations were combined with $NaBH_4$ reductions. Reference materials from the International Humic Substance Society (IHSS) were first tested to examine if these tests could provide information about structural differences among humic substances. Also, because humic substances are collected from different locations, differences seen in the samples could then be related to source. Suwannee River natural organic matter (SRNOM) was not previously investigated and thus is compared herein to Suwannee River Fulvic Acid (SRFA) and Pony Lake Fulvic Acid (PLFA), which were previously examined. Reduction and pH titration of these reference materials indicate that SRNOM and SRFA are highly similar while PLFA displays unique responses to the chemical tests. Irradiated SRNOM, SRFA and PLFA were also examined to probe the effect of photodegradation on the optical properties and response to reduction and pH titration. Comparisons between the untreated and irradiated samples also provides information about structural changes occurring during photobleaching. Irradiation can cause isomerization, bond cleavage, and photolysis which can destroy some absorbing structures which causes the CDOM to become photobleached.

4.2 Introduction:

CDOM is found ubiquitously throughout the aquatic environment and due to its prevalence and influence in the environment[1,2,4,5,18,23,49,89,104] numerous studies have examined its source and structure. Many of these studies have focused on its optical

properties, [3,5,23,45,105] or its chemical,[5,16,21,24,35] and/or photochemical[18,21,48,49] properties in relation to the optical properties. Prior research has shown that DOM contains a variety of functional groups including carbonyl-containing structures such as aromatic ketones, aldehydes and quinones, as well as phenols and carboxylic acids[14,46,140–142]. However, how and to what extent these functional groups contribute to the optical properties of CDOM from diverse natural waters is still not well understood. Two chemical tests that have been used to probe the structural basis of the optical properties of CDOM are reduction with $NaBH_4$ and acid base titrimetry[46,58,68].

Prior studies on humic substances have shown that reduction with $NaBH_4$ irreversibly reduces ketones/aldehydes to alcohols and reversibly reduces quinones to hydroquinones. These studies have also noted that following the reduction of these moieties there are significant changes in the optical properties.[57,60,68,143,144] Reductions have also been shown to produce noticeable changes in the optical properties of both natural waters containing CDOM and extracted CDOM samples [16,35,46,57]. The reduction of these ketone and aldehyde moieties and the subsequent change in the optical properties have been used to investigate the contribution of carbonyl-containing species to the optics and structure of CDOM. These studies have all shown a preferential loss of visible absorption following reduction along with enhanced, blue-shifted fluorescence emission[16,18,21,35,46–49,56,139]. Although the loss of UV absorption can be attributed to the reduction of aromatic ketones and aldehydes thought to be in CDOM, the proposed structures do not absorb in the visible[145,146], and thus the loss of visible absorption must be due to other factors[46,58,68].

pH titrations have also been shown to provide information about the chemical structure of moieties contributing to the absorption.[56,59,61] Deprotonatable groups such as carboxylic

acids and phenols are known to be present in CDOM.[52,59,139,140,143] Thus, the extent of the absorption changes when sample pH is adjusted over the pKa ranges of these moieties can provide insights into their contribution to the optical properties. Absorbance difference spectra acquired with increasing pH relative to a lower pH reference (often pH ~2.0) have been shown to provide information about the spectral changes with increasing pH as well as the contribution of particular moieties. Past studies on humic substances have revealed that there is a broadband increase in absorbance with increasing pH throughout the UV and visible region [56,58]. For most humic substances, the largest change was seen at pHs >8.0, which is in line with the deprotonation of phenols, while there was a smaller change around pH ~3.0 – 5.0 consistent with the pKa's of carboxylic acids. Because the UV and visible absorbance only increases and the increase in absorbance is large (as much as two-fold), this pH effect cannot be fully explained by the deprotonation of moieties such as phenols and carboxylic acids.[58]

Combining reduction and pH titrations probes the role that ketones and aldehydes play in the pH dependence, and allows further examination of their contribution to the optical properties. Reduction not only produces significant losses in absorbance, but the pH dependence of a sample following reduction is highly attenuated, especially in the visible and near-IR. This result indicates that there is coupling between reducible groups and deprotonatable groups.

On the basis of these results it is evident that the optical properties of CDOM and the changes brought about by reduction and pH titration are inconsistent with a simple superposition of chromophores or fluorophores. Instead the optical properties and response to chemical tests suggest that there are interactions between different functional groups

present within the CDOM. One proposed explanation of how these functional groups produce the unique optical properties seen in CDOM is a model involving electronic interactions between functional groups[21,22,46,56,58]. In this model, electronic interactions, including short-range charge transfer interactions, give rise to some of the optical properties including the long wavelength absorbance. The model states that electronic-rich donor moieties such as phenols and/or methoxylated phenols and substituted aromatic carboxylic acids can form charge transfer complexes with electronic-deficient acceptors such as aromatic ketones and aldehydes as well as quinones thus contributing to the long-wavelength (near-UV and visible) absorption [21,22,24]. The absorption at wavelengths $\leq$ 375 nm on the other hand is proposed to be due predominantly to individual moieties including both the acceptors and donors absorbing independently (Fig. 1.5).

The CT model is further supported by past results of $NaBH_4$ reductions[46] and the combined effects of pH titration[58]. It can explain the loss of absorbance following reduction, because reduction of ketones and aldehydes to alcohols removed electron acceptors resulting in the loss of charge transfer interactions and thus visible absorption. The long wavelength pH dependence can also be explained in the CT mode. As carboxylic acids and phenols are deprotonated they become better electron donors and thus CT interactions are enhanced producing longer wavelength absorbance. This explanation of the pH dependence is further validated by the loss of pH dependence in the visible region when titrating reduced samples. Because there are fewer electron acceptors following reduction, improving the electron donating capacity of the phenols and carboxylic acids no longer has a large effect in the visible region, illustrating that the two functional groups are indeed interacting to produce the observed optical properties.

Reference materials from the IHSS including SRNOM, SRFA and PLFA were evaluated. PLFA and SRFA have been previously evaluated.[58] SRNOM was not previously tested thus all three samples were evaluated for direct comparison. SRNOM and SRFA were used because the majority of the DOC present in these HS, which were collected from the Suwannee River, is thought to be derived from decomposing vegetation, and act as a good standard for terrestrially sourced CDOM. In contrast, PLFA was collected from a eutrophic saline pond on the coast of Antarctica referred to as Pony Lake; this fulvic acid reference material is thought to be derived solely from microbes (Fig. 4.1).[9] Thus SRNOM/SRFA acts as a reference for terrestrial sourced CDOM and PLFA as a more microbial source. Aliquots of the SRNOM, SRFA and PLFA samples were also photodegraded, to explore the possible impact of light exposure on the optical properties. Following irradiation the samples were then titrated and $NaBH_4$ reduced, and compared to the untreated reference materials to provide insight into how photodegradation impacts the

Figure 4.1: (**left**) location of Pony lake indicated by the red star where PLFA is collected, and (**right**) location of Suwannee river where SRNOM, SRFA are collected.

optical and chemical properties of the sample and what possible structural changes occur during irradiation.

4.3 Methods:

4.3.1 Sample preparation

Solutions of Suwannee River Natural Organic Matter (SRNOM: 2R101N), Suwannee River Fulvic Acid (SRFA: 2S101F) and Pony Lake Fulvic Acid (PLFA: 1R109F) reference materials from the International Humic Substance Society (IHSS) were prepared in purified water at concentrations matching the absorbance of an 80 mg L^{-1} SRFA solution at 350 nm at neutral pH. Their pH was adjusted to ~7.0 using diluted $HClO_4$, and they were filtered through a 0.2 µm nylon syringe filter (Fig. 4.2).

4.3.2 Optical measurements

Absorption spectra were recorded over the range of 190 to 820 nm employing a Shimadzu UVPC 2401 benchtop spectrophotometer equipped with a 1 cm quartz cell. The dual-beam spectrometer was baselined with air in both sample and reference beam paths, then spectra of all samples were recorded versus an air reference. A blank spectrum was collected by taking an absorption scan of purified water referenced to air and was subtracted from the sample spectra during data analysis.

The spectra were fit to an to an exponential model [25] over a 300-700 nm range using a nonlinear least squares fitting routine,

$$a(\lambda) = a(\lambda_0)e^{-S(\lambda-\lambda_0)} \qquad \textbf{Eq. 4.1}$$

where λ_0 is a reference wavelength and S is the spectral slope [1].

4.3.3 $NaBH_4$ reduction

The pH of 3 mL aliquots of each sample were first adjusted to pH ~10.0 using dilute NaOH and the absorption spectra were recorded. Then ~6.0 mg of $NaBH_4$ was added, and

the samples were then allowed to reduce at room temperature for 48 h in the dark. After 48 h, the absorption spectra were first recorded at pH ~10.0, and then after adjustment to pH ~7.0 with $HClO_4$. To allow for reoxidation of reversibly-reduced species, samples were kept at pH ~7.0 for 72 h, with their absorption spectra subsequently recorded.

To quantify the absorption loss, the percent absorption loss following reduction was calculated for each sample using Eq. 4.2.

$$\text{Absorbance loss (\%)} = \frac{A(\text{untreated}_{\lambda(x)}) - A(\text{reduced}_{\lambda(x)})}{A(\text{untreated}_{\lambda(x)})} * 100 \qquad \textbf{Eq. 4.2}$$

where $A(\text{untreated}_{\lambda(x)})$ is the absorbance of the sample before reduction, and $A(\text{reduced}_{\lambda(x)})$ is the absorbance of the sample after reduction at a given wavelength (x). Because the absorbance loss following reduction is wavelength dependent, an average loss was calculated between 250 and 500 nm using Equation 4.3.

$$\text{Average percent abs loss} = \frac{1}{250}\sum_{i=250}^{500} \frac{A(\text{untreated}_{\lambda(i)}) - A(\text{reduced}_{\lambda(i)})}{A(\text{untreated}_{\lambda(i)})} * 100 \qquad \textbf{Eq. 4.3}$$

4.3.4 pH titration

pH titrations were performed on both the untreated and $NaBH_4$ reduced samples. The pH was lowered to ~2.0 using $HClO_4$ and increased to 12 using NaOH, with the absorption spectra recorded at ~1 pH unit intervals from ~2 to 12. To check for reversibility and hysteresis, the pH was adjusted incrementally back down to ~2.0 using $HClO_4$, with absorption spectra acquired at every ~1 pH interval.

Difference spectra as a function of pH were generated to evaluate the spectral changes in absorbance due to changes in the pH for the untreated, reduced and irradiated samples (Eq. 4.4) as well as for the absorption lost upon reduction and or irradiation (A_{lost}) (Eq. 4.5), following a method presented in Dryer et al. (2008).

$$Delta\ A\ (\Delta A) = A_{pHx} - A_{pH2} \quad \textbf{Eq. 4.4}$$

where A_{pH2} is the absorbance of the sample at pH 2.0 and A_{pHx} is the absorbance of the sample at a higher pH (x). The absorption loss upon reduction or irradiation (A_{lost}) was calculated at each pH using Equation 4.5 were the absorbance post reduction or irradiation at a given pH is subtracted from the absorbance prior to reduction or irradiation.

$$A_{lost\ pHx} = A_{untreated\ pHx} - A_{treated\ pHx} \quad \textbf{Eq. 4.5}$$

where $A_{untreated\ pHx}$ is the absorption of the untreated sample at a given pH x and $A_{treated\ pHx}$ is that of the reduced or irradiated sample at that same pH x were x ranges from 2-12.

Fractional difference absorption spectra (ΔA_{frac}) also provide information about the change in absorption with increasing pH and were generated by taking the difference spectra calculated using Eq. 4.4 normalized to the absorbance at pH 2 using Eq. 4.6.

$$\Delta A_{frac} = \left(\frac{A_{pHx} - A_{pH2}}{A_{pH2}}\right) \quad \textbf{Eq. 4.6}$$

To compare the effect of pH on the spectral slope, the percent change in spectral slope relative to the slope at pH 2 was calculated using Equation 4.7;

$$\text{Percent change in Spectral Slope} = \frac{(S_{pH2} - S_{pHx})}{(S_{pH2})} * 100 \quad \textbf{Eq. 4.7}$$

where S_{pH2} is the spectral slope at pH 2 and S_{pHx} is the spectral slope at pH x from 2 to 12.

4.3.5 Photo-irradiation

Four mL of an SRNOM, SRFA and PLFA solution (~100 mg/L) were placed in a 1 cm path length quartz cuvette and irradiated for up to ~50 hours employing a 300 W xenon lamp polychromatic radiation source. A 325 nm long-pass cut off filter along with

a 20 cm water jacket were placed between the lamp and the cuvette to remove short wavelengths and infrared radiation respectively (Fig.S4.1). The spectral output of this source was determined with an Ocean Optics USB2000 Miniature Spectrometer (Fig. 4.2).

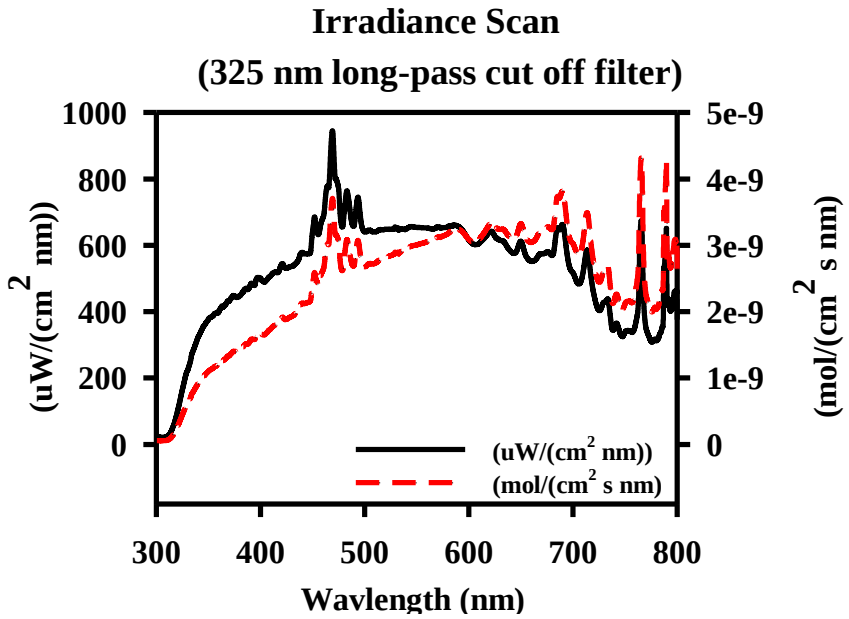

Figure 4.2: Irradiance scan obtained with Ocean Optics spectrometer at the front face of the quartz cuvette.

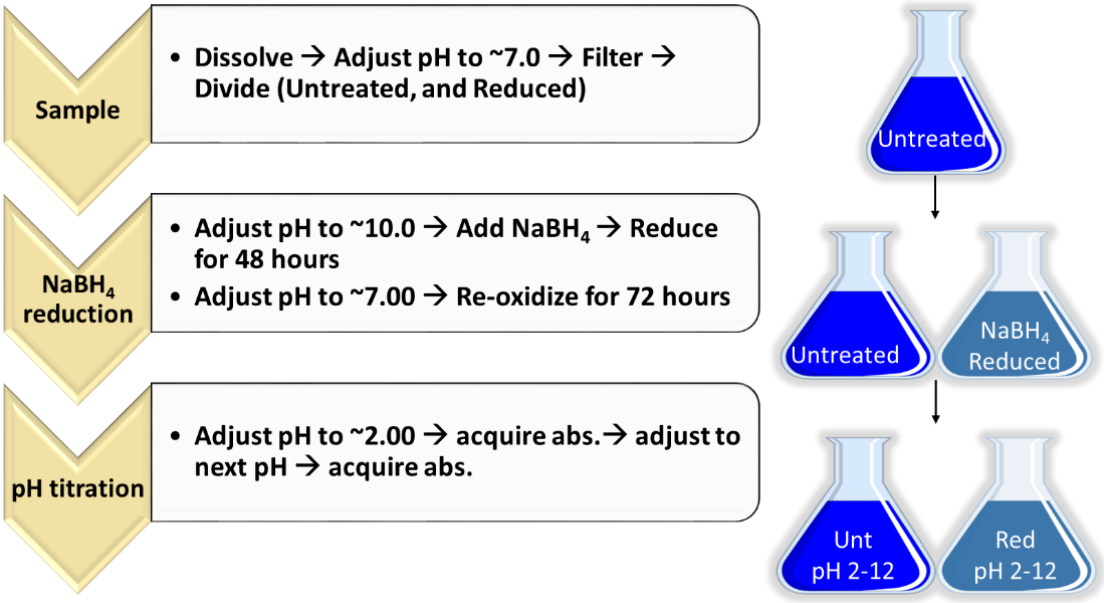

Figure 4.3: Flow chart and diagram of reference material preparation as well as NaBH4 reduction and pH titration.

4.4 Results:

4.4.1 Effects of $NaBH_4$ Reduction and pH on reference materials

The effect of reduction on SRFA and PLFA is consistent with prior work,[56,57] and SRNOM (not previously tested) displays nearly identical responses to that of SRFA. Following reduction with $NaBH_4$, all reference materials displayed a decrease in absorbance at all wavelengths with the greatest percent loss at longer wavelengths (Fig. 4.4 and 4.4). The substantial loss in absorption at longer wavelengths is better highlighted by plotting the natural log of the normalized absorbance for both the untreated and reduced samples, (Fig. 4.4 right axis). The percent loss in the visible region for the different reference materials decreased in the order: SRNOM (~65%) > SRFA (~55%) > PLFA (~40%) (Fig. 4.5). However, despite significant losses for all reference materials there was still absorption remaining following reduction even in the visible region.

Following reduction, the spectral slope ($S_{300-700}$) for all samples increased due to the preferential loss of visible absorption (Fig. 4.6). The increase in spectral slope

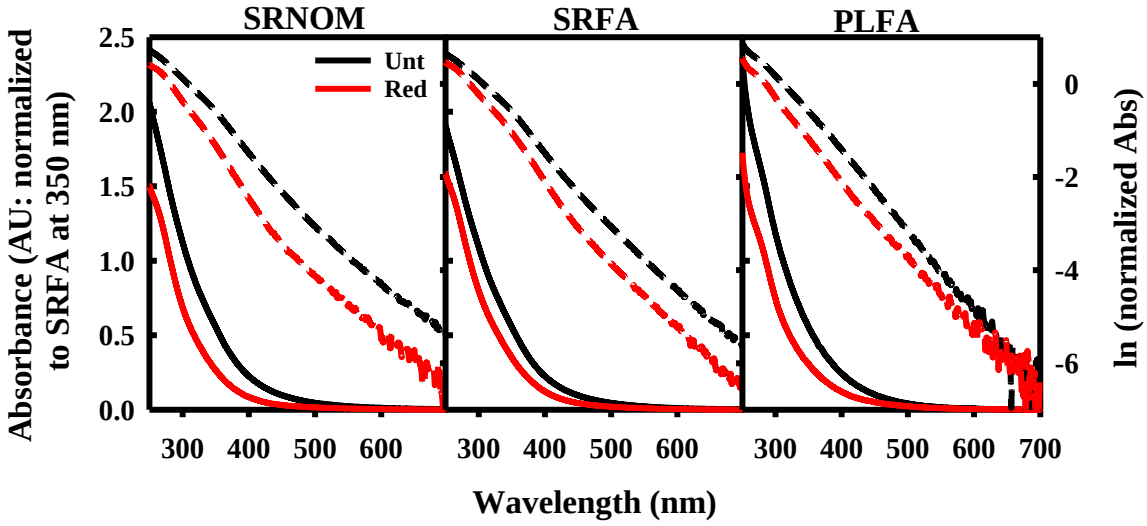

Figure 4.4: Absorbance of SRNOM, SRFA, and PLFA stock solutions before (**black**) and after (**red**) reduction. Left axis: Normalized absorbance (solid lines), Right axis: natural log of the normalized absorbance (dashed lines).

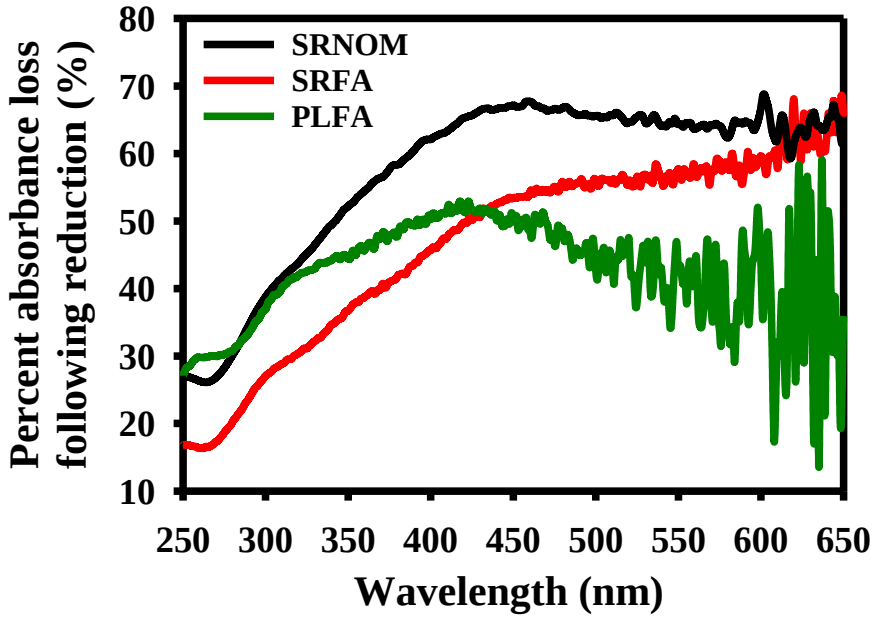

Figure 4.5: Percent absorbance loss following reduction with $NaBH_4$ for both SRNOM (**black**), SRFA (**red**) and PLFA (**green**).

following reduction followed the same trend as the percent absorption loss SRNOM > SRFA > PLFA. (Fig. 4.5 and 4.6).

The absorbance of all the reference materials (SRNOM, SRFA and PLFA) both untreated and reduced was enhanced with increasing pH at all wavelengths (Fig. 4.7 and S4.2-S4.3). The changes seen in absorbance with increasing pH were reversible when the pH was lowered. The largest fractional change in absorption with increasing pH was observed in the visible region. For the untreated samples from pH ~2 to 12 there was ~100-150 % increase for SRNOM and SRFA and ~60 % increase for PLFA at wavelengths >450 nm. Larger enhancements were observed for all samples at higher pHs (>8) compared to lower pHs (<6). Because increasing pH preferentially enhanced the visible region decreased spectral slopes ($S_{300-700}$) were observed. Larger decreases in $S_{300-700}$ are observed at higher pHs (>8.0). For untreated SRNOM and SRFA there was ~ 4% decrease in S_{300-}

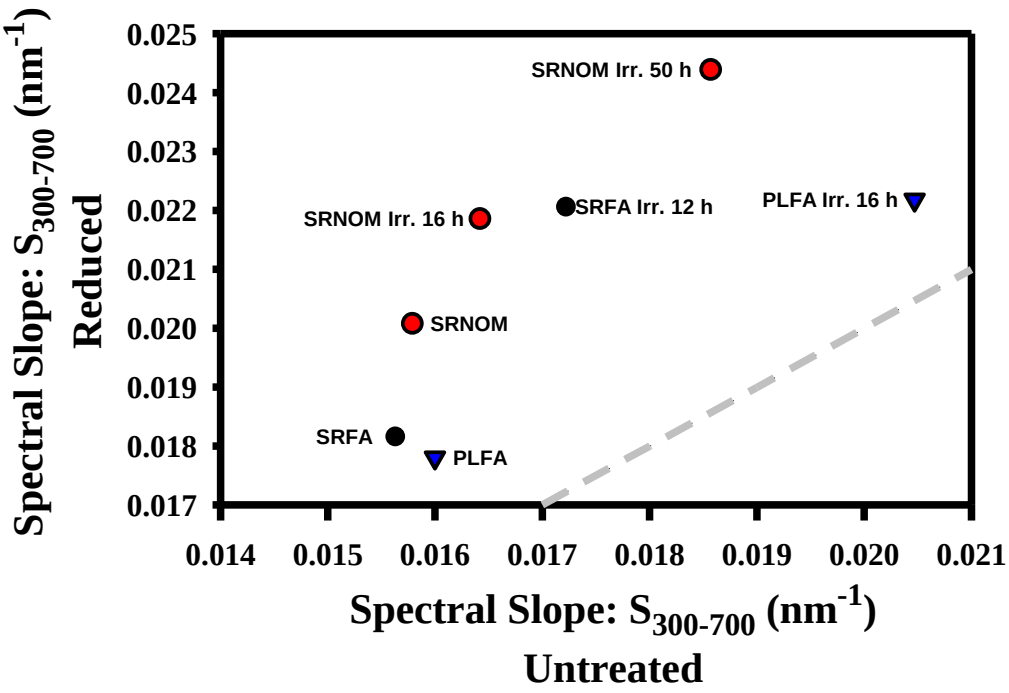

Figure 4.6: Spectral slope values for SRFA, SRNOM and PLFA both before and after reduction.

$_{700}$ from pH 2-6 while from pH 7-12 there was ~20% decrease. Untreated PLFA on the other hand had only ~1% decrease at low pH and only ~9% decrease at high pH. (Fig. S4.4)

Due to the broad unstructured nature of the increases in absorbance with pH it is challenging to observe changes in spectral shape with increasing pH from the direct absorption spectra; instead difference spectra relative to pH 2 were generated (Eq. 4.3: Fig. 4.8). Although absorption across the entire spectrum is enhanced with increasing pH, the difference spectra (ΔA) reveals three main regions where distinct spectral responses were observed with the increasing of pH: region A) at ~280 nm increases predominantly at low pHs (< 5); region B) a broader band at ~ 300-400 nm that increases predominantly at high pHs (≥ 8); and region C) broadband absorption (> 450 nm) that increases at all pHs, but more significantly at higher pH (>8). For SRFA and SRNOM these three regions were present and followed nearly identical trends. However, PLFA did not have the same band

around ~280 nm (region A) seen in the other reference materials. Instead, for PLFA there is a broader band at ~320 nm and the ~300-450 nm band is not as pronounced (Fig. 4.8 and S4.3). The results for SRFA and PLFA are in line with prior work.[58]

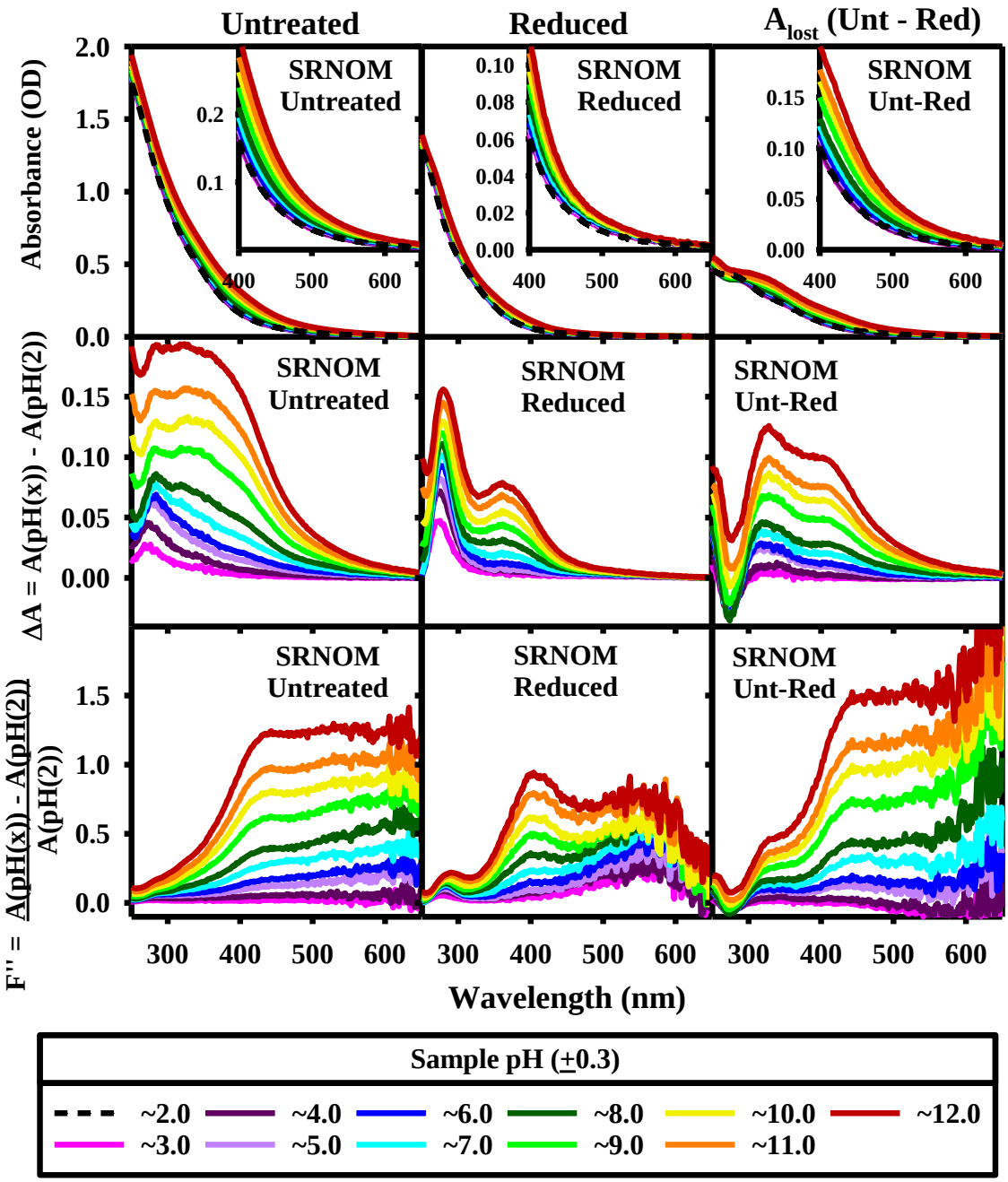

Figure 4.7: pH titration of SRNOM, (**top**) normalized absorbance at increasing pHs (**middle**) difference spectra, and (**bottom**) fractional difference spectra. (**Left**) untreated sample, (**center**) reduced sample and (**right**) untreated – reduced (A_{lost}).

Reduced samples displayed smaller increases in absorbance with increasing pH compared to the untreated sample due to the overall loss of absorbance upon reduction. For SRFA and SRNOM the same three regions seen in the untreated difference spectra were present in the reduced samples. However, there were some dramatic changes following reduction. Following reduction, the bands at ~280 nm (region A) and ~300-450 nm (region B) were more pronounced because overall there was a loss of background absorption enhancement with increasing pH. With the exception of the ~280 nm band the difference spectra were less intense for the reduced sample compared to the untreated sample (Fig. 4.8). The difference spectra for the A_{lost} ("untreated – reduced") more clearly indicates the impact that reduction has on the spectral dependence of the absorption enhancement caused by increasing pH. In the A_{lost} ("untreated – reduced") difference spectra positive values indicate a loss in absorption enhancement following reduction while negative values indicate increased absorption enhancement following reduction. For SRNOM and SRFA the absorption lost upon reduction (A_{lost}: Fig. 4.8 and S4.2-S4.3) calculated using Eq. 4.5 displays increased absorbance with increasing pH over the entire spectrum except in region A (~280 nm). At wavelengths $\geq$ 300 nm there is significant positive pH dependence in the A_{lost} difference spectrum indicating that the reduced sample has a smaller degree of absorption enhancement with increasing pH compared to the untreated sample. The only region in the A_{lost} difference spectrum that is negative and thus indicates increased absorption enhancement with increasing pH following reduction is the band around ~ 280 nm. PLFA is significantly different and shows a smaller degree of absorption enhancement with increasing pH at all wavelengths following reduction. This indicates that the pH dependence of the samples is highly attenuated at most wavelengths following reduction.

Following reduction the visible region is still preferentially enhanced with increasing pH, but the enhancement is attenuated, thus the spectral slopes for all samples do not decrease as significantly following reduction (Fig. S4.4).

The difference and fractional difference spectra can also be examined at select wavelengths by plotting the intensity vs pH (Fig. S4.5). This plot shows that for SRNOM at 280 nm the reduced sample has larger difference and fractional difference changes compared to the untreated, while PLFA is the reverse. At 350 and 500 nm reduction of SRNOM decreases the enhancement in absorption observed with increasing pH, but the fractional changes are nearly identical for the untreated and reduced samples. Reducing PLFA on the other hand attenuated the enhancement in absorption with increasing pH as well as decreased the fractional change with increasing pH at 350 and 500 nm. For all samples there are two zones with different degrees of enhancement with increasing pH present at all wavelengths: one at low pH (<6) and one at high pH (>8). Except for at ~280 nm where the change with pH is much larger for the higher pHs (Fig. S4.4).

4.4.2 Irradiation of SRNOM, SRFA and PLFA

Upon irradiation, the absorption of SRNOM, SRFA and PLFA decreases across the entire wavelength regime investigated (250-650 nm) with greatest percent loss at longer wavelengths (Fig. 4.9). At the start of the irradiation all samples were significantly inner filtered at wavelengths less than ~450 nm. The pH of the samples was not adjusted throughout the irradiation and was allowed to fluctuate. The starting pH for all samples was ~7.0 ±0.3 and the final pH was ~5.5 ±0.5. The spectral slope values were also monitored during the irradiation and the values increased with increasing irradiation time (Fig.4.10).

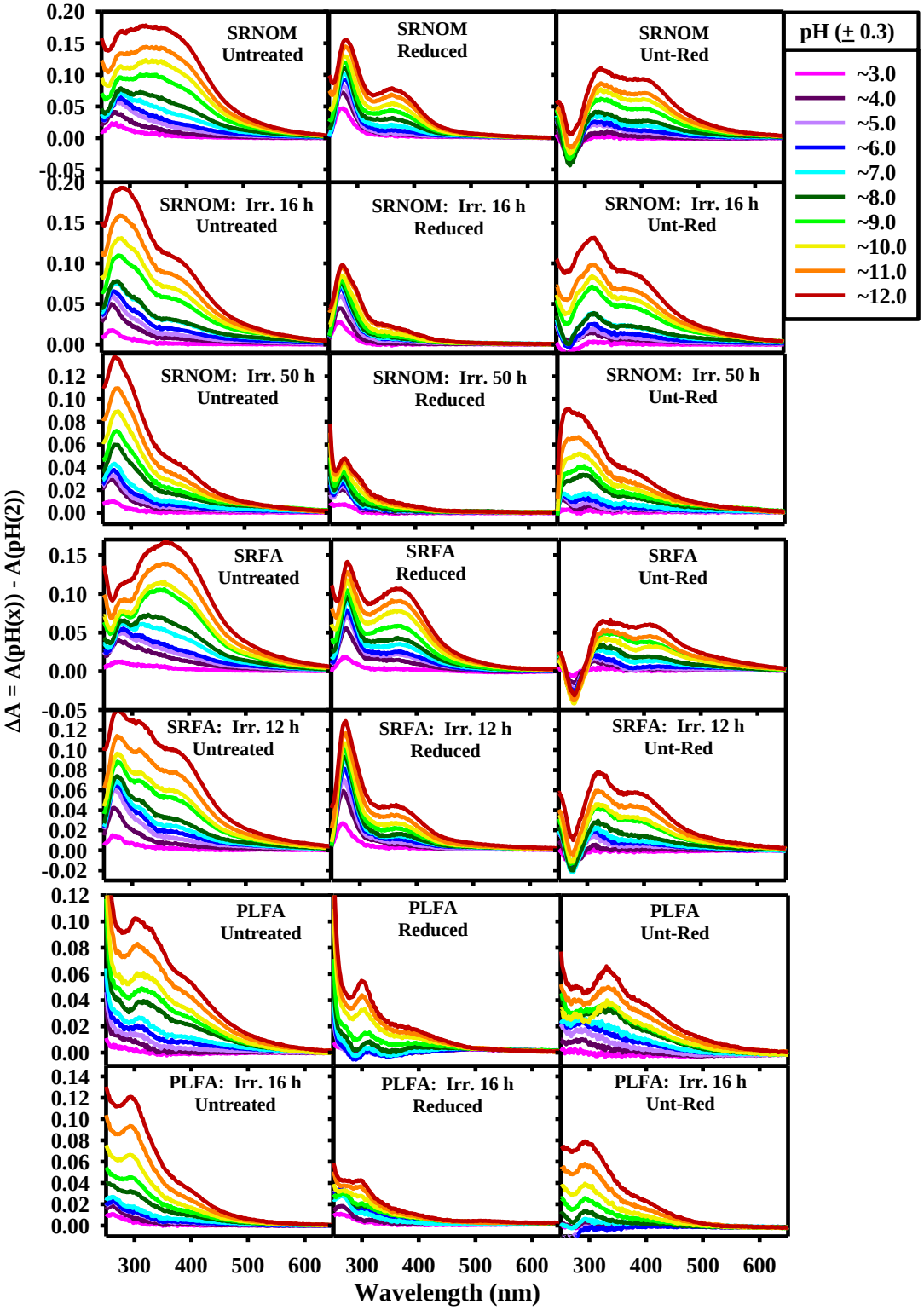

Figure 4.8: Difference spectra relative to pH 2 for untreated (**left**), reduced (**middle**) and unt-red (**right**) reference materials. SRNOM samples that underwent increasing amount of irradiating (0, 16 and 50 h) (**Top**), SRFA untreated and 12 h irradiated (**center**), and PLFA untreated and 16 h irradiated (**bottom**).

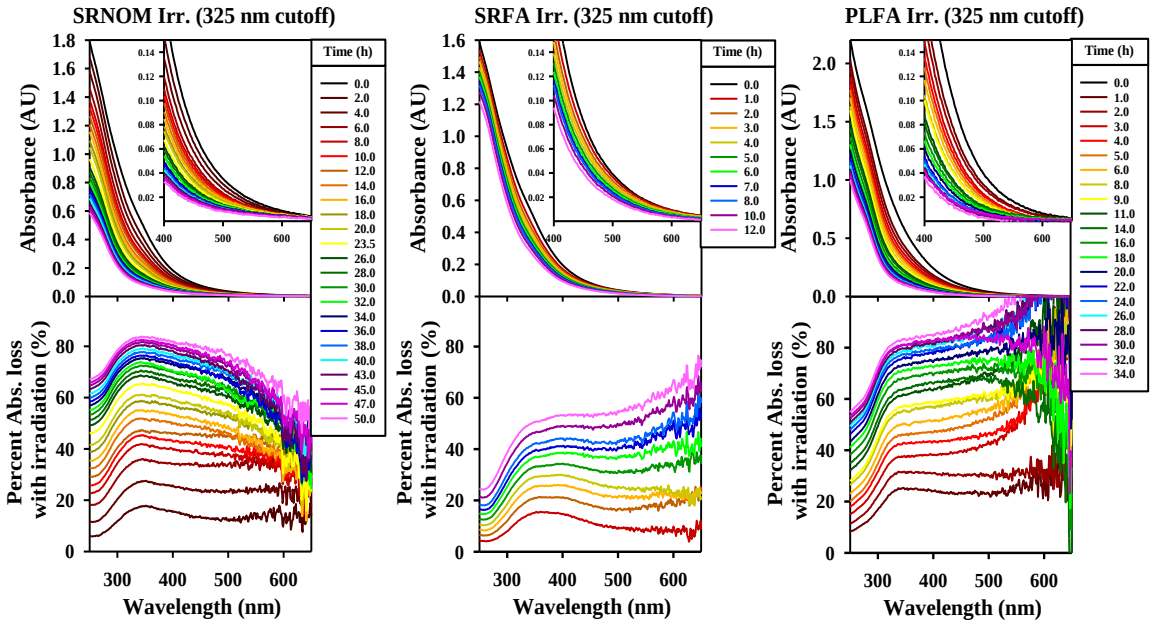

Figure 4.9: Absorbance of SRNOM (**left**) SRFA (**middle**) and PLFA (**right**) with increasing irradiation (**top**) and the percent absorbance loss with increasing irradiation relative to time 0.0 h (**bottom**).

4.4.3 Effects of pH and $NaBH_4$ Reduction on irradiated reference materials

Following irradiation the now photodegraded reference materials were reduced with $NaBH_4$ and titrated from pH ~2.0 to ~12.0 in the same manner as the original samples. The effect of $NaBH_4$ reduction on the irradiated samples was highly comparable to that of the untreated reference materials. There was a decrease in absorbance at all wavelengths following reduction with the largest percent loss occurring at long wavelengths (>450 nm). However, for the irradiated samples there was ~15% more absorbance loss in the long wavelengths following reduction (Fig. 4.11). Similar to the untreated samples the spectral slopes for the irradiated samples also increased following reduction due to the preferential loss of long wavelength absorbance, but the increase was relatively more substantial. (Fig. 4.6).

The effect of pH on the irradiated samples was also evaluated. Like the untreated

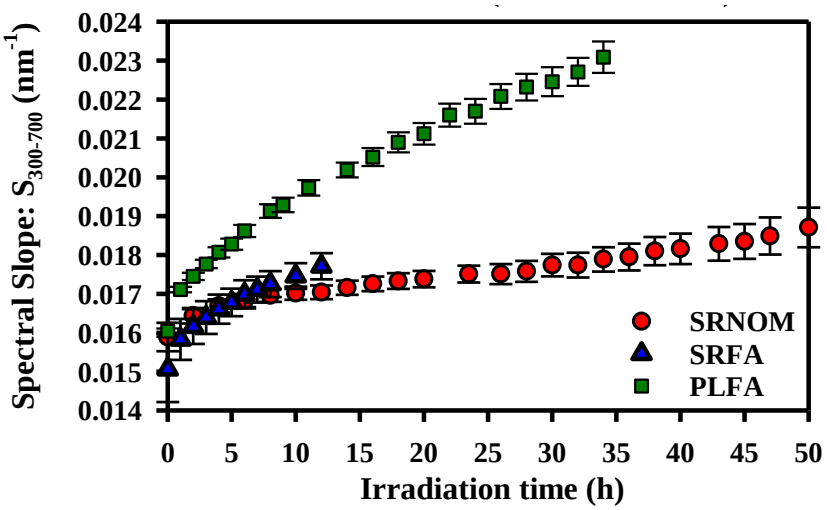

Figure 4.10: Spectral slope ($S_{300-700}$) with increasing irradiation time SRNOM (**red**) SRFA (**blue**) and PLFA (**green**).

samples and reference materials, the irradiated samples displayed enhanced broadband absorption with increasing pH at all wavelengths (Fig. 4.12a Top). Difference spectra relative to pH ~2 were also generated for the irradiated samples. For SRNOM and SRFA the same three regions (A, B and C) were still noticeable, but there were some distinct changes. The band around ~280 nm (region A) was broader and slightly enhanced

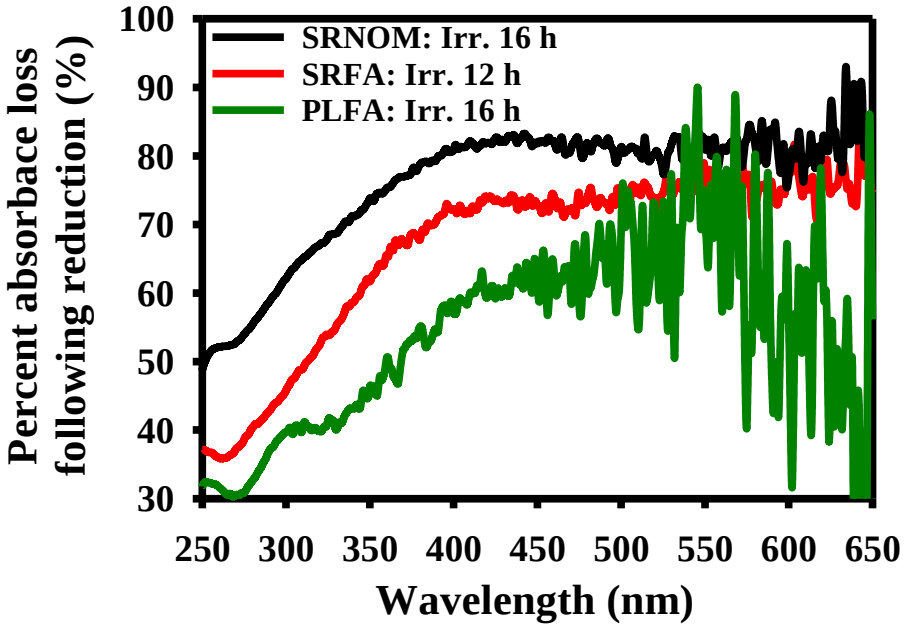

Figure 4.11: Percent absorbance loss following reduction with $NaBH_4$ for irradiated reference materials: SRNOM (**black**), SRFA (**red**) and PLFA (**green**).

following irradiation, while the broad band around ~300-450 nm (region B) was significantly attenuated. The broadband absorption at wavelengths >450 nm that was enhanced with increasing pH in the untreated samples was still present in the irradiated samples but it was also significantly attenuated (Fig. 4.12a bottom).

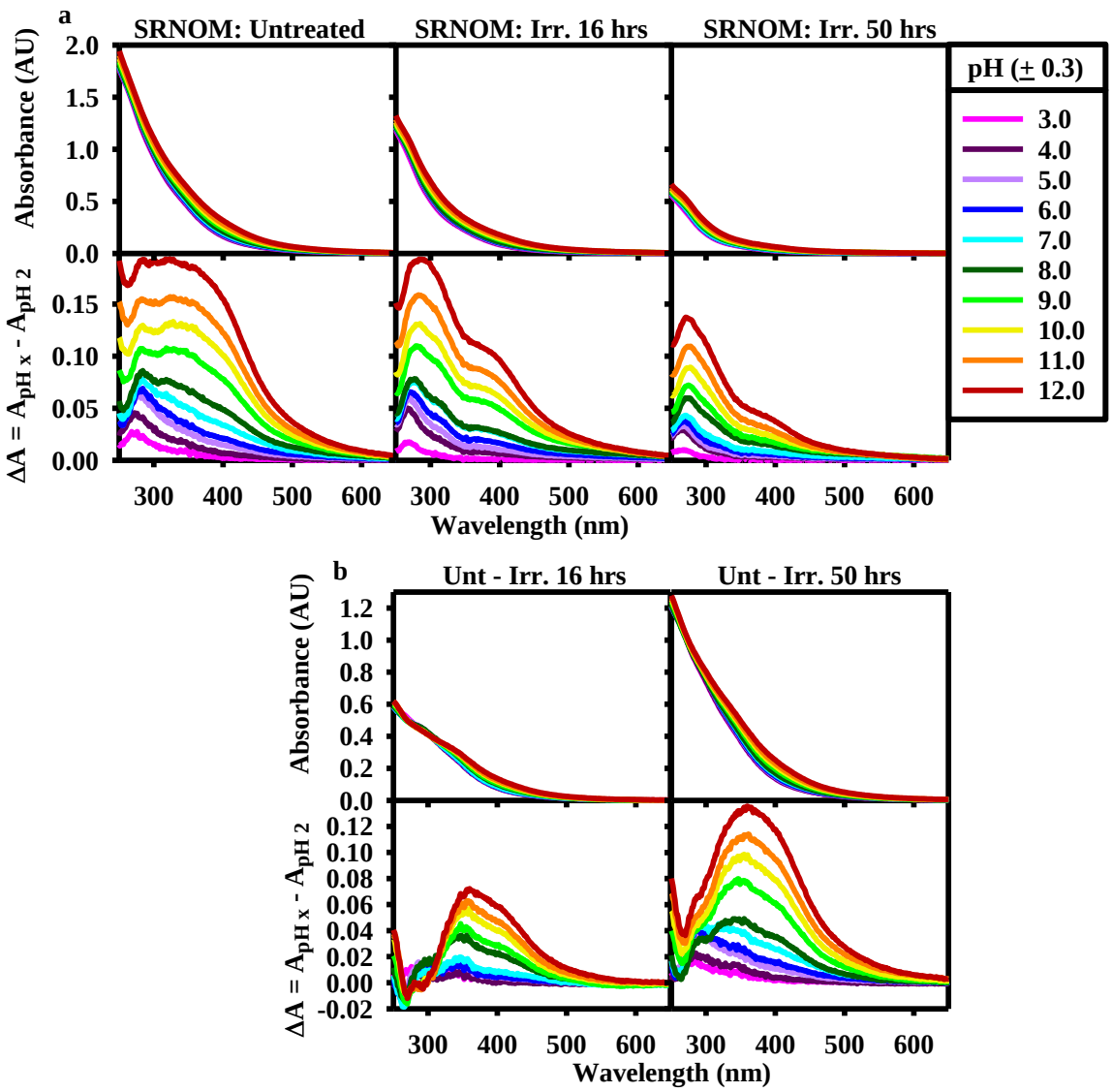

Figure 4.12: (**a: top**) SRNOM absorbance and (**a: bottom**) difference spectra relative to pH ~2 of (**left**) untreated, (**center**) irradiated 16 h. and (**right**) irradiated 50 h samples. (**b: top**) Irradiated sample absorbance subtracted from the untreated absorbance, and (**b: bottom**) difference spectra relative to pH 2, of (**left**) irradiated 16 h sample, and (**right**) irradiated 50 h sample.

The absorbance lost upon irradiation (A_{lost}: "untreated – irradiated") calculated using Eq. 4.5 also displayed enhanced absorption with increasing pH except at wavelengths < 300 nm where there is little change (Fig. 4.12b-4:13 and S4.6-S4.7). This result indicates that the irradiation only moderately impacted the ~280 nm band seen in the untreated sample, while it significantly decreased the enhancement in the ~300-450 nm region, as well as in the long wavelengths. This indicates that irradiation, like reduction, attenuated the pH dependence. However, the wavelength dependence of the attenuation was different between reduction and irradiation. Most notably in the differences spectra the band around ~280 nm displays slight gain in pH dependence following reduction while there is minimal change following irradiation. Also, the pH dependence lost in the ~300-450 nm region is more structured for reduced samples with slight peaks around ~320 and ~420 nm, while the irradiated samples show more broad band loss centered around ~390 nm.

Reduction of the irradiated reference materials not only causes a decrease in absorbance at all wavelengths but it significantly decreases the enhancement in absorption seen with increasing pH. Reduction of SRNOM that was irradiated for ~50 h almost completely eliminated the enhancement with increasing pH, with only a very weak band remaining in the difference spectra at ~280 nm that tailed slightly into the visible. SRFA was only irradiated for 12 hours and did not display as dramatic of a change, but the reduction of the irradiated sample still attenuated the enhancement. The irradiated PLFA samples (16 h) also shows a loss in the enhancement of the absorption with increasing pH following reduction, with only a small band present in the difference spectra at wavelengths <320 nm.

By subtracting the absorbance of the reduced irradiated samples from that of the

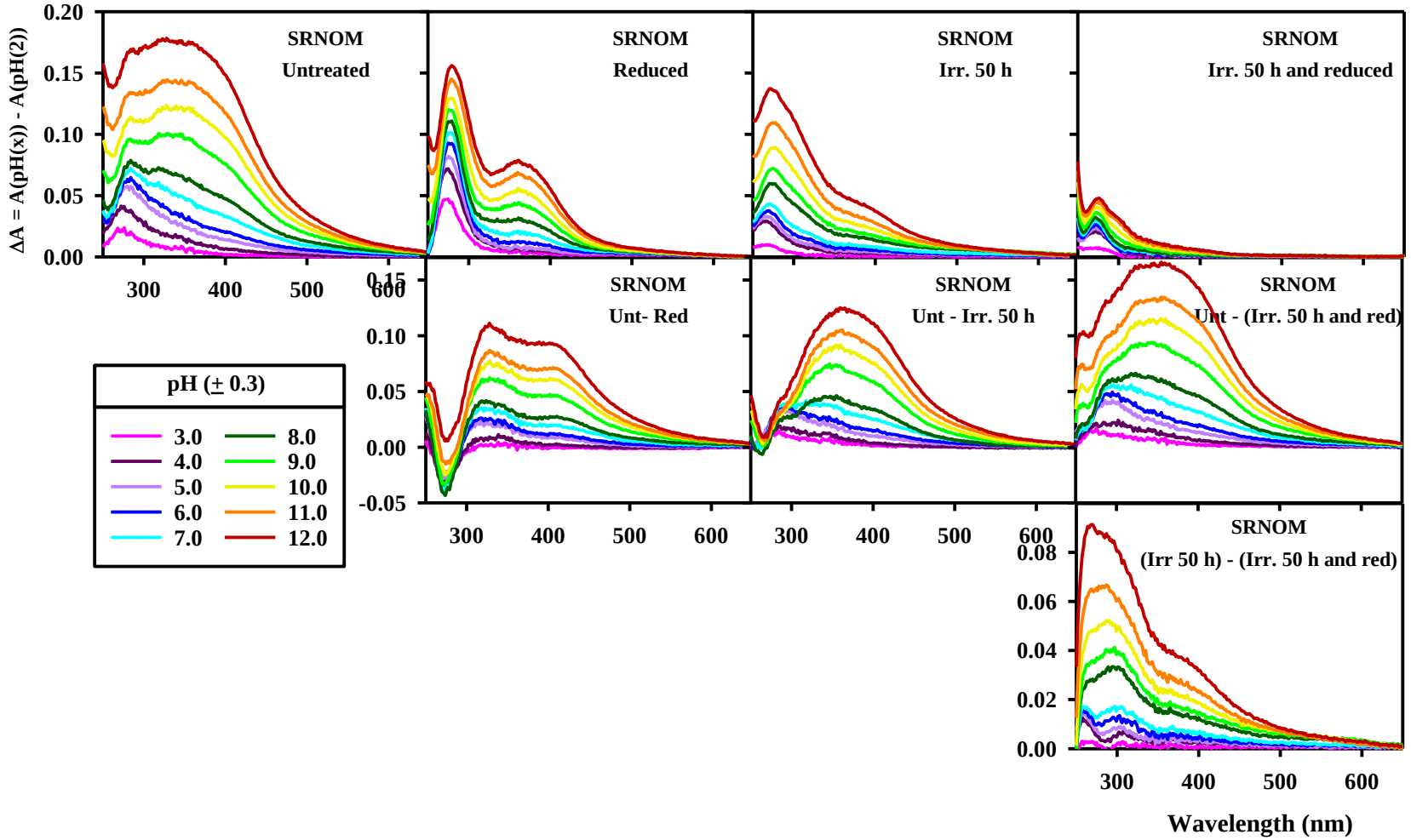

Figure 4.13: Difference spectra for untreated, reduced, irradiated and irradiated and reduced SRNOM (**top**). Along with the difference spectra for the absorbance lost following reduction, irradiation and irradiation and reduction (**middle**). Also the difference spectra for the absorbance lost following reduction of the irradiated sample (**bottom**).

irradiated samples at all pHs (Eq. 4.5) it is possible to look at the impact that the reduction has on the pH dependence of the irradiated samples. Difference spectra relative to pH 2 can also be generated from these spectra and show the wavelength dependence of the change. For SRNOM the band around 280 nm in the difference spectra (region A) was enhanced and broadened following irradiation (16 and 50 h), but when the irradiated sample is reduced with borohydride this band is almost completely removed. In the difference spectra there is also a broad band around ~300-450 nm (region B) which is very pronounced in the untreated sample, then significantly attenuated following irradiation and finally in the irradiated (50 h) and reduced sample it is eliminated. SRFA follows similar trends, but the irradiation was only carried out for 12 h. and thus the ~280 nm band is not as enhanced and broadened and the ~300-450 nm band is not as attenuated following irradiation. The reduction of the irradiated sample also does not show as dramatic attenuation of the enhancement in absorption with increasing pH as in SRNOM (irr 50 h). The reduction of the irradiated (16 h) PLFA sample does show almost complete elimination of the ~320 nm band that was enhanced following irradiation of the untreated sample.

4.5 Discussion:

4.5.1 Absorption of reference materials at neutral pH

All samples have broad absorption spectra that extend into the lower energy visible wavelength region, and the entire absorption spectra was impacted by $NaBH_4$ reduction (**section 4.5.2**) as well as pH titration (**section 4.5.3**). The visible absorbance is impacted by $NaBH_4$ reduction (suggesting carbonyl involvement) as well as pH titration (suggesting phenols or carboxylic acid involvement). However, the carbonyl, carboxylic and phenolic

structures currently proposed to be present within CDOM do not absorb across the visible or in the near-IR. Thus the absorbance in the long wavelengths being impacted by $NaBH_4$ reduction and pH titration suggests that there are electron-rich donor moieties such as aromatic phenols and carboxylic acids as well as electron-deficient acceptors such as aromatic ketones and aldehydes present in the samples. These moieties could contributing to the long-wavelength absorption through electronic interactions and would be impacted by both reduction and pH titration[21]. The presence of these moieties (both donors and accepters) in reference materials has been previously reported,[12,18,30,46,68,137,140,142,147,148] and the influence that CT interactions have on the absorbance has also been previously studied.[21,22,46–48]

4.5.2 $NaBH_4$ reduction of reference materials

The significant irreversible loss in absorbance following reductions at all wavelengths indicates that SRNOM, SRFA and PLFA have reducible groups (ketones and aldehydes) and that these groups contribute not only to the short wavelength absorbance but also to the long wavelength absorbance (Fig. 4.4 - 4.6). Because these groups should not directly absorb low-energy long wavelength radiation[145,146,149,150], this absorbance can be attributed to charge transfer interactions. The ketones and aldehydes are acting as electron acceptors, thus following their reduction to alcohols these interactions were dramatically reduced causing the significant decrease in long wavelength absorbance.

The incomplete loss of long wavelength absorbance could be due to several factors or a combination of them as previously discussed (**section 1.5.1**). Due to the complex nature of NOM and fulvic acids, there may be incomplete reduction of ketones and aldehydes, which would result in absorbance remaining in the visible region. Also because

samples are reduced and then allowed to reoxidize and stabilize in an oxic environment quinones would reoxidize and subsequently could participate in charge transfer interactions causing visible absorption to remain[68]. Finally there could also be chromophores that absorb in the visible region that are unaffected by the $NaBH_4$ reduction.

4.5.3 pH titration of reference materials

SRFA was previously titrated[56] and SRNOM displayed near identical pH dependence (Fig. 4.7, and S4.2). Overall the absorbance was enhanced at all wavelengths with increasing pH, with the largest enhancement occurring at pHs >8. The difference spectra indicated three main spectral regions impacted by increasing pH. The increase in absorption in region A (~280 nm band) occurred predominantly at low pHs and is tentatively assigned to the deprotonation of carboxylic acids; which have pKas between ~3 and 6 [140]. Region B (300 – 450 nm band) on the other hand was enhanced predominantly at high pH and is tentatively assigned to the deprotonation of phenols; the pKas of which falls above ~8 [62]. The absorbance in region C (> 450 nm) was enhanced at all pHs. Region C enhancement could be due to better donors facilitating enhanced CT interactions, because phenolate anions and carboxylate anions have enhanced electron donating ability compared to their acidic form. The enhancement of region C is more significant at pHs above ~7-8, which is most likely associated with the phenolate anions being significantly better electron donors. Due to the preferential enhancing of the long wavelength absorbance the spectral slopes decrease with increasing pH for SRNOM and SRFA with the decrease becoming more sever at pHs >8. This further suggests that the deprotonation of phenols influences the extent of the charge transfer interactions occurring within the sample.

Following reduction, there was not only a loss of absorption at all wavelengths, but there was also attenuation of the absorption enhancement with increasing pH following reduction. Because the reduction impacts the pH dependence this suggests that the reducible groups are coupled to deprotonatable groups such as phenols and carboxylic acids. This is in line with the electronic interaction model which suggests that these groups could form charge transfer interaction with one another thus giving rise to the long wavelength absorbance and the broadband absorption enhancement with increasing pH. Then, because reduction lowers the number of available acceptors by reducing ketones and aldehydes to alcohols there is less CT interactions.

The change in pH dependence following reduction indicates that some of the absorption enhancement with increasing pH seen in the untreated samples was due to coupling between reducible groups such as ketones and aldehydes, and deprotonatable groups such as phenols and carboxylic acids. The absorbance of the reduced sample is not as enhanced with increasing pH compared to the untreated sample in regions B and C, while in region A the absorption enhancement with increasing pH is slightly larger in the reduced sample. The loss in absorption enhancement with increasing pH following reduction suggests that even as the donors (phenols as carboxylic acids) are deprotonated at higher pHs and become better donors they do not form charge transfer complexed due to the limited availability of acceptors.

PLFA does display some similarities to SRNOM and SRFA, such as enhanced absorbance with increasing pH and loss of absorption following reduction suggesting that some of the same functional groups are present in all samples. However, there are significant differences as well, which point to these functional groups not being present in

the same proportions, and possible structural differences. The lack of a pH dependent band around ~280 nm and the smaller pH dependence in region B would suggest that the structure of PLFA does differ from that of SRFA or SRNOM and that these differences impact the optics. Region B was tentatively assigned to phenols and based on the carbon distribution in these reference materials determined using ^{13}C NMR PLFA does have a relatively smaller phenol content (Table S4.1). Based on the contribution of particular ranges of chemical shifts in the NMR to the total integrated peak area, SRNOM and SRFA also have higher carbonyl and aromatic carbon content compared to PLFA which has more aliphatic carbon. This lower phenol content is in line with the minimal enhancement in absorbance with increasing pH seen in region B. The lower carbonyl content for PLFA could also explain the lower percent absorbance loss following reduction. (Fig. S4.6 and S4.3).

Because the reduction decreases the absorbance at all wavelengths the pH dependence of the untreated and reduced sample can also be compared on a fractional basis. The fractional difference in the absorption with increasing pH is also wavelength dependent and PLFA displays different trends that SRNOM and SRFA. In region A at 280 nm both SRNOM and SRFA display increased fractional difference spectra for the reduced sample compared to the untreated sample. While there is very little change in the fractional difference spectra at 350 and 500 nm. Minimal changes in the fractional difference spectra suggest that the structures responsible for the pH dependence at these wavelengths are still present following reduction. At 350 nm the majority of the pH dependence has been tentatively assigned to phenols which should not be impacted by reduction and thus the pH dependence of fractional difference spectra would not change following reduction.

Because the long wavelength absorption enhancement with increasing pH has been associated with CT interactions, the fractional difference spectra remaining constant following reduction suggests that there was incomplete reduction and CT complexes are still being enhanced when donor moieties are deprotonated. PLFA is significantly different and shows a loss in the fractional difference spectra at all wavelengths especial 500 nm. This change in fractional difference spectra following reduction suggests that the moieties contributing to the absorbance and pH dependence of the reduced sample have changes or are interacting differently.

4.5.4 Irradiation of reference materials:

Following irradiation, the absorbance for all samples decreased significantly at all wavelengths with the largest percent loss occurring at long wavelengths (> ~400 nm). Spectral slopes ($S_{300\text{-}700}$) were enhanced due to the loss of long wavelength absorbance. This would indicate that the irradiation alters discrete functional groups (both donors and acceptors) as well as eliminated some charge transfer complexes. This is in line with research that have shown irradiation of CDOM leads to photobleaching which is the destruction of chromophores.[151] Absorption of light by CDOM has also been shown to produce lower molecular weight DOM, and generates inorganic species including CO and CO_2 possibly through photodecarboxylation[33,51,108,152,153].

4.5.5 Effect of pH and NaBH4 reduction on Irradiated reference materials

Following irradiation there is a larger percent loss in absorbance for all samples (SRNOM, SRFA and PLFA) upon reduction. This could be in part due to some ketone and aldehyde moieties being more accessible after irradiation due to the increase in the lower molecular weight fraction (simpler structures). This could also indicate that the non-

reducible groups are lost (bleached) at a higher rate during the irradiation compared to reducible groups. Preferential loss of other chromophores during irradiation would increase the percent of the absorption contributed by ketones and aldehydes in the irradiated sample compared to the untreated sample. Thus, following reduction there would be a larger percent loss in absorbance for the irradiated sample. Both of these factors are most likely at play because irradiation of CDOM has been shown to decrease the average molecular weight[15,104] and it has also been shown that phenols are significantly degraded by irradiation.[51,126,138,148,151,154]

Following irradiation the absorbance was significantly diminished for all samples, but there was still absorption enhancement with increasing pH. The difference spectra showed less absorption enhancement with increasing pH over the majority of the spectrum (regions B and C). However, region A (~280 nm band) following irradiation actually showed increased enhancement with increasing pH and the band was broadened. This was true for all samples (SRNOM, SRFA and PLFA), and this increase in absorption enhancement could indicate that the irradiation is forming new species that are impacting the absorbance in this region. Another possible explanation for the increase in absorption enhancement is that irradiation decreases intramolecular interaction by reducing the average molecular weight. The disruption of CT complexes could allow individual donor or acceptor moieties that are no longer participating in charge transfer interaction to absorb independently and some may contribute to this region. For SRNOM and SRFA the absorption enhancement with increasing pH in region B (300-450 nm), which has been tentatively assigned to phenols, is attenuated significantly more than other regions, which is in line with past research showing the loss of phenols during photobleaching as

referenced above. PLFA is slightly different from SRNOM and SRFA with less change in region B following irradiation, again suggesting it is structurally different with phenols contributed less to the optics. Also for all samples the absorption enhancement in region C (>450 nm) is attenuated following irradiation suggesting that there is a loss of charge transfer interactions following irradiation. This is consistent with photodegradation decreasing the average molecular size of CDOM and reference materials, thus decreasing the possible intramolecular CT interactions. Also, phenols are proposed to be electron donors, thus if the irradiation destroys phenols this would also decrease CT interactions, by eliminating possible electron donors. (Fig. 4.10b, and S4.5-4.7).

Reduction of the irradiated samples had a similar impact on the pH dependence as the reduction on untreated samples. However, region B is almost eliminated and the long wavelength enhancement with increasing pH is significantly decreased because these regions are attenuated by both irradiation and reduction. Also region A (~280 nm band) that displayed increased enhancement and was broadened following irradiation was significantly attenuated following reduction of the irradiated samples. Thus if the enhancement and broadening of region A (~280 nm band) was caused by the irradiation forming new species or disrupting intramolecular interactions, a loss of this band following reduction would indicate that the enhancement was due to groups that were irreversibly reduced with $NaBH_4$, indicating that they are ketones or aldehydes. The attenuation of the absorption enhancement with increasing pH in region A (~280 nm) following reduction of the irradiated sample is significantly different than the increase in enhancement seen in this region following reduction of the untreated sample. This change in response to reduction

is another indication that the irradiation is influencing the compounds that are contributing to the absorbance in region A.

4.6 Conclusion:

The pH titration, reduction and irradiation of SRNOM, SRFA and PLFA, show that there are some distinct differences in the reference materials from different sources. SRNOM and SRFA (proposed to be from a more terrestrial source) are highly similar while PLFA (proposed to be more microbial in origin) was more unique. The high similarity between SRNOM and SRFA is consistent with both materials being extracted from the Suwannee River where the majority of the DOC is thought to come from decomposing vegetation. PLFA is thought to be more microbial in origin and does display some different responses to reduction and pH titration which indicates that it is structurally different. The three most pronounced differences between SRNOM/SRFA and PLFA are: 1) PLFA has a significantly smaller loss of absorption following reduction, 2) the pH difference spectra do not have a band around ~280 nm for PLFA, and 3) there is significantly less pH dependence at high pHs for PLFA compared to SRNOM or SRFA. The difference in reduction suggests that reducible groups such as ketones and aldehydes do not contribute as much to the optical properties of PLFA. While the differences in pH suggest that PLFA has a smaller phenol content compared to the other reference materials. These results are consistent with the chemical properties of humic substances provided by the IHSS[155,156]. So although PLFA may contain the same functional groups as SRNOM and SRFA they are present in different proportions and the overall structure of PLFA is different. Thus monitoring the optics during these chemical tests can help not only determine the structures responsible for the optical properties but can help determine the source of the CDOM.

These tests also indicated that a simple superposition model does not fully account for the optical properties and the observed responses to pH titration and $NaBH_4$ reduction. However, an electronic interaction model can better account for these responses. This suggests that there are charge transfer interactions occurring between electron rich donors and electron poor acceptors present within the reference materials.

Chapter 5: Absorbance changes seen in C18 extracted organic matter (C18-OM) following $NaBH_4$ reduction and pH titration: Are there differences depending on the geographical local?

5.1 Abstract:

In this chapter the techniques detailed in chapter 4 are applied to natural water CDOM that was isolated using solid phase extraction employing C18 columns. Water samples were collected from a variety for geographic locales from rivers to the open ocean. The combined effects of pH and borohydride reduction across these samples were compared in order to probe the sources and structure of the CDOM. Overall there were four general responses that remained consistent throughout all samples tested: 1) monotonically decreasing and unstructured absorbance with increasing wavelength; 2) loss of absorption upon $NaBH_4$ reduction at all wavelength, with the largest percent loss in the visible; 3) enhanced absorption with increasing pH at all wavelengths; 4) attenuation of absorption enhancement with increasing pH following reduction in most regions. Samples from the deep ocean (Atlantic and Pacific) showed the highest degree of similarity. These results suggest that there may be similar structures in all samples and thus suggests a possible terrestrial component to the CDOM in the open ocean.

5.2 Introduction:

In this study, we examine the combined effects of borohydride reduction and pH on the absorption of samples from diverse geographical locales, by titrating both untreated and reduced C18 extracted organic matter (C18-OM) samples. Evaluating the similarities and differences between locations can provide information about the possible source and structure of CDOM in these environments. This study includes the evaluation of samples from the North Pacific Ocean (NPO), Equatorial Atlantic Ocean (EAO), Middle Atlantic

Bight (MAB), and the Delaware River and Bay. Comparisons are also drawn between the C18-OM samples and the reference materials and irradiated reference materials previously tested and detailed in Chapter 4. Samples from the environment, especially surface samples, could become very photodegraded due to exposure to solar radiation. Thus bleaching of a reference material could also provide insight into how this will affect the optics and chemical properties. Irradiation of humic substances and CDOM samples has been shown to significantly increase the spectral slope due to preferential loss of long wavelength absorbance.[33] This loss of absorption often referend to as photobleaching is due to destruction of chromophores within CDOM due to photolysis and other processes and has been shown to result in CDOM with a different distribution of carbon and lower molecular size.[33,42,108,148,157]

Comparisons of the optics and the chemical properties (in relation to the optics: reduction and pH) for samples from rivers to open oceans detailed in this work, indicated a high degree of similarity between these samples and suggests samples from these diverse locales may have some structures in common.

5.3 Methods:

5.3.1 Sampling locations

Extracts and natural waters were acquired from the North Pacific Ocean in December 2014 onboard the R/V Kilo Moana at Station ALOHA (22^{o} 45' N, and 158^{o} 00' W); from the Equatorial Atlantic Ocean (EAO) in 2009 in May and June onboard the R/V Endeavor; from the Delaware River and Bay and the Middle Atlantic Bight during several cruises from September 2005 to August 2006 onboard the R/V Cape Henlopen and the R/V Hugh R. Sharp, and from July 2016 onboard the R/V Hugh R. Sharp. (Fig. 5.1). Offshore samples

collected at depths between 2 – 15 meters are referred to as surface samples while samples collected below 800 m are considered deep samples.

5.3.2 Sample collection

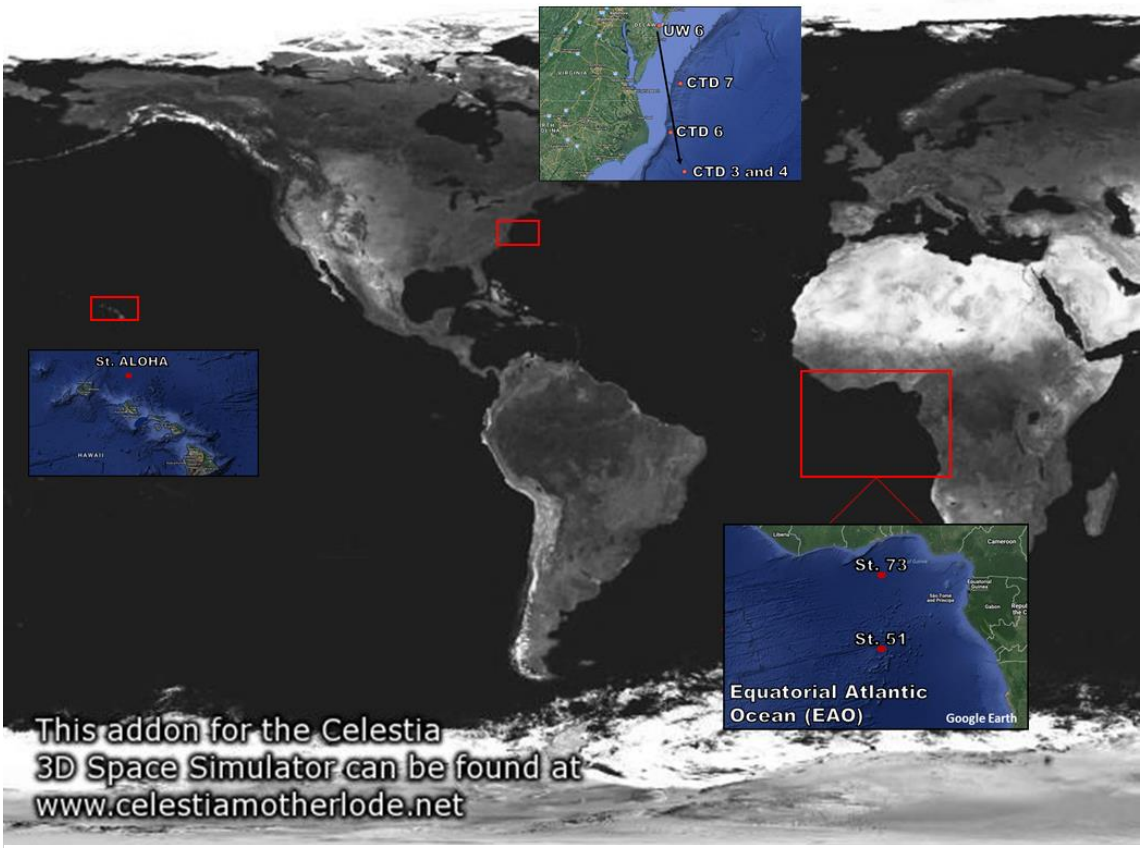

Figure 5.1: Sampling locations, Delaware River and bay, MAB, NPO and EAO.

C18 extracts were obtained with the same protocol at all sites as described in Boyle (2009).[24] Briefly, natural water samples from each location were collected using either a surface pumping system that provided water from a depth of ~ 2 - 15 m, or with a CTD rosette equipped with Niskin bottles. Samples were collected in acid rinsed carboys (20 L) and immediately filtered through 0.2 µm double layer HT Tuffryn hydrophilic polysulfone filters (maxi capsule-Pall Corporation), that had been previously rinsed with purified water. To further rinse the filter, a small volume of the natural water (~ 1 L) was passed though the filter and discarded. The filtered water (~20 L) was then acidified to pH ~2.0 using

~100 mL of HCl (~2 M), and drawn over C18 columns (United Chemical Technologies, Inc.) using a peristaltic pump at a flow rate of ~50 mL min^{-1}. All C18 extraction columns were preconditioned by passing 100 mL of MeOH and 50 mL of acidified purified water at pH 2 over the column prior to use. Following extraction, the columns were rinsed with acidified purified water (~100 mL, pH 2) to remove salts, and stored in the dark at 4°C. Prior to DOM elution, the cartridges were rinsed with an aqueous solution of formic acid (0.1% by volume), and gently dried with N_2 gas. DOM was eluted with 50 mL of high purity MeOH. The first 5 mL of eluent were discarded to remove any remaining aqueous fraction, with the remaining eluent roto-evaporated at ~35°C until dry. The dried DOM was dissolved in purified water and adjusted to neutral pH with NH_4OH or NaOH. This concentrated extracted material (referred to as "extracts" or C18-OM) was stored frozen in the dark.

5.3.3 Sample preparation

Concentrated C18-OM was first diluted with purified water to match the absorbance at 350 nm of either a ~80 or ~30 mg/L Suwannee River Fulvic Acid (SRFA) sample. The sample pH was then adjusted to ~7.0 using diluted $HClO_4$, with the sample then filtered through a 0.2 µm nylon syringe filter.

5.3.4 Optical measurements and chemical tests:

Absorption measurements of the C18-OM samples were performed in the same manner as the reference material samples described in Chapter 4 (*4.3.3 optical measurements*) employing a Shimadzu UVPC 2401 benchtop spectrophotometer and a quartz cell (1 cm). In order to draw comparisons between samples the absorbance for all

samples was normalized to that of a ~80 Suwannee River Fulvic Acid (SRFA) sample at 350 nm.

$NaBH_4$ reductions and pH titrations were also conducted using the same methods described in Chapter 4 (*4.3.4 NaBH4 Reduction* and *4.3.5 pH titration*; respectively).

5.4 Results:

5.4.1 Optical properties

As previously observed,[1,16,25,35] the absorption of all samples decreased with increasing wavelength in an approximately exponential fashion independent of sample location. (Fig. 5.2) Deep NPO waters exhibit a weak shoulder at ~420 nm. The absorption decreased with increasing wavelength more rapidly for samples from the open oceans as compared to coastal samples and reference material, with the surface samples showing the largest decrease; this trend is better highlighted by normalizing the absorption spectrum of each sample to the absorption of an 80 mg L^{-1} SRFA solution at pH ~7.0 at 350 nm (Fig. 5.2). Consistently, surface samples from the Pacific and Atlantic oceans exhibit the largest spectral slope ($S_{300\text{-}700}$: ~0.020 – 0.025 nm^{-1}) followed by deep ocean samples (~0.017 – 0.014 nm^{-1}), river/bay samples and reference materials (SRFA, SRNOM and PLFA) (~0.015- 0.016 nm^{-1}) (Fig. 5.3).

5.4.2 $NaBH_4$ reduction

Following reduction with $NaBH_4$, all samples displayed a decrease in absorption at all wavelengths but the greatest fractional losses were observed at longer wavelengths (Fig. 5.4). The substantial loss in absorption at longer wavelengths is better highlighted by plotting the natural log of the absorbance for both the untreated and reduced samples, (Fig. 5.4 right axis). The largest percent loss (Eq. 4.2) in absorption in the visible

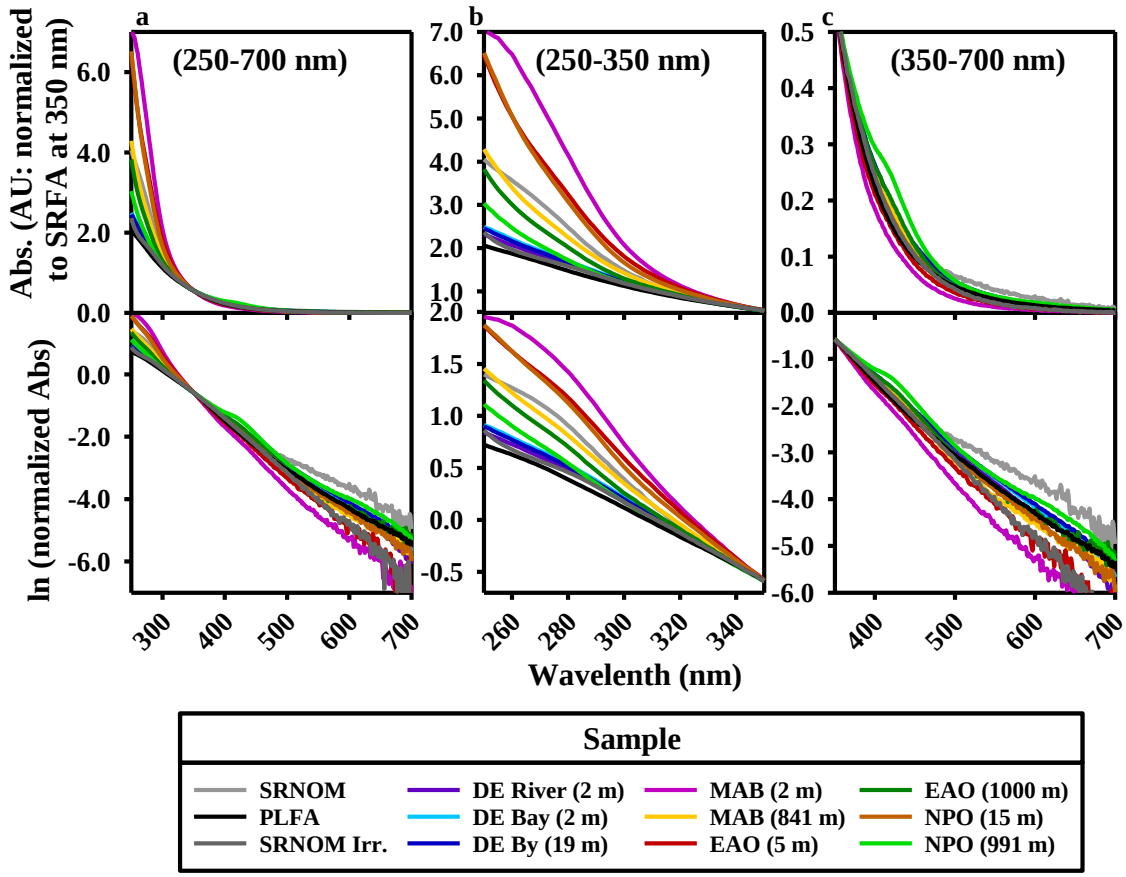

Figure 5.2: (**Top**) Absorbance of C18-OM extracts from multiple geographic locations normalized to the absorbance of an 80 mg/L SRFA reference solution at 350 nm along with SRNOM untreated and Irradiated 50hrs and PLFA. (**Bottom**) Natural log of the normalized absorbance. (**a**) Full spectrum from 250 – 700 nm, (**b**) spectrum from 250-350 nm, and (**c**) spectrum from 350 – 700 nm.

region calculated using Eq. 4.2 was observed for the Delaware samples (river and bay) and SRNOM (~60-70 %) compared to the open ocean samples and PLFA (≤ 45%) (Fig. S5.1). The average percent absorption loss over the 250-500 nm region was also calculated for each sample using Eq. 4.3; the river and bay samples lost the most absorption (~52%)

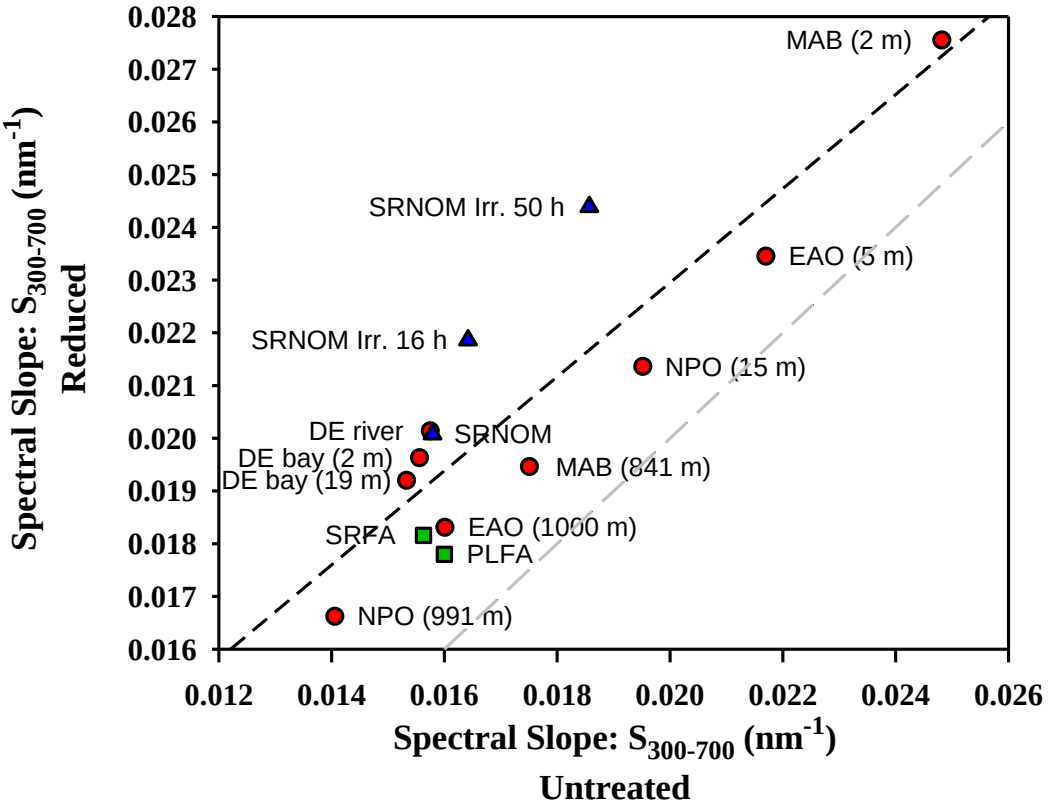

Figure 5.3: Spectral Slope ($S_{300\text{-}700}$) values for untreated and reduced (**red, circles**) C18-OM extracts from multiple geographic locations, (**blue, triangles**) SRNOM untreated and Irradiated (16, and 50 h) and (**green, squares**) SRFA and PLFA; *(–) linear regression, (--) 1:1 line*

followed by open ocean deep samples (~38%), and the least amount of absorption loss was seen in the open ocean surface samples (~33%) (Fig. 5.5). However, despite significant loss for all samples especially in the long wavelength region, absorption still remained following reduction in both the UV and visible regions.

Following reduction, the spectral slope ($S_{300\text{-}700}$) for all samples increased due to the preferential loss of visible absorption (Fig. 5.3). The percent increase in spectral slope following reduction followed the same trend as the percent absorption loss, with spectral slopes for the irradiated SRNOM increasing the most (~30-33 %) followed by the Delaware samples (river and bay) and SRNOM (~ 25-27%), then by the deep open ocean samples

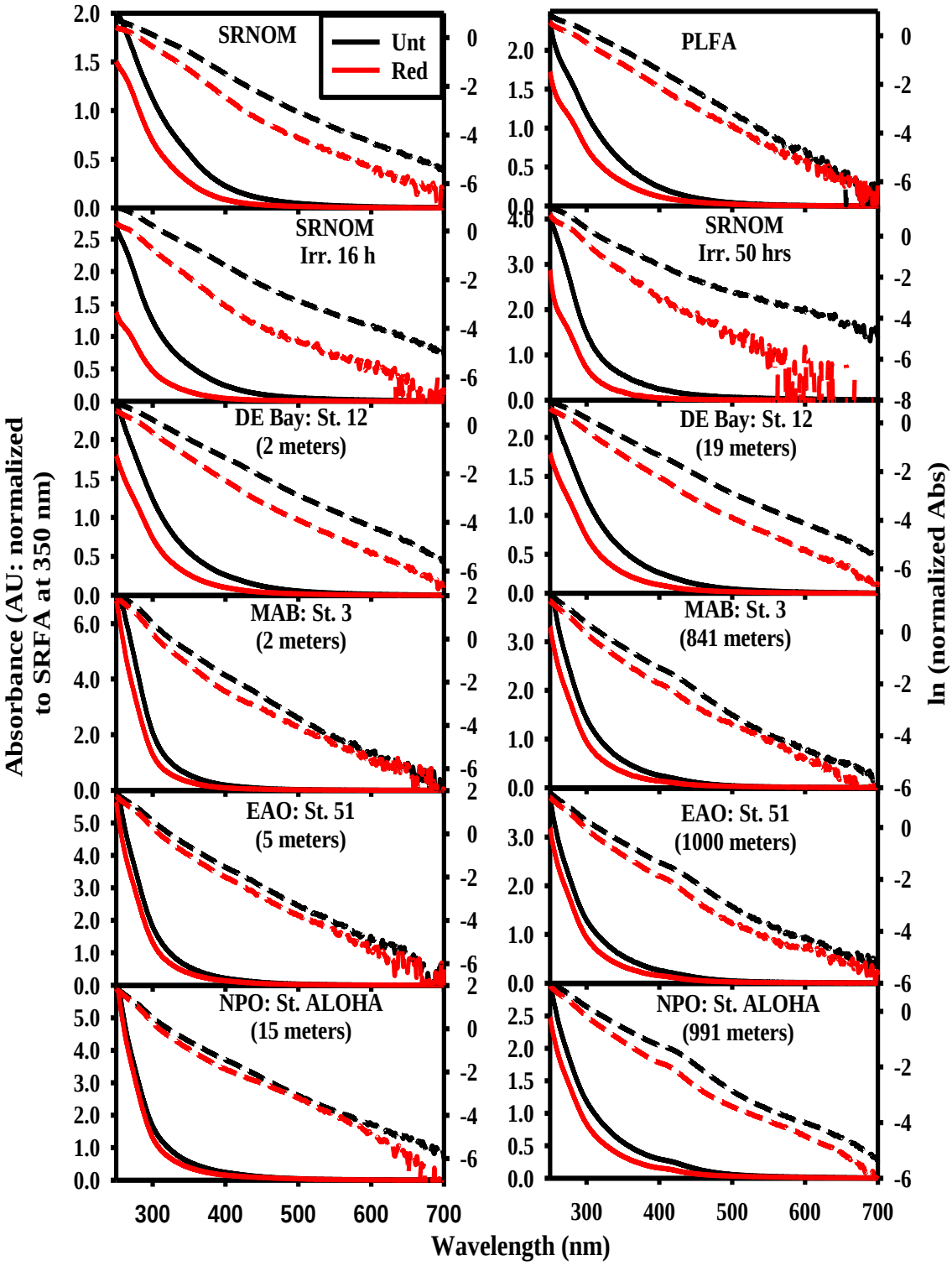

Figure 5.4: Normalized absorbance (AU) (**solid lines**) for both untreated (**black**) and reduced (**red**) samples for various locations along with the natural log of the normalized absorbance (**dashed lines**) for the same samples.

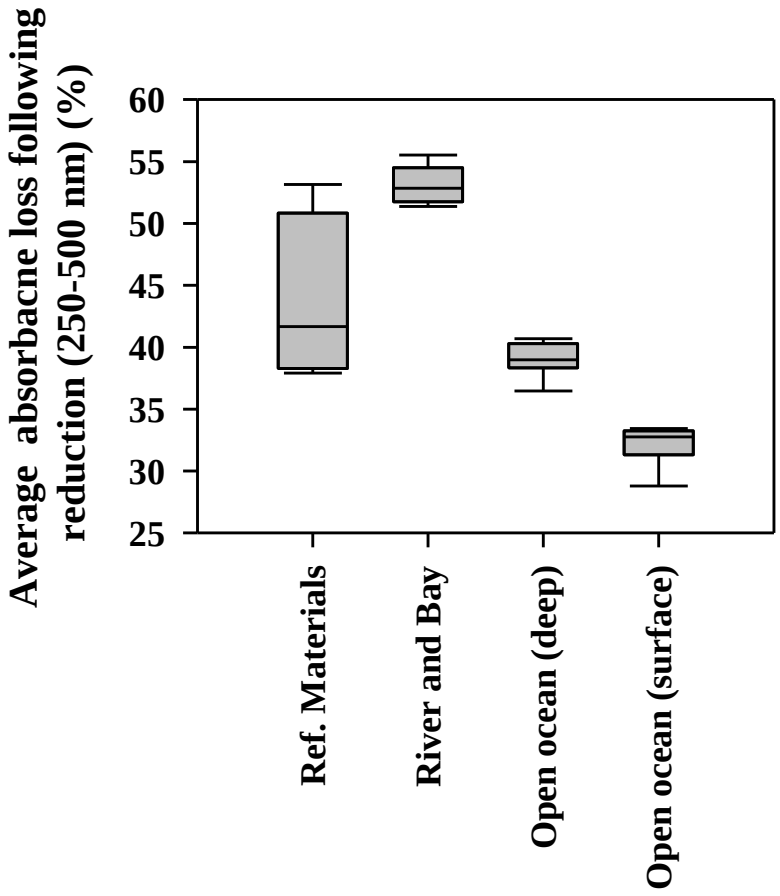

Figure 5.5: Average percent absorbance loss over the 250-500nm wavelength range following reduction. Samples grouped by general locations including Delaware River and bay samples (n=5), open ocean deep (n=9) and surface (n=6) samples, as well are reference materials (SRHA, SRFA, SRNOM, and PLFA) for comparison.

(~15 %) and finally surface open ocean samples and PLFA (~9-11%) which increased the least (Fig. 5.3).

5.4.3 Effect of pH on the optical properties

A comparison was made between SRNOM, PLFA and three C18-OM samples from a transect that started in the Delaware River and ended in the MAB: 1) Delaware River, 2) Delaware Bay and 3) Middle Atlantic Bight shelf, (Fig 5.1). This transect enabled the

evaluation of the pH dependence of C18-OM samples moving offshore. Overall the same trends that were present in SRNOM were also present in all the C18-OM samples along this transect. (Fig. 5.6 and S5.2-S5.4) The absorption for all samples (untreated and reduced) increased at all wavelengths with increasing pH even into the visible region. As seen previously, reduction significantly attenuated the absorption enhancement with increasing pH.

The difference spectra of all the samples clearly indicated the same three regions (A, B, and C) seen in SRNOM/SRFA and discussed in chapter 4. For the river sample all regions (A,B and C) were nearly identical to SRNOM. Region A and B (~280 nm band and the ~300-450 nm band, respectively) were still very pronounced and region B was very broad and unstructured. In the lower bay sample region B becomes more structured and less broad with a slightly more defined band visible around ~350-420 nm. The shelf sample loses even more of the broadband background absorbance enhancement with increasing pH. This made the bands at ~280 more defined, and accentuated two clear bands in region B: one centered around ~420 nm and another around ~310 nm. The changes in region B (~ 300-450 nm) are the most noticeable changes along the transect. Overall the difference spectra become more structured and lose background broadband absorption enhancement with increasing pH moving offshore.

Similar to the reference materials, the attenuation of the absorption enhancement with increasing pH caused by reduction can be evaluated by subtracting the absorbance of the reduced sample from that of the untreated sample (A_{lost}: "untreated – reduced" Eq, 4.5). The absorbance lost following reduction (A_{lost}) also increases with increasing pH except in region A (~280 nm). These means that following reduction there was a loss of absorption

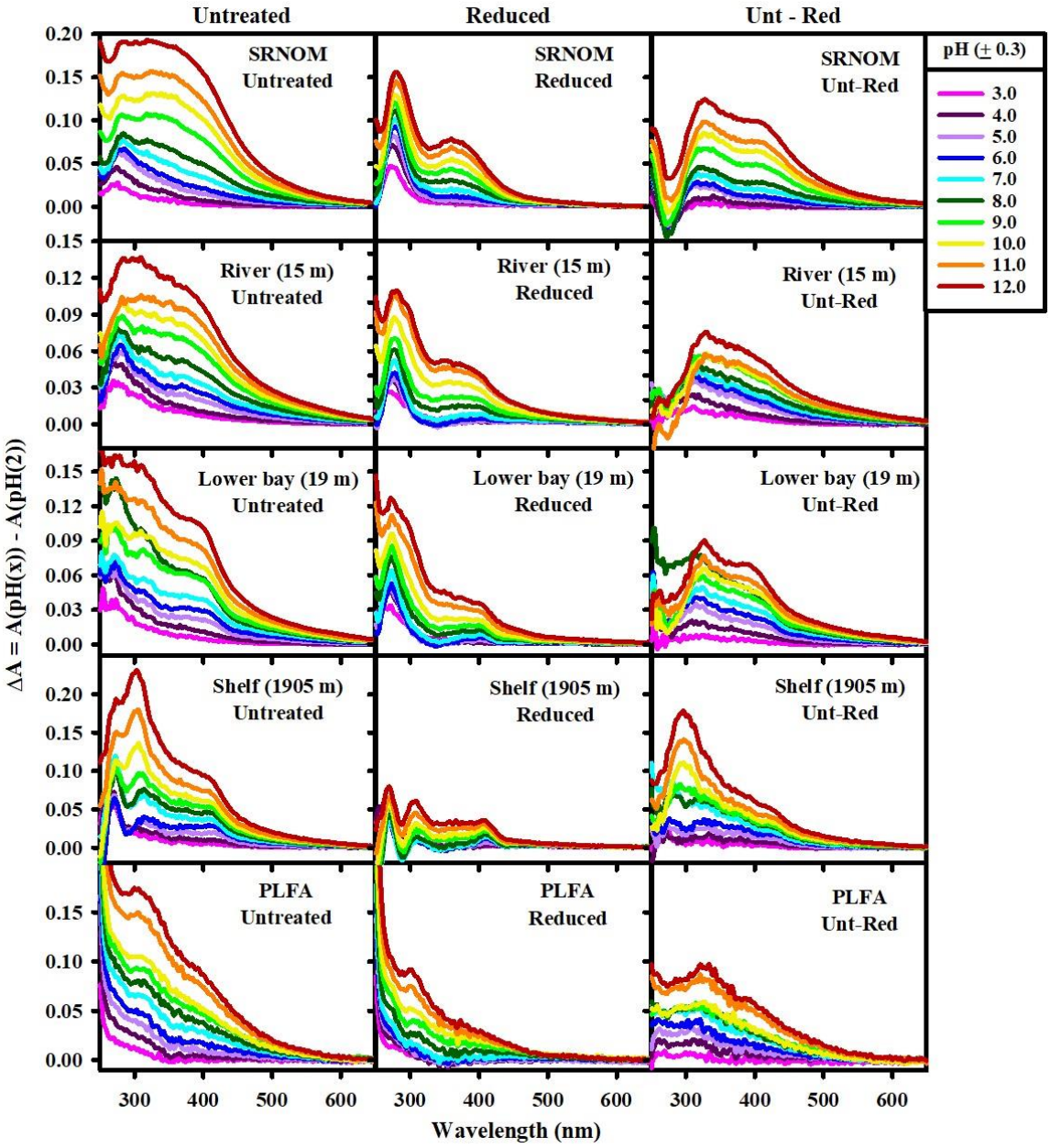

Figure 5.6: Difference spectra relative to pH 2 for untreated (**left**), reduced (**middle**) and unt-red (**right**) C18-OM samples along a transect from the Delaware River to the shelf with SRNOM at the top and PLFA at the bottom for comparison.

enhancement with increasing pH at all wavelengths except at ~280 nm where there was a slight increase or minimal change in the enhancement with increasing pH following reduction. The difference spectra for the A_{lost} ("untreated – reduced") shows a very high degree of uniformity for all samples along the profile (Fig. 5.6, right panel). The river and

bay sample are nearly identical to SRNOM. However, moving offshore region A (~280 nm band) initially shows increased absorption enhancement with increasing pH following reduction indicated by negative values, but in the bay sample there is no change and the shelf sample shows a loss in absorption enhancement in this region following reduction indicated by positive values.

All the deep open ocean samples display very similar pH dependence. Like the MAB shelf sample shown earlier, the other deep open ocean samples display an increase in absorbance with increasing pH at all wavelengths and the difference spectra for the MAB, EAO and NPO are highly comparable (Fig. 5.7 and S5.5). All have several bands in the difference spectra that grow in at low pHs one in region A around ~270-280, and two in region B around ~310 and ~420 nm and long wavelength enhancement at all pHs. Not only was this response consistent between sample location but all deep samples from the NPO between 300-4500m shared the same response (Fig. S5.6) as did the deep MAB samples (Fig. S5.7). When comparing deep open ocean samples from the NPO, EAO and MAB, it is clear that they all have nearly identical pH dependence and response to reduction (Fig. 5.7). Again the difference and fractional difference spectra were compared at individual wavelengths (280, 350 and 500 nm) to illustrate the change with increasing pH. Unlike SRNOM the fractional difference spectra of the reduced deep open ocean samples did not display increased absorption enhancement with increasing pH at 280 nm, instead they showed a loss. SRNOM displayed little difference in the fractional absorption enhancement with increasing pH at wavelengths 350 and 500 nm while the deep ocean sample displayed significant loss following reduction (Fig. 5.8).

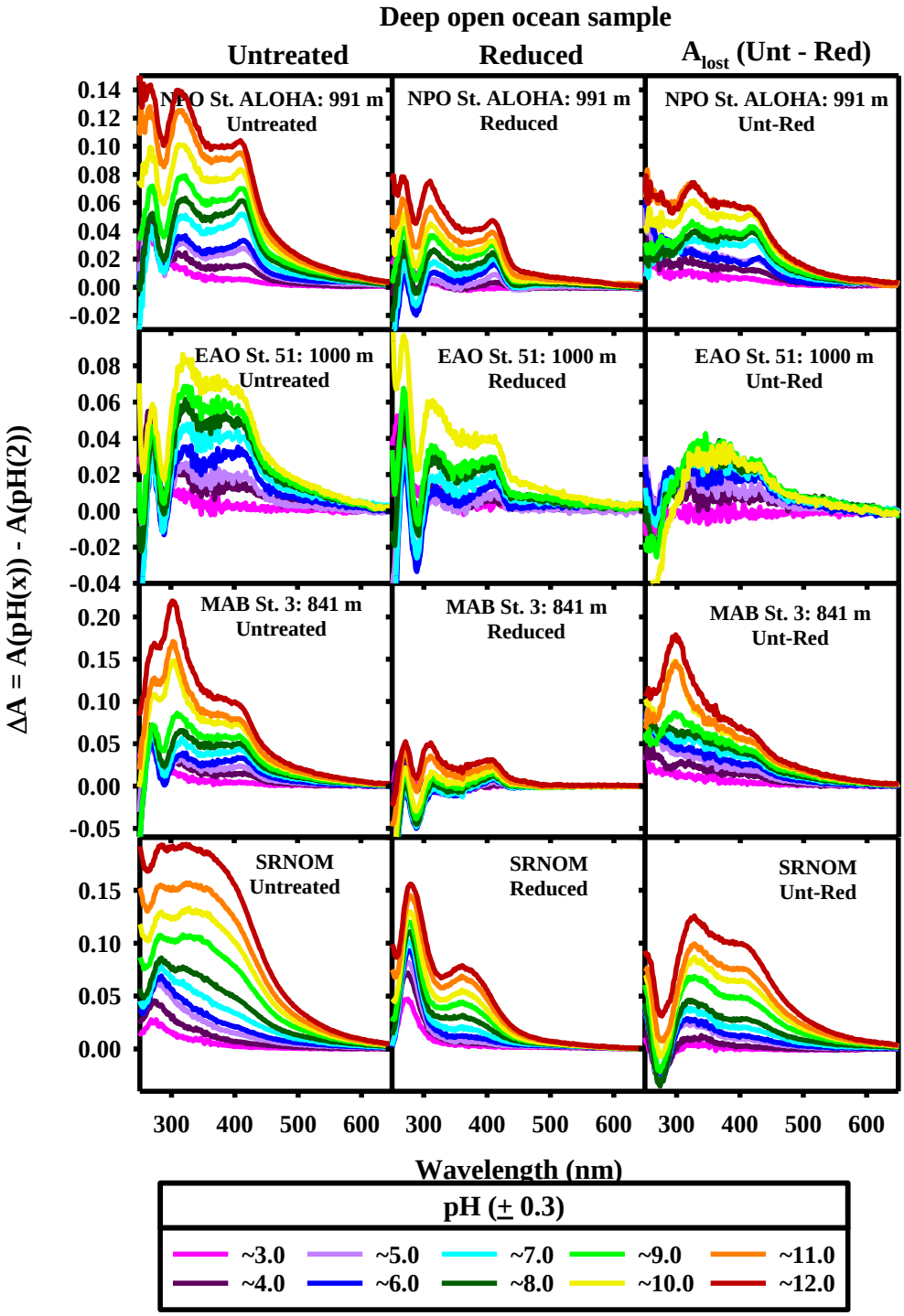

Figure 5.7: Difference spectra relative to pH 2 for untreated (**left**), reduced (**middle**) and unt-red (**right**) C18-OM samples from the deep open ocean. SRNOM is at the bottom for comparison.

For all deep open ocean samples the ~270-280 nm band is present at all pHs, while the ~310 and 420 nm bands grow in at low pHs between 4-7. The ~310 nm band continue

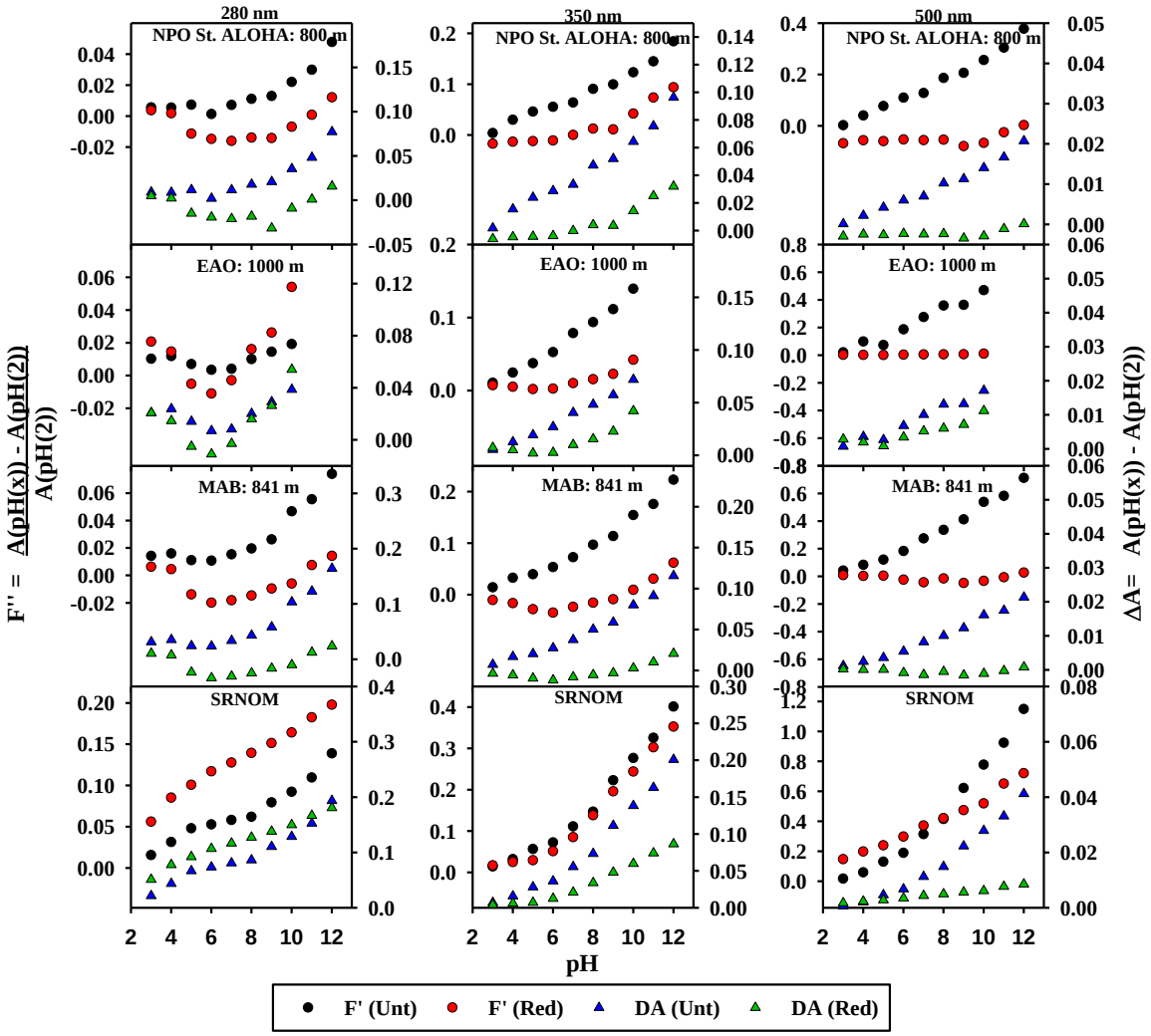

Figure 5.8: pH dependence of the difference (**triangle**) and fractional difference (**circles**) spectra at select wavelengths (280, 350 and 500 nm), for deep open ocean samples with SRNOM at the bottom for comparison.

to be significantly enhanced at all pHs up to pH 12 while the ~420 nm band is only slightly enhanced at high pHs. These more defined bands fall in similar regions as seen in SRNOM, but the change at high pH especially at long wavelengths is not nearly as dramatic which can be seen when comparing the change in spectral slope with pH (Fig. 5.9 and S5.8). Due to the increase in long wavelength absorption at high pHs for SRNOM the spectral slopes decrease dramatically at pHs > 8; this same decrease is seen for other reference materials as well but not for PLFA[56] (Fig. 5.9). However, the spectral slope for open ocean samples

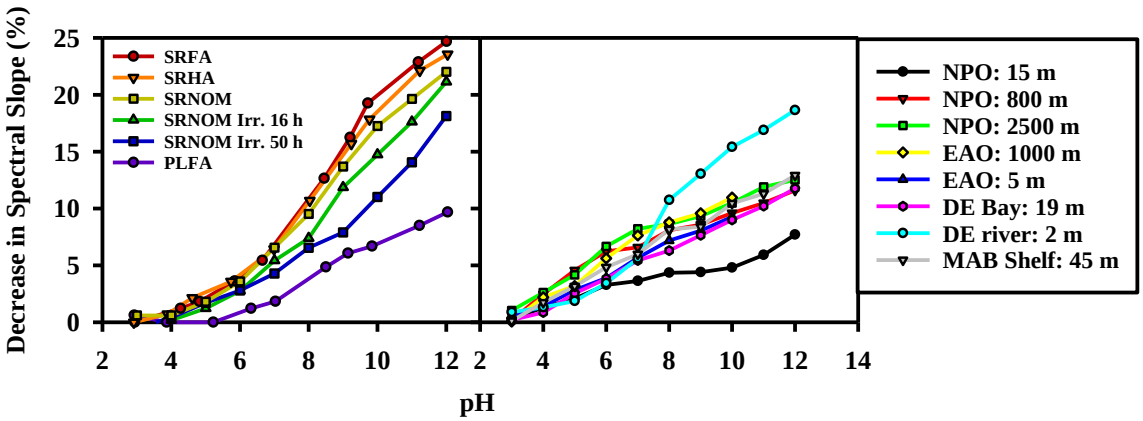

Figure 5.9: Percent decrease in spectral slope ($S_{300\text{-}700}$) with increasing pH for (**left**) reference materials and for (**right**) select C18-OM extracts.

do not show this same dramatic decrease at high pHs. Instead, the decrease is more uniform at all pHs. The only sample that displays an identical trend to SRNOM is the Delaware River sample. The irradiated SRNOM samples do show a slightly smaller decrease in spectral slope at high pHs compared to untreated SRNOM, but they still are not comparable to the open ocean samples.

All surface waters show similar characteristics to one another but they differ greatly from the deep water samples. The absorbance is enhanced with increasing pH and the difference spectra for surface samples display defined bands at ~270-280 and ~310 (Fig. 5.10). The band at ~420 nm that is fairly well defined in the deep samples is less pronounced in the surface samples. The long wavelength absorption enhancement with increasing pH for surface samples is also less than that of deep samples by~2-3 fold. Following reduction there was again little change in the absorption enhancement with increasing pH in region A (~280 nm) while there was decreased absorption enhancement in regions B and C with region C (>450 nm) losing almost all of the absorption enhancement with increasing pH. These changes following reduction are highly comparable to deep open ocean samples and similar to SRNOM.

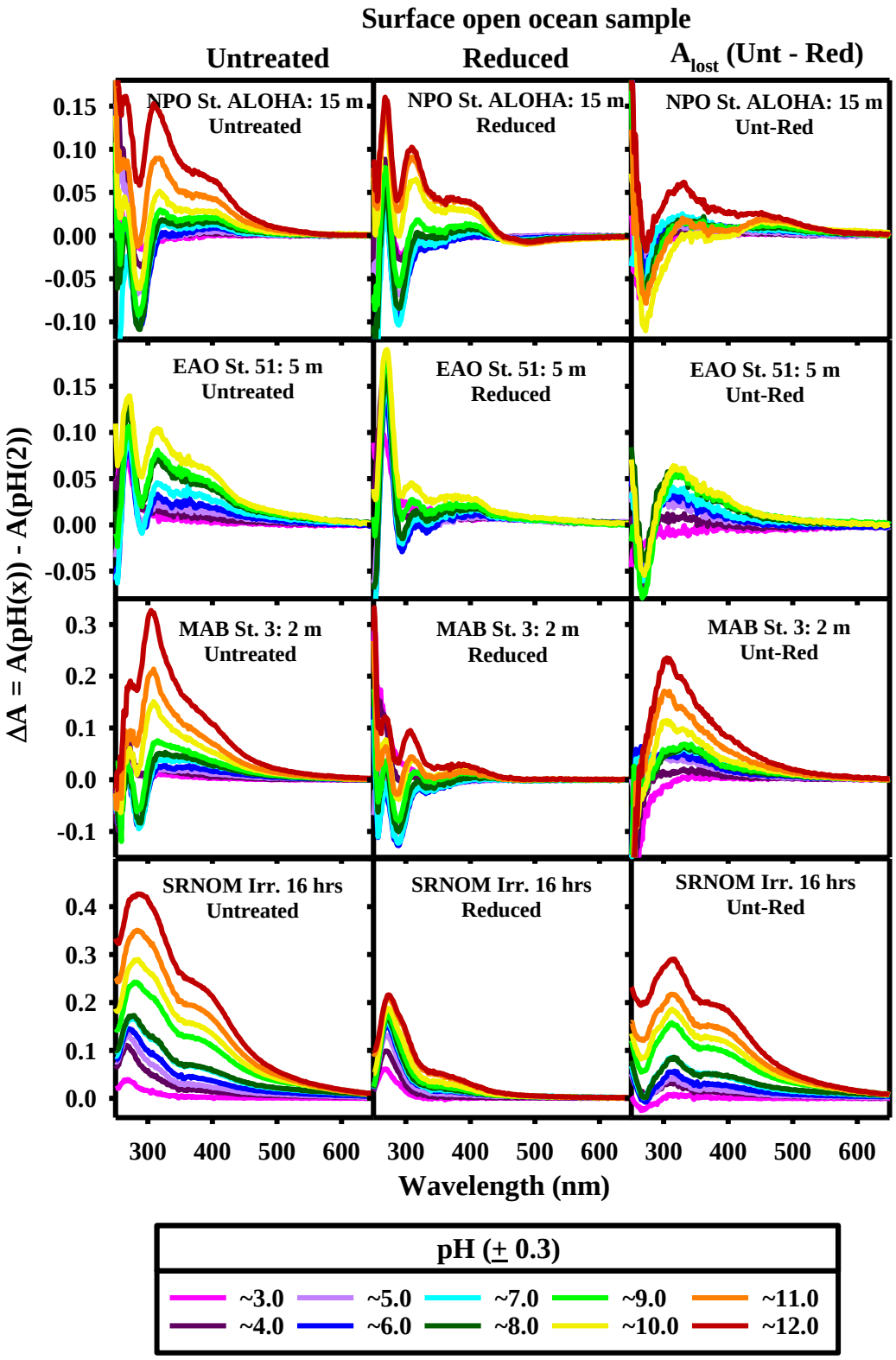

Figure 5.10: Difference spectra relative to pH 2 for untreated (**left**), reduced (**middle**) and unt-red (**right**) C18-OM samples from the surface open ocean. An irradiated SRNOM sample is at the bottom for comparison.

5.5 Discussion:

5.5.1 Absorption

The lack of defined bands in the absorbance for all samples (Fig.5.2) is in part due to the extraction process which has been shown to preferential extract the more "humic-like" CDOM [7] (Fig. 3.3-3.6), but the natural waters for these samples displayed minimal bands or shoulders [7,16,35]. The high similarity in these absorption spectra provides evidence that there are similar structures present in the C18-OM samples from all locations. All samples have broad absorption spectra that extend into the lower energy, visible wavelength region which can be explained by an electronic interaction model, where electronic interactions including short-range charge transfer interactions give rise to some of the optical properties of the sample [21].

5.5.2 $NaBH_4$ Reduction

As with the reference materials, the significant loss in absorbance following reduction at all wavelengths indicates that all samples have reducible groups (ketones and aldehydes) and that these groups contribute not only to the short wavelength absorbance but also to the long wavelength visible absorbance (Fig. 5.3-5.4, S5.1). The possible reasons for incomplete loss of long wavelength absorption following reduction of the C18-OM samples is the same as that for the reference materials (section 4.5.2). Briefly, the C18-OM samples may not be fully reduced, there could be quinones that are reversibly reduced and there could be chromophores that absorb in the visible region that are unaffected by the $NaBH_4$ reduction.

The similar response to $NaBH_4$ reduction seen in C18-OM samples from different geographical locations from rivers to open oceans provides evidence that the CDOM present in these regions has structural similarity and indicates that there may be a modified

terrestrial component contributing to CDOM even in the open ocean. The percent reduction for deep open ocean samples is lower than river and bay samples and the surface ocean samples' percent reduction is even smaller; this could be due to degradation of the CDOM through photobleaching or microbial action. The more degraded CDOM could have fewer reducible groups contributing to its absorption. The smaller percent absorbance loss following reduction for the open ocean samples compared to SRNOM and river/bay samples could also suggesting that there are charge transfer complexes between ketones/aldehydes and carboxylic acids/phenols in the ocean samples that are not accessible and thus are not impacted by reduction.

5.5.3 pH titration

Overall the transect samples are highly similar to SRNOM, but as you move offshore several trends become evident. First the broad absorption in region B (~300-450 nm) becomes less pronounced and more structured (Fig. 5.6). This result suggests a decreasing of charge transfer interactions that contribute to the broad nature of the absorbance spectra and pH dependence. Moving from river samples to open ocean samples the average molecular size of the DOM has been shown to decrease.[54,76,138,158] This decrease in molecular size would decrease the possibility for intramolecular charge transfer interactions which is in line with the loss of broadband absorption enhancements with increasing pH. With a lesser contribution from charge transfer interactions, the pH dependence due to individual classes of chromophores becomes more evident and thus causes the difference spectra to be more structured (Fig. 5.6).

These changes could be caused in part by modification of the terrestrial material as it is transported to the open ocean. One possibility is that photobleaching is altering the

sample giving rise to the change in pH dependence. Region B becoming less pronounced in more offshore samples which is in line with the losses observed during the irradiation of the reference materials. However, not all changes in the pH dependence and reduction seen along the transect fall in line with the changes seen in SRNOM during irradiation. For example a band at ~420 nm starts to appear in the shelf sample and is seen in other open ocean samples, but this band does not appear during irradiation of the SRNOM. This may be due to the SRNOM being extracted before it was irradiated and the deration of the photodegradation between the ocean samples and the SRNOM was very different. Also the SRNOM solution was made in purified water and thus the matrix is simpler compared to natural water which would have other components which could influence the irradiation such as iron which has been shown to catalyze the photoxidation of CDOM. [4,157] However, other factors impacting the change in optics seen in the offshore and open ocean samples cannot be ruled out. There could be microbial modification of the terrestrial source material. There could also be a local source of CDOM that is contributing to the pH dependence. Most likely the differences seen in the open ocean samples are due to a combination of all of these factors.

The high similarity in the A_{lost} difference spectra throughout the transect and with SRNOM could indicate that the effect of reduction on the samples was consistent throughout the transect. This indicates that a reducible fraction of CDOM is present throughout the transect and because the pH dependence of this fraction is similar, the reducible groups throughout the transect are coupled with deprotonatable groups.

Deep open ocean C18-OM samples are highly comparable with one another, and show a near identical pH dependence and response to reduction, suggesting high similarity

in the structures contributing to the optical properties. This high similarity in the deep oceans is also present in mass spectrometry analysis of DOM. Deep ocean samples share many of the same mass spec. peaks (m/z) and there is significant overlap of peaks on Van Krevelen diagrams. [54,79] During pH titration the more defined bands seen in the difference spectra for the open ocean samples (~310 and 420 nm) are in part due to loss of background absorbance that was present in the river and bay samples due to charge transfer interactions (Fig. 5.7). The loss of charge transfer and the presence of these more discrete bands could have several causes as discussed earlier.

For deep ocean samples there was a smaller fractional absorption enhancement with increasing pH for the reduced sample compared to the untreated sample, this change can be seen in the fractional difference spectra. Following reduction the fractional change was smaller at wavelength ~420-500 nm and was nearly eliminated at wavelengths >500 nm (Fig 5.8). This change in the fractional absorption enhancement is different from that of SRNOM and river/bay samples which show little change following reduction. The decrease in the fractional absorption enhancement following reduction indicates that the components contributing to the pH dependence of the reduced sample are different from the untreated samples.

The enhancement in absorbance at high pHs for the open ocean samples is significantly smaller than SRNOM. This could indicate that phenols do not play as large of a role in the optics for these samples. The loss of absorption enhancement with increasing pH for the ocean samples compared to SRNOM can be very clearly seen when comparing the percent change in spectral slope. For SRNOM as well as SRFA, SRHA and the Delaware river sample, there is a large change in spectral slope ($S_{300\text{-}700}$) at high pHs

(>8). The spectral slope decreases for these samples at high pHs because the long wavelengths exhibit significant enhancement with increasing pH. This enhancement is most likely as a result of deprotonated phenols being better electron donors and thus enhancing charge transfer interactions. However, the ocean samples do not show this long wavelength absorption enhancement at high pHs, possibly due to a smaller contribution from phenols. With fewer phenols the long wavelength absorption is not as enhanced at high pHs when the phenols become phenolate anions (better donors). The trend in the spectral slopes ($S_{300\text{-}700}$) of the ocean samples is more in line with PLFA which also does not show dramatic changes at high pHs and has been shown to have a lower phenol content (Table S5.1).

The surface open ocean samples have many of the same traits as deep ocean samples and are different from SRNOM in many of the same ways as the deep samples including, a loss of background absorbance, more defined peaks, and a lack of a pronounced band at 300-400 nm that grows in at the high pHs.

The surface samples are exposed to solar radiation and therefore undergo intense photodegradation which could account for some of the differences in the reduction and pH dependence. Although the C18-OM present in the deep ocean could have been exposed to radiation during its transit to the open ocean, C18-OM at the surface could experience more prolonged bleaching thus the effects of photobleaching are more significant for these samples. These samples appear to have even more significant loss of background absorbance and the band at ~420 nm seen in the deep ocean is almost completely eliminated suggesting these structures are susceptible to photodegradation. Open ocean surface samples also do not display the same degree of absorption enhancement with increasing

pH at long wavelengths >450 nm following reduction. However, the A_{lost} difference spectra indicate that the fraction that is lost following reduction for the surface samples is highly comparable to the deep ocean samples and SRNOM again suggesting similar structures in all samples.

5.6 Conclusion:

Examining the combination effect of pH titration and $NaBH_4$ reduction on the absorbance of C18-OM and reference materials provided a more detailed picture of the contribution of particular functional groups to the absorbance. Similarities and differences between samples also provided more information about the composition of CDOM throughout the aquatic environment. Although surface and deep open ocean samples show some major differences, surface samples from the Atlantic and Pacific are highly similar as are deep samples. Deep ocean samples also have similar responses when compared to SRNOM, SRFA and riverine samples. The change in absorbance seen following reduction and change in pH has a high degree of overlap for all of the samples indicating that similar structures are present from rivers to open oceans. This indicates that there is a possible terrestrial source of carbon that is long lived within the aquatic environment and is not easily degraded. This component can thus be transported to the open ocean and ends up in the deep ocean were it is transported to all ocean basins through deep ocean currents.

The changes seen in the absorbance also strongly support an electronic interaction theory that includes charge transfer interactions between electron rich donor moieties and electron poor acceptor moieties that are in close proximity to one another.

The methods detailed and tested in chapters 3-5 including solid phase extraction, $NaBH_4$ reduction and pH titration, were applied to a wide range of samples to better

understand the source and structure of CDOM in the environment. These tests now make up a "Tool-box" which if appropriately applied to CDOM samples will provide valuable information about the structures responsible for the optical properties, and if applied consistently will allow for comparison of a wide range of samples. **Supplemental 5b** illustrates the application of these tests to evaluate CDOM from a discrete source, Mangrove leaves.

Chapter 6: Critical evaluation of Parallel Factor Analysis (PARAFAC) as a means of analyzing Excitation Emission Matrixes (EEMs) of environmental samples.

This work was completed in collaboration with Rossana Del Vecchio[1], Danielle Le Roux[2], Marla Bianca[2], and Leanne Powers[3]

Danielle Le Roux collected the EEMs for the pyrene study, Marla Bianca collected EEMs for the humic and fulvic acid study, and Leanne Powers collected EEMs for the Sargassum study.

[1] University of Maryland, College Park, Earth System Science Interdisciplinary Center
[2] University of Maryland, College Park, Department of Chemistry and Biochemistry
[3] University of Maryland, Center for Environmental Science, Chesapeake Biological laboratory

6.1 Introduction:

CDOM is also fluorescent (FDOM) and is often characterized using three dimensional excitation emission matrices (EEMs) which are a combination of emission spectra acquired at increasing excitation wavelengths. EEMs give a three dimensional view of the fluorescence by providing a plot of excitation wavelength versus emission wavelength versus fluorescence intensity.

Using fluorescence to monitor and characterize CDOM/FDOM has gained popularity because of the high sensitivity and relatively inexpensive instrumentation required. However, EEMs can be challenging to analyze due to the complex nature of the fluorescence emission and the large number of EEMs that are often collected in field studies. For many of these large datasets, comparison of samples is critical but difficult to perform. Thus, many researchers have employed curve fitting techniques to separate the EEMs into different components having distinct excitation and emission spectra. These components are then employed to characterize the variability in fluorescence across the dataset. One method that has gained popularity is parallel factor analysis (PARAFAC).

This tool has been used to track CDOM distribution and dynamics in many aquatic environments, in an attempt to gain information about CDOM/FDOM composition and structure.

PARAFAC can decompose data that is arranged in three-way arrays into its underlying components and be used for datasets with multiple EEMs (sample, excitation wavelength and emission wavelength). When PARAFAC is used to analyze EEM datasets the fluorescence is decomposed into a set of trilinear terms (Eq. 6.1), any variability not accounted for by the decomposition makes up the residual array (e_{ijk}).

$$X_{ijk} = \sum_{f=1}^{F} a_{if} b_{jf} c_{kf} + e_{ijk} \qquad \textbf{Eq. 6.1}$$

In this equation, f corresponds to a PARAFAC component, i corresponds to the sample, j and k correspond to the emission and excitation wavelengths, respectively. The values range from f = 1, 2,…,F; i = 1,2, …, I; j = 1,2,…, J; and k = 1,2,…,K. Each component (*f*-*F*) has an a-value or score for each sample (*i*-*I*), a b-value for each emission wavelength (*j*-*J*) and a c-value for each excitation wavelength (*k*-*K*). PARAFAC models assume that each component (*f*-*F*) should: **1**) be unique, meaning that no two components have identical spectra, **2**) have variability, meaning that the fluorescence intensity for separate components does not covary, **3**) be additive, meaning that the total fluorescence intensity of a sample can be accounted for by superimposition of individual components, **4**) be chemically meaningful, meaning that the emission spectra do not vary with excitation wavelength and the excitation spectra do not vary with emission wavelength, and **5**) follow Beer's Law, meaning that the fluorescence intensity will increase linearly with concentration under optically thin conditions (low absorbance).

The results of a PARAFAC model can often be highly misleading, because these assumptions are not always met especially when modeling environmental samples. Two examples of deviation from these assumptions would be if the samples contained fluorophores that are interacting electronically, or if the environment of the fluorophores is different in different samples (pH, presence of quenchers, etc.) Thus using PARAFAC to model EEMs is not always straightforward and can lead to faulty conclusions.

To test the usefulness and limitations of the PARAFAC technique, several datasets were compiled and analyzed. These datasets included: 1) mixtures of various non-interacting fluorophores, 2) mixtures of interacting fluorophores and 3) environmental samples. These tests showed that modeling non-interacting fluorophores was successfully accomplished with PARAFAC. However, when modeling interacting fluorophores and environmental samples PARAFAC often returned components that were not physically reasonable and thus did not provide useful chemical or structural information of the original samples.

6.2 Methods:

6.2.1 Materials and samples collection

Reference materials included Suwannee River fulvic and humic acid (SRFA and SRHA), Pony Lake fulvic acid (PLFA), Leonardite humic acid (LHA), and Elliot Soil humic acid (ESHA) were obtained from the International Humic Substances Society (IHSS). Alkali-extracted and carboxylated lignin (LAC) was obtained from Sigma-Aldrich. Tyrosine, trimethylphenol (TMP), tryptophan, quinine sulfate (QS), riboflavin and pyrene were all obtained from Sigma-Aldrich. Purified water was obtained from a Milli-Q Plus purification system by Milli-Pore.

Sargassum samples were collected aboard the R/V *Henry Stommel* 9 km off the coast of Bermuda in September 2016 and were transferred to outdoor tanks housed at the Bermuda Institute of Ocean Sciences, with continuously flowing seawater within 2 h of collection as described in Powers et al. (under review GBC). At the 27 h of the incubation experiment, tank water housing the Sargassum was filtered through pre-combusted Whatman 0.7 µm GF/F glass fiber filters and stored at 4C.

CDOM from the North Pacific Ocean (NPO) was collected from Station ALOHA in December 2014 as described in chapter 3 section *3.3.1*; all NPO samples were filtered through 0.2 µm filters.

Natural water samples were also collected from Goose Cove, Main Creek and Bodkin Creek, which are located in Pasadena Maryland and are tributaries of the Chesapeake Bay (CB). Collected on board a Maryland Department of the Environment (MDE) research boat (MD 1324 DA) and from the shoreline during several separate trips between October 2018 and March 2019 (Fig. 6.1, and Table S6.8) in collaboration with John McKay (MDE) and Stephane Scholloert-Uz (NASA). All CB samples were collected from surface waters

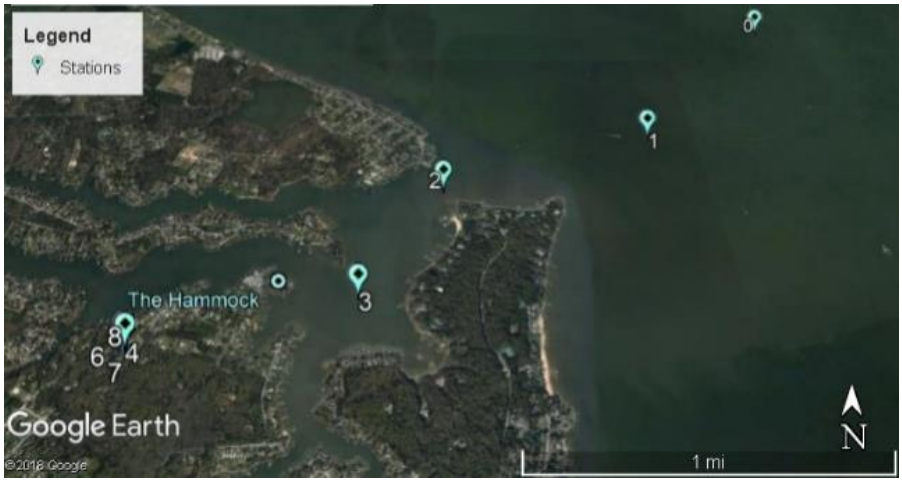

Figure 6.1: Station locations for Chesapeake Bay samples.

at a depth of ~10 cm, in precleaned glass vials. The unfiltered natural waters were stored for ~ 1 day, with one ~5 mL aliquot then filtered through 0.2 µm nylon filters.

6.2.2 Instrumentation

A Thermo-Scientific micro pH electrode coupled to an Orion 4 Star pH ISE benc6top meter was employed for pH measurements. Fluorescence measurements were acquired with a Horiba Fluoromax-4 luminescence spectrometer and in some cases with a Horiba Aqualog spectrometer. Three dimensional excitation- emission matrixes (EEMs) were collected, with the excitation wavelengths typically varied from ~240 to 600 nm, and the emission spectra scanned from ~290 to 700 nm (further detail given in Table S6.1). Spectra were corrected using instrument correction factors supplied by Horiba.

6.2.3 Sample preparation

Tyrosine, TMP, tryptophan, QS, riboflavin and SRFA stock solutions were prepared in purified water. These stock solutions where then used to create a variety of solutions with combinations of the five compounds varying from containing only one of the five compounds to a mixture containing all five (Table S6.2 and S6.3). These samples were diluted in purified water and the resulting concentration of each compound in the solution was ~1 mg L^{-1}, except for riboflavin which was kept at ~0.5 mg L^{-1} and SRFA which was kept at ~3 mg L^{-1} in all mixtures. Additional samples were also prepared with increasing concentrations of tryptophan ranging from 0.5 – 2.0 mg L^{-1}. Solutions of pyrene were made in purified water at increasing concentrations ranging from 0.09 – 6.0 mM (Table S6.4).

Solutions of SRFA, SRHA, PLFA, LHA, ESHA, and LAC were made in purified water at pH ~7 and filtered through 0.2 µm nylon filters, at increasing concentrations (~3 to 100 mg L^{-1}).

$NaBH_4$ reductions and pH titrations were also conducted using the same methods described in Chapter 4 (*4.3.4 NaBH4 Reduction* and *4.3.5 pH titration*; respectively). Reductions were performed on the NPO natural water samples (Table S6.6 and S6.7) and on the reference materials (Table S6.5). pH titrations were performed on the reference materials with EEMs being collected for both untreated and reduced samples at pH 3, 7 and 10.

The exudate from the Sargassum sample was collected and filtered through a 0.2 µm filter and then irradiated. Irradiations of the Sargassum sample was conducting using a system that has been described in detail elsewhere (Timko et al. 2015)[159]. Briefly, the sample was continuously pumped from an equilibrator (i.e. a 10 mL round bottom flask with three necks) to a custom-built flow cell with a 2 mm wide by 1 mm deep flow path (SCHOTT Borofloat, Hellma Analytics, 70 to 85% transmission between 300 and 350 nm, and 85% transmission at wavelengths >350) under an Oriel Sol2A Class ABA solar simulator (Newport Corporation, Irvine, CA) at ~1mL/min. The sample then entered a 10x4 mm flow cell housed in a Horiba Aqualog spectrofluorometer and then returned to the equilibrator that was temperature controlled to 25 °C with a recirculating water bath and the pH of the solution was monitored with a Thermo Orion 8220BNWP microelectrode. The sample was adjusted to pH 8 and maintained with a J-Kem Infinity II reaction controller coupled with a dual syringe pump using 0.1 M HCl or 0.1 M NaOH solutions.

6.2.4 PARAFAC analysis

PARAFAC analysis of all the datasets was performed as in Murphy et al (2008, 2013)[75,128]. A MATLAB correction program from the decomposition routines for Excitation Emission Matrices (drEEM) toolbox was run to remove Raman scattering, while the N-way and drEEM toolbox were used to perform PARAFAC[128]. The datasets were normalized to give high and low-intensity samples similar weight (Fig. S6.1, S6.7, S6.12, S6.16, S6.20, S6.24, S6.28 and S6.33), and the non-negativity constraint was imposed on the model scores and loadings to insure all modeled components have positive fluorescence intensity (Fig. S6.3, S6.9, S6.14, S6.18, S6.22, S6.26, S6.30, S6.35).

Below is a table with the details for each of the eight datasets used to develop PARAFAC models during this study. The number of EEMs in each model ranged from 11 in the NPO PARAFAC models to 130 in the Sargassum PARAFAC model (Table 6.1). The final number of components selected for each model is also provided along with any correlation between components. The ideal number of components chosen for each dataset was determined by evaluating the core consistency (Fig. S6.2b, S6.8b, S6.13b, S6.17b, S6.17b, S6.21b, S6.25b, S6.29b, and S6.34b), performing a split-half validation on the model (Fig. S6.4, S6.10, S6.15, S6.19, S6.23, S6.27, S6.31, and S6.36), analyzing the residuals and by performing a close examination of the optical signature for each component to determine if the loadings were physically reasonable (Fig. S6.2, S6.8, S6.13, S6.17, S6.17, S6.21, S6.25, S6.29, and S6.34). The core consistency for each dataset ranged from 99.9 for the five component PARAFAC model of the non-interacting fluorophores to 1.3 for the seven component PARAFAC model of the Chesapeake Bay (CB) sample. Although core consistency is often a useful diagnostic for determining the appropriateness

Table 6.1: Details of each PARAFAC model used during this study.

Dataset	Number of EEMs	Number of components selected	Components correlated	Components with the strongest correlation: R^2	Core Consistency	Percent explained	Split Validated
Non-interacting fluorophores	35	4	No	C2,C3: 0.11	99.9	99.7	Yes
Non-interacting fluorophores + SRFA	45	5	No	C2,C3: 0.13	99.2	99.4	Yes
Pyrene	12	2	Yes	C1,C2: 0.96	98.4	96.5	Yes
NPO Untreated	11	4	No	C3,C4: 0.51	49	98.4	Yes
NPO Reduced	11	4	No	C2,C3: 0.50	59.2	99.1	Yes
Sargassum	130	4	Yes	C3,C4: 0.94	41.8	99.5	Yes
HA and FA ref materials	36	6	No	C4,C5: 0.54	28.7	99.2	Yes
Chesapeake Bay(CB) samples	31	7	Yes	C3,C5: 0.97	1.3	99.8	Yes

of a model, a low core consistency does not exclude a model especially when analyzing environmental datasets. Thus, the low core consistency in some of the models was overlooked when determining the ideal number of components, because other factors suggested it was the best fit for the dataset. The percent of the data explained by each PARAFAC model was always above 96.5%.

6.3 Results/Discussion:

6.3.1 Non-interacting fluorophores

The first test of the PARAFAC tool was performed by creating a dataset with five different non-interacting fluorophores including trimethylphenol (TMP), tyrosine, tryptophan, quinine sulphate (QS) and riboflavin. A four component model was found to be ideal and the loadings had direct chemical interpretations with each fluorophore being

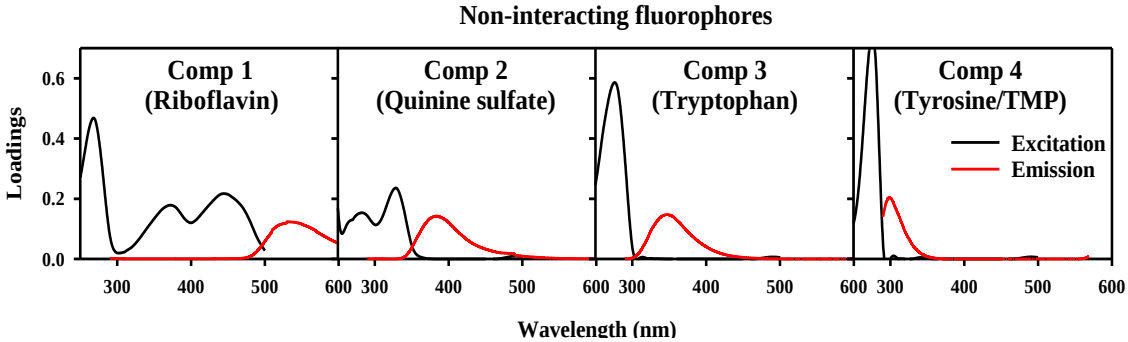

Figure 6.2: Loadings for the four component PARAFAC model generated using the non-interacting fluorophores dataset; excitation spectra (**black**) and emission spectra (**red**).

identified as an individual component except for tyrosine and TMP which were modeled as one component due to the high similarity in their fluorescence excitation and emission (Fig. 6.2). The loadings were also physically reasonable, with minimal overlap between the excitation and emission spectra. All emission spectra had only one distinct peak, and the excitation spectra with multiple peaks always had absorption between the peaks (Fig. 6.2). With this dataset, the PARAFAC tool was able to correctly identify the fluorophores that contributed to the emission in both pure samples (Fig. S6.5 and S6.6) as well as mixtures (Fig. 6.3). Samples with increasing concentrations of tryptophan were included in the dataset to test if the model was able to account for changes in concentration. The fluorescence intensity at the maximum (Fmax) was analyzed for these samples and if modeled correctly, the Fmax for the component associated with tryptophan (Fmax3) should

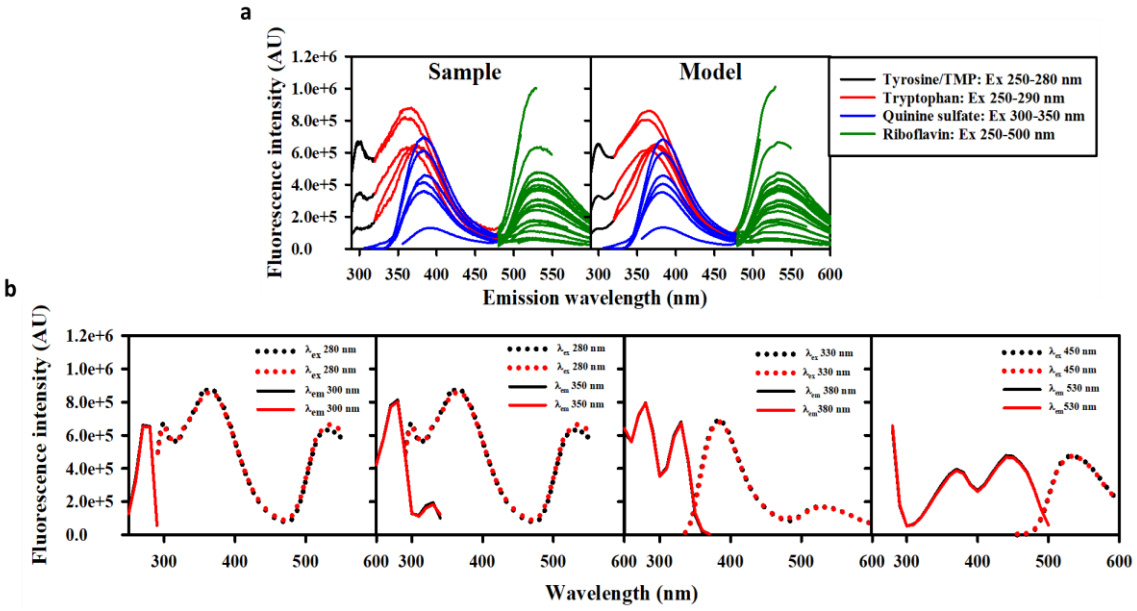

Figure 6.3: a) EEM of a sample (**left**) containing all the non-interacting fluorophores (Sample #8) and the PARAFAC model (**right**) of that sample. The different colors represent the contribution of the different fluorophores as indicated in the legend. **b)** Excitation and emission spectra at the peak of each non-interacting fluorophores: solid lines are excitation spectra, dotted lines are emission spectra, **black** lines are the sample and **red** lines are the PARAFAC models.

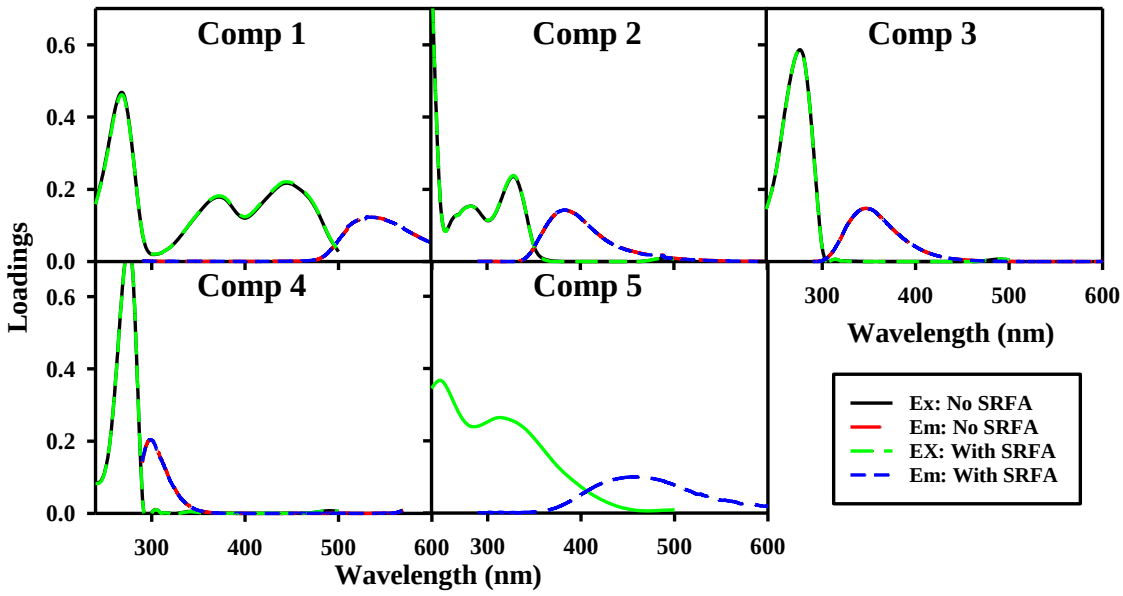

Figure 6.4: loadings for the 4 component model generated with the non-interacting fluorophore data set (excitation spectra (**Black**) and emission spectra (**Red**)), overlaid by the loadings for the 5 component model generated with the non-interacting fluorophores + SRFA dataset (excitation spectra (**Green**) and emission spectra (**Blue**)).

increase linearly with increasing concentration. The Fmax generated by the PARAFAC model did in fact increase linearly with concentration with an R^2 of 0.9988 (Fig. S6.6).

This test clearly indicates that the PARAFAC tool is capable of isolating the contribution of individual fluorophores or groups/classes of compounds contributing to the overall fluorescence of a sample if the compounds are not interacting with one another. This dataset also indicates that the Fmax value does correlate well with concentration and can be used to examine changes in contribution of particular components within a dataset.

6.3.2 Non-interacting model compounds with SRFA

The dataset with non-interacting fluorophores showed that PARAFAC can provided an accurate model under ideal conditions (all the assumptions of the technique are met). To further test the PARAFAC tool, EEMs of mixtures of non-interacting

fluorophores (trimethylphenol, tyrosine, tryptophan, quinine sulphate and riboflavin) and SRFA were analyzed as part of one dataset (Table S6.3 and Fig. S6.7). The addition of SRFA to the dataset added only one component to the PARAFAC model despite the complexity of SRFA emission spectra (Fig. 6.4). In an attempt to better fit SRFA, models with more than five components were considered, but the additional loadings were not physically reasonable and were thus rejected (Fig. S6.8). The four components from the dataset without SRFA were again identified with no changes and properly fit the model compounds and the loadings for these components were again chemically meaningful and physically reasonable (Fig. 6.4). However, the new component that was identified with the addition of SRFA did not properly model SRFA. Instead the fifth component added to the PARAFAC model had a constant emission at ~460 nm (Fig. 6.5), thus the red shifting emission typical of humic substances was not modeled correctly. The inability of the PARAFAC tool to model this red shifting emission is because most the shifts are too small and PARAFAC would need an extremely large number of components to model this. This red shifting likely arises from interactions between compounds, and thus violates one of the PARAFAC tool's assumptions. This fifth component also deviated slightly from the typical characteristic of non-interacting fluorophores in that there was a greater than 50 nm overlap between the onset of the emission spectra and the loss of the excitation spectra, indicating that this component is not physically reasonable and thus not chemically meaningful. Samples containing just SRFA were included in the dataset, but components 1-4 which are associated with the model compounds were identified in the pure SRFA despite those compounds not being present (Fig. S6.11). This is most likely due to the complexity of SRFA and the model trying to make the best fit possible. This can most

clearly be seen in the modeled SRFA at long excitation wavelengths where there is a clear band present in the model that is not present in the sample. This is due to the model trying to account for the red shifting emission by including component 1 in the model from SRFA.

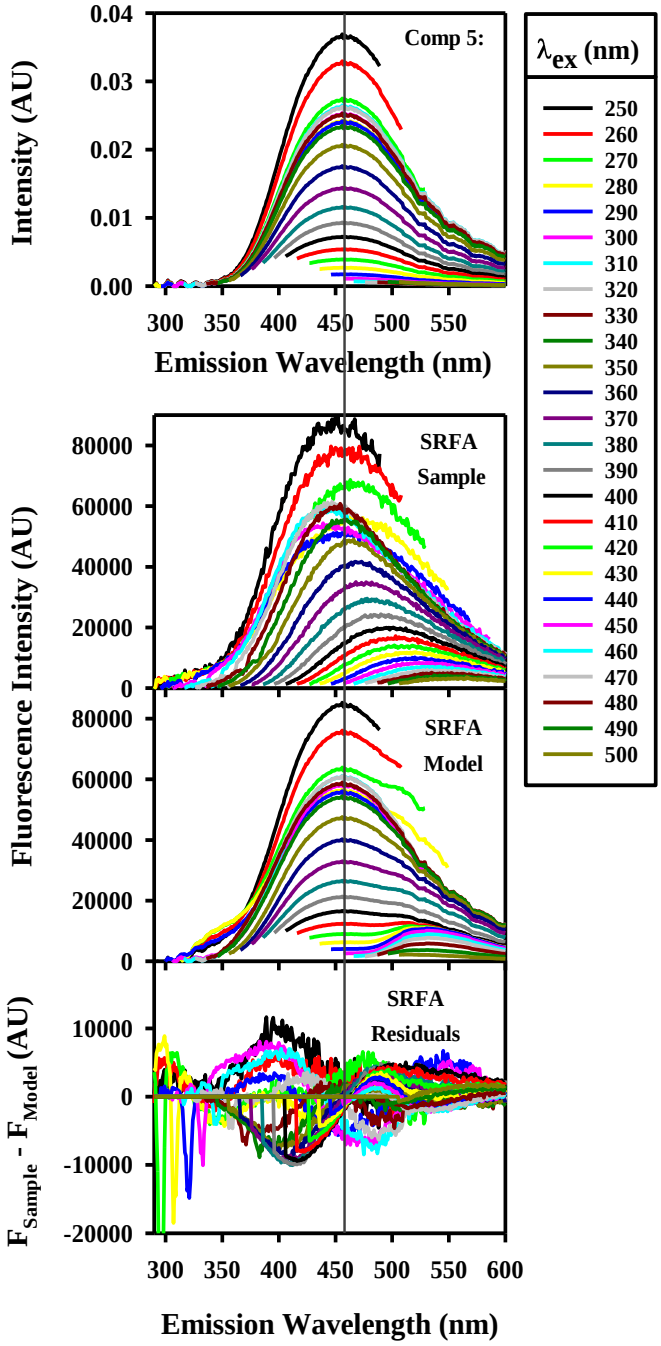

Figure 6.5: Emission spectrum for: **a**) component 5, **b**) the SRFA sample input into PARAFAC model, **c**) the final PARAFAC model for the SRFA sample and, **d**) the residual emission which is the emission from the sample not accounted for by the model.

However, component 1 is modeling riboflavin thus does not properly model the long wavelength emission from SRFA. (Fig. 6.5)

Due to this limitation, the modeling of SRFA could be influenced significantly by the other samples included in the dataset. For this model the dataset included SRFA and 5 other model compounds thus the spectrum of the model compounds influenced the modeling of the pure SRFA sample. This shows that how an individual sample such as CDOM from natural waters gets modeled by PARAFAC could be significantly influenced by the other samples included in the dataset.

6.3.3 Pyrene and its excimer

Pyrene was used to test how PARAFAC deals with excited state interactions. At low concentrations of pyrene only monomer emission is observed. However, with increasing concentration emission from the excimer (excited state dimer of pyrene) increases and monomer emission decreases. To test how excimer formation or the presence of interacting compounds may impact a PARAFAC model, a dataset with varying concentrations (0.09 – 6.0 mM) of pyrene was tested (Table S6.4, and Fig S6.12). The final PARAFAC model had two strongly correlated components (Table 6.1): one component that modeled the monomer and another that modeled a mixture of the monomer and excimer (Fig. 6.6). Examining the Fmax values for this dataset does clearly show that with increasing concentration of pyrene the contribution of the component associated with the mixture of monomer and excimer increases which is in line with the increased formation of the excimer (Fig. 6.7). This test indicates that if samples have interacting compounds the analysis with PARAFAC will be more complex and could result in strongly correlated components. Correlated components is often a cause for decreasing the number

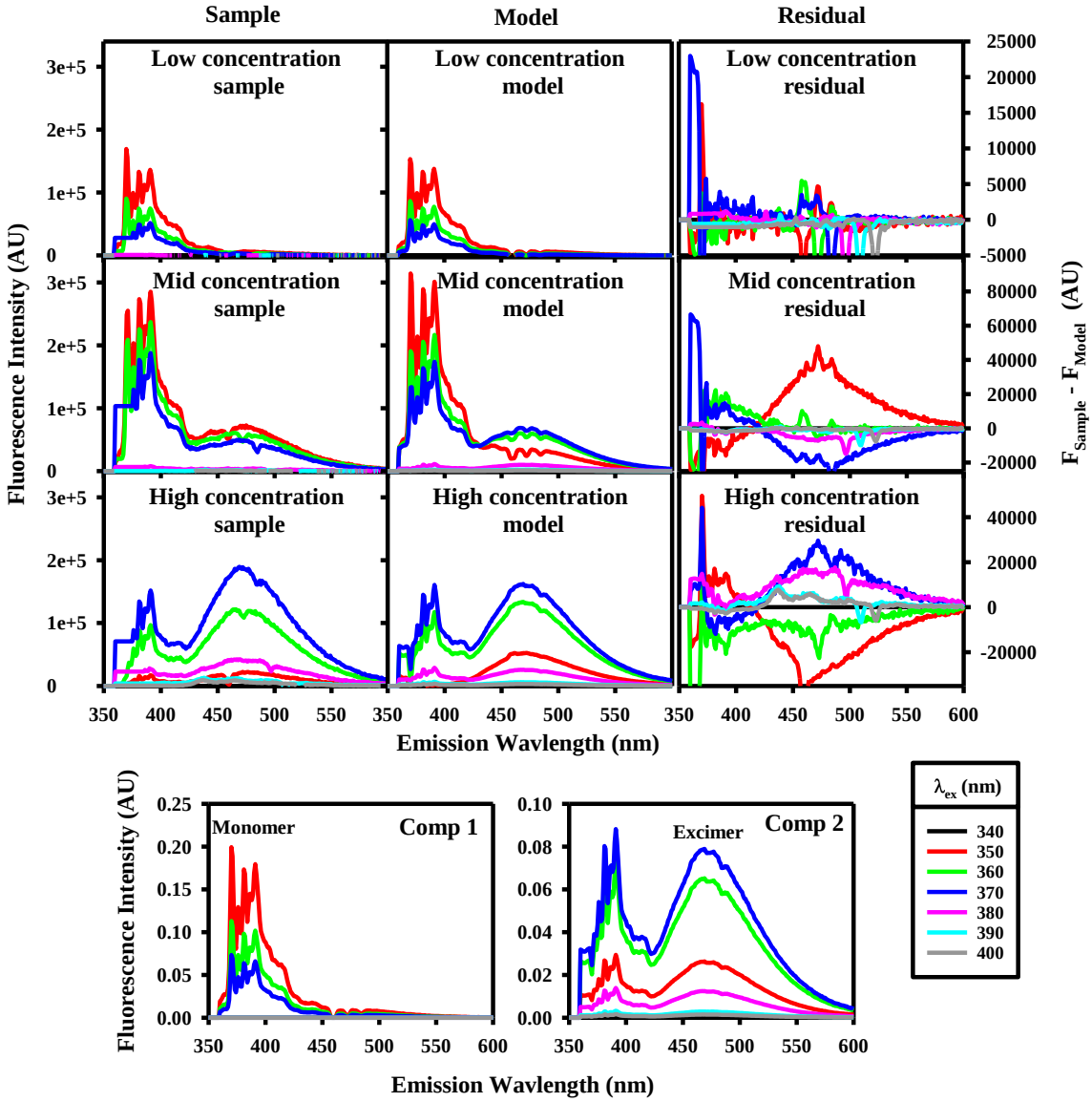

Figure 6.6: EEMs for the (**left**) samples, (**middle**) models and (**right**) residuals of select samples from the Pyrene PARAFAC model at (**top**) low, (**center**) mid and (**bottom**) high concentrations. As well as the emission spectra for components 1 and 2 for the final PARAFAC model for this dataset.

of components used to model a dataset because correlation between two or more components would violate the assumption that all components should be variable. The formation of the pyrene excimer can be easily understood and could be accounted for in a model, but more complex interactions such as those thought to exist in CDOM could prove

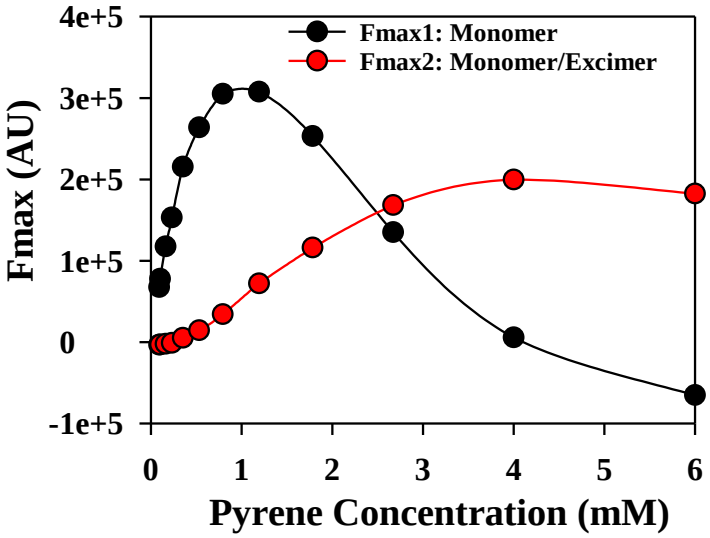

Figure 6.7: Fmax scores for components 1 and 2 with increasing concentration of pyrene in solution.

to be very detrimental to the modeling process, and cause the PARAFAC model to lose its meaning.

6.3.4 Reference materials

A dataset comprised of the EEMs of reference materials (SRFA, SRHA, PLFA, LHA, ESHA, and LAC) dissolved in purified water collected at three pHs (pH 3, 7 and 10) both before and after $NaBH_4$ reduction was tested to further probe the modeling of humic and fulvic acids by PARAFAC (Table S6.5 and Fig. S6.16). For each sample, solutions of different concentrations (~3 to 100 mg L^{-1}) were employed to obtain emission spectra across the UV and visible wavelengths with high signal to noise ratios, while maintaining optically thin conditions (absorbance at excitation wavelength $\leq$ 0.1 AU). Then the individual spectra were normalized for concentration and combined to create one EEM. .For this dataset a six component model was found to be ideal (Table 6.1).

The humic substances samples are made from extracted material and there are no major bands or shoulders observed in the EEMs; instead there is a continuously red shifting

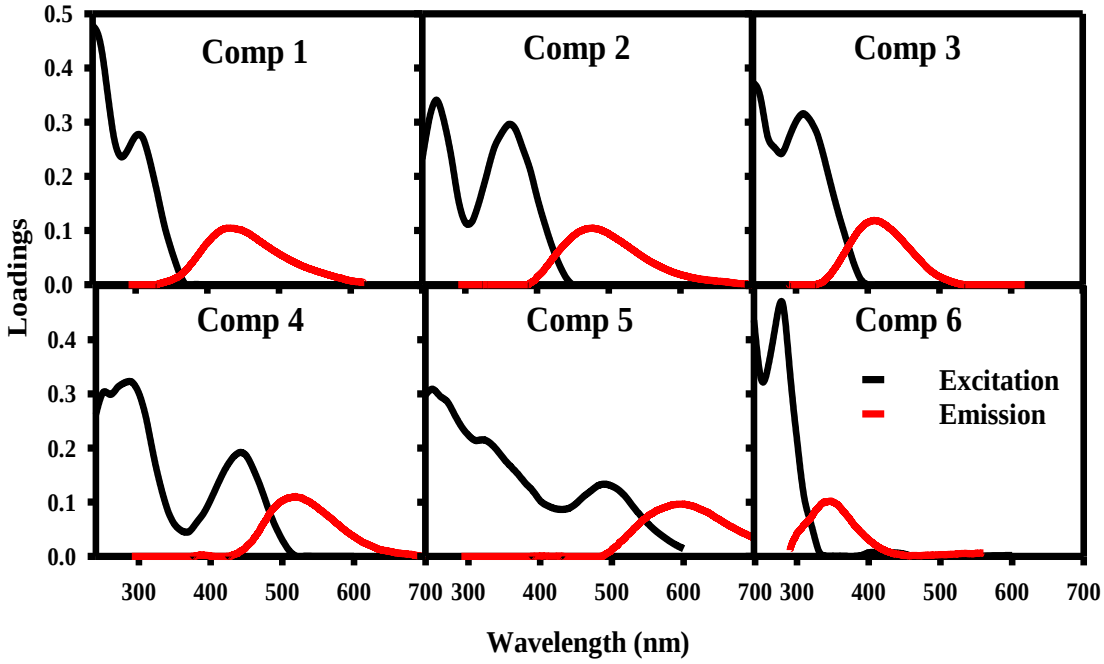

Figure 6.8: Excitation (**black**) and emission (**red**) spectra for the six component PARAFAC model generated for the reference material dataset.

emission maxima and decreasing emission intensity with increasing excitation wavelength. All of the modeled components were very broad with the exception of component six (Fig. 6.8). Although, the components contributed differently to each of the reference materials, no components were unique to one reference material and almost all of the reference materials contained all six components (Fig. 6.9). These components were most likely influenced by local emission maxima in the untreated and reduced samples for the different reference materials.

The model did not show any major differences between the untreated and reduced sample emission. Upon reduction, it has been shown that the fluorescence emission of humic and fulvic acids is enhanced and blue-shifted[46,56,57,68]. For each reference material the Fmax of each component did increase following reduction (Fig. 6.9), which is in line with the enhanced emission seen in reduced samples, but the same components are

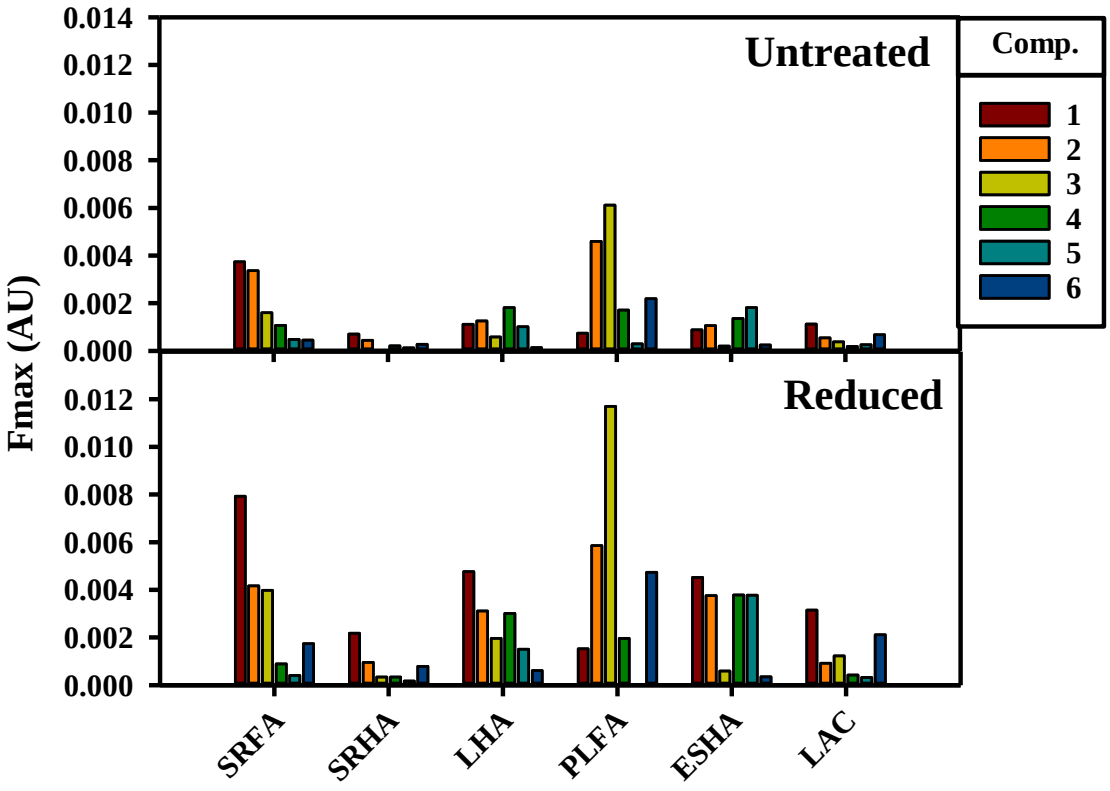

Figure 6.9: Fmax scores for components 1-6 for the reference material PARAFAC model.

identified in both untreated and reduced samples. Also there are no components that are unique to particular pHs and overall there is little to no changes in the distribution of components with change in pH. This indicates that the PARAFAC model is not picking up on the slight changes in the emission structure following reduction or change in pH. Overall the components and model provided by the PARAFAC tool did not provide any meaningful information about differences in structure of the reference materials. Using PARAFAC to try and improve the chemical interpretation of this dataset is also limited because the loadings themselves are not very physically meaningful. Most loadings have large overlaps between the excitation and emission spectra, which again is most likely a result of the PARAFAC tool's inability to model interacting fluorophores.

6.3.5 Environmental samples

Several datasets containing natural water samples were analyzed with the PARAFAC tool to test how well it modeled environmental samples. Several modifications (filtration, and $NaBH_4$) were made to the sample to test the impact that they would have on the model. One final dataset that was used to probe the PARAFAC tool comprised of emission scans of a Sargassum exudate collected at different time points during an irradiation experiment.

The first test on environmental samples was on natural water collected from the NPO separated into two datasets: one for untreated samples and the second for $NaBH_4$ reduced samples (Table S6.6 and S6.7, and Fig S6.20 and S6.24). The ideal number of components for both the untreated and reduced datasets was chosen to be four (Table 6.1). Two of the components (1 and 4) modeled unique UV emission bands seen in most of the samples. Component 3 modeled an emission band centered at ~400 nm present in several of the natural water samples. Thus, component 2 is an attempt to model the longer wavelength red shifting emission, but it has a constant emission centered around ~470 nm. (Fig 6.10) Components 1, 3 and 4 are most likely accurately modeling discrete groups of fluorophores such as proteins or local in situ source material, and are being correctly identified in the NPO samples. Component 2 clearly does not appropriately model the "humic like" emission seen in all of the NPO samples and is being identified to try and provide a better fit for the samples. The excitation and emission spectra of component 2 are most likely not chemically meaningful and are instead a result of the model trying to account for the fluorescence arising from interacting fluorophores which, based on its operating principles, is not something PARAFAC is capable of. The loadings for

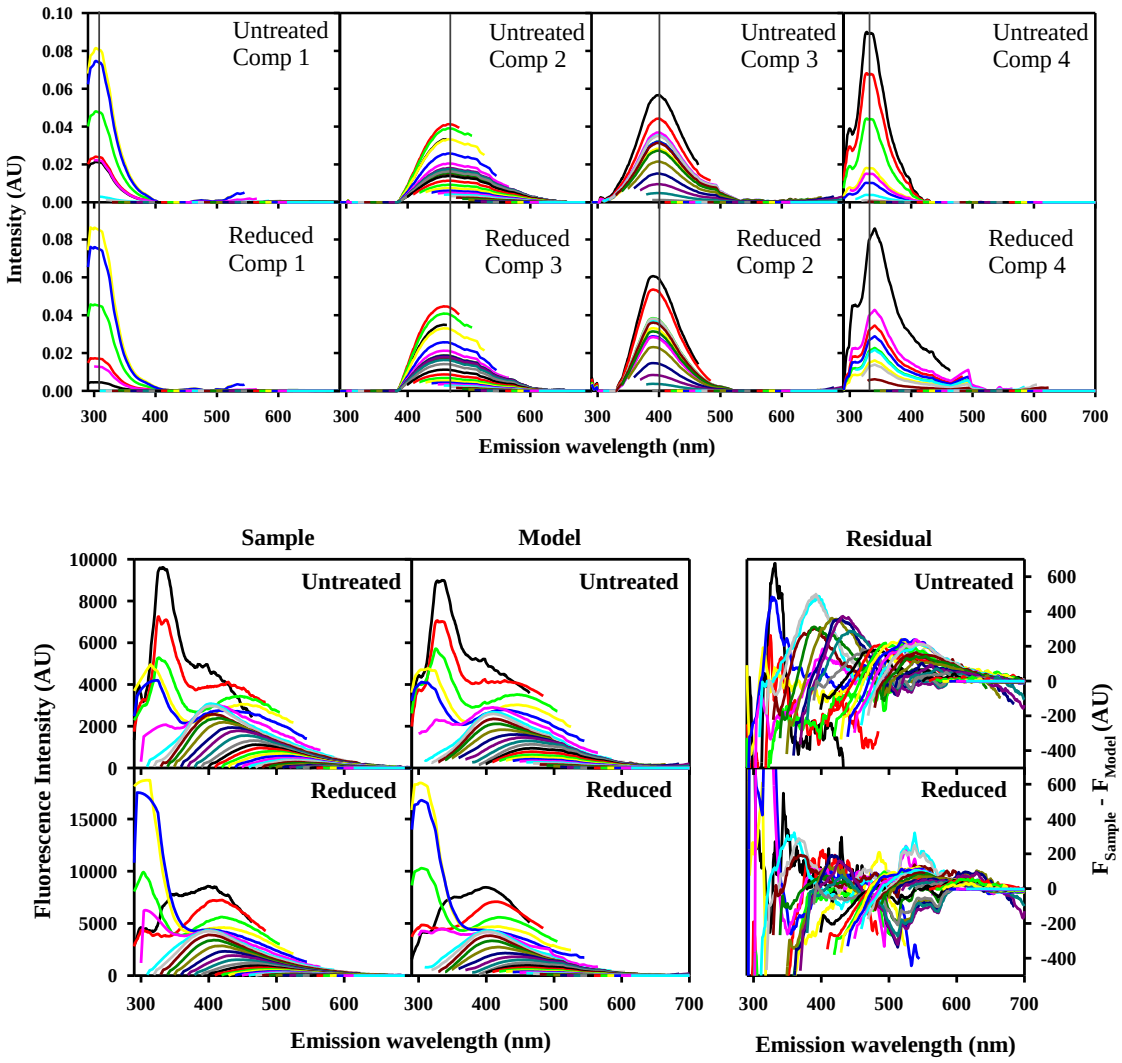

Figure 6.10: (**top**) PARAFAC components for both the untreated and reduced models, and (**bottom**) emission spectra for the (**left**) sample, (**middle**) model, and (**right**) residual for both an untreated and reduced NPO sample.

component 2 also show the largest overlap between the excitation and emission spectra with ~100 nm overlap. It is clear from the residuals for both the untreated and reduced sample that the model is not accounting for the red shifting emission and instead is trying to fit the data to a strict superposition of individual fluorophores.

When comparing the untreated dataset, to the reduced dataset minimal differences in the four components are present. There is a slight blue shift in components 2 and 3 which is the correct trend seen following reduction, but the degree of the shift is less than that

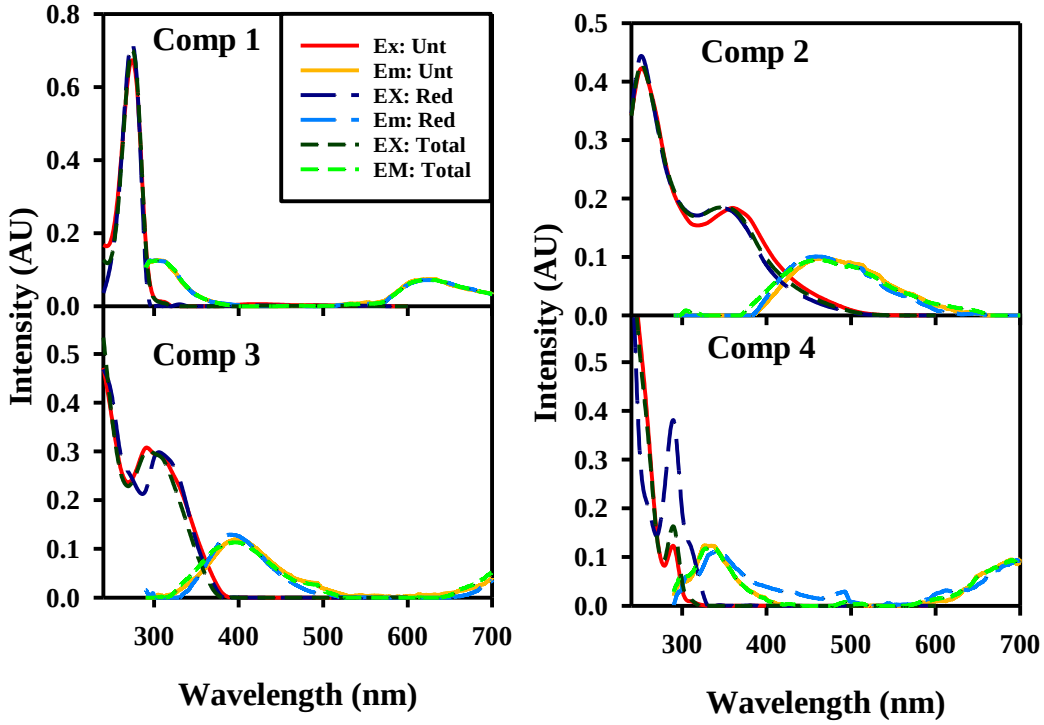

Figure 6.11: Loadings for components 1-4 for PARAFAC models containing untreated (**red and orange**), reduced (**light and dark blue**) and untreated and reduced (**light and dark green**) NPO samples.

seen in the sample data. Also, when the two datasets are combined and run as one, there are still only four components identified, indicating that PARAFAC is not able to pick up on the slight differences between the untreated and reduced sample emission as seen in the reference material dataset, thus demonstrating another limitation of the tool. (Fig 6.11)

From the NPO dataset it was clear that the PARAFAC tool was able to identify and isolate discrete bands. To further highlight the potential of PARAFAC to properly identify discrete bands, a test was performed using EEMs of both filtered and unfiltered natural water samples collected from the tributaries of the Chesapeake Bay (Table S6.8). The majority of the emission from the samples was that typical of river and bay waters with the wavelength of max emission staying fairly constant at short excitation wavelengths and the

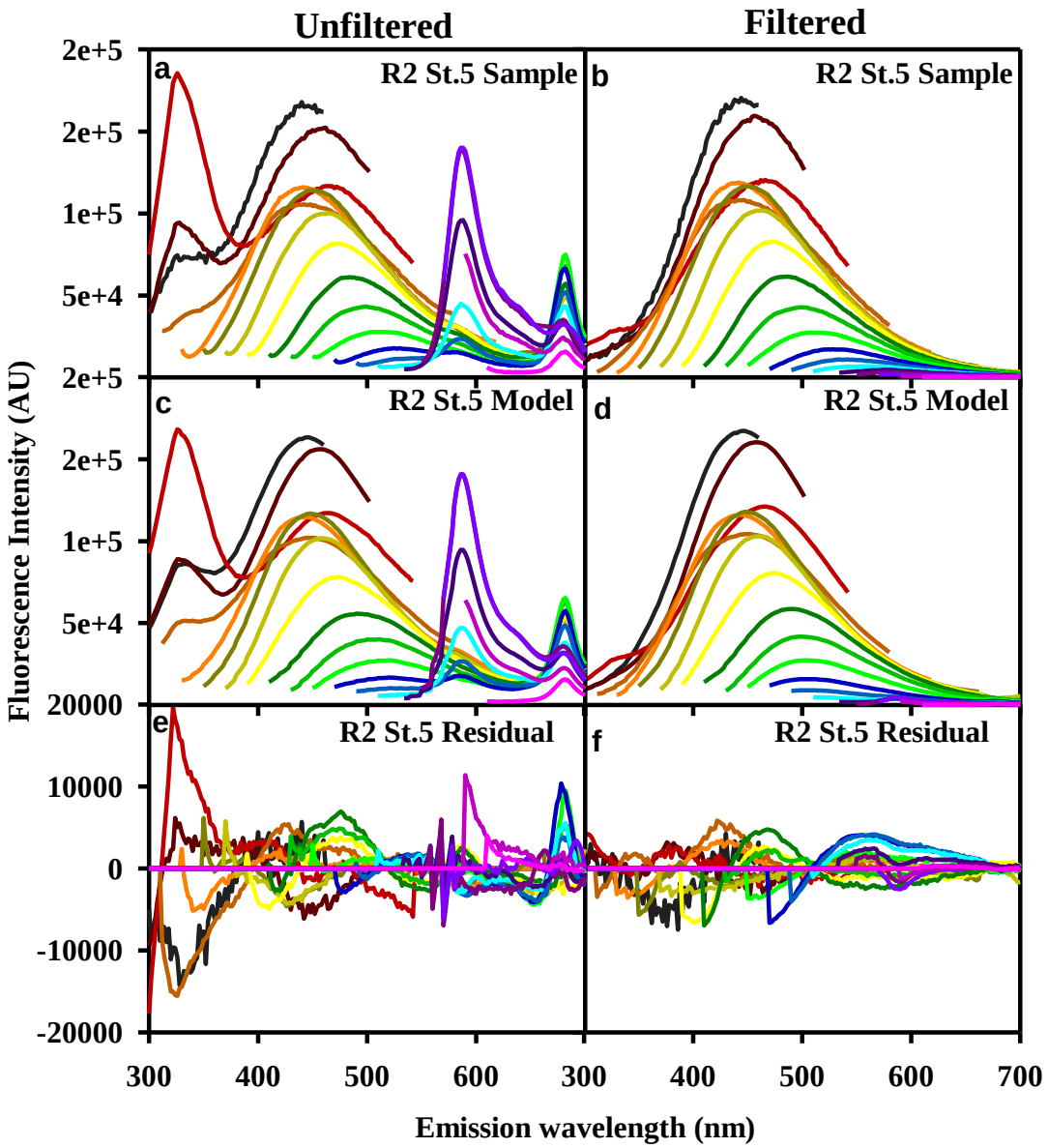

Figure 6.12: Sample emission (**a-b**), modeled emission (**c-d**) and residual (**e-f**) for an unfiltered (**left**) and filtered (**right**) natural water sample from station 5.

emission maxima continuously shifting to the red with increasing excitation wavelength ("humic like" emission: Fig S6.28 and Fig. 6.12 a-b). However, some of the unfiltered samples also had several unique emission bands. One discreet band was observed in the UV with peak emission occurring at $\lambda_{ex}/\lambda_{em}$: 280/330 while two bands were observed in the visible ($\lambda_{ex}/\lambda_{em}$: 440/680 and 550/590) (Fig. 6.12a). The PARAFAC tool identified

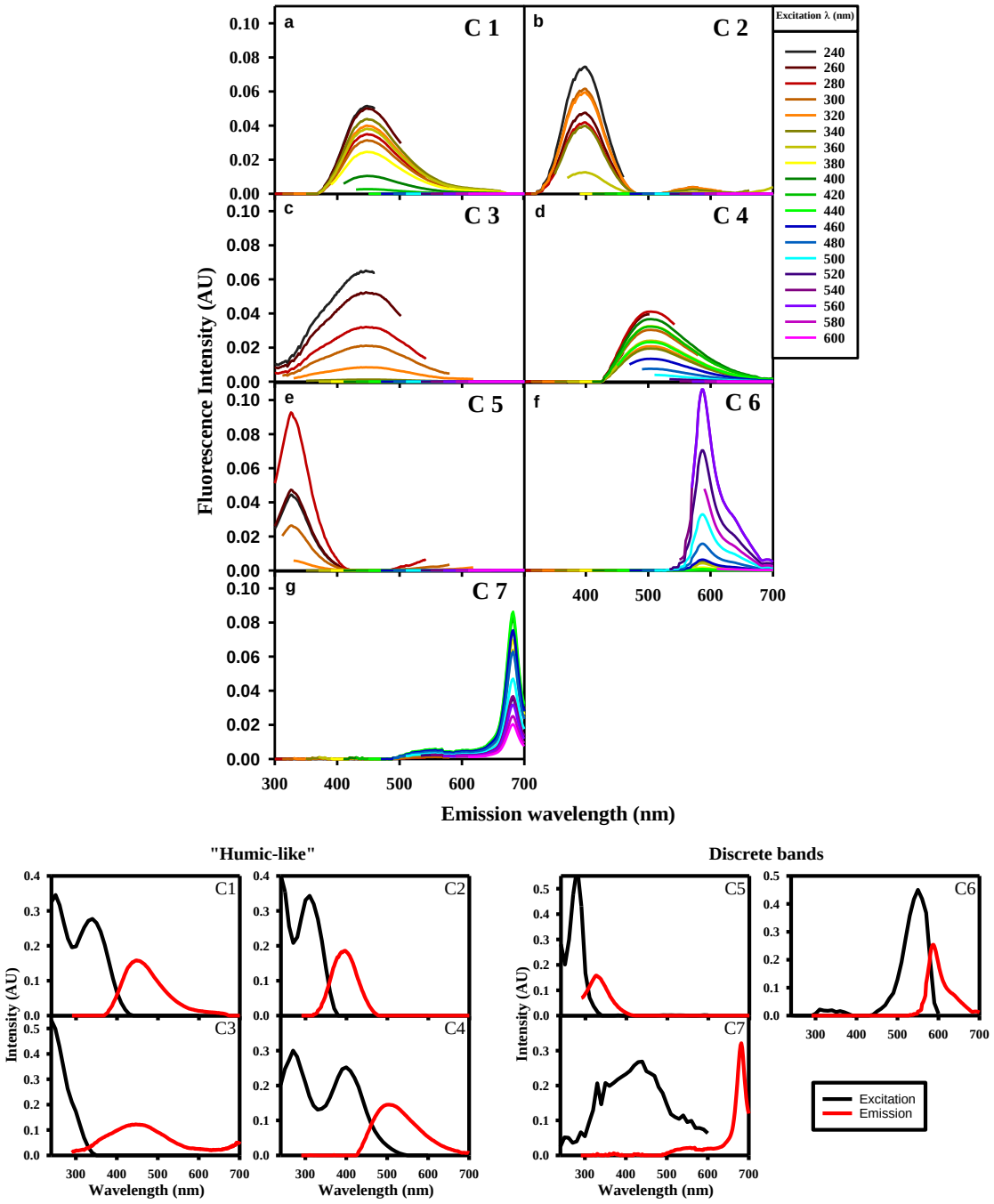

Figure 6.13: Components 1-7 for the PARAFAC model of the CB samples. (**Top**) Fluoresces emission spectra for components 1-7 with increasing excitation wavelength. (**Bottom**) loadings for components 1-7 for the PARAFAC model, excitation (**black**) and emission (**red**) spectra for the seven component PARAFAC model.

seven components for this dataset (Fig. 6.13a-g) with 99.8% of the data explained (Table 6.1). Four components (1-4) modeled the more "humic like" emission while the other three

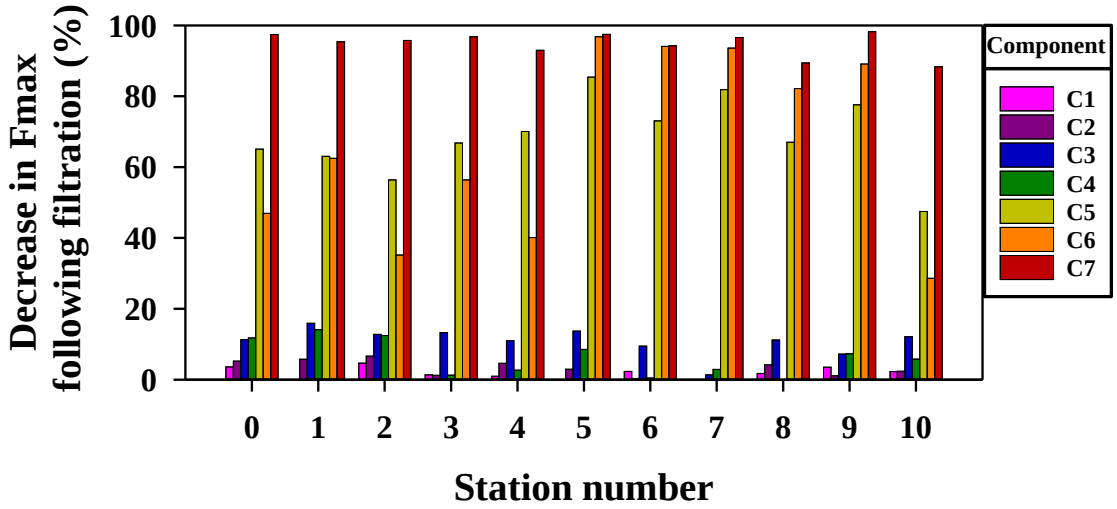

Figure 6.14: Percent change in Fmax for each component (1-7) following filtration.

components (5-7) modeled the discrete bands. The seven component model thus did successfully account for each of the discrete bands and identified them as individual components.

The discrete bands present in some samples were almost completely eliminated from the EEMs following filtration, while the "humic like" emission was unchanged. By comparing EEMs for the same sample before and after filtration the ability of PARAFAC to pick the unique bands and model the "humic like" emission was examined. Following filtration the Fmax for components 1-4 did not change, while the Fmax for components 5-7 were significantly decreased (Fig. 6.14). This suggests the PARAFAC tool was able to identify the discrete bands and indicate their presence or absence in a particular sample and components 1-4 did not interfere with the unique bands. Thus using PARAFAC to track or monitor the presence and intensity of unique bands would be an ideal use for this tool especially in large data sets where the time needed to perform detailed analysis of each individual EEM would become prohibitive.

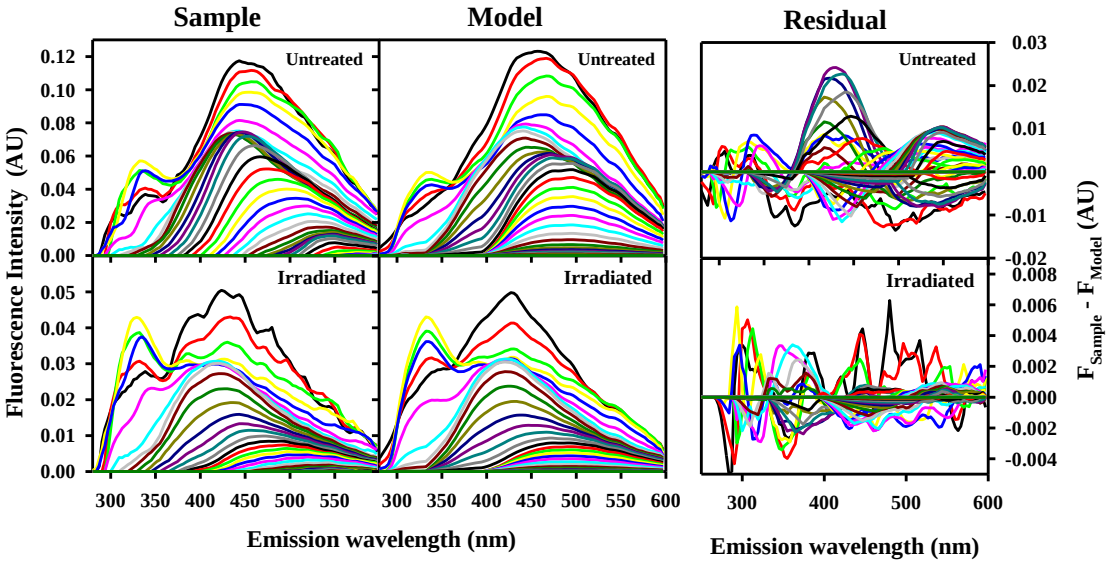

Figure 6.15: EMMs for (**left**) sample, (**middle**) model, and (**right**) residual, for both an (**top**) untreated and (**bottom**) irradiated sample included in the Sargassum dataset.

Despite the proper isolation of the unique bands PARAFAC assigned four components to model the "humic like" emission due to the fact that it cannot account for the red shifting emission. Thus components 1-4 are not truly identifying unique fluorophores or classes of compounds instead they are an attempt to model the continuously red shifting emission.

The last dataset compiled to test the PARAFAC tool included emission scans of a Sargassum exudate at different time points during an irradiation experiment (Fig. S6.32, and 6.15). This dataset is a bit different from the others because only one sample was used so the variability in the EEMs only came from the treatment applied (irradiation). A four component model was found to be ideal for this dataset, but there was high correlation between components (Table 6.1), which could be anticipated due to the nature of the EEMs in the dataset. Although four components were identified the chemical significance of these components is questionable. This is due to the large degree of overlap between the

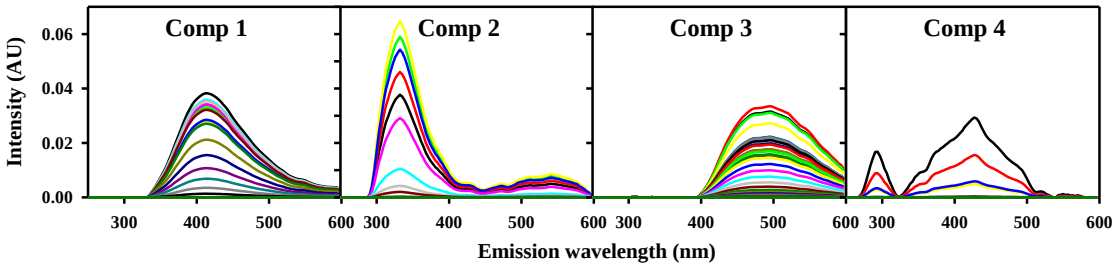

Figure 6.16: Components 1-4 for Sargassum PARAFAC model.

emission and excitation spectra in several of the loadings and several of the components have two distinct emission peaks (Fig. S6.34 and 6.16). These loadings are thus not photo-physically correct if the component is modeling a single fluorophore or group of fluorophores with similar emission. Also the PARAFAC model again failed to account for the red shifting emission which can be clearly seen when comparing the sample and the modeled emission (Fig. 6.15). However, PARAFAC analysis of the EEMs did show some interesting trends and provide some information that could be helpful when analyzing this dataset. With increased irradiation time, the Fmax for components 1 and 3 decreased

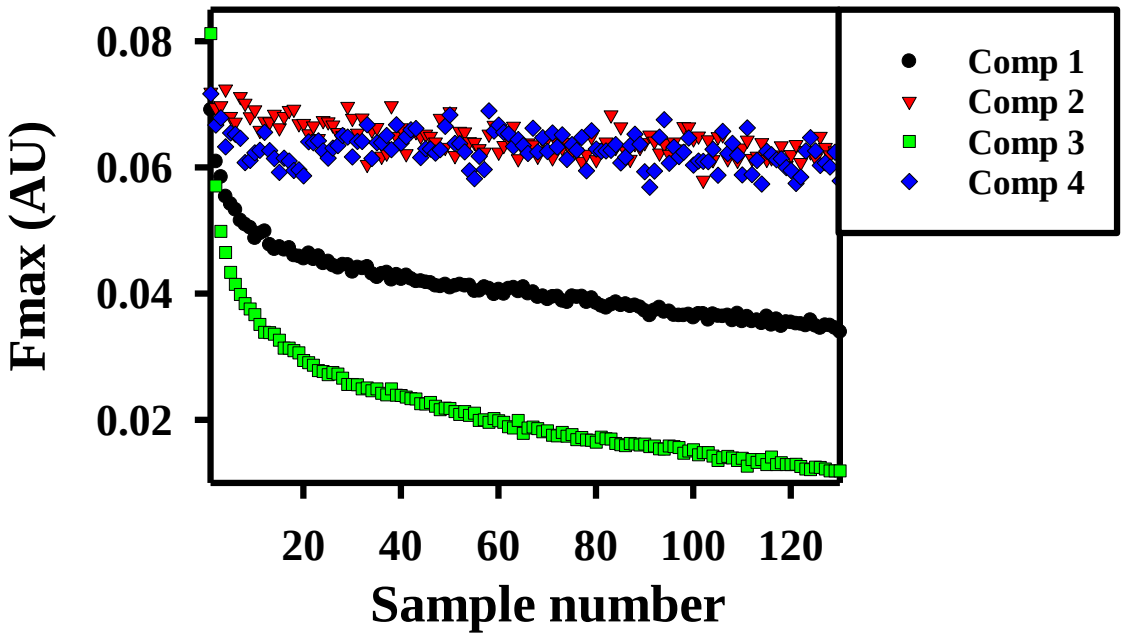

Figure 6.17: Fluorescence intensity at the maximum (Fmax) for component 1-4 for the Sargassum dataset with increasing sample number indicating increasing irradiation time.

significantly (50% and 85% respectively) while components 2 and 4 were relatively unchanged (Fig. 6.17). This would imply that there are very different chemical structures present in the sample that are impacted by irradiation differently. Therefore, PARAFAC was able to indicate sections of the EEMs that were more or less affected by irradiation, even if the emission of the identified components is not overly meaningful chemically.

6.4 Conclusion:

6.4.1 Uses for and limitations of PARAFAC analysis

The main goal of these tests of the PARAFAC tool was to identify situations in which PARAFAC could be useful as well as situations in which it may add more confusion instead of clarification to a dataset. As have been seen in many studies, and by the tests performed here, PARAFAC analysis works well when there are discrete bands and when samples include non-interacting fluorophores. The ability of PARAFAC to properly distinguish between discrete bands and the more "humic like" fluorescence means that it could be used to track the presence or absence as well as intensity of these discrete components in environmental samples. However, PARAFAC's inability to model interacting fluorophores means that it often provides components that are not physically reasonable when modeling the more "humic like" emission seen in most FDOM samples collected from natural waters from rivers to open oceans. The red shifting emission is not modeled and the loadings provided by the PARAFAC tool do not provide insights into the structure or chemical makeup of the samples. This would suggest that PARAFAC should be used only to separate the distinct bands such as the UV bands seen in many of the NPO samples from the visible "humic like" emission.

Chapter 7: Conclusion and future work.

7.1 Conclusions:

Originally, experiments were conducted on natural waters using minimal measurements such as select optical values or indexes, which often led to confusion due to the limited dataset examined. With the chemical tests described in this thesis (pH titration, and $NaBH_4$ reduction) and a more uniform way of examining the optical properties of CDOM samples, more reliable and meaningful structural information can be gathered. $NaBH_4$ reduction highlighted the significant influence that ketones and aldehydes had on the optical properties of CDOM samples from all locals. At the same time, pH titrations indicated a sizable phenolic contribution to the optics and the presence of carboxylic acids in all samples.

Samples studied thus far have led to two main conclusions: 1) samples from riverine and coastal areas to open oceans share many of the same optical and chemical properties suggesting structural similarity as well as a possible terrestrial component to CDOM even in the open ocean; 2) the optical properties and responses to chemical tests do not fall in line with a superposition model but instead suggest the presence of electronic interactions.

The optical properties of natural water samples and C18-OM extracts from the NPO, EAO and MAB all contained a "humic-like" component that exhibits very similar properties to those observed for terrestrially-dominated aquatic environments. The main differences in the absorbance and fluorescence emission of the open ocean samples were seen in the more unique absorbing and emitting bands that were predominantly located in the ultraviolet. Tracking the emission of these unique bands may be an appropriate use for PARAFAC as shown in chapter 6. Further evaluation of these samples using chemical tests

continued to indicate significant structural similarities in all samples. pH titration, and $NaBH_4$ reduction provide valuable information about the structures present in CDOM that influence the optical properties. Conducting these tests on reference materials, natural waters and extracted DOM indicated that reducible groups such as ketones and aldehydes as well as deprotonatable groups such as carboxylic acids and phenols contribute significantly to the optical properties of CDOM in all samples examined independent of location.

The optical properties and chemical responses of the CDOM samples from all geographic locals are highly comparable, indicating that there is a terrestrial source of CDOM throughout the aquatic environment. Although photodegradation and microbial degradation influences the structure of CDOM in the environment there appears to be a pool of CDOM that is not easily degraded (possibly modified lignin) and this fraction remains in the open ocean. This along with deep ocean currents would explain the high degree of similarity in all deep open ocean samples evaluated. Having a more complete view of the changes in CDOM throughout the aquatic environment will provided a way to estimate what changes in certain CDOM sources may do to the larger CDOM pool. If, as this work suggests there is a significant terrestrial component to CDOM in the open ocean, changes in river discharge would have a significant impact on CDOM in the ocean. With current climate change droughts and flooding as well as changes in land use can significantly impact the CDOM exported to the ocean and thus will impact the CDOM present in the open ocean.

An electronic interaction model is not only able to better explain the long wavelength absorbance and florescence emission that is continuously redshifted, but it is

also supported by the results of $NaBH_4$ reductions, and pH titrations. Following reduction there is preferential loss of long wavelength absorbance, but the aromatic ketones and aldehydes thought to be present in CDOM do not absorb in the visible. This means that the loss of absorbance in the visible cannot be accounted for solely by the removal of these ketones and aldehydes, but instead could be due to the loss of charge transfer interactions. Reduction also cause enhanced and blue shifted fluorescence emission which can be attributed to increased emission coming from donor compounds (aromatic carboxylic acids and phenols) that are no longer part of charge transfer complexes and are thus no longer quenched. pH titration of CDOM samples shows increased absorbance at all wavelengths. This is inconsistent with a superposition model in which there would be enhancement in the absorption from the conjugate base, but decreased absorption from the acid form. However, a net gain in absorption at all wavelengths suggests that there are other factors in play, especially since the enhancement in the absorption with increasing pH extends into the visible where neither phenolate anions or carboxylate anions absorb.

Finally, the absorption lost following reduction is coupled to the enhancement in absorption with increasing pH. Two observations lead to this conclusion. First the broadband absorption that is significantly enhanced with increasing pH is highly attenuated following reduction, and with increasing pH this loss of broadband absorption due to reduction increases. These results can be explained by electronic interaction, because as phenols and carboxylic acids (thought to act as electron donors) are deprotonated they become better electron donors and thus would enhance charge transfer interactions giving rise to the broadband absorption increase seen with increasing pH. Also following reduction there are fewer acceptors available due to the reduction of ketones and aldehydes so having more

efficient donors does not impact the absorbance as significantly causing the enhancement with increasing pH seen in the untreated sample to be highly attenuated. All of these results point to an electronic interaction model being a more complete explanation of the optical properties of CDOM samples.

At the same time that the optical properties of these CDOM samples were being investigated, high resolution mass spectra were also collected on both untreated and $NaBD_4$ reduced samples. This work is currently being completed by Marla Bianca, and will be combined with the optical properties to further probe the structures present in DOM/CDOM. Combining both optical measurements as well as mass spectra, a more complete view of DOM/CDOM can be developed. So far the mass spec results are in line with the optics and chemical tests; showing high degrees of similarity in the NPO and in all deep ocean samples with respect to molecular formula as well as the degree of reduction. Also, the transect from the Delaware River to the MAB did show a high degree of overlap in m/z ratio, there are some very notable changes just as seen with the optics and chemical tests. The combination of optical and chemical tests with high resolution mass spec to the analysis DOM/CDOM samples from the environment provides a more complete view of the samples and their structure and sources.

If, as these results suggest there is a significant terrestrial component to the CDOM in the open ocean

7.2 Future work:

7.2.1 Expansion of samples investigated

Evaluating the optical and chemical properties has proven to provide informative data on the sources and structure of CDOM in the environment. Thus now that a more

complete system for analyzing CDOM samples has been tested the next step would be to apply these techniques to other environmental samples. This would allow for the evaluation of fluctuations in sources and structure with location as well as time.

Other discrete sources of CDOM could also be tested using these same methods just as the mangroves leaves were examined. Testing point sources could help to pin down the cause of some differences in the optics and response to chemical tests see in different geographic locals.

On top of testing other samples more detailed fluorescence measurements could be conducted on existing and future samples. The change in fluorescence emission with increasing pH should be evaluated for natural water samples and C18-OM extracts.

Finally reduction and pH titrations should be applied to model compounds as well as mixtures of compounds to further test the superposition and electronic interaction model. Compounds such as guaiacyl and syringyl phenols that are known to be related to lignin could be tested individually and in mixtures to examine the optical and chemical properties. These results could then be compared to reference materials from the IHSS as well as natural waters and extracted CDOM samples.

7.2.2 Further tests

Deep and surface natural water samples from the open ocean did display some different responses to reduction and pH titration and some of these differences may be related to photodegradation. Preforming irradiations on deep water samples could be used to test if photodegradation does account for changes in the surface samples. Irradiating deep water samples for varying amounts of time and checking the optics and chemical responses could provide more information as to the root of the differences.

Dithionite reductions should also be performed on samples from all locations in order to estimate the contribution of quinones to the optical properties and structure of CDOM samples. $NaBH_4$ reductions probe the contribution of aldehydes and ketones, but quinones are reversibly reduced and thus after exposure to air their contribution is not accounted for. Preforming dithionate reductions under nitrogen would make it possible to better evaluate their contributions.

Size exclusion chromatography paired with the optical and chemical testes detailed in this thesis could also provide more information about the differences in CDOM from riverine to open ocean environment. The size distribution before and after photobleaching could also be evaluated.

Supplemental

S1 - Supplemental Chapter 1:

The change in fluorescence emission with increasing pH is a more complex than the changes in absorbance and for the reference materials it was suggested that it could indicate structural reorganization of the humic substances.[58]

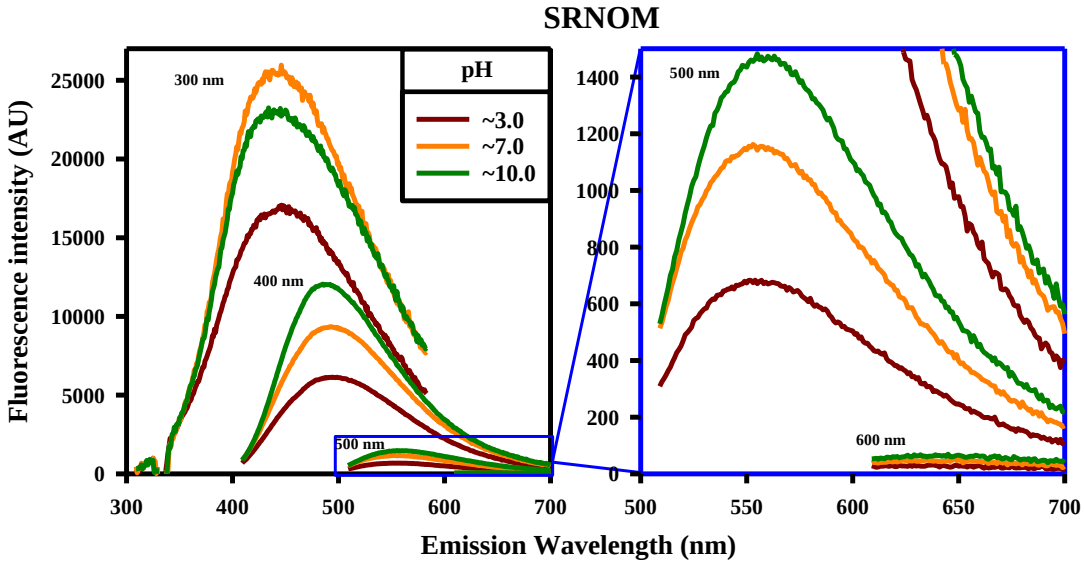

Figure S1.1: pH dependence of the fluorescence emission intensity for an SRNOM solution pH 2.0 (**red**), 7.0 (**orange**) and 10.0 (**green**). Emission recorded every 1 nm and excitation every 100 nm (indicated by black labels).

S2 - Supplemental Chapter 2:

Non-linearity is known to be a problem with setups like the WPI ultrapath, thus detectors integration time as set so that the obtained signal does not exceed 70-80% of the full scale. To test that changes in intensity due to the use of salt solutions does not produce non-linearity, the integration time was set to give a max intensity of 50 % and then adjusted to give 70% max intensity for purified water. The spectrum of the salt solutions were then tested under both conditions and were unaffected. Given here is the data collected for cell V (~50 cm). The integration time was set to 760 ms to achieve 70% as well as 540 ms to achieve 50 %.

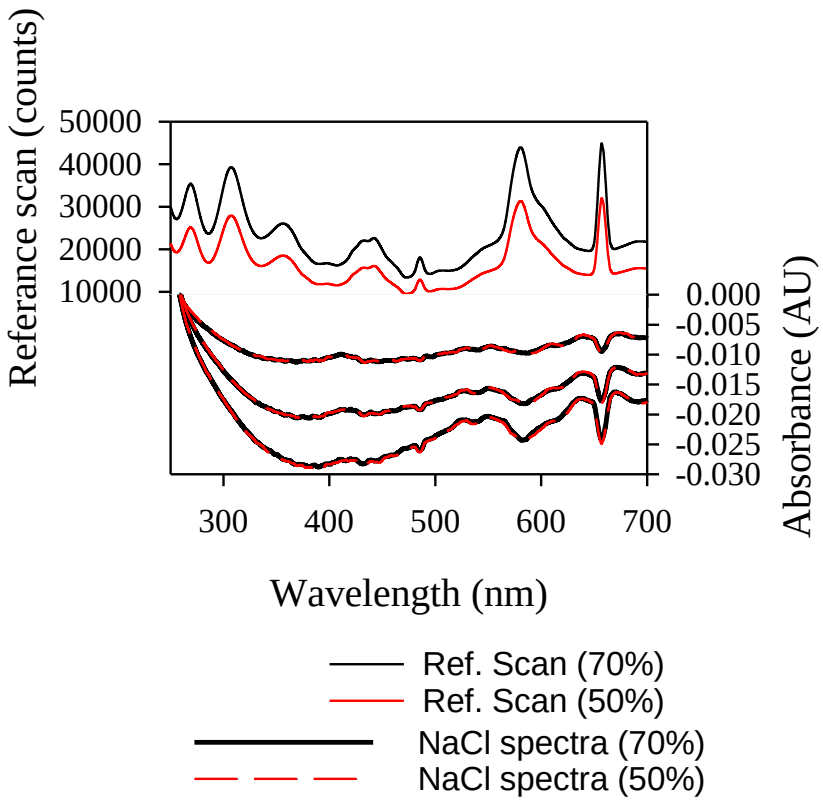

Figure S2.1: (top) lamp intensity using both 540 ms (**red**) and 760 ms (**black**) integration time. (**Bottom**) Absorption spectra of NaCl solutions using both integration time 540 ms (**red**) and 760 md (**black**).

S3 - Supplemental Chapter 3:

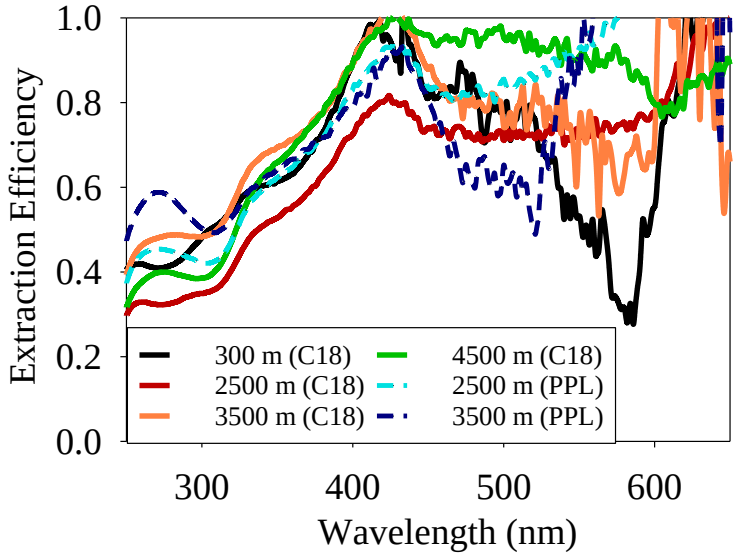

Figure S3.1: Extraction efficiency comparison between C18 and PPL resin.

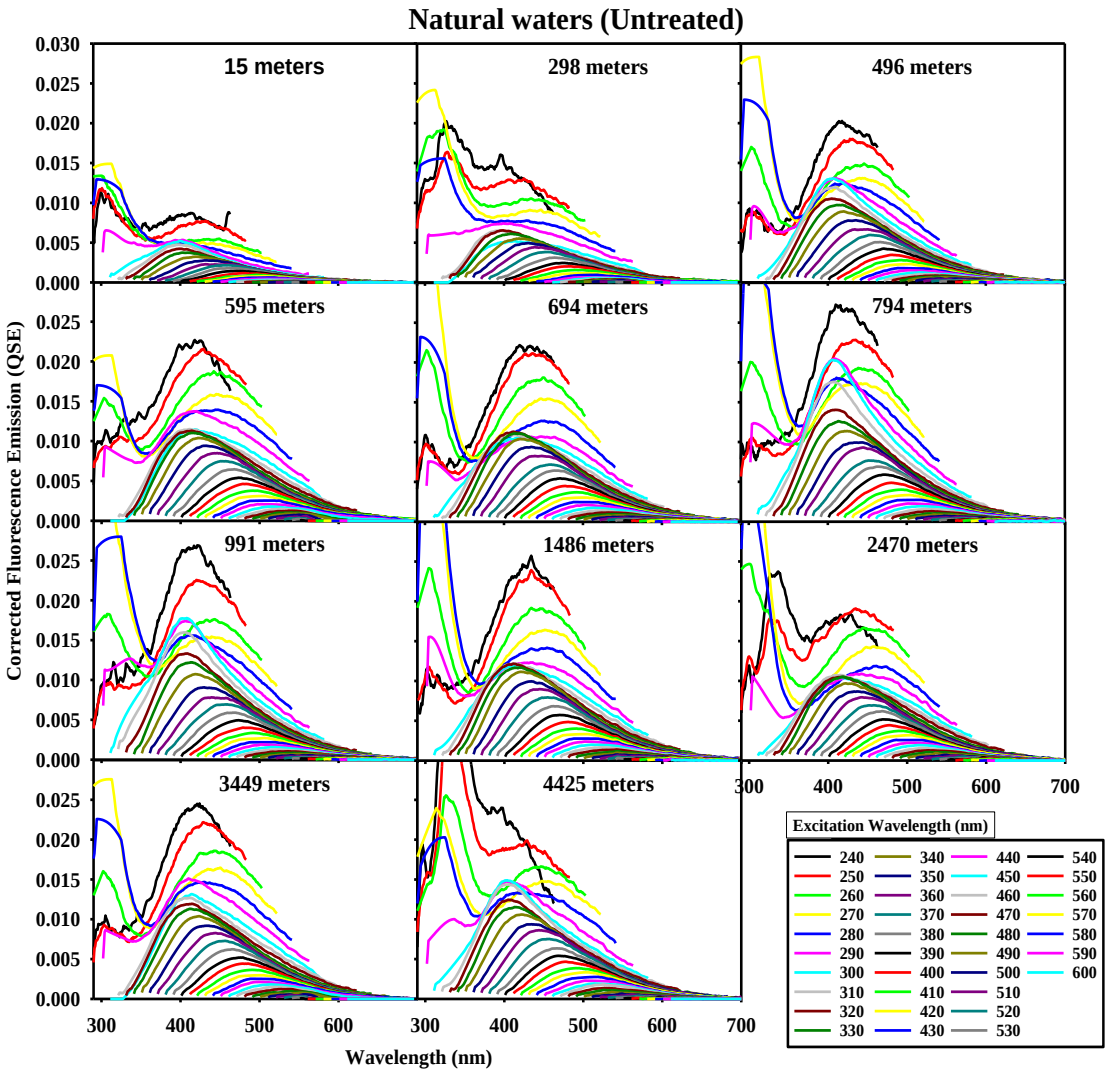

Figure S3.2: Depth dependence of EEMs for CDOM samples collected at Station ALOHA.

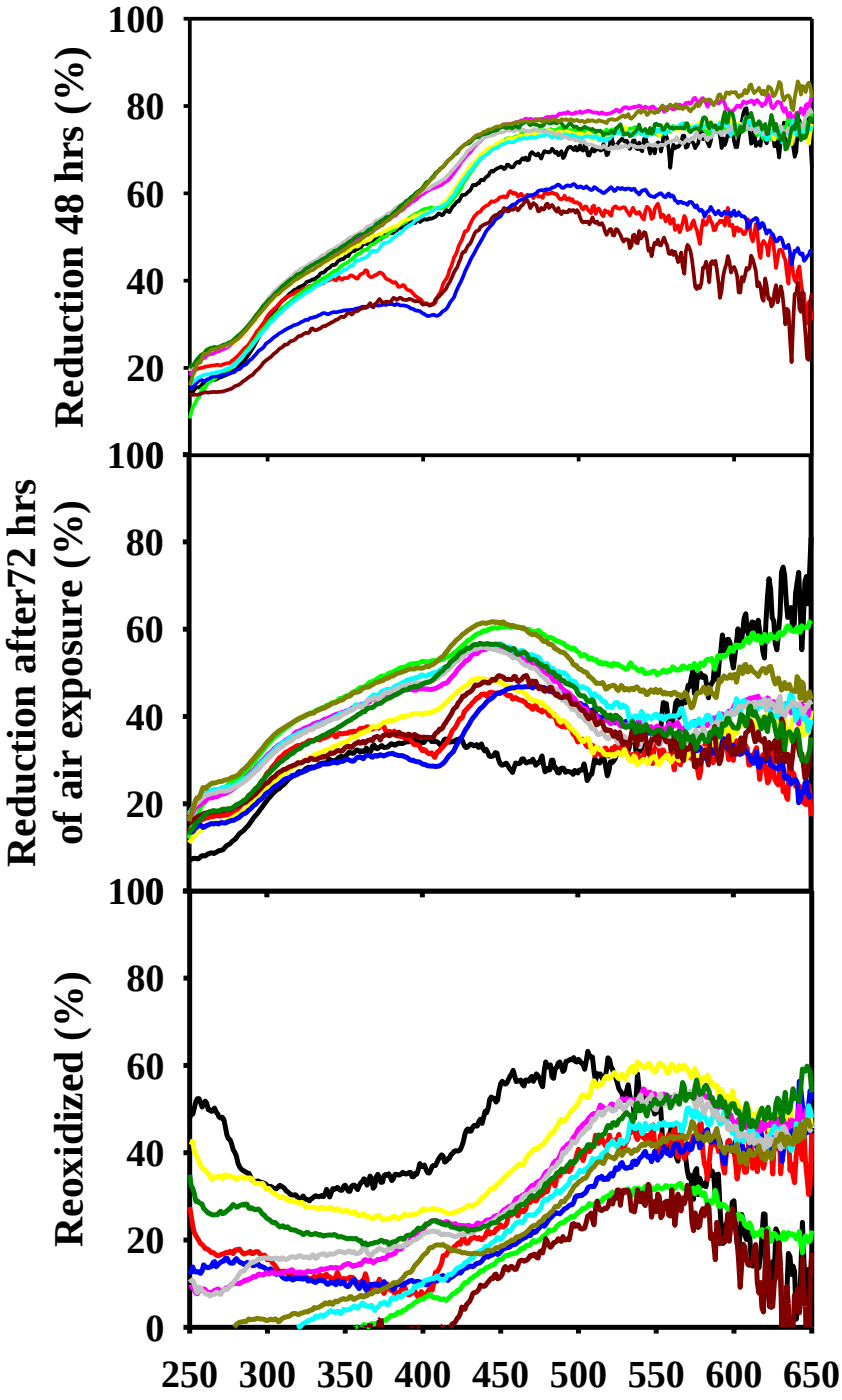

Figure S3.3: Percent absorbance loss following reduction with NaBH4 after 48 hours (**top**) and then the same reduced sample after 72 hours of air exposure (**middle**). Percent absorbance recovered following air exposure for 72 hours after a 48 hour reduction (**bottom**).

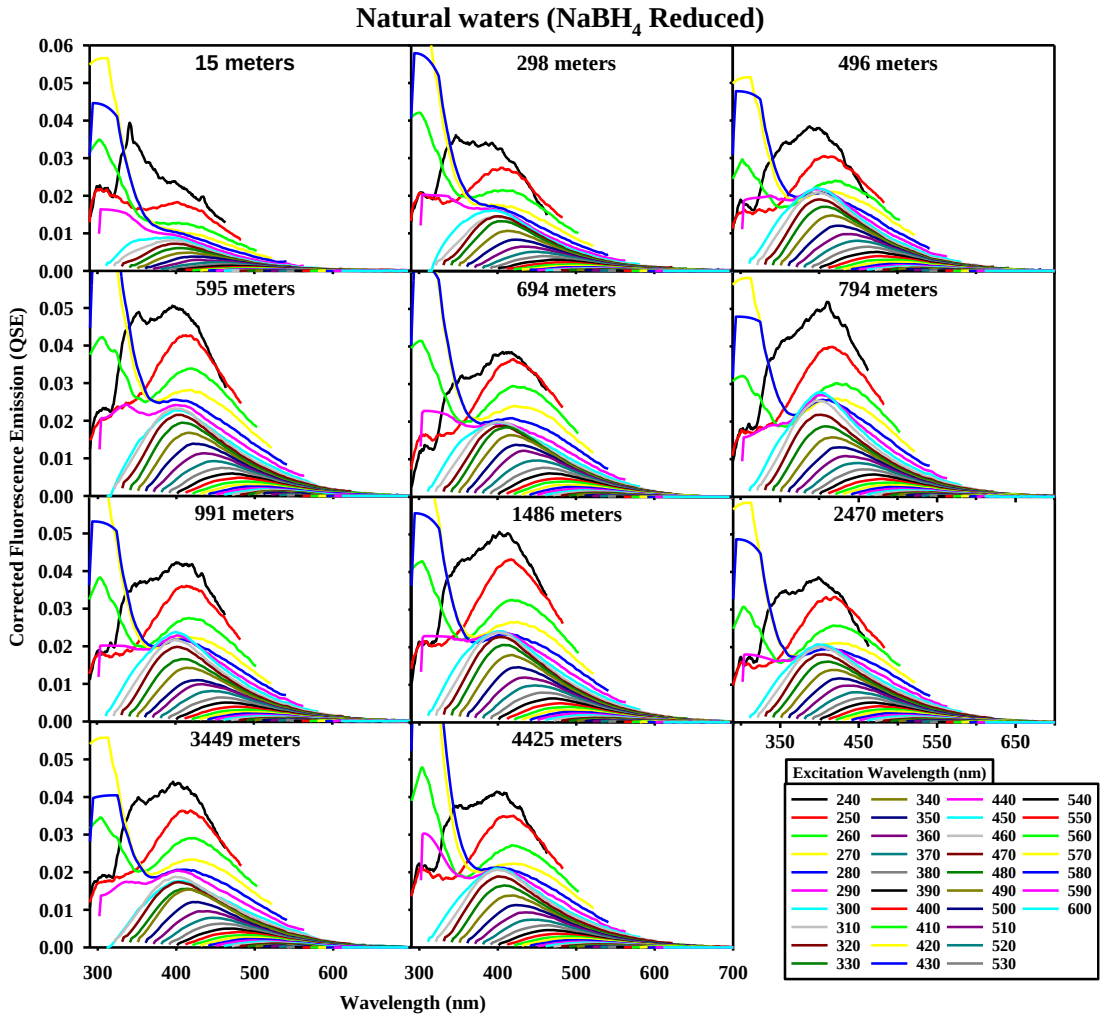

Figure S3.4: Depth dependence of EEMs for CDOM samples collected at Station ALOHA.

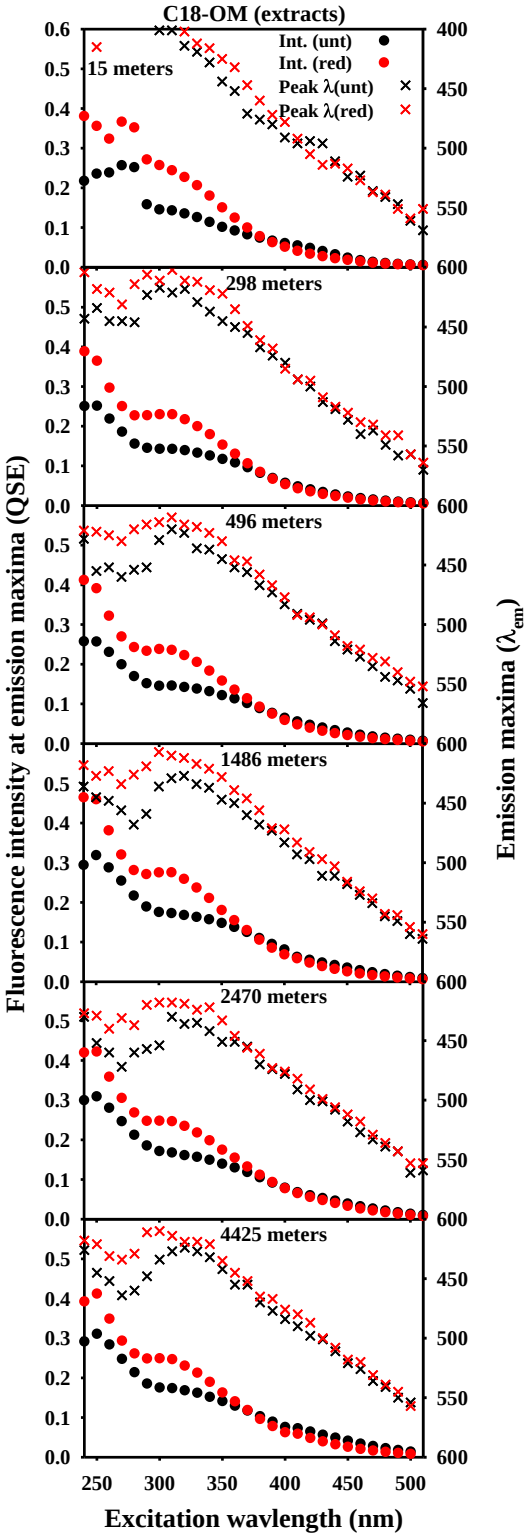

Figure S3.5: C18-OM fluorescence emission intensity (**x**) at the max emission wavelength (●) at each excitation wavelength for both untreated (**black**) and reduced (**red**) samples.

S4 - Supplemental Chapter 4:

Table S4.1: Chemical properties of humic substances provided by the IHSS.

	Acidic Functional groups pH titrations (meq/g C)		Carbon distribution ^{13}C NMR (% peak area)			
	Carboxyl	**Phenolic**	**Carbonyl**	**Carboxyl**	**Aromatic**	**Aliphatic**
SRNOM	11.21	2.47	8	20	23	27
SRFA	11.17	2.84	5	17	22	35
PLFA	7.09	1.75	1.2	17	12	61

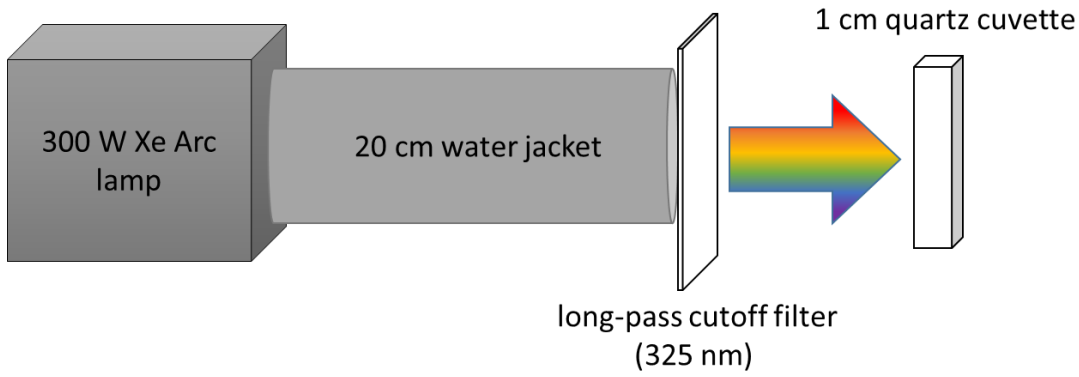

Figure S4.1: Block diagram of the irradiation setup used to irradiate SRFA, SRNOM and PLFA samples.

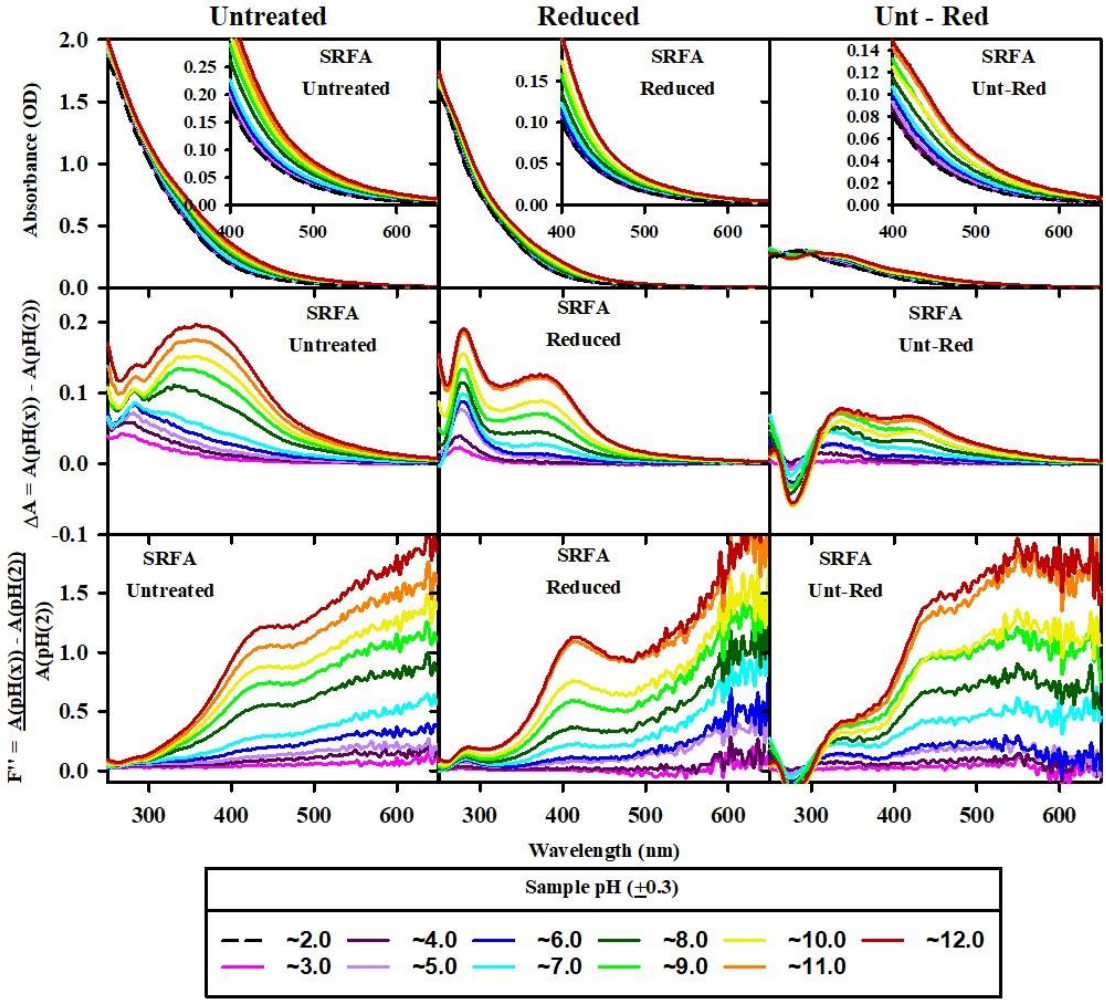

Figure S4.2: pH titration of SRFA, (**top**) normalized absorbance at increasing pHs (**middle**) difference spectra, and (**bottom**) fractional difference spectra. (**Left**) untreated sample, (**center**) reduced sample and (**right**) untreated – reduced (A_{lost}).

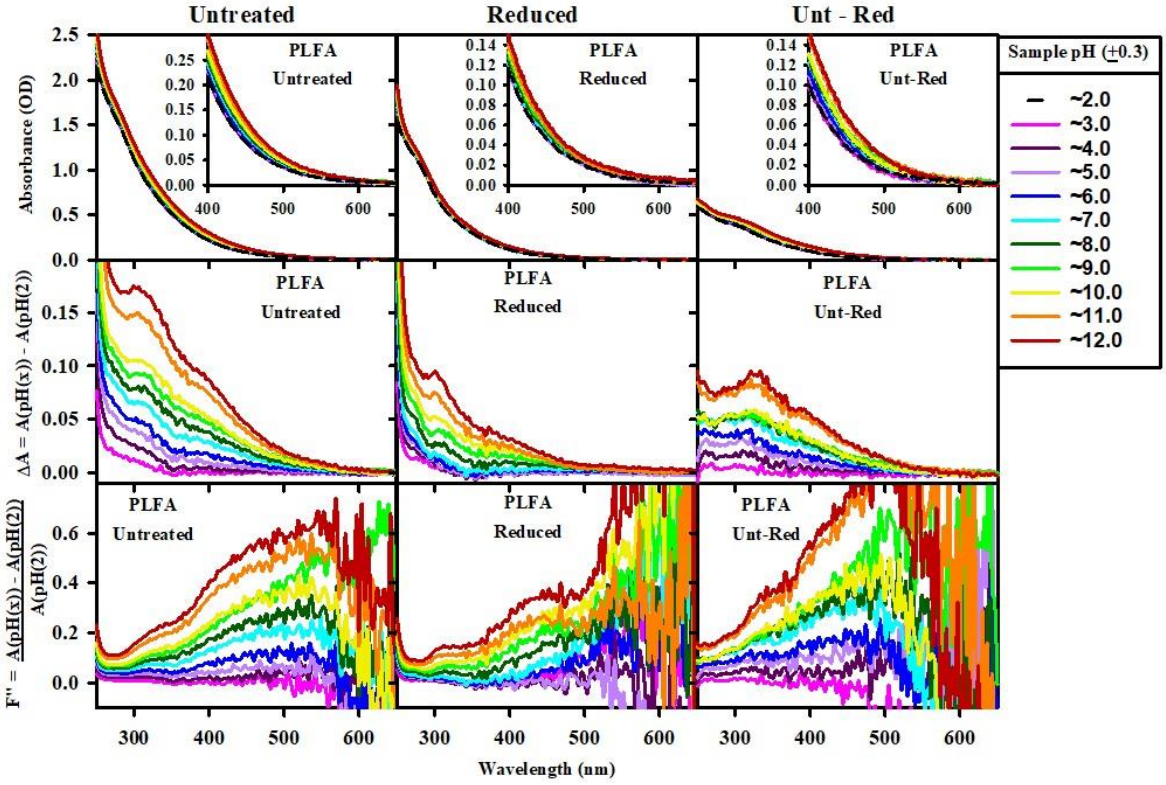

Figure S4.3: pH titration of PLFA, (**top**) normalized absorbance at increasing pHs (**middle**) difference spectra, and (**bottom**) fractional difference spectra. (**Left**) untreated sample, (**center**) reduced sample and (**right**) untreated – reduced (A_{lost}).

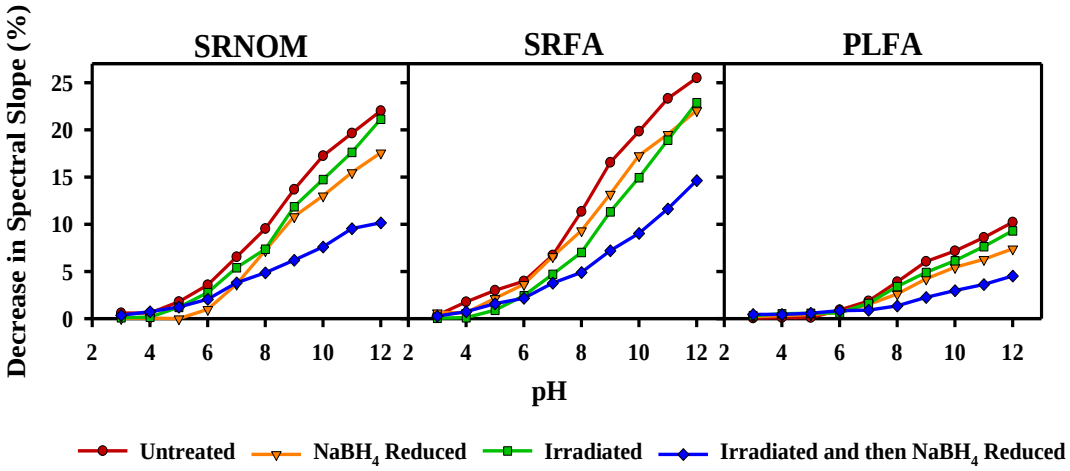

Figure S4.4: Percent decrease in spectral slope (S300-700) with increasing pH for untreated, reduced, irradiated, and irradiated and reduced samples of (**left**) SRNOM, (**middle**) SRFA, and (**right**) PLFA.

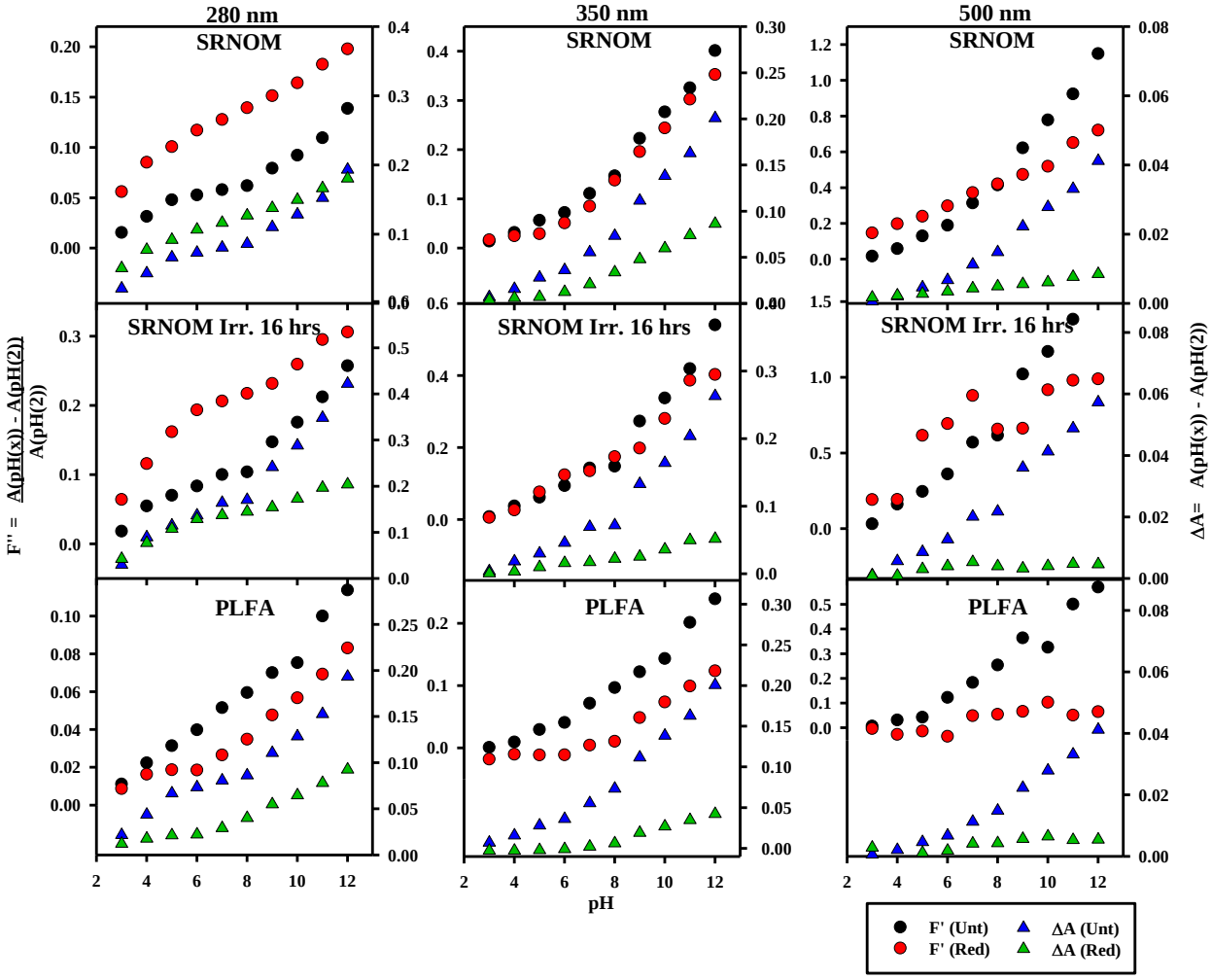

Figure S4.5: pH dependence of the Difference (**triangle**) and fractional difference (**circles**) spectra at select wavelengths (280, 350 and 500 nm), for SRNOM (**top**) Irradiated SRNOM (**middle**) and PLFA (**bottom**).

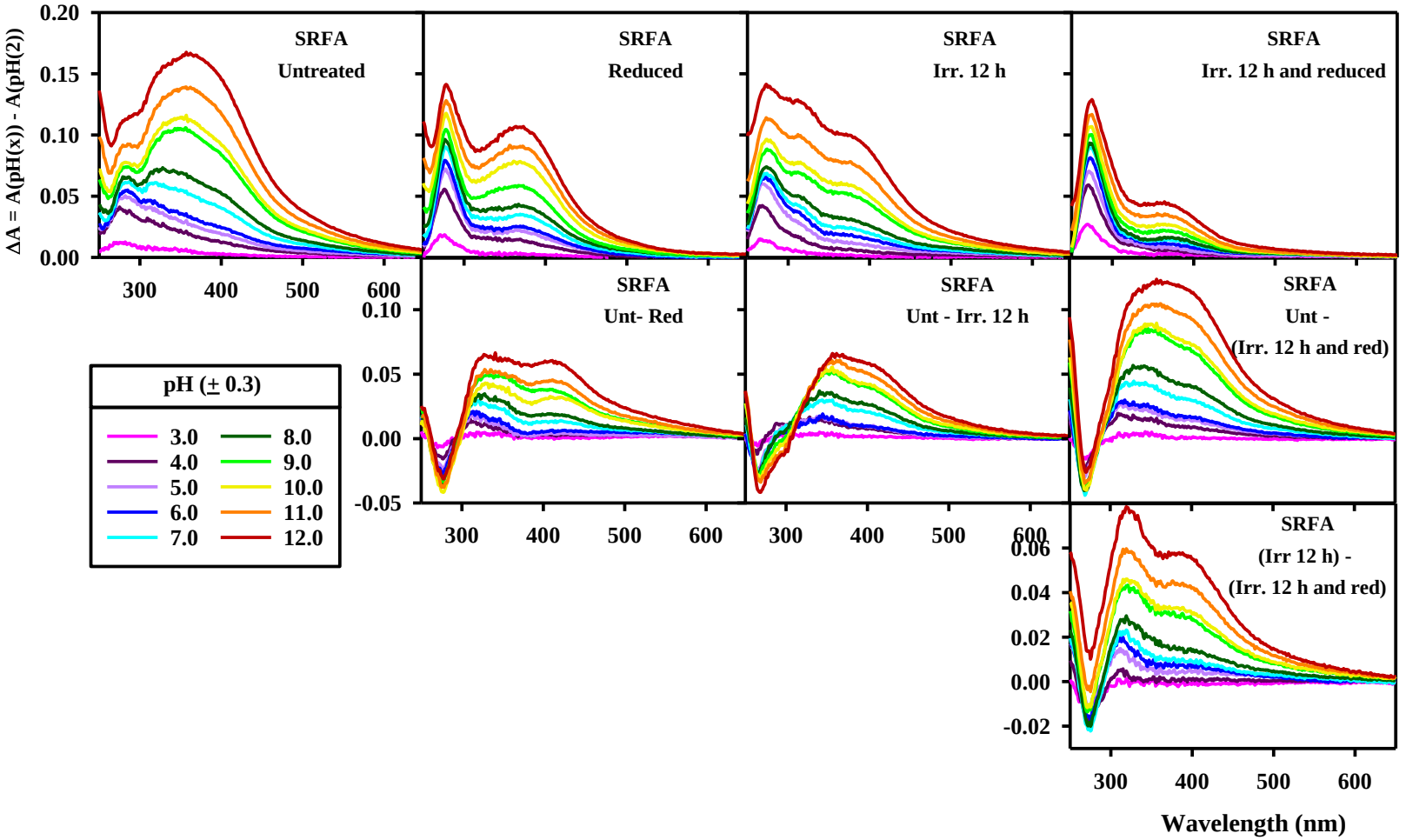

Figure S4.6: Difference spectra for untreated, reduced, irradiated and irradiated and reduced SRFA (**top**). Along with the difference spectra for the absorbance lost following reduction, irradiation and irradiation and reduction (**middle**). Also the difference spectra for the absorbance lost following reduction of the irradiated sample (**bottom**).

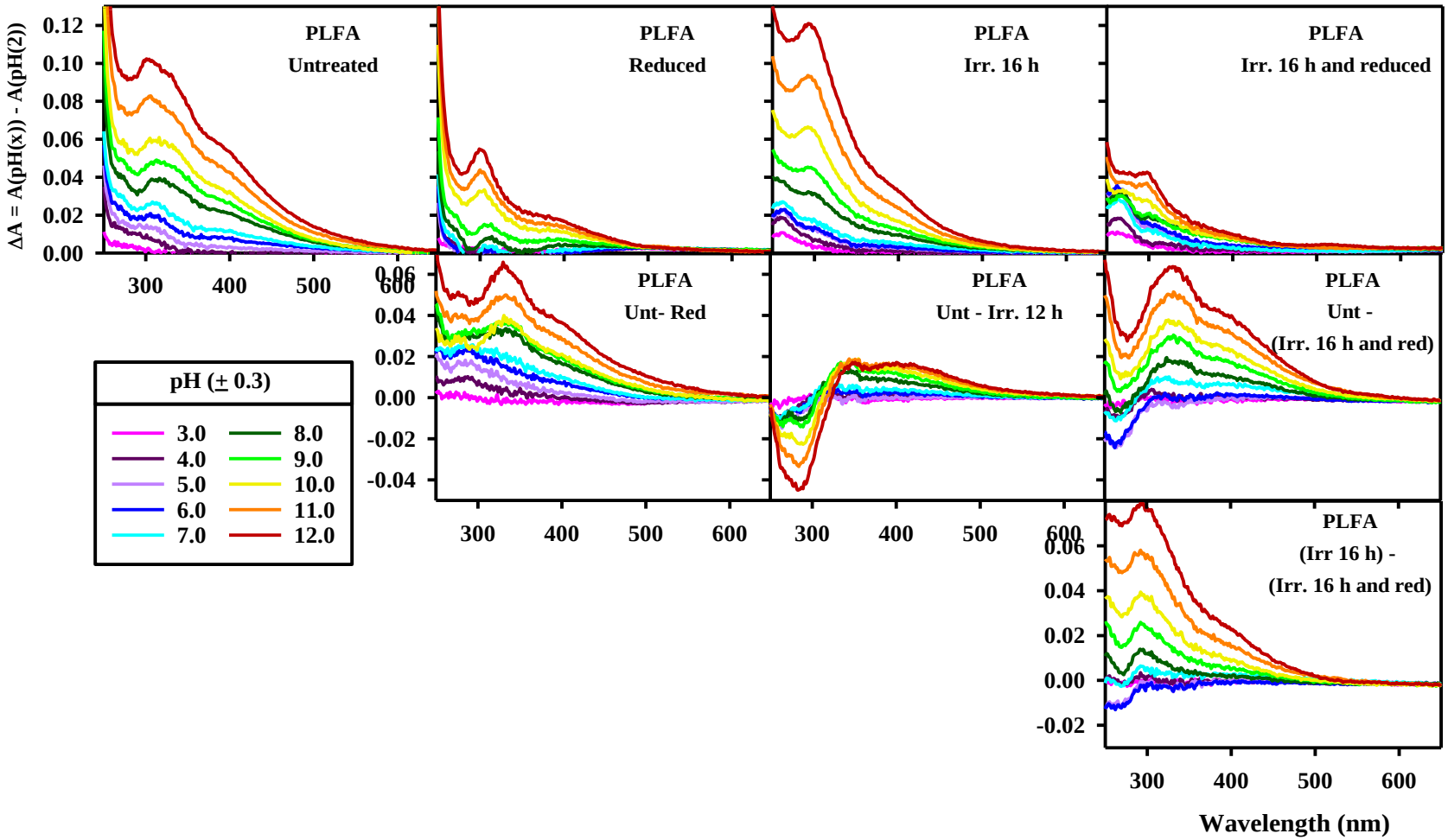

Figure S4.7: Difference spectra for untreated, reduced, irradiated and irradiated and reduced PLFA (**top**). Along with the difference spectra for the absorbance lost following reduction, irradiation and irradiation and reduction (**middle**). Also the difference spectra for the absorbance lost following reduction of the irradiated sample (**bottom**).

S5- Supplemental Chapter 5:

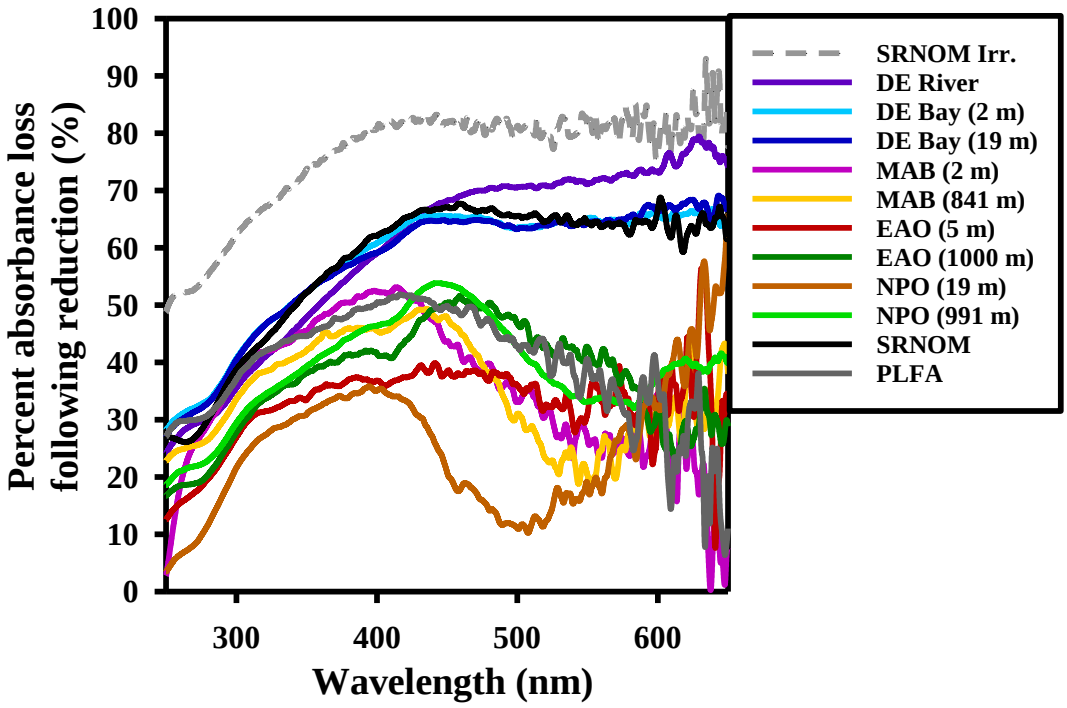

Figure S5.1: Percent loss of absorbance following sodium borohydride reduction for various locations.

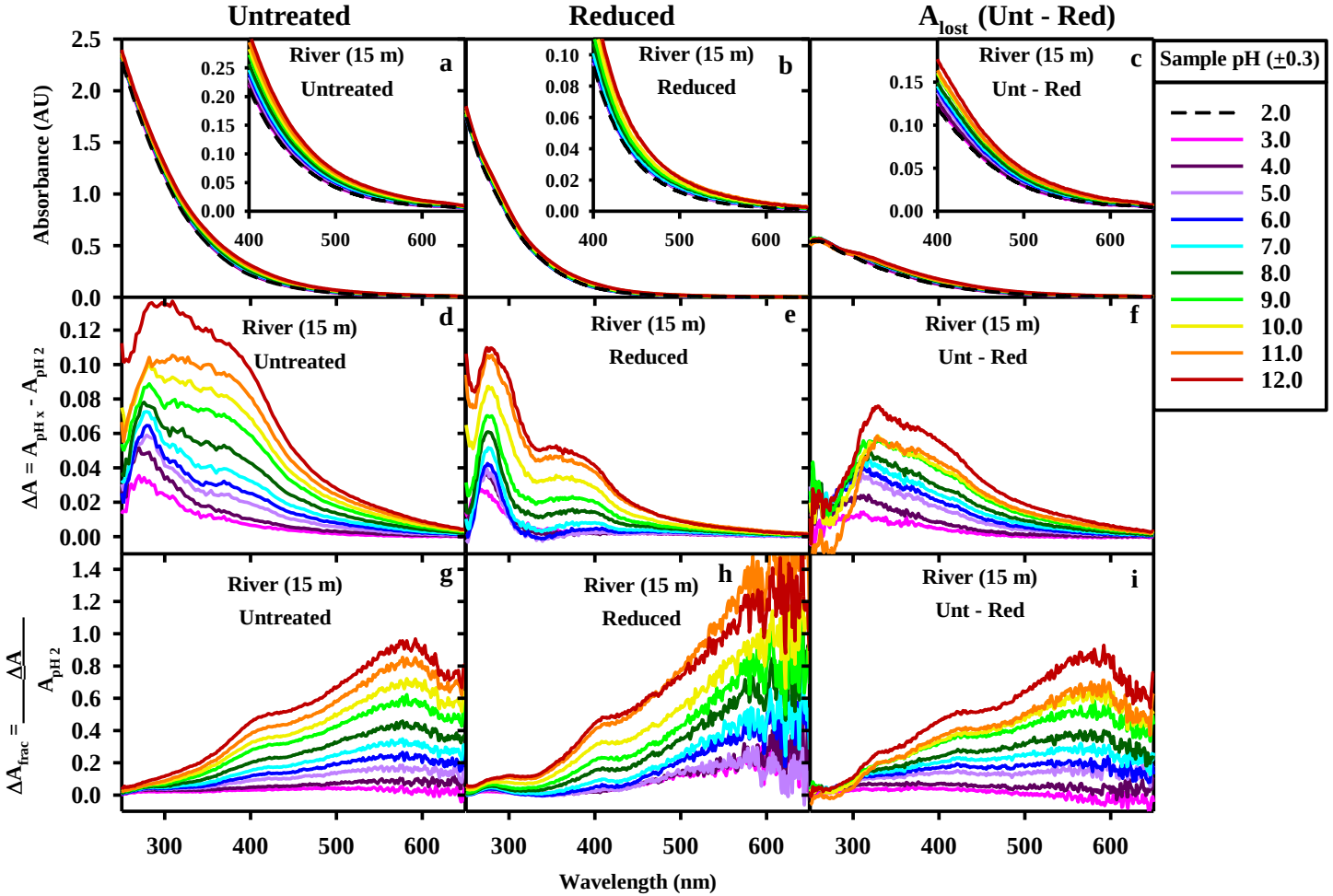

Figure S5.2 pH titration of a Delaware River C18-OM sample, (**top**) normalized absorbance at increasing pHs (**middle**) difference spectra, and (**bottom**) fractional difference spectra. (**Left**) untreated sample, (**center**) reduced sample and (**right**) untreated – reduced (A_{lost}).

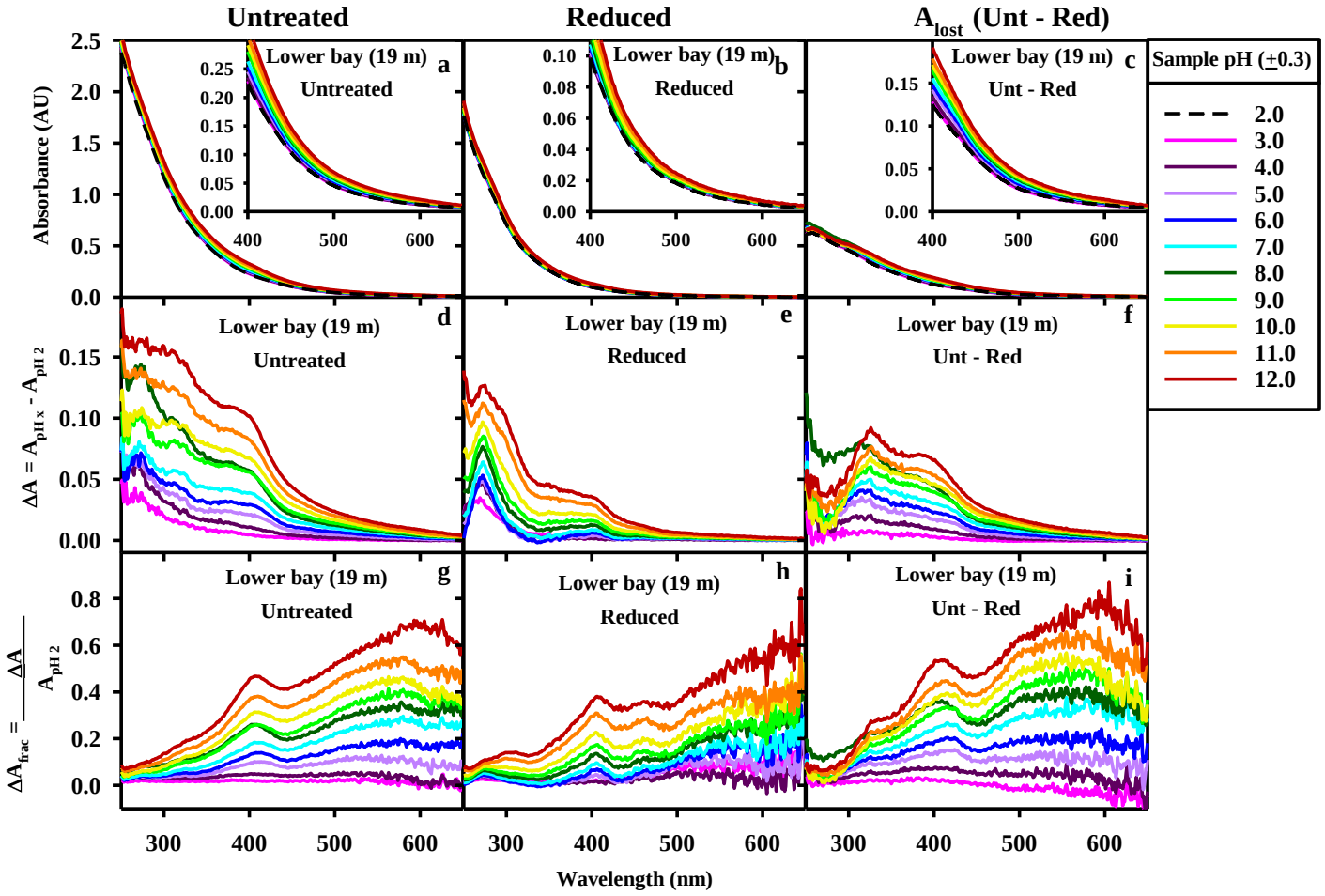

Figure S5.3: pH titration of a Lower Delaware Bay C18-OM sample, (**top**) normalized absorbance at increasing pHs (**middle**) difference spectra, and (**bottom**) fractional difference spectra. (**Left**) untreated sample, (**center**) reduced sample and (**right**) untreated – reduced (A_{lost}).

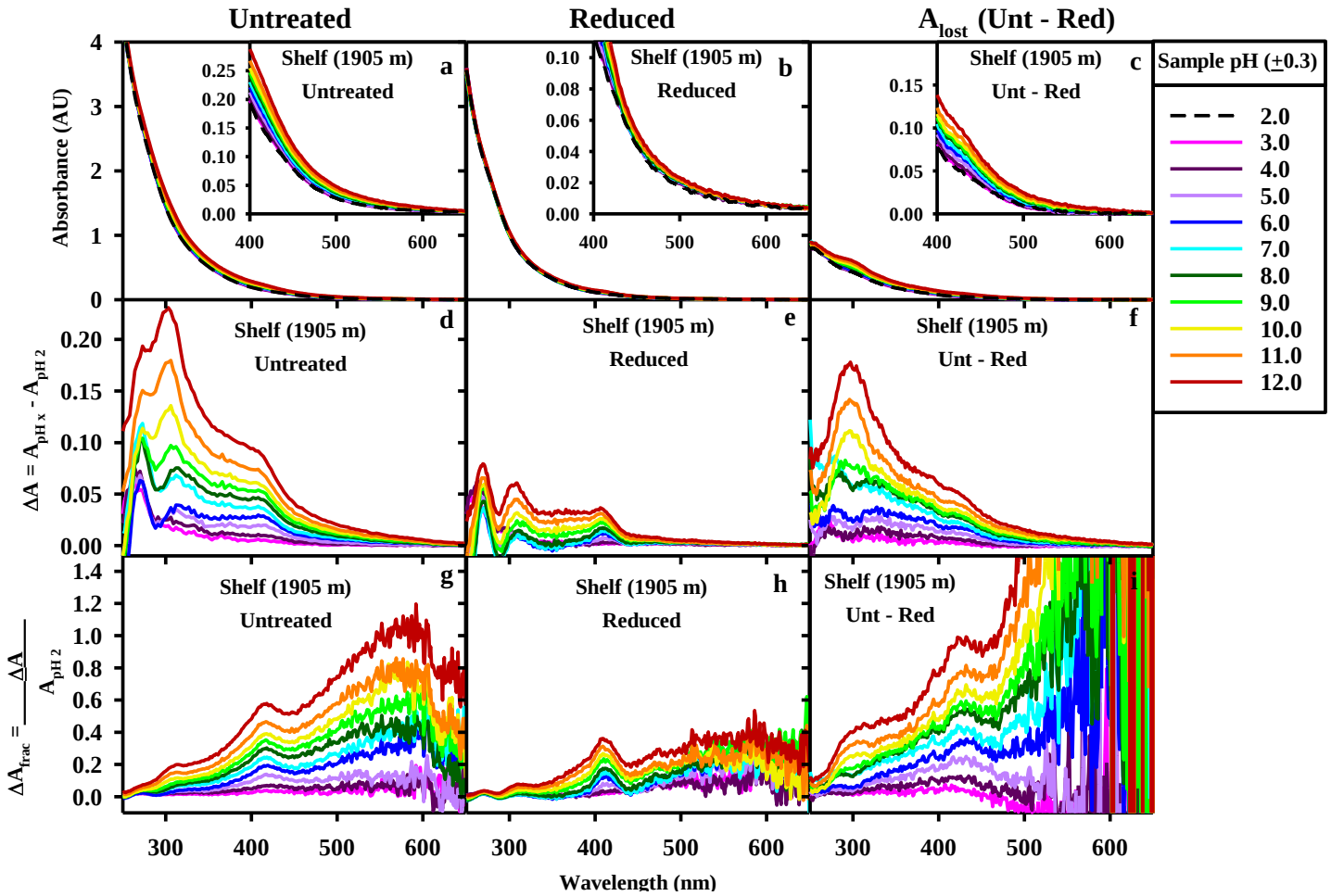

Figure S5.4: pH titration of a MAB shelf C18-OM sample, (**top**) normalized absorbance at increasing pHs (**middle**) difference spectra, and (**bottom**) fractional difference spectra. (**Left**) untreated sample, (**center**) reduced sample and (**right**) untreated – reduced (A_{lost}).

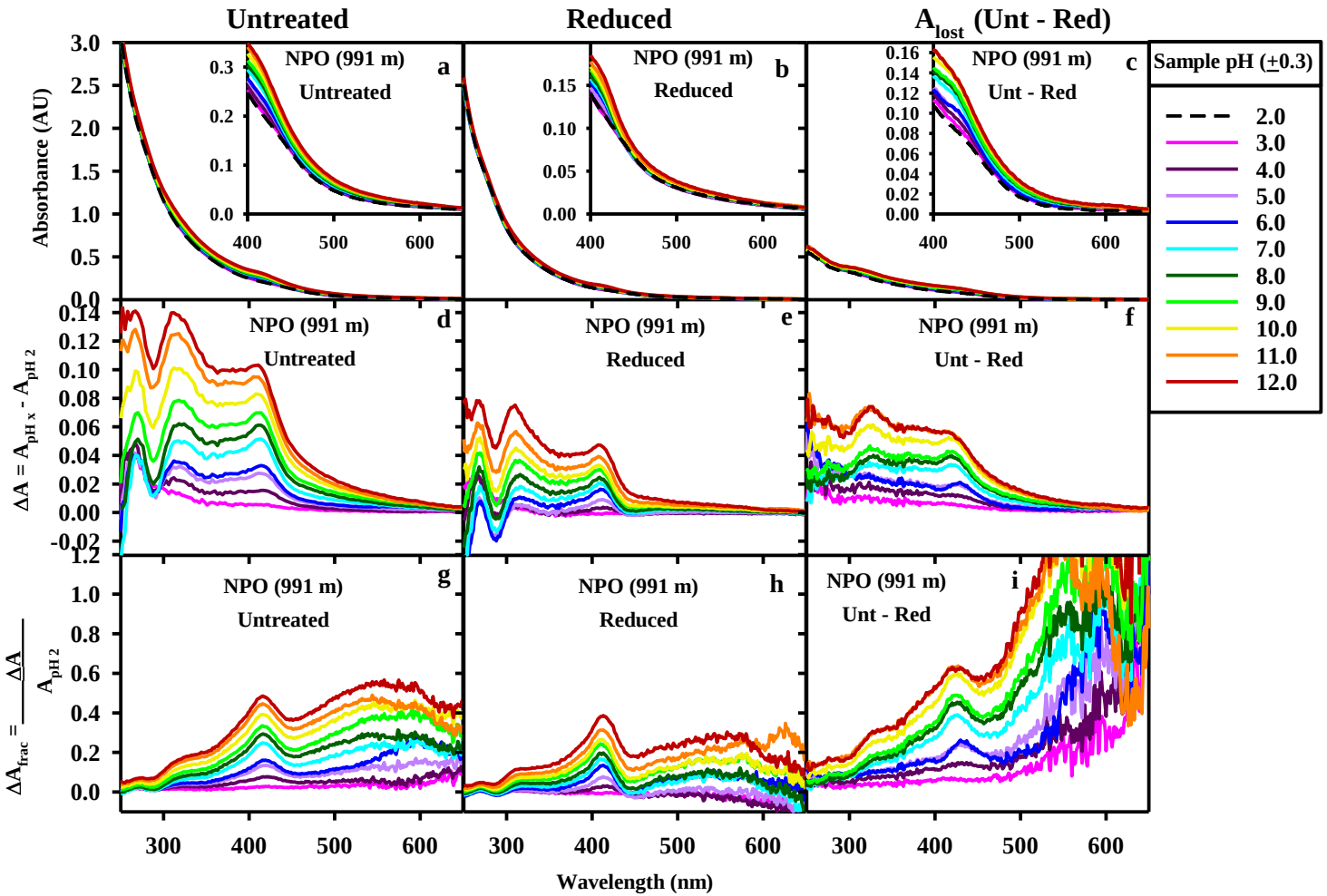

Figure S5.5: pH titration of a MAB shelf C18-OM sample, (**top**) normalized absorbance at increasing pHs (**middle**) difference spectra, and (**bottom**) fractional difference spectra. (**Left**) untreated sample, (**center**) reduced sample and (**right**) untreated – reduced (A_{lost}).

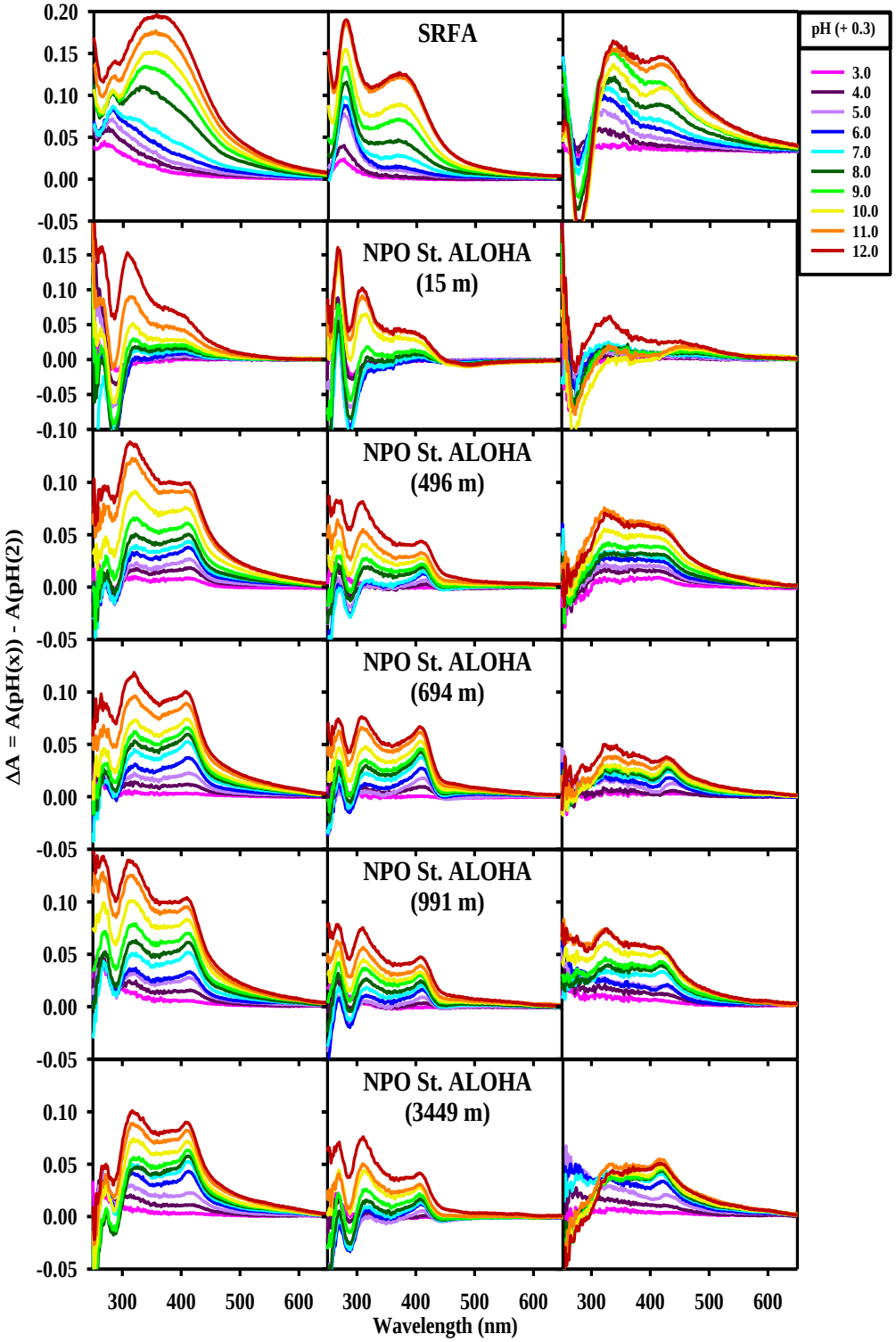

Figure S5.6: Difference spectra relative to pH 2 for untreated (**left**), reduced (**middle**) and unt-red (**right**) C18-OM samples from the NPO St. ALOHA.

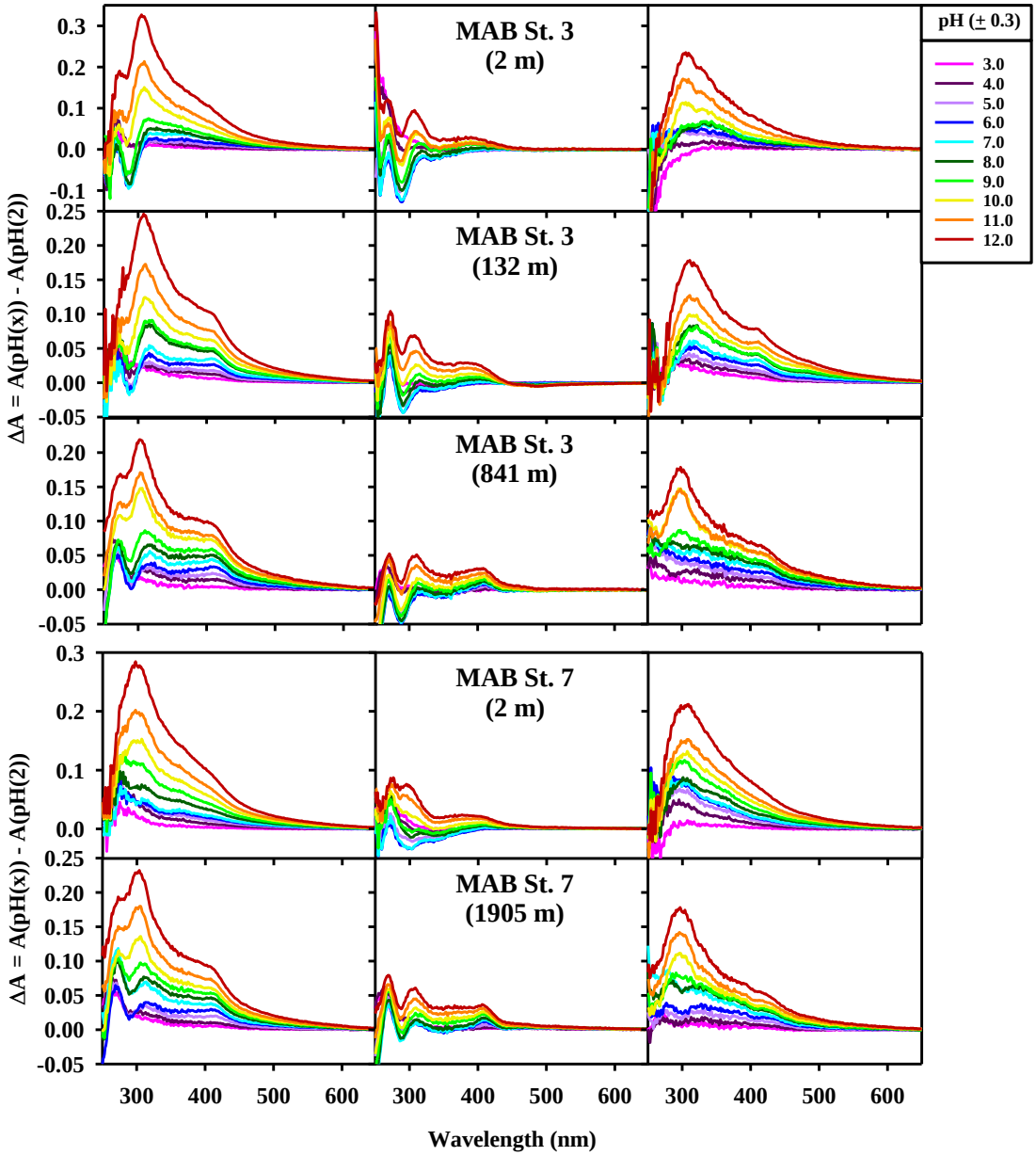

Figure S5.7: Difference spectra relative to pH 2 for untreated (**left**), reduced (**middle**) and unt-red (**right**) C18-OM samples from the NPO St. ALOHA.

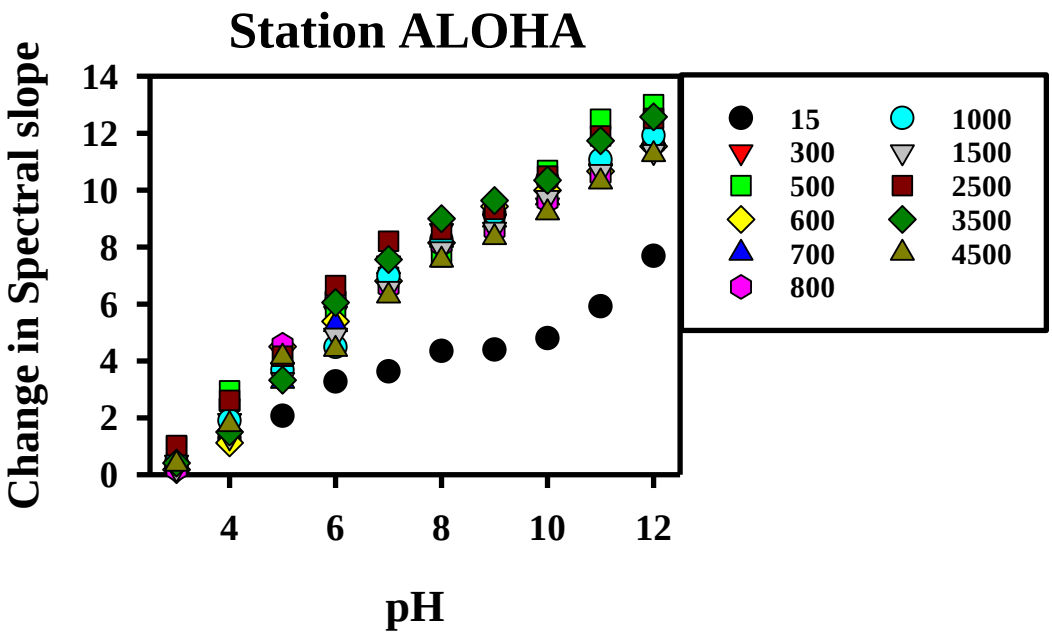

Figure S5.8: Percent decrease in spectral slope ($S_{300\text{-}700}$) with increasing pH for NPO samples.

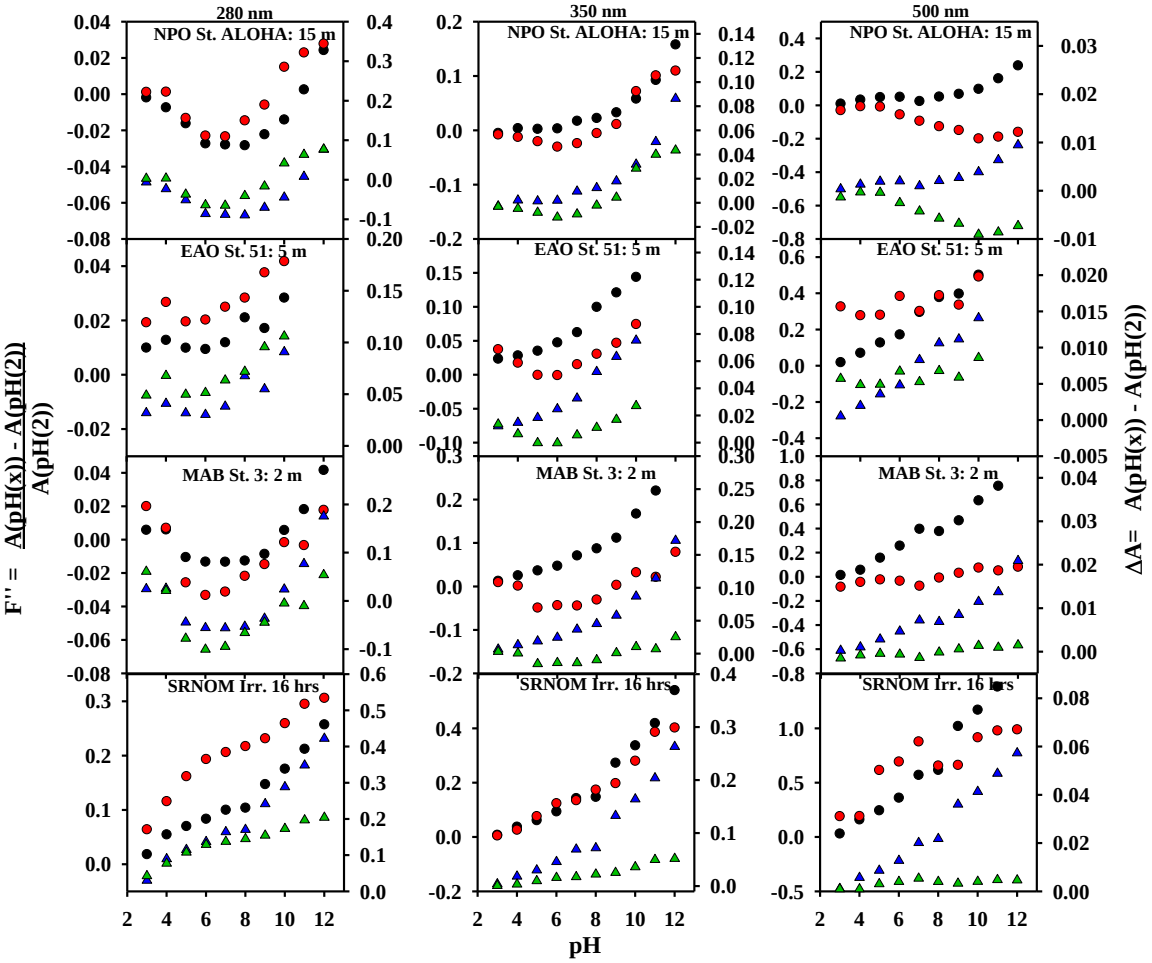

Figure S5.9: pH dependence of the difference (**triangle**) and fractional difference (**circles**) spectra at select wavelengths (280, 350 and 500 nm), for surface open ocean samples with an irradiated SRNOM sample at the bottom for comparison.

S5b- Chemical and optical properties of DOM released from Mangrove.

S5b.1 Background:

CDOM in the natural environment has many sources that vary by location. In some tropical or subtropical coastlines mangroves can grow in the transition zone between the land and the coastal ocean[160,161], thus mangrove leaves and leaf litter may contribute significantly to the CDOM pool in these regions, and may be transported offshore and distributed globally though ocean currents[162]. Material leaching from mangrove leaves is a critical stage in the degradation of the leaves and could be a significant source of DOM in areas with mangrove trees. A significate amount of the DOM released from the leaves is tannins.[53,163,164] Tannin consists of two main types, condensed and hydrolysable tannin. Condensed tannins are typically oligomers and polymers of flavanols. Hydrolysable tannins on the other hand are made up of gallic acid and its derivatives often esterified to polyols (Fig. S5b.1). There is a third type of tannin referred to as phlorotannins that are found in brown algae such as Sargassum, the main building block of this group is phloroglucinol.[164] Both condensed and hydrolysable tannins are found in the leachate from mangrove leaves, but hydrolysable tannins are leached to a greater extent.

The optical and chemical properties of the DOM leached from mangrove leaves can be investigated in the same manner as natural waters and extracted DOM. Then comparisons between the mangrove leaf samples and other DOM samples can be used to indicate if DOM from mangrove leaves is structurally similar to and a possible source of DOM in other geographical locals.

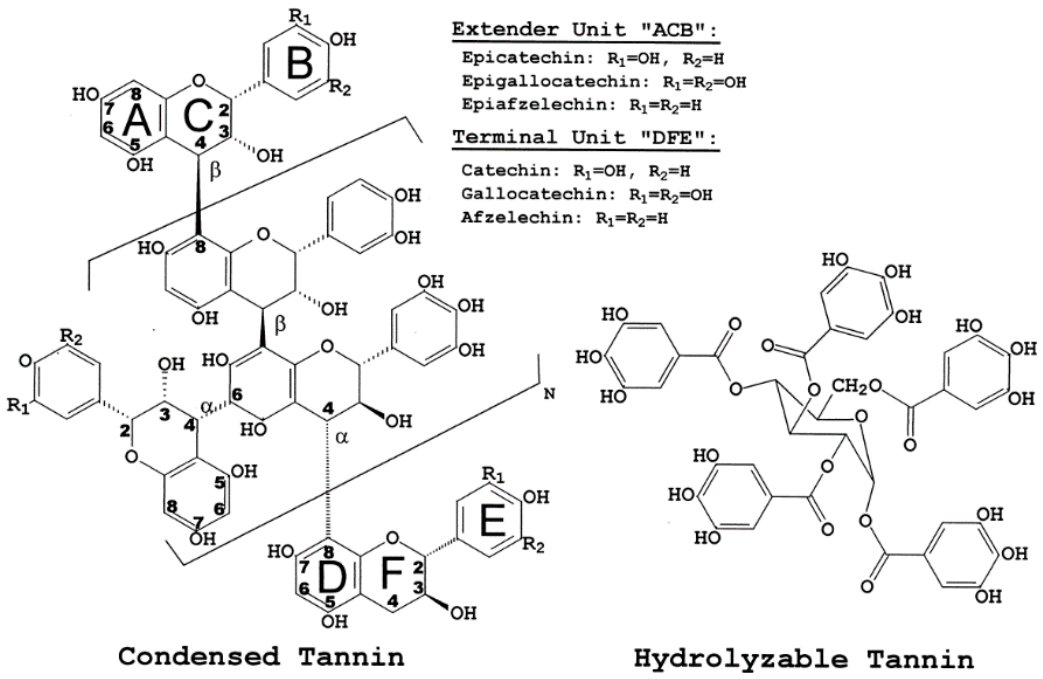

Figure S5b.1: Theoretical structures of typical condensed and hydrolysable tannins from Hernes, 2001.

S5b.2 Methods:

Mangrove leaves (green and yellow) were collected from trees near the Shark River (Fig. S5b.2) in November 2017 (FCE LTER site SRS6; 25.36460, -81.07790;). The leaves were shipped from Florida to the University of Maryland were they were stored at ~4 °C before being cleaned and incubated.

Prior to incubation the leaves were lightly rinsed with purified water to remove any debris. The leaves were then separated by color and incubated for ~48 hours in the dark at room temperature. The incubation was conducted in 1 L Pyrex beakers filed with 1.0 L of purified water adjusted to pH 7-8 using NaOH. For each incubation ~ 10 g of wet leaves were used and a stir bar was placed in the beaker and used to create slight movement of the leaves and water. Aliquots were taken at different time points throughout the incubation to monitor the material being released from the leaves with time. The samples taken at

Figure S5b.2: Map showing sample collection site (SRS6).

each time point had their pH adjusted to ~7-8, and were filtered through 0.2 μm Nylon filters, then the optical properties were recorded and selected chemical analyses performed. (Fig. S5b.3)

Absorbance spectra at each time point were collected as previously described in section (**4.3.3**), also reductions and pH titrations were also performed on select samples as previously described in section (**4.3.4**) and (**4.3.5**) respectively. After pH titration select samples were left at pH ~11 open to air in the dark to monitor any possible oxidation.

S5b.3 Results and discussion:

S5b.3.1 Incubations

Both the green and yellow leaves released copious amounts of DOM throughout the incubations. The amount of colored material released was fairly uniform with time until ~48 h., and the structure of the absorption spectra did not dramatically change at different

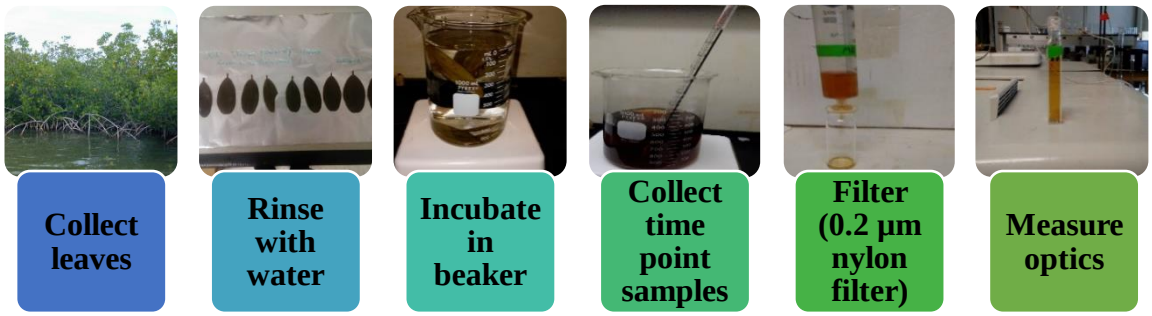

Figure S5b.3: Summery of collection and workup of leaves.

time points. (Fig. S5b.4 and S5b.5) This indicates that the structure of the material being release may also be fairly uniform.

Like SRNOM and riverine CDOM samples the absorption spectra of the material released by both the green and yellow leaves decreases with increasing wavelength and extends well into the visible region. However, the CDOM from the leaves has more discrete bands and shoulders than seen in Shark River DOM (Andrew et al., in prep.). The yellow leaves in particular had several pronounced bands from ~280-400 nm, and a broad shoulder centered at ~500 nm. (Fig. S5b.4)

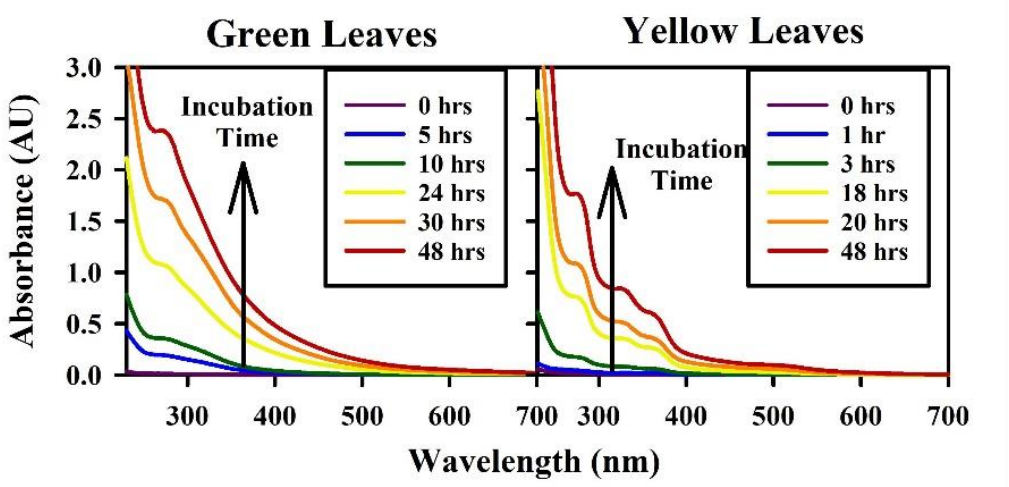

Figure S5b.4: Absorbance of colored material released at different time points throughout the 48 hour incubation of Green (**left**) and Yellow (**right**) leaves.

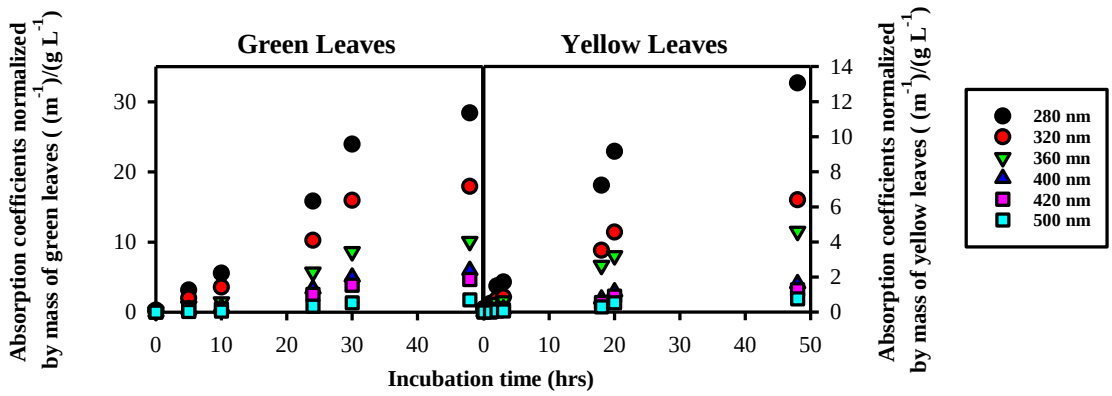

Figure S5b.5: Absorption coefficients at select wavelengths for Green (**left**) and Yellow (**right**) leaves normalized by the mass of the leaves using during the incubation.

S5b.3.2 Chemical tests:

To further compare the structure of the mangrove leave CDOM to riverine and ocean CDOM reductions and pH titrations were performed. $NaBH_4$ reductions explored the contribution of carbonyl groups to the absorption including ketones and aldehydes which get irreversibly reduced to alcohols. Like seen in other CDOM samples reduction significantly decreased the absorbance at all wavelengths, but the longer wavelengths experienced the largest percent loss. (Fig. S5b.6) This is very similar to SRNOM as well as riverine and ocean CDOM, but due to the bands and shoulders present in the mangrove leave CDOM (especially the yellow) the absorbance loss following reduction is much more structured because all of the discrete bands were impacted by the reduction. This suggests that the structures responsible for the bands and shoulders in the absorption spectra contain reducible groups. Another difference observed in the yellow leaves is the presence of possible significant reversible reduction. This can be seen when comparing the percent reduction after 4 hour to that after 48 hour. After 48 hours the sample has actual increased in absorbance compared to the 4 hour sample at most wavelengths. This could be due to

the contribution of reduced species that can re-oxidize in air such as quinones. However, as will be shown later the absorbance of the CDOM released by the yellow leaves is enhanced when the sample is left at a high pH open to air. Because the reductions were carried out at a pH of ~10 with the sample exposed to air the increase seen at 48 hours in the yellow leave sample could be due to changes in moieties not involved in the reduction. Over all, the percent absorbance loss is very similar between the green and yellow leaves and is comparable to other CDOM samples.

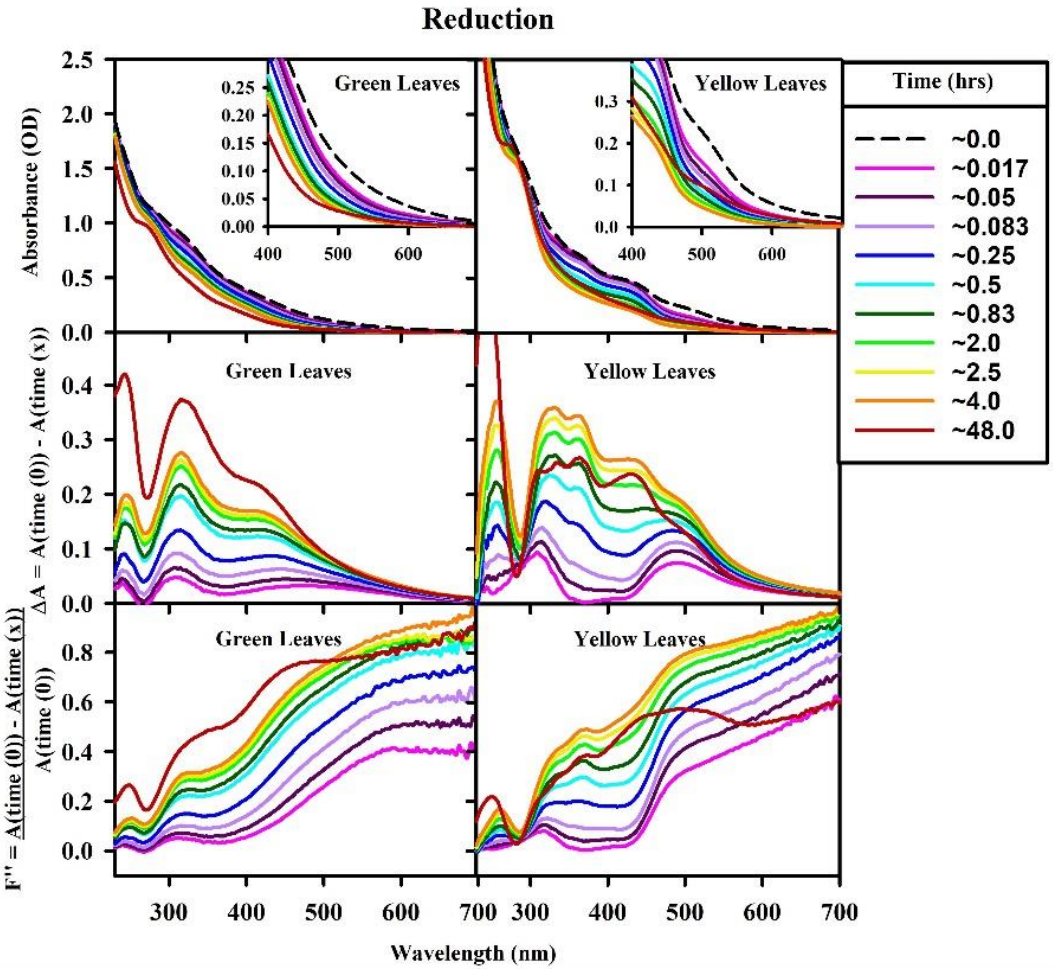

Figure S5b.6: (**top**) absorbance of Green (**left**) and Yellow (**right**) leave samples at different time points during the $NaBH_4$ reduction, (**middle**) absorbance lost during reduction (untreated – reduced) , and (**bottom**) fractional absorbance loss during reduction.

pH titrations were also performed on the untreated material released from the Green and Yellow leaves. Carboxylic acids and phenolic groups are both anticipated to occur in the exudate from the leaves due to the release of tannins. As stated previously hydrolysable tannins result from the polymerization of gallic acid and its derivatives.[164] To test for the occurrence of these functionalities, the change in absorption with increasing pH was investigated for the mangrove leave samples. The absorption increased with increasing pH, preferentially from pH ~8 to ~12, but also over the low pH range (< 5) although to a lower extent. This is consistent with the deprotonation of phenolic groups and carboxylic acids.[21,56,59,61,62] (Fig S5b.7) The pH titration of the mangrove leave samples does share several features with the titration of reference materials and C18-OM samples. The most striking similarity is that the pH dependence continues well into the visible region supporting the idea that there are electronic interactions occurring in these samples, just as in the reference materials and natural water samples. However, the more defined bands in the difference spectra suggest that this material may be less complex compared to riverine CDOM thus the more discrete species give rise to more distinct bands. In samples containing lower molecular weight compounds there may be fewer electronic interactions thus there will be less broadband absorption due to fewer charge transfer complexes and the absorbance from individual moieties will be more prominent. As with the reference materials and natural waters titrations on the reduced samples would provide more information about the contribution of both donor and accepter moieties to the absorbance.

Following pH titration the samples were left at pH ~11.0 for 18 hours to examine any possible alkaline air-oxidation which can introduce carbonyl-containing compounds (such as aromatic ketones/aldehydes and quinones) and structural changes that could alter

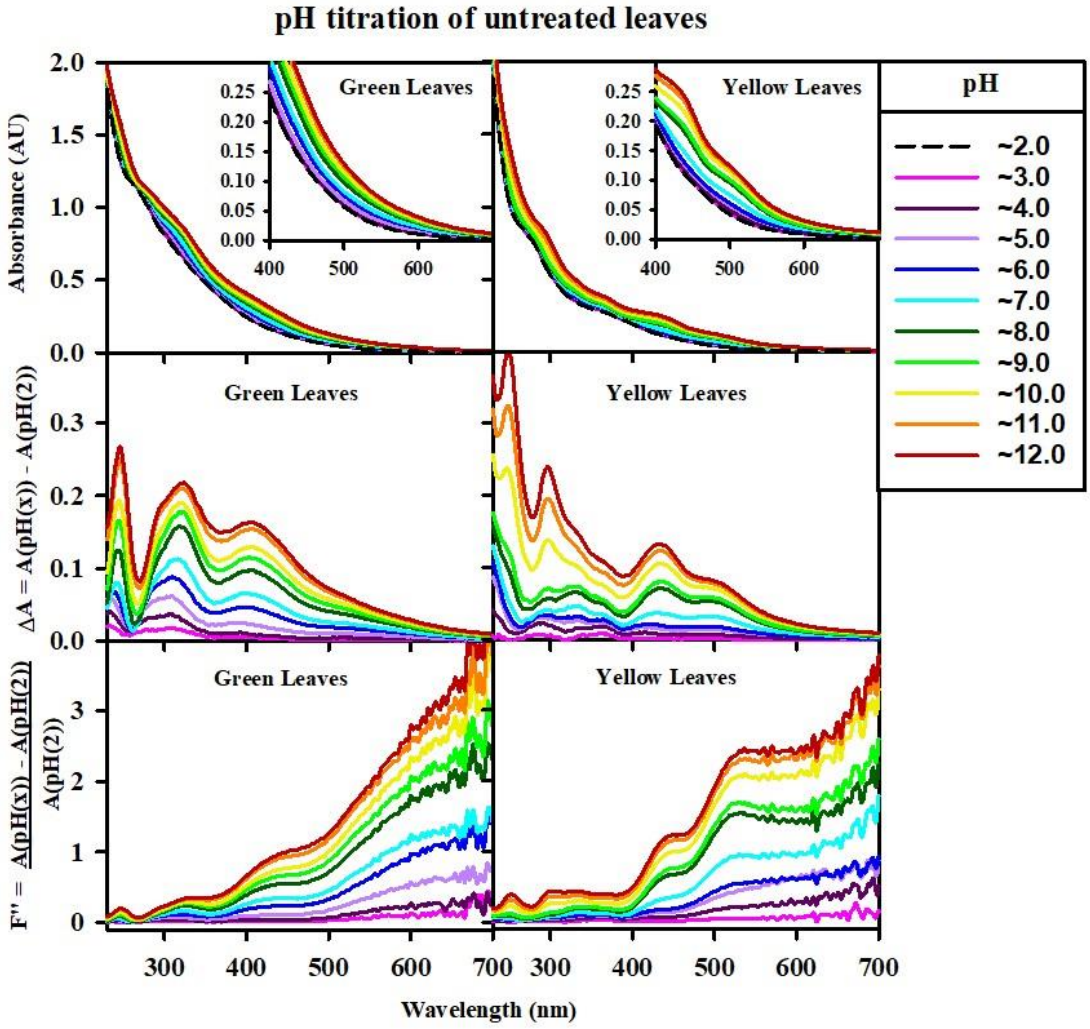

Figure S5b.7: (**top**) absorbance of Green (**left**) and Yellow (**right**) leaves with increasing pH from ~2.0 -12.0, (**middle**) change in absorbance with increasing pH relative to pH 2.0, and (**bottom**) fractional increase in absorbance relative to pH 2.0.

the optical properties of the mangrove leave samples. The alkaline air-oxidation test showed very different results for the Green and Yellow mangrove leave samples not only to one another but to riverine and oceanic CDOM. The absorbance of the Green leaf sample decreased at all wavelengths with increasing amount of time spent at pH ~11.0. However, the Yellow leaf sample absorbance increase at wavelengths > 280 nm, while it decreased at wavelengths < 280 nm. (Fig S5b.8) These differences suggest differences in structure of

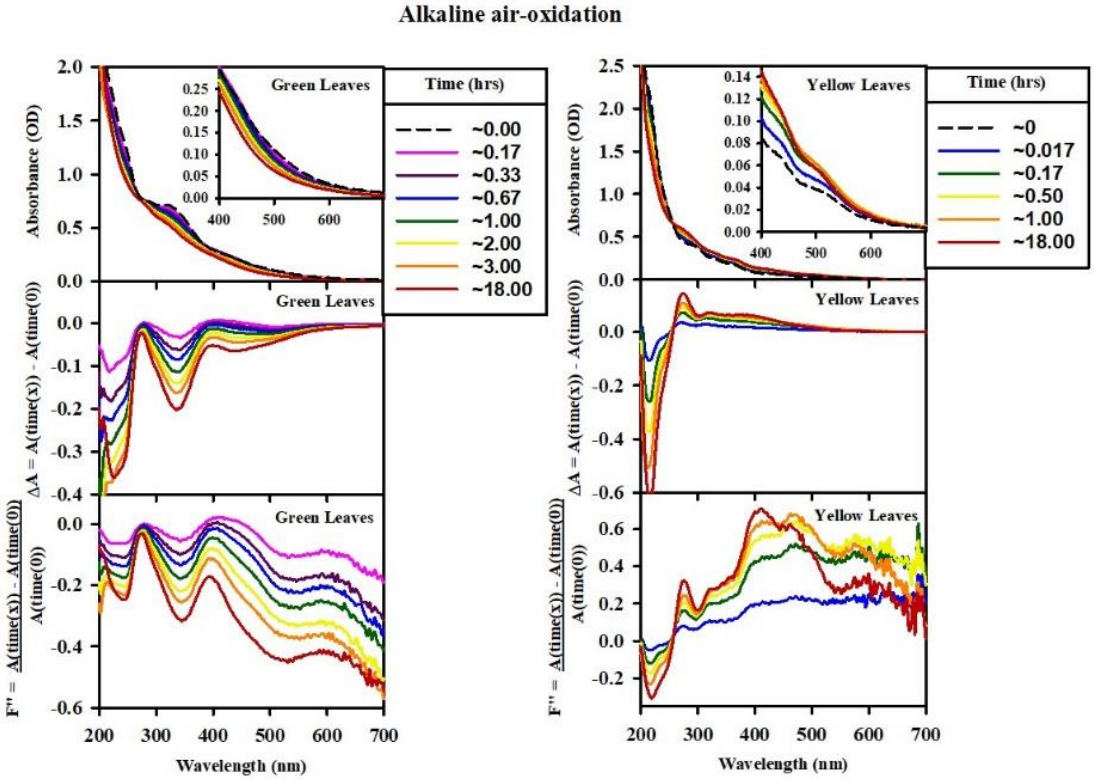

Figure S5b.8: (**top**) absorbance of Green (**left**) and Yellow (**right**) leaves with increasing time exposed to air at pH ~11.0, (**middle**) change in absorbance with time relative to time 0.00 hours, and (**bottom**) fractional change relative to time 0.00 hours.

the DOM released by the Green and Yellow leaves. Also IHSS reference materials and riverine and oceanic C18-OM sample do not show any significant change at high pH over 18 hours. This could indicate that the material released from the mangrove leaves is more reduced than the natural water sample. Also the mangrove samples do not undergo any extraction process prior to the oxidation experiment whereas the reference materials and C18-OM do, which could cause differences in the response of the samples.

S5b.4 Conclusion*:*

Although these tests on CDOM released by mangrove leaves were very preliminary, they do show that reductions and pH titrations can be applied to a variety of environmental samples to gain more information about the structures responsible for the

optical properties. Also through comparison to other samples these tests could provide information about the importance of certain sources of CDOM. For example these leaf samples were collected near the Shark River in Florida, if the chemical responses seen here are in line with the responses seen from natural waters collected from the river this could indicate that mangrove leaves are an important local source of CDOM.

Further studies into the impact of degradation states (for example: green vs yellow leaves) on the structure and optical properties of CDOM released by mangrove leaves needs to be completed in order to develop a complete picture of how this local source could be impacting the water in these coastal areas. Leaf litter from around the trees that has been submerged would also be important to study.

Because this was preliminary work the incubations were carried out using purified water, but it would be important to test how other environmental factors would influence the leaching of material from the leaves. Because mangroves grow in coastal environments the water often has a high salinity and other compounds that are present in the natural waters could impact the leaching. Environmental factors such as temperature, movement of the water and solar radiation would also be factors to consider. Irradiation of the material leached from the leaves and monitoring of the absorbance would be critical to determine how long the CDOM released from these leaves remains in the environment and how far it could be transported.

Although there is many directions that this work could take the overall conclusion from this study is that developing a well-defined and reproducible set of tests or "tool-box" that can be applied to a variety of environmental samples will help to illuminate the source and structure of CDOM in the environment. Optical measurements combined with $NaBH_4$

reduction, pH titrations and alkaline air oxidations have also been performed on Sargassum exudates (Powers et. al: in progress) as well as material released from hydrothermal vents (Lin et. al: in progress) to demonstrate just a few more applications of these tests. Continuing to collect detailed optical measurements and preform chemical tests is critical to improving our understanding of the structures responsible for the optical properties of CDOM throughout the environment.

S6 - Supplemental Chapter 6:

Table S6.1: Excitation and Emission wavelength range and steps used to collect EEMs included in each dataset.

Dataset	Instrument	Excitation wavelength range (nm)	Excitation Steps (nm)	Emission wavelength range (nm)	Emission Steps (nm)
Non-interacting fluorophores	Horiba: Fluoromax-4	250-500	10	290-600	1
Non-interacting fluorophores + SRFA	Horiba: Fluoromax-4	250-500	10	290-600	1
Pyrene	Horiba: Fluoromax-4	350-450	10	360-600	1
NPO Untreated	Horiba: Fluoromax-4	240-600	10	290-700	1
NPO Reduced	Horiba: Fluoromax-4	240-600	10	290-700	1
Sargassum	Horiba: Aqualog	231-600	3	~233-597	~3
HA and FA ref materials	Horiba: Fluoromax-4	240-600	10	290-700	1
Chesapeake Bay (CB) samples	Horiba: Fluoromax-4	240-600	10	300-700	2

Table S6.2: Composition of samples included in the non-interacting fluorophore dataset.

Sample #	Compounds included in sample				
	Riboflavin	Quinine sulphate	Tryptophan	Tyrosine	Trimethyl-phenol
1	✓	✓			✓
2	✓	✓	✓		✓
3	✓	✓	✓	✓	
4	✓	✓	✓		
5		✓	✓		✓
6		✓	✓	✓	
7	✓	✓		✓	✓
8	✓	✓	✓	✓	✓
9		✓		✓	✓
10	✓	✓		✓	
11		✓		✓	✓
12	✓	✓			
13		✓			✓
14		✓	✓		
15		✓		✓	
16		✓			
17	✓				
18	✓			✓	✓
19	✓				✓
20			✓		✓
21					✓
22			✓		
23			✓		
24			✓		
25			✓		
26	✓		✓		✓
27	✓		✓		
28			✓		
29	✓		✓	✓	✓
30	✓		✓	✓	
31			✓	✓	✓
32	✓			✓	
33				✓	✓
34			✓	✓	
35				✓	

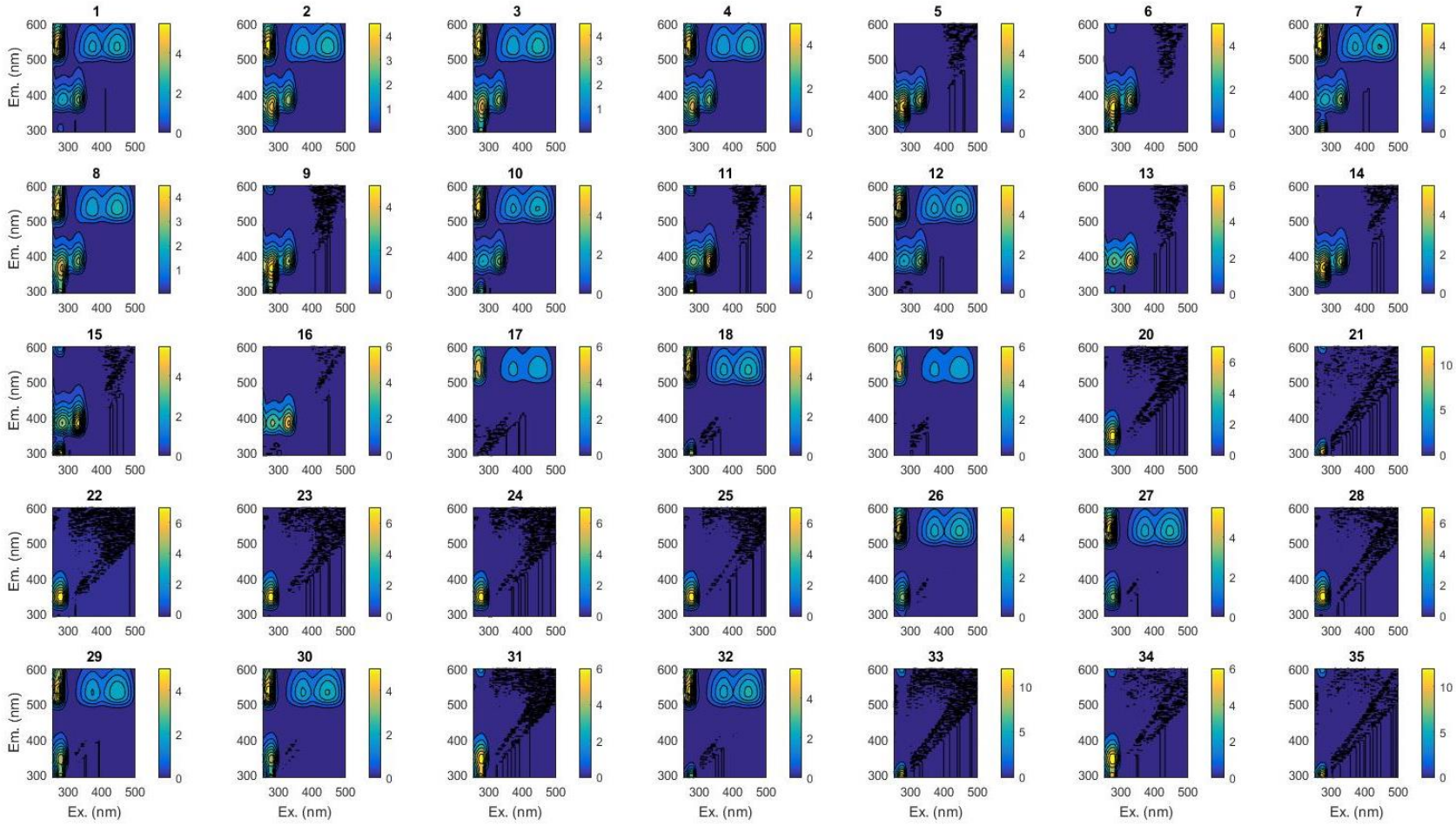

Figure S6.1: EEMs for samples included in the non-interacting fluorophore dataset after normalization.

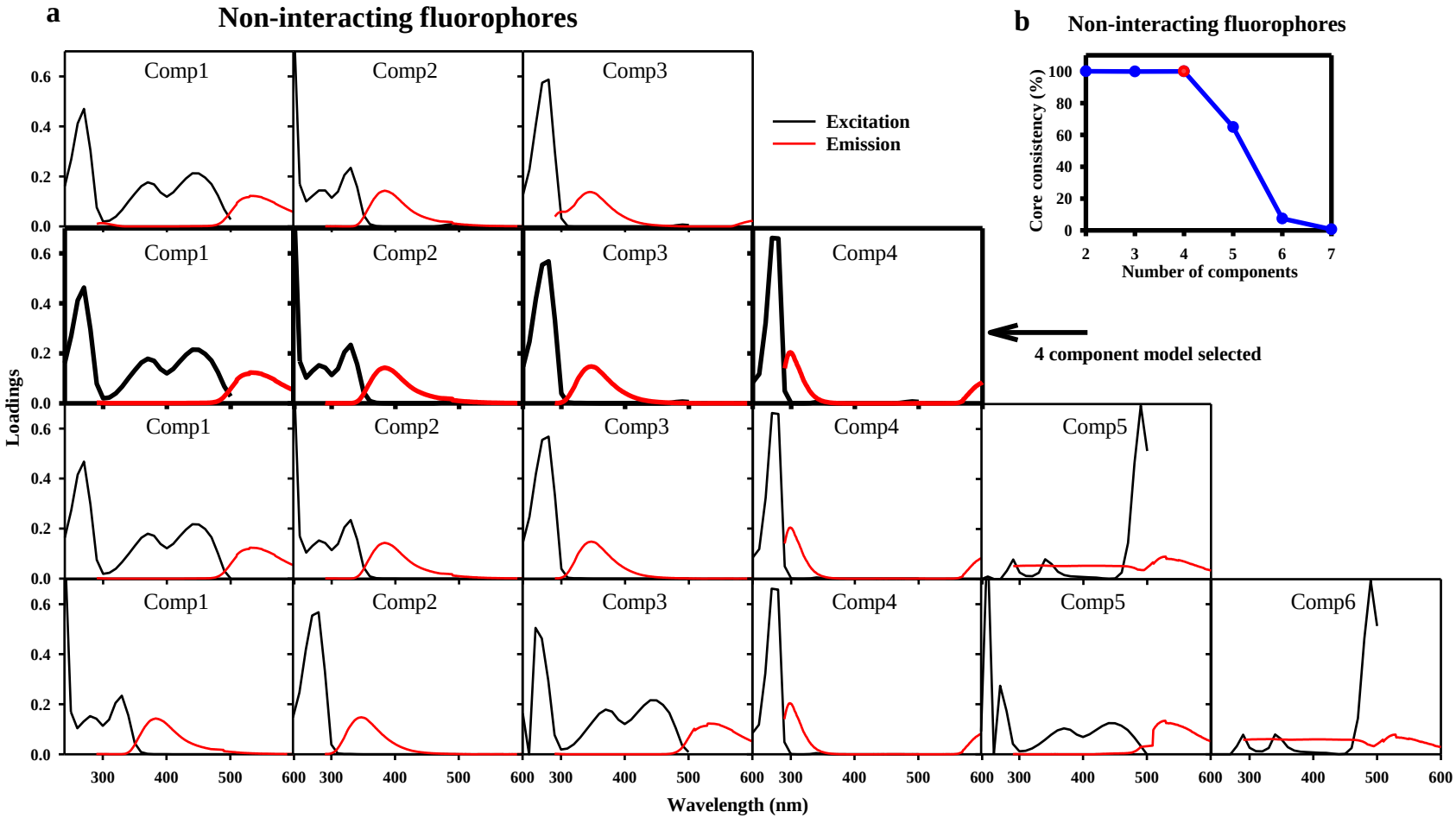

Figure S6. 2: (**a**) Loadings generated by PARAFAC for models with increasing numbers of components for the non-interacting fluorophore dataset. The components chosen for the ideal model are bolded. (**b**) The core consistency with increasing numbers of components with the red point indicating the number of components chosen for the ideal model

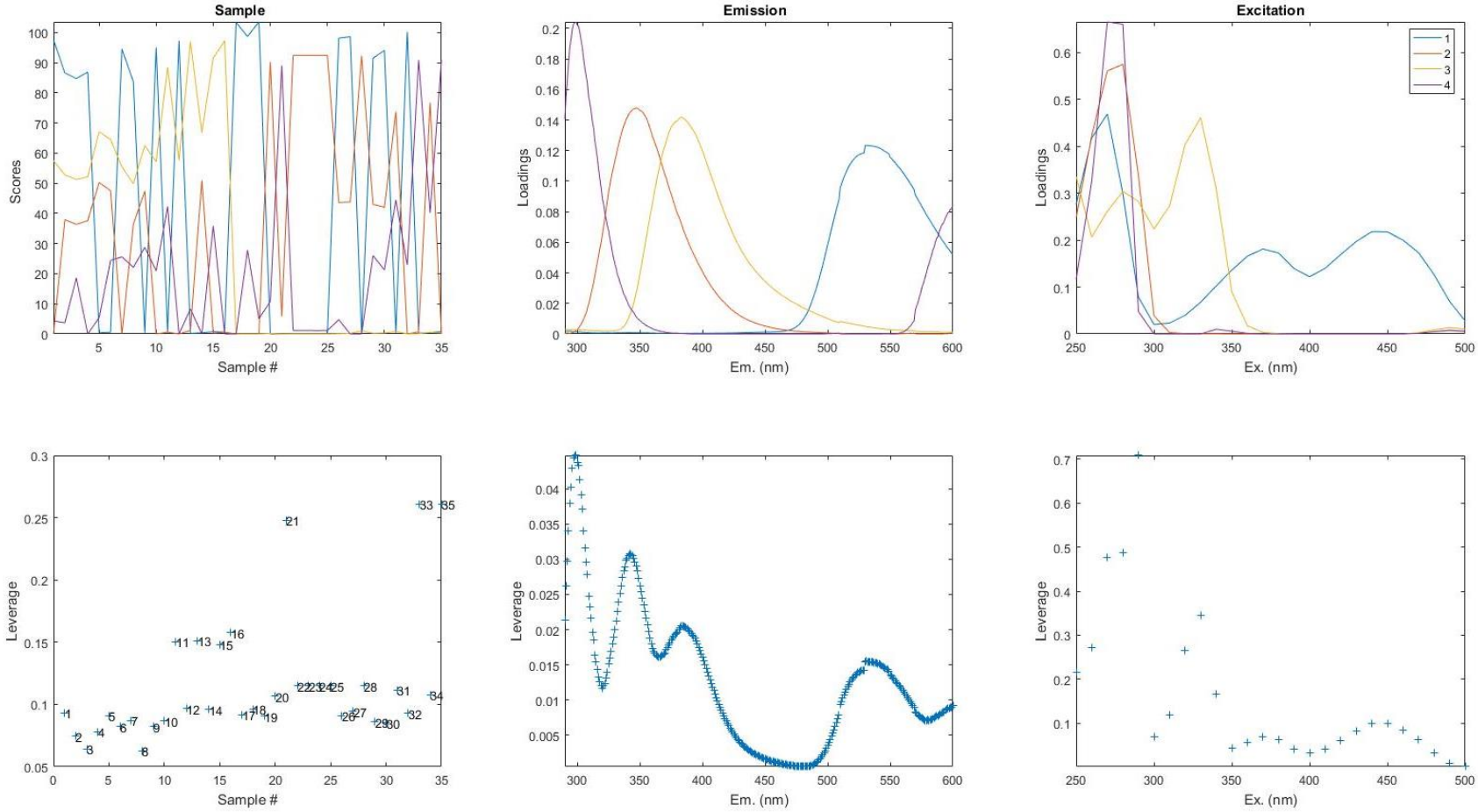

Figure S6.3: Non-interacting fluorophore dataset, loadings and Leverages for the 4 component model.

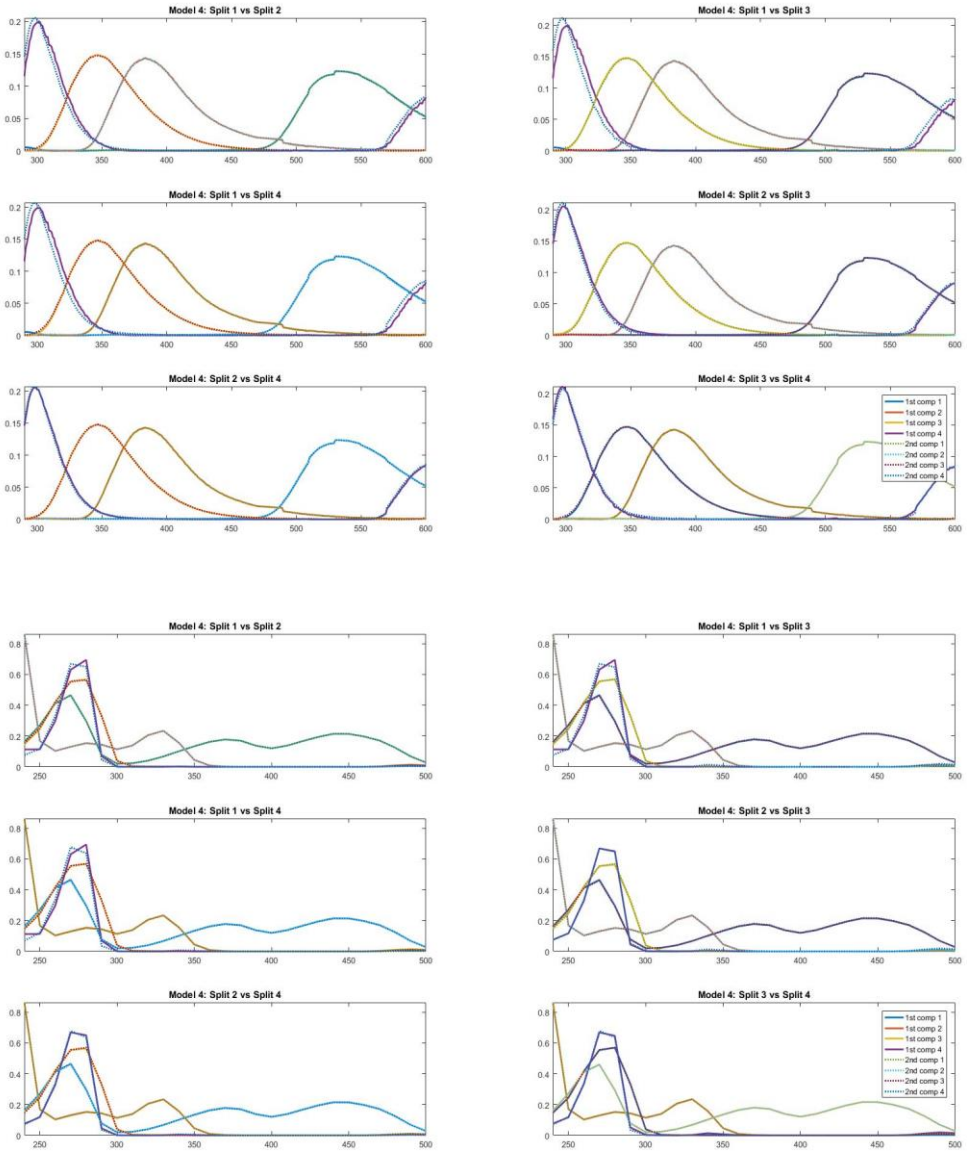

Figure S6.4: Non-interacting fluorophore dataset, split-half validation

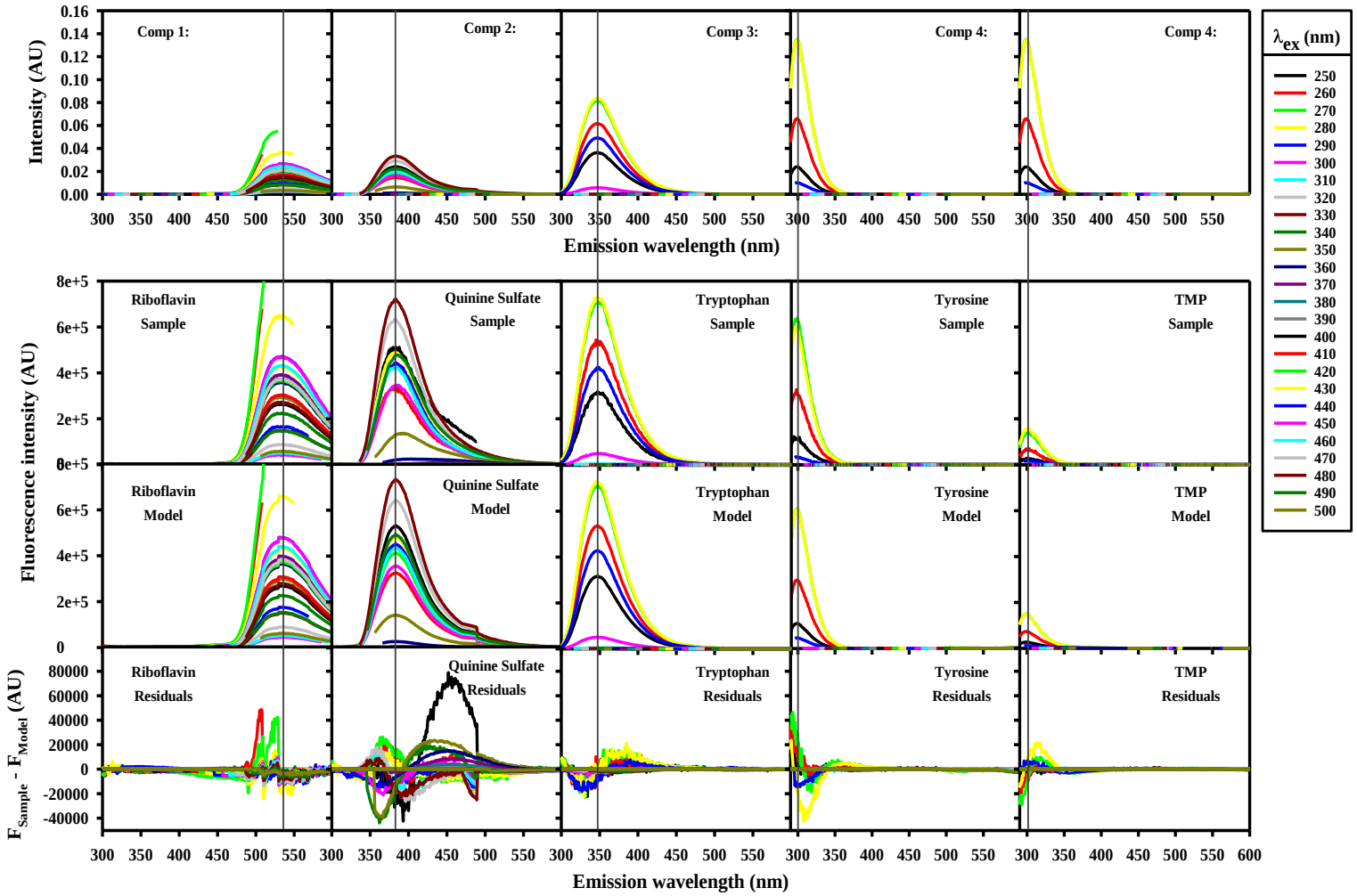

Figure S6.5: Emission spectra of (**row 1**) four components determined by PARAFAC model, (**row 2**) select samples input into the model, (**row 3**) final PARAFAC model for the same samples, and (**row 4**) the residual emission for each sample which is the emission not accounted for by the model (Fsample – Fmodel).

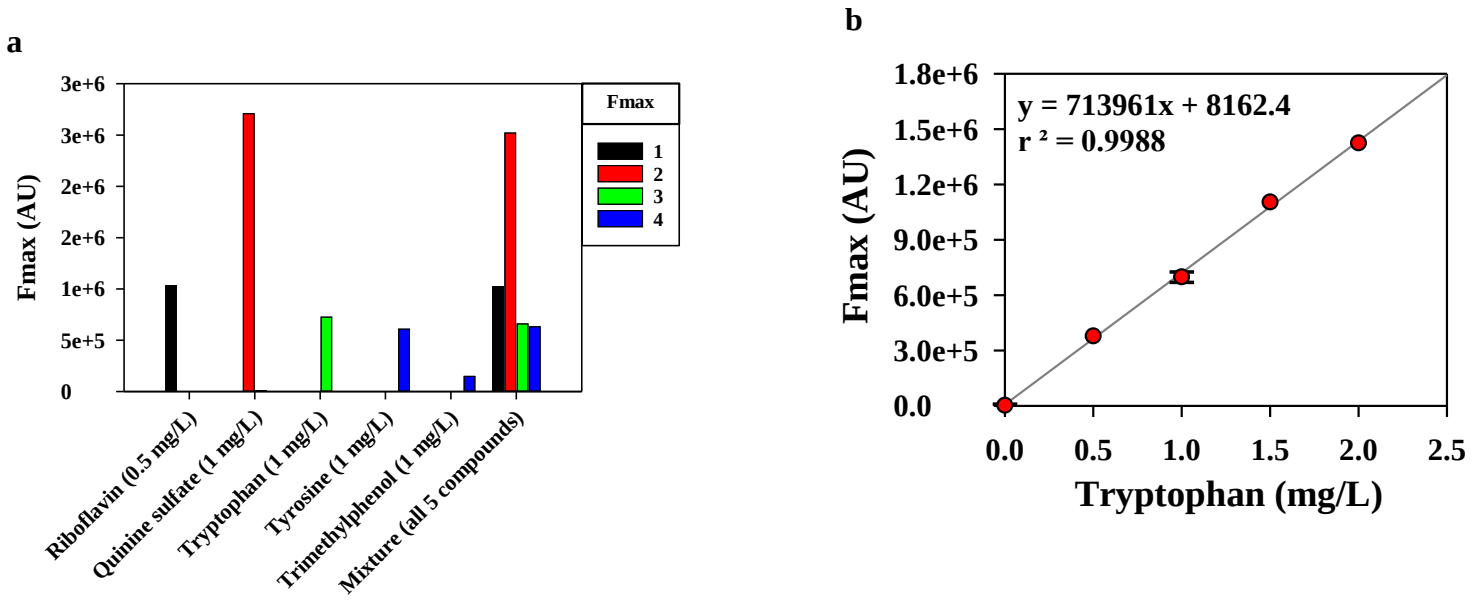

Figure S6.6: a) Fmax values for each component (1-4) for select samples and **b)** Fmax values (component 3: identified as tryptophan) for samples with increasing amounts of tryptophan error bars for the 0.0 and 1.0 mg/L points are based on the standard deviation calculated from 15 individual samples.

Table S6.3: Composition of samples included in the non-interacting fluorophore + SRFA dataset.

	Compondes included in sample					
Sample #	Riboflavin	Quinine sulphate	Tryptophan	Tyrosine	Trimethyl-phenol	SRFA
1	✓	✓	✓	✓	✓	✓
2						✓
3	✓	✓			✓	
4	✓	✓	✓		✓	
5	✓	✓	✓	✓		
6	✓	✓	✓			
7		✓	✓		✓	
8		✓	✓	✓		
9	✓	✓		✓	✓	
10	✓	✓	✓	✓	✓	
11		✓		✓	✓	
12	✓	✓		✓		
13		✓		✓	✓	
14	✓	✓				
15		✓			✓	
16		✓	✓			
17		✓		✓		
18		✓				
19	✓					
20						✓
21						✓
22		✓				✓
23	✓					✓
24					✓	✓
25				✓		✓
26			✓			✓
27						✓
28	✓			✓	✓	
29	✓				✓	
30			✓		✓	
31					✓	
32			✓			
33			✓			
34			✓			
35			✓			
36	✓		✓		✓	
37	✓		✓			
38			✓			
39	✓		✓	✓	✓	
40	✓		✓	✓		
41			✓	✓	✓	
42	✓			✓		
43				✓	✓	
44			✓	✓		
45				✓		

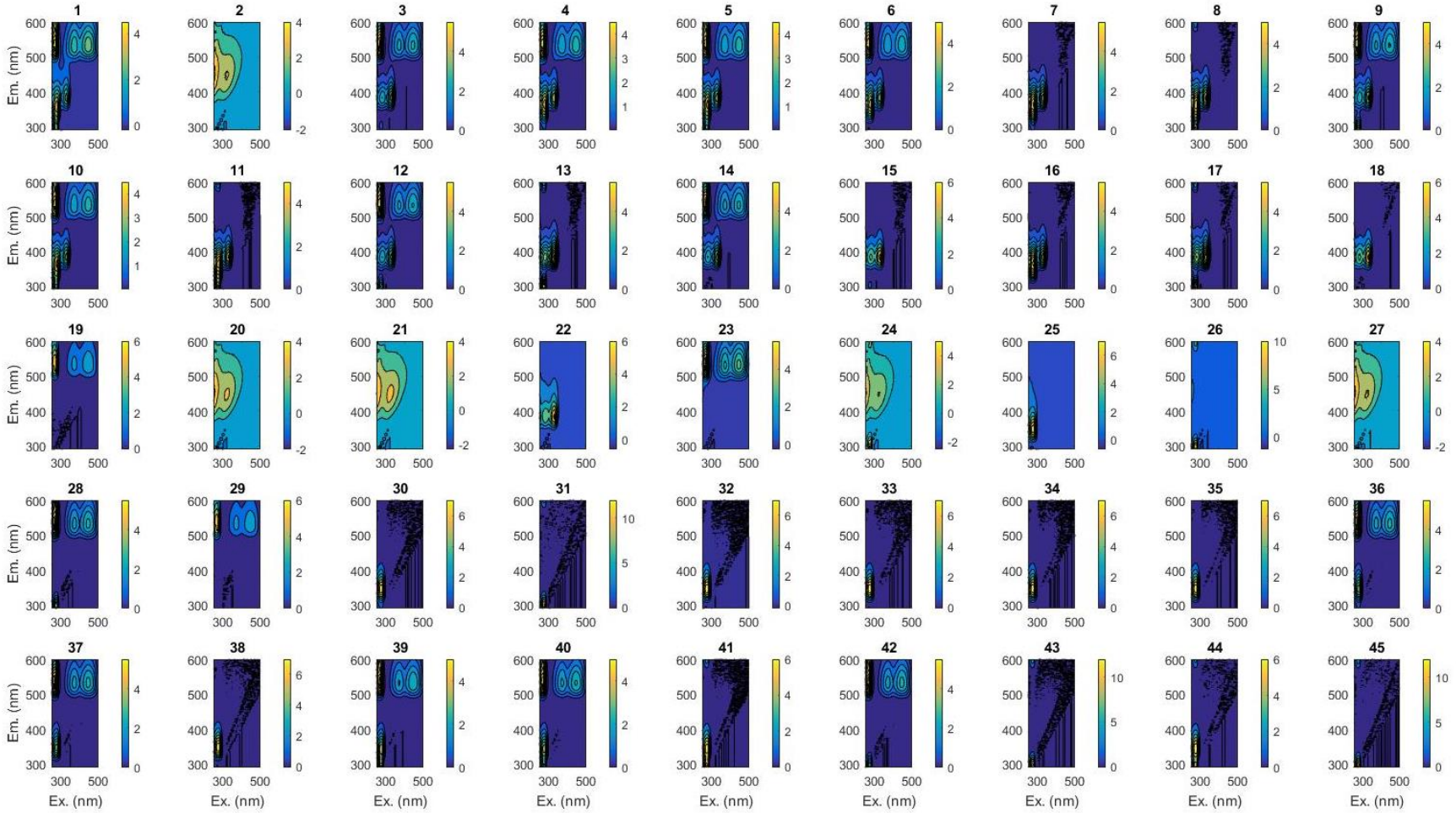

Figure S6.7: EEMs for samples included in the non-interacting fluorophore + SRFA dataset after normalization

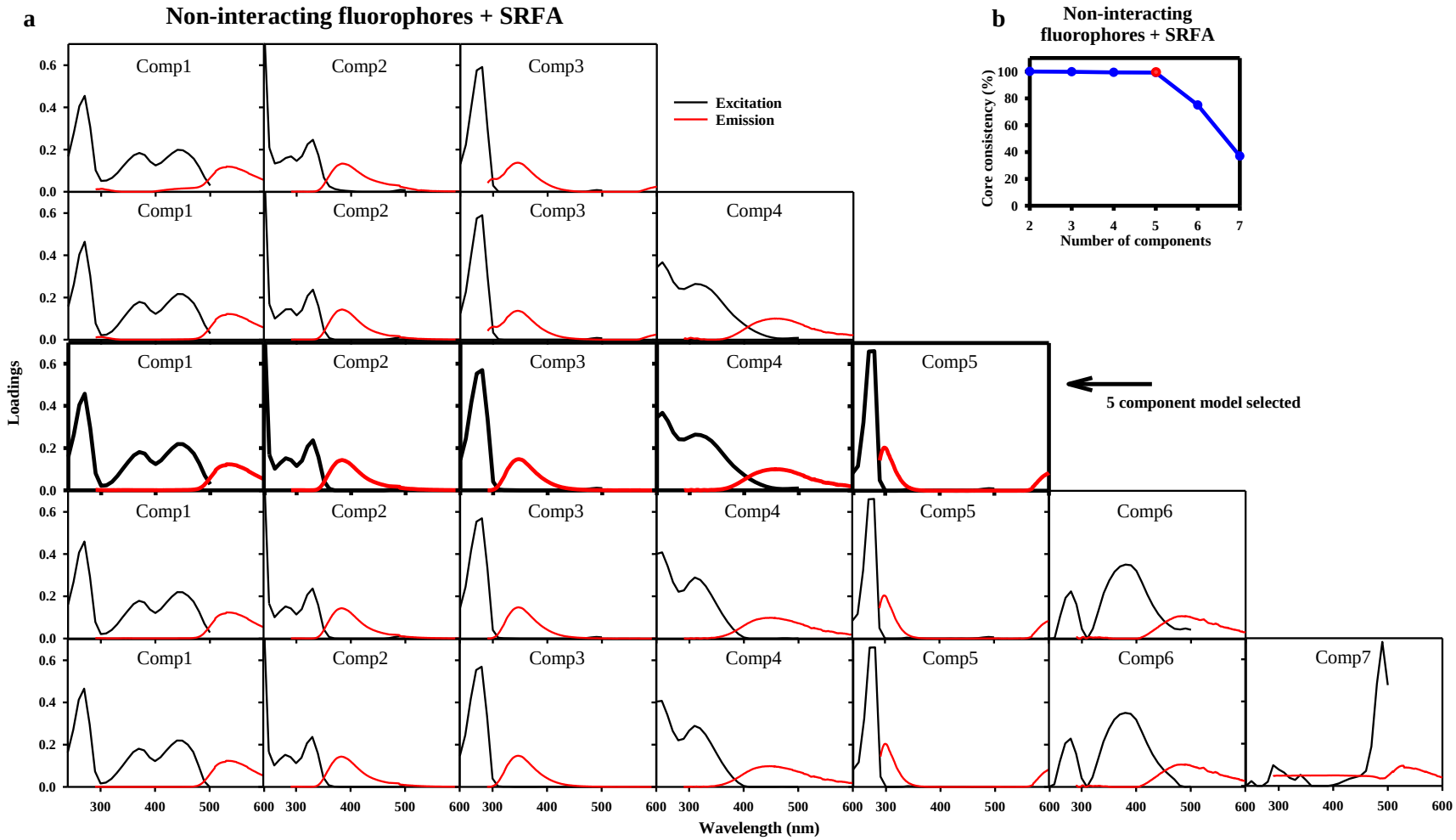

Figure S6.8: (**a**) Loadings generated by PARAFAC for models with increasing numbers of components for the non-interacting fluorophore + SRFA dataset. The components chosen for the ideal model are bolded. (**b**) The core consistency with increasing numbers of components with the red point indicating the number of components chosen for the ideal model

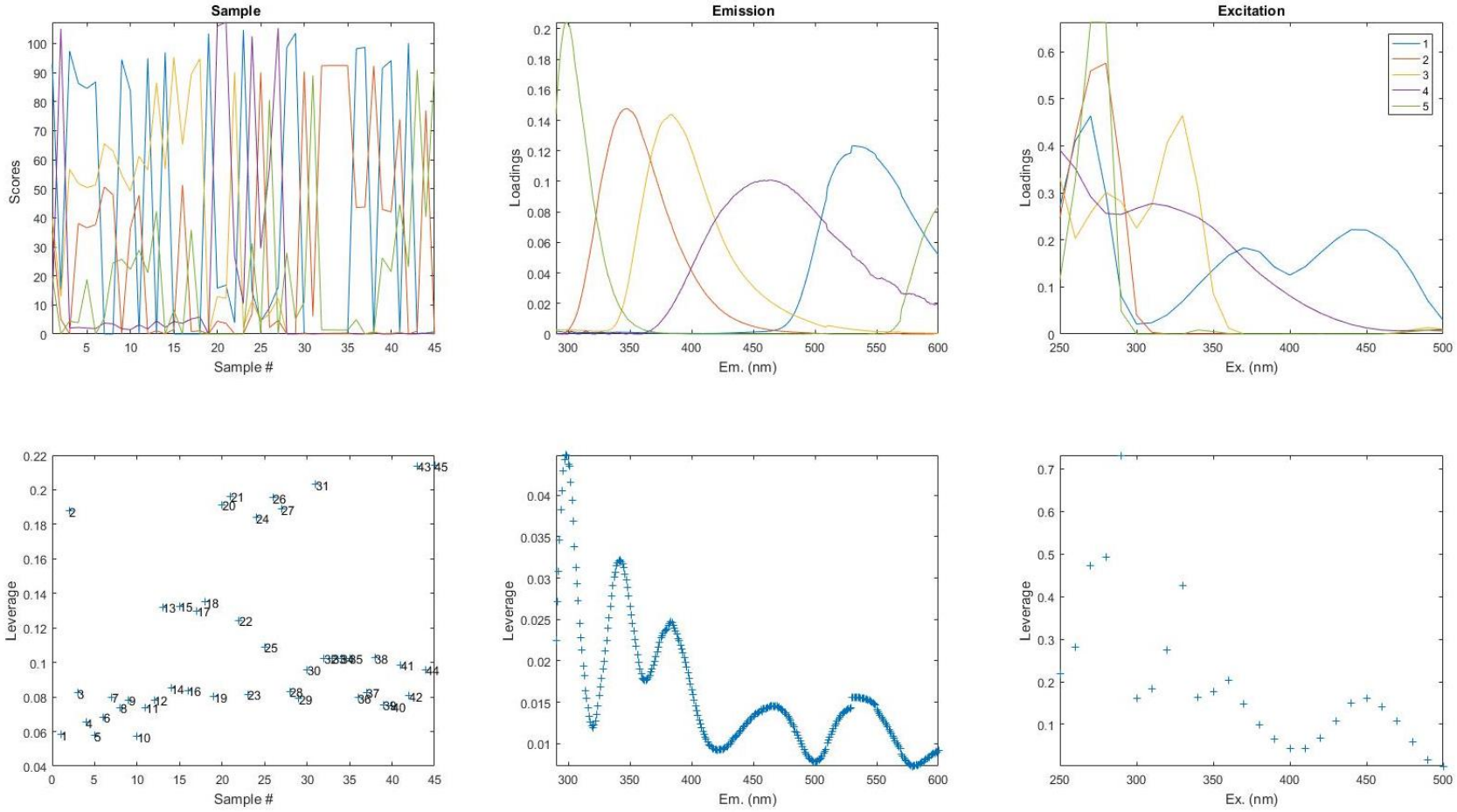

Figure S6.9: Non-interacting fluorophore + SRFA dataset, loadings and Leverages for the 5 component model.

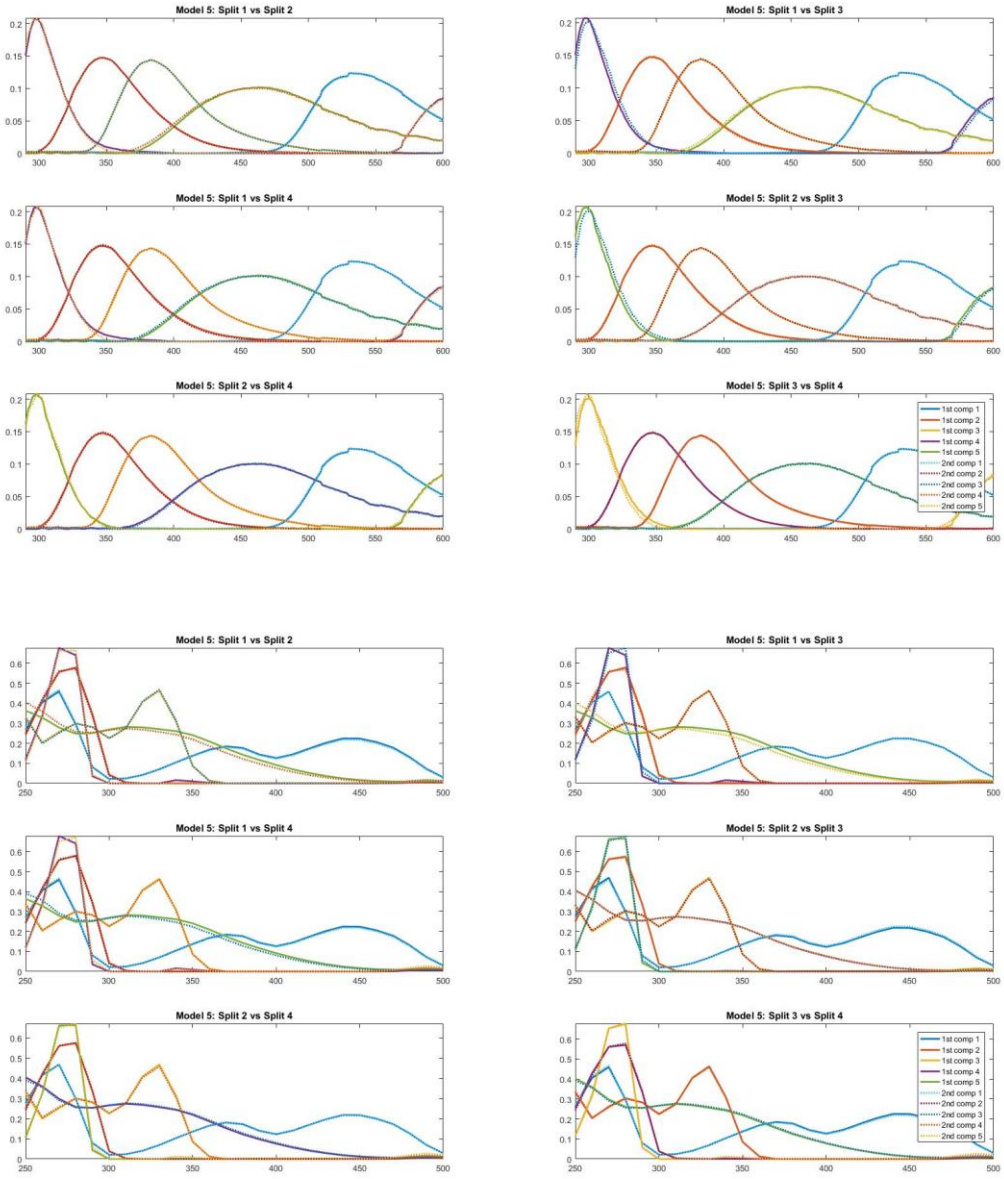

Figure S6.10: non-interacting fluorophore + SRFA dataset, split-half validation

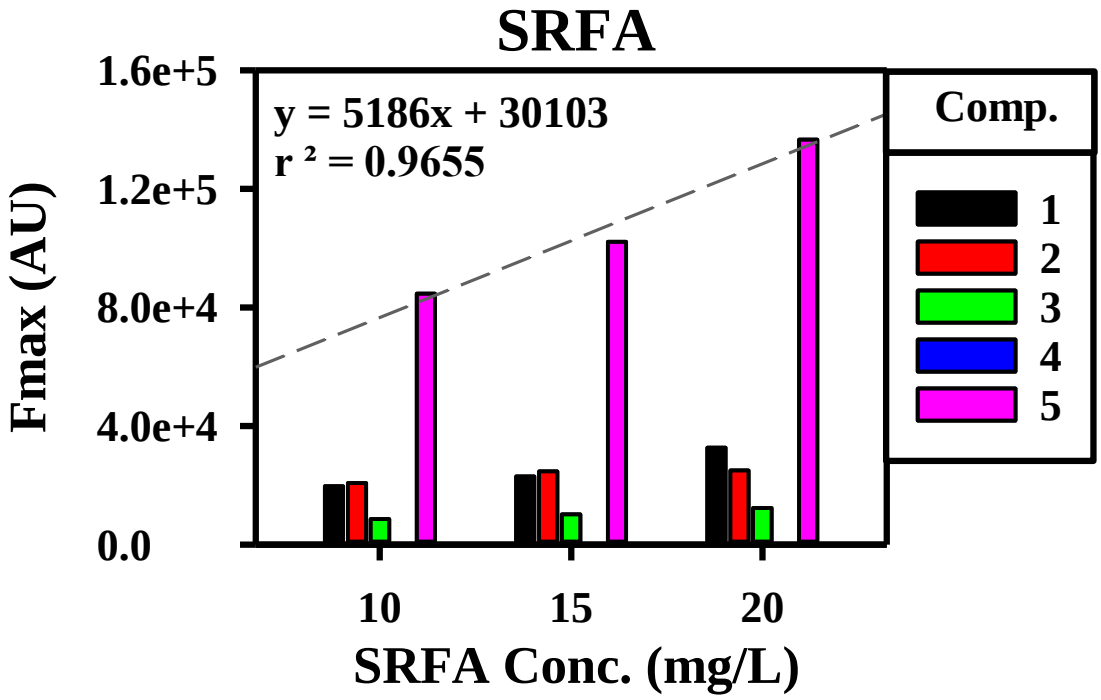

Figure S6.11: Fmax for components 1-5 for three samples containing just SRFA at varying concentrations. The regression line is for the 5th component that is most associated with SRFA.

Table S6. 4: Concentration of Pyrene samples included in the dataset

Sample #	Concentration of Pyrene (mM)
1	0.09
2	0.10
3	0.16
4	0.23
5	0.35
6	0.53
7	0.79
8	1.19
9	1.78
10	2.67
11	4.00
12	6.00

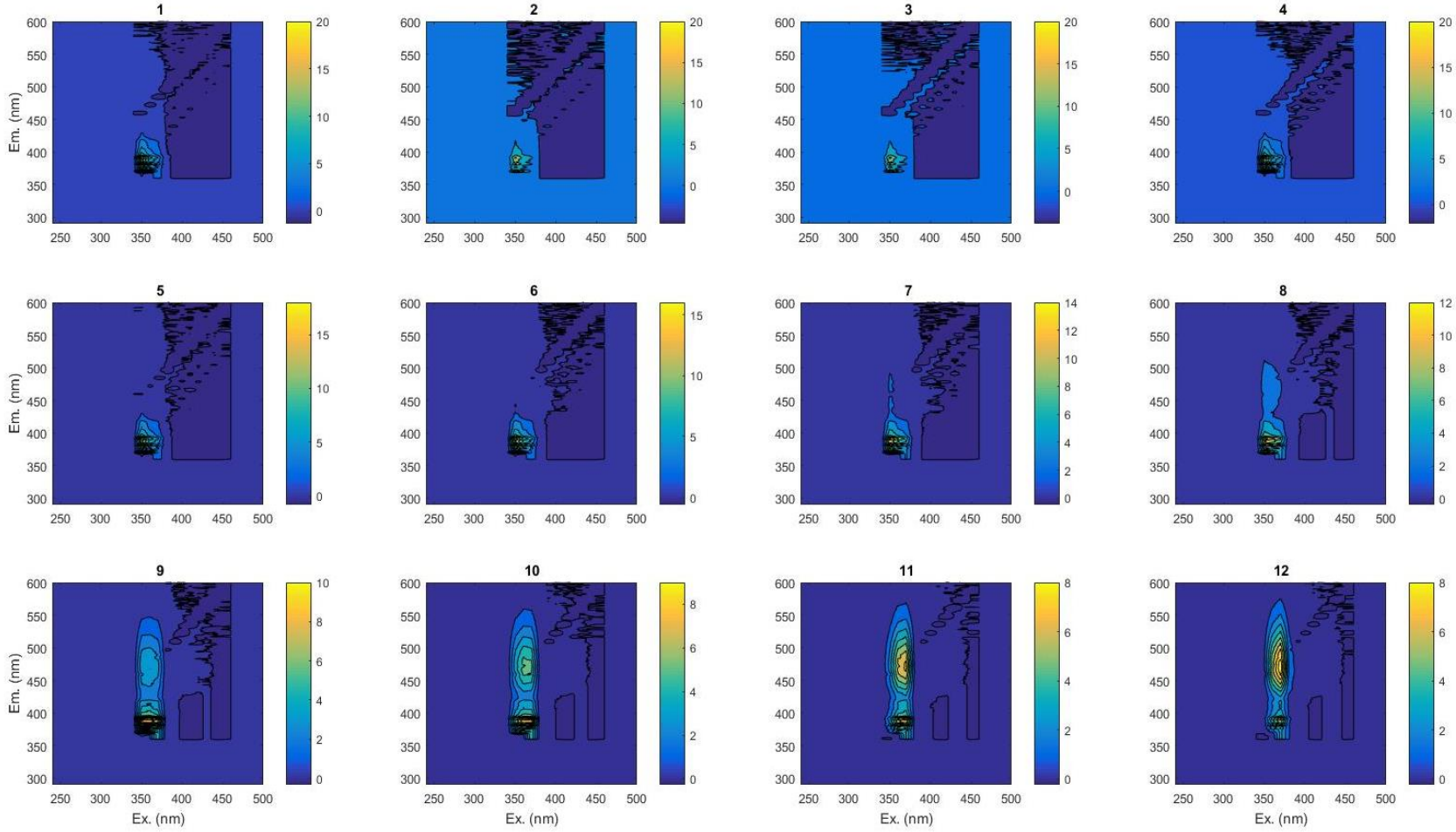

Figure S6.12: EEMs for samples included in the pyrene dataset after normalization

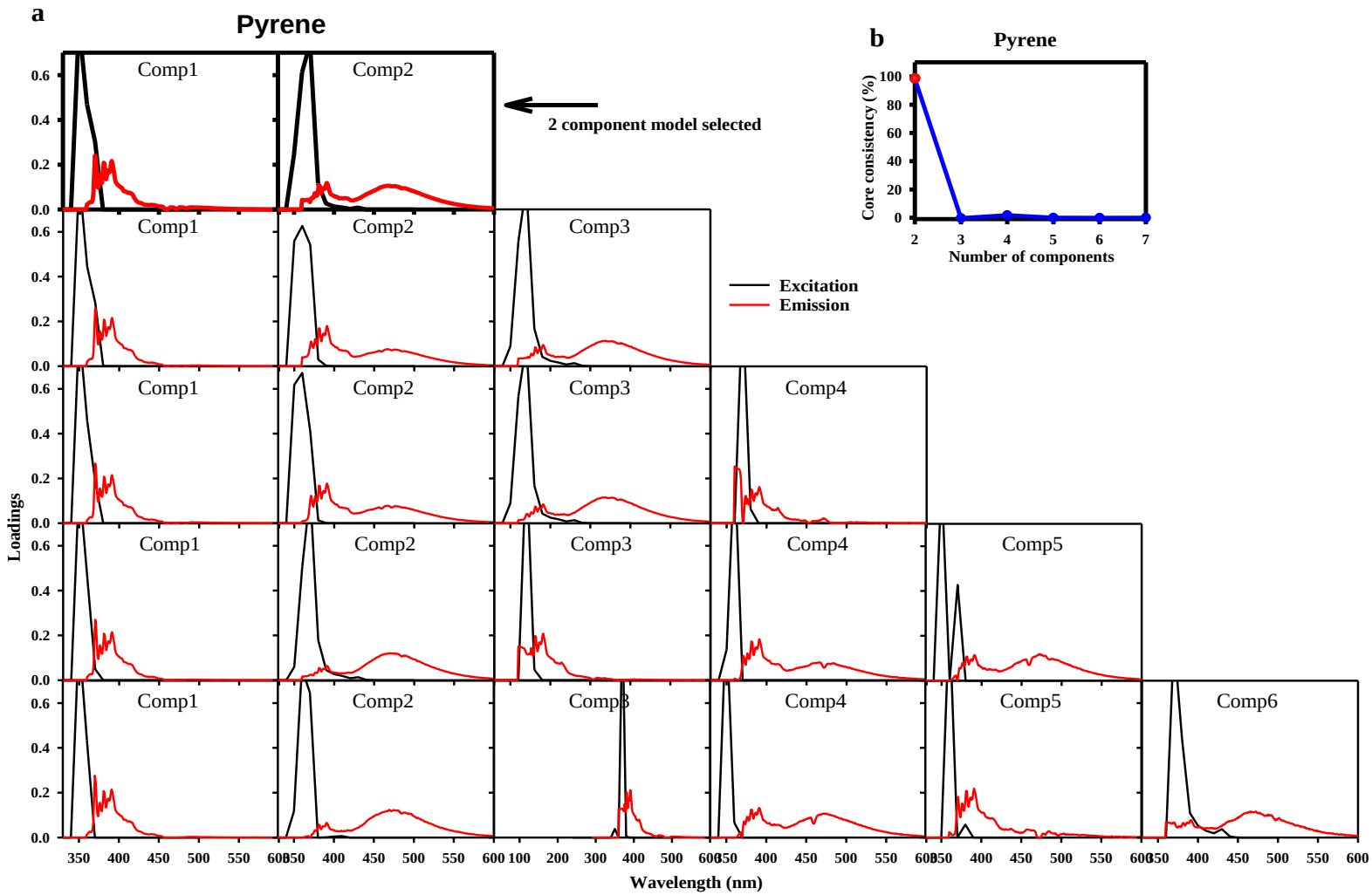

Figure S6.13: (**a**) Loadings generated by PARAFAC for models with increasing numbers of components for the pyrene dataset. The components chosen for the ideal model are bolded. (**b**) The core consistency with increasing numbers of components with the red point indicating the number of components chosen for the ideal model.

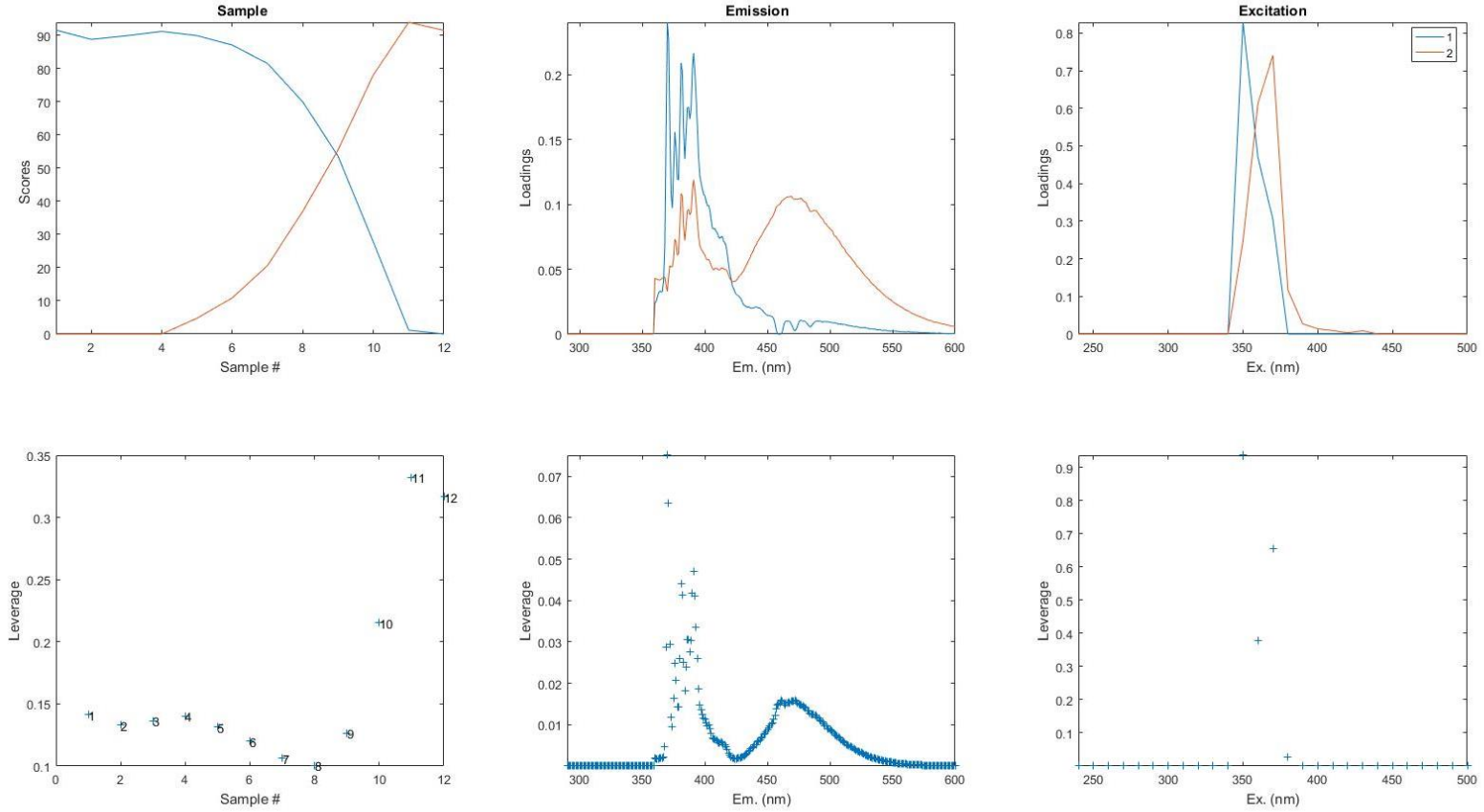

Figure S6.14: Pyrene dataset, loadings (**top**) and Leverages (**bottom**) for the two component model.

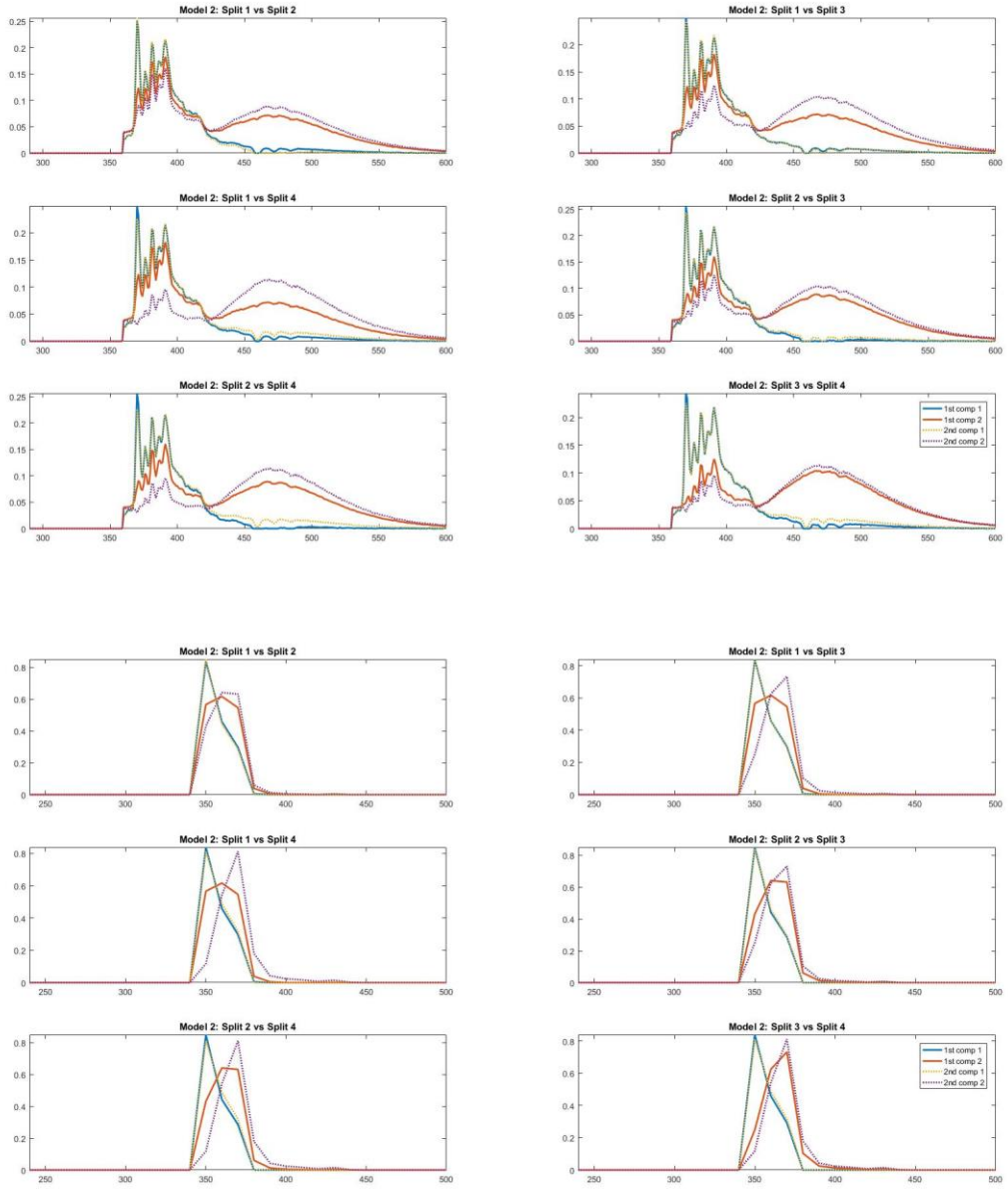

Figure S6.15: Pyrene dataset, split-half validation; emission spectra (**top**) and excitation spectra (**bottom**) for a two component model.

Table S6.5: Samples included in the HA and FA reference materials dataset

Sample #	Reference material	pH	$NaBH_4$ reduced
1	SRFA	3	
2	SRFA	7	
3	SRFA	10	
4	SRFA	3	✓
5	SRFA	7	✓
6	SRFA	10	✓
7	SRHA	3	
8	SRHA	7	
9	SRHA	10	
10	SRHA	3	✓
11	SRHA	7	✓
12	SRHA	10	✓
13	LHA	3	
14	LHA	7	
15	LHA	10	
16	LHA	3	✓
17	LHA	7	✓
18	LHA	10	✓
19	PLFA	3	
20	PLFA	7	
21	PLFA	10	
22	PLFA	3	✓
23	PLFA	7	✓
24	PLFA	10	✓
25	ESHA	3	
26	ESHA	7	
27	ESHA	10	
28	ESHA	3	✓
29	ESHA	7	✓
30	ESHA	10	✓
31	LAC	3	
32	LAC	7	
33	LAC	10	
34	LAC	3	✓
35	LAC	7	✓
36	LAC	10	✓

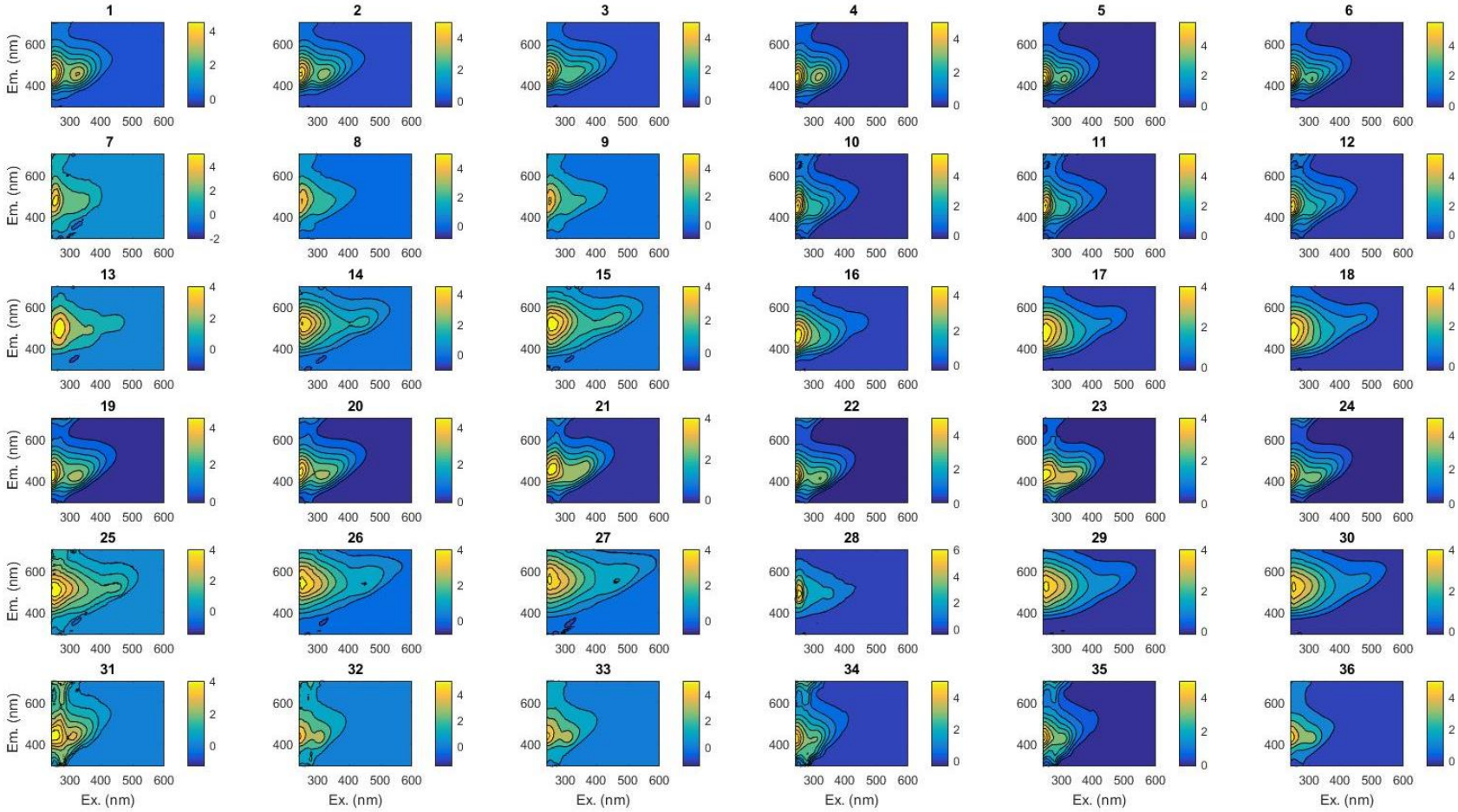

Figure S6.16: EEMs for samples included in the HA and FA reference materials dataset after normalization

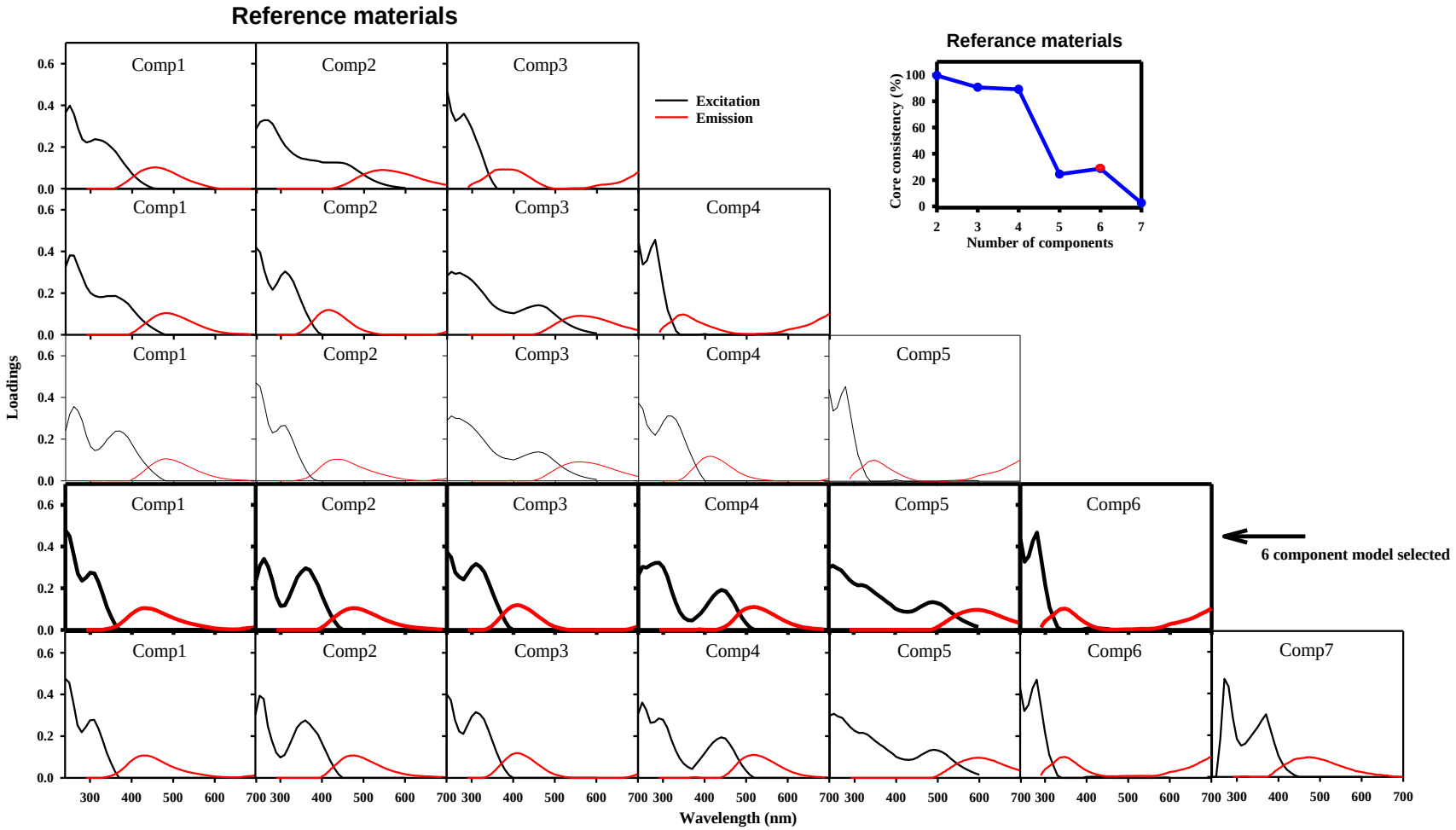

Figure S6.17: (**a**) Loadings generated by PARAFAC for models with increasing numbers of components for the HA and FA reference materials dataset. The components chosen for the ideal model are bolded. (**b**) The core consistency with increasing numbers of components with the red point indicating the number of components chosen for the ideal model.

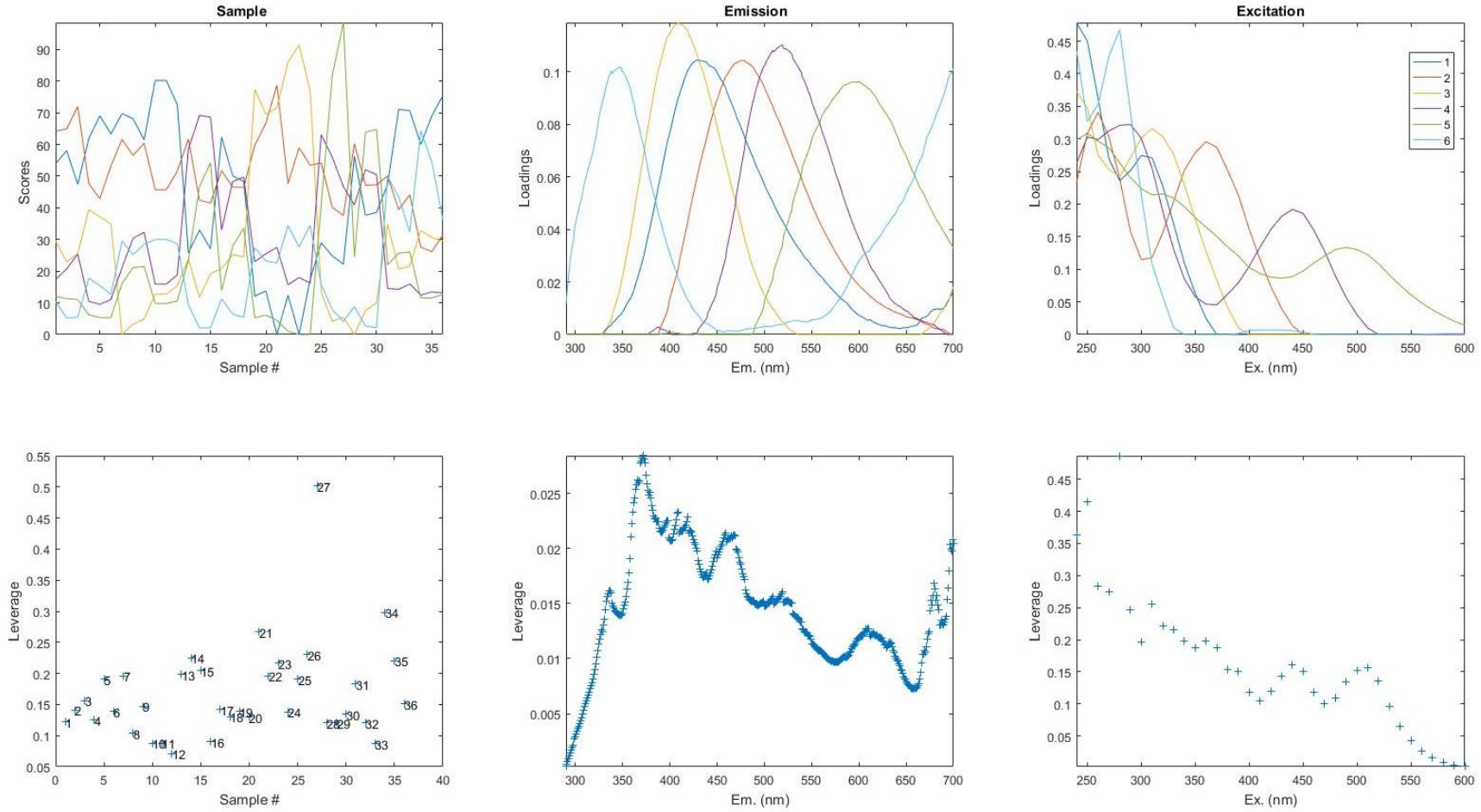

Figure S6.18: HA and FA reference materials dataset, loadings (**top**) and Leverages (**bottom**) for the two component model.

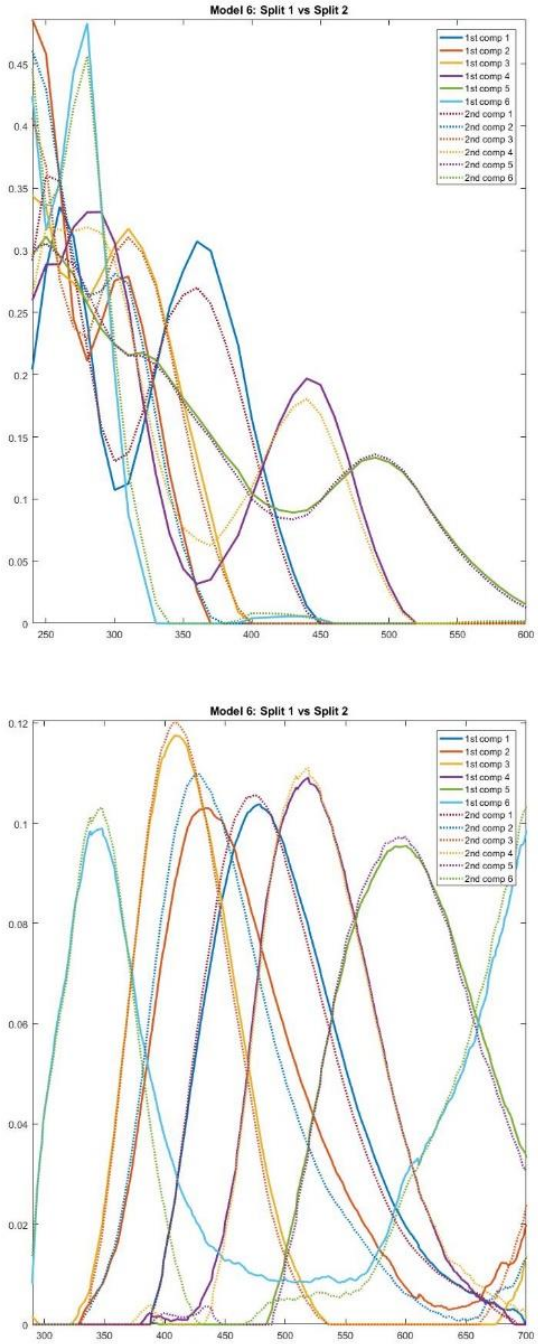

Figure S6.19: HA and FA reference materials dataset, split-half validation; emission spectra (**top**) and excitation spectra (**bottom**) for a six component model.

Table S6.6: Location and depth of the filtered natural water samples used in the NPO Untreated dataset.

Sample #	Location	Depth (m)
1	NPO: St. ALOHA	991
2	NPO: St. ALOHA	1486
3	NPO: St. ALOHA	15
4	NPO: St. ALOHA	2470
5	NPO: St. ALOHA	298
6	NPO: St. ALOHA	3449
7	NPO: St. ALOHA	4425
8	NPO: St. ALOHA	496
9	NPO: St. ALOHA	596
10	NPO: St. ALOHA	694
11	NPO: St. ALOHA	794

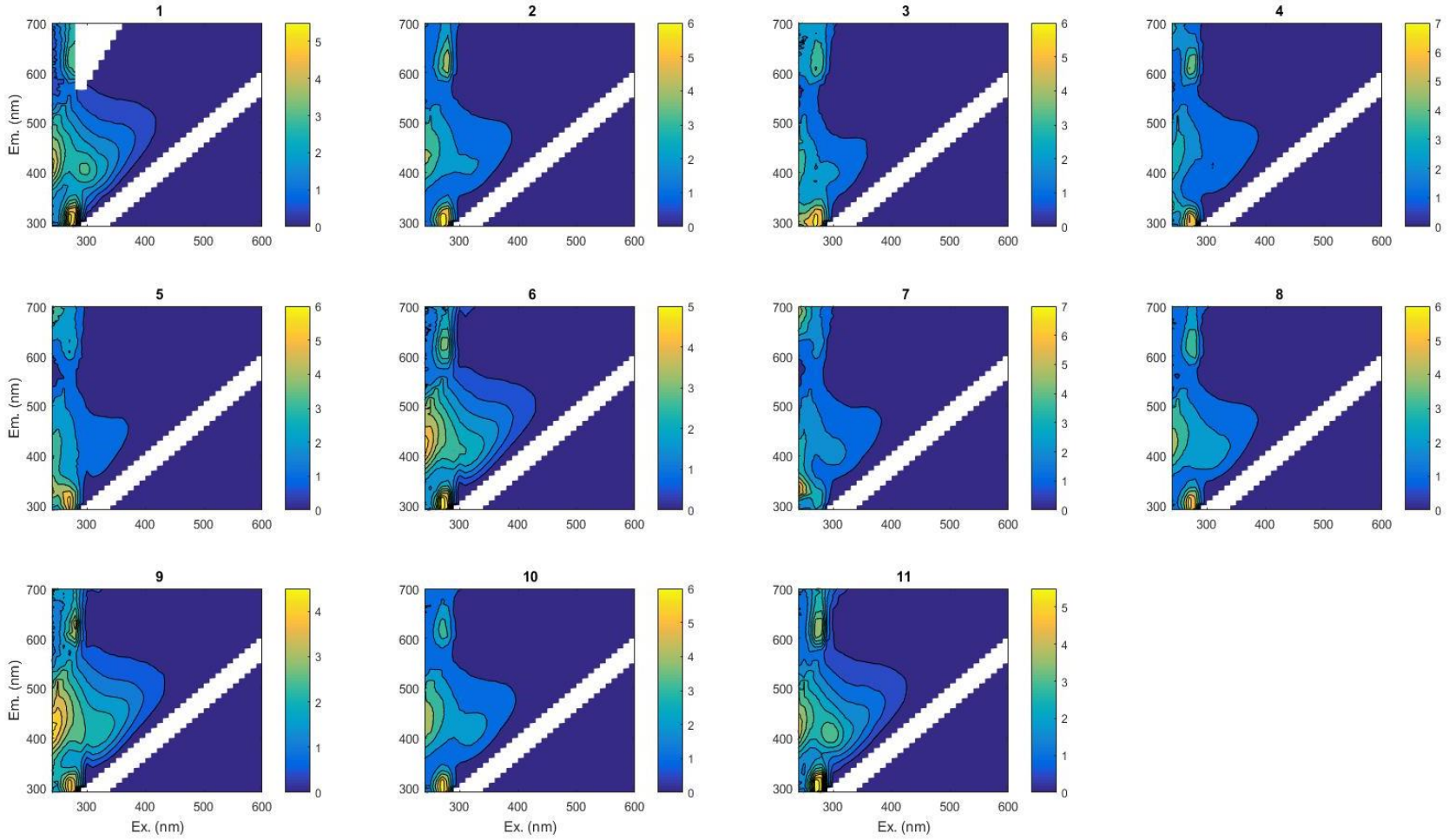

Figure S6.20: EEMs for samples included in the NPO untreated dataset after normalization

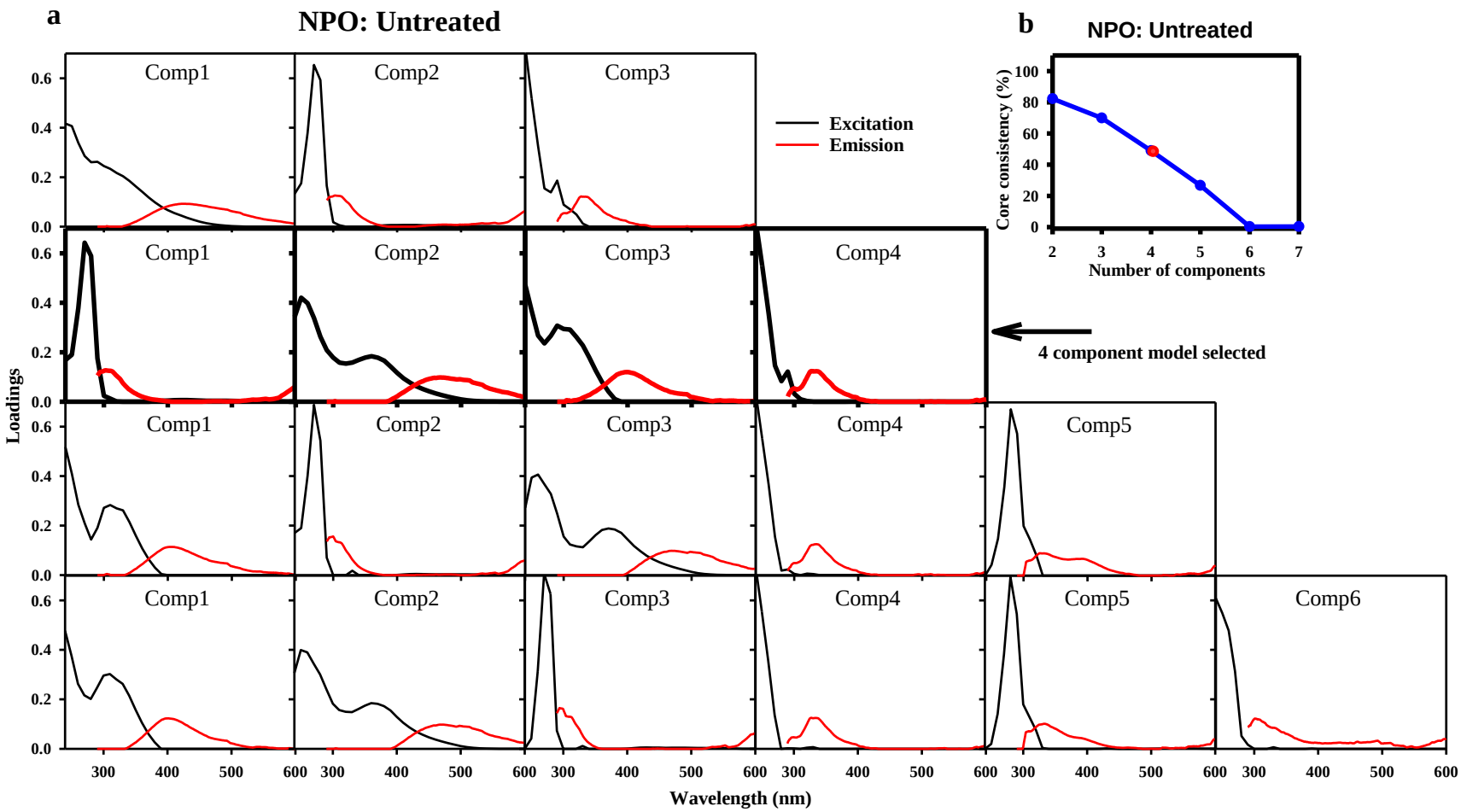

Figure S6.21: (**a**) Loadings generated by PARAFAC for models with increasing numbers of components for the NPO untreated dataset. The components chosen for the ideal model are bolded. (**b**) The core consistency with increasing numbers of components with the red point indicating the number of components chosen for the ideal model.

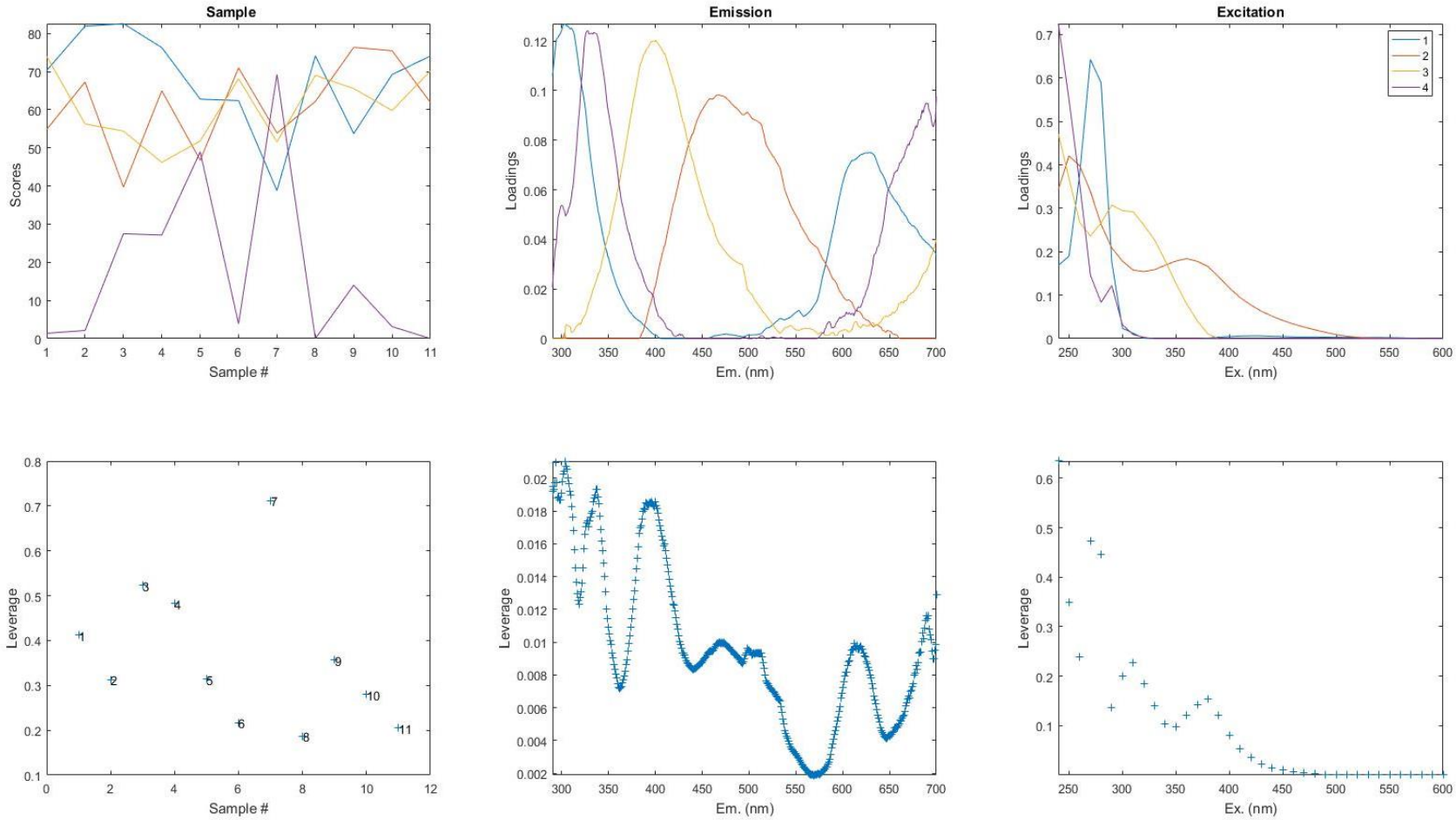

Figure S6.22: NPO untreated dataset, loadings (**top**) and Leverages (**bottom**) for the four component model.

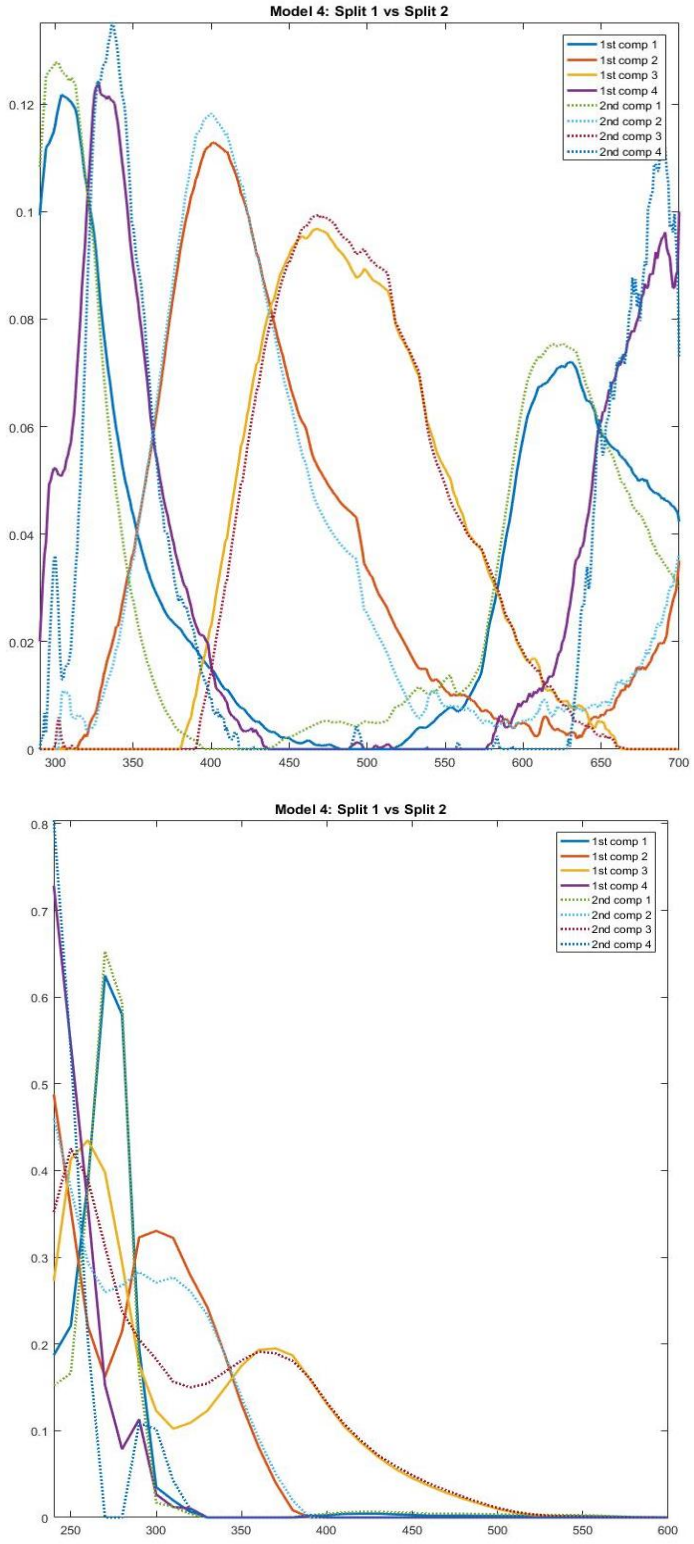

Figure S6.23: NPO untreated dataset, split-half validation; emission spectra (**top**) and excitation spectra (**bottom**) for a four component model.

Table S6.7: Location and depth of the filtered natural water samples used in the NPO reduced dataset. Each sample was reduced with $NaBH_4$ prior to collection of the EEM.

Sample #	Location	Depth (m)	$NaBH_4$ reduced
1	NPO: St. ALOHA	991	✓
2	NPO: St. ALOHA	1486	✓
3	NPO: St. ALOHA	15	✓
4	NPO: St. ALOHA	2470	✓
5	NPO: St. ALOHA	298	✓
6	NPO: St. ALOHA	3449	✓
7	NPO: St. ALOHA	4425	✓
8	NPO: St. ALOHA	496	✓
9	NPO: St. ALOHA	596	✓
10	NPO: St. ALOHA	694	✓
11	NPO: St. ALOHA	794	✓

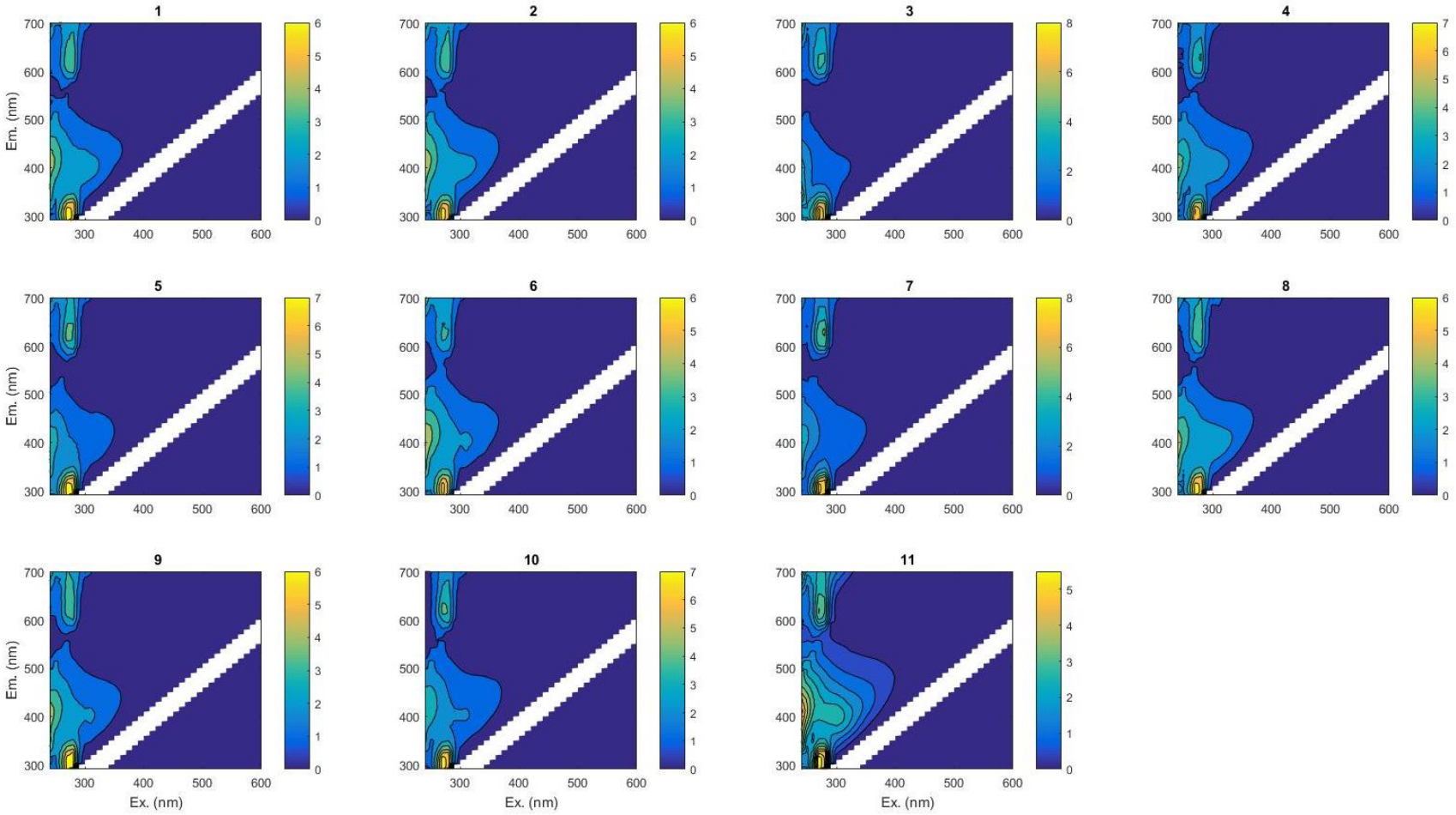

Figure S6.24: EEMs for samples included in the NPO reduced dataset after normalization

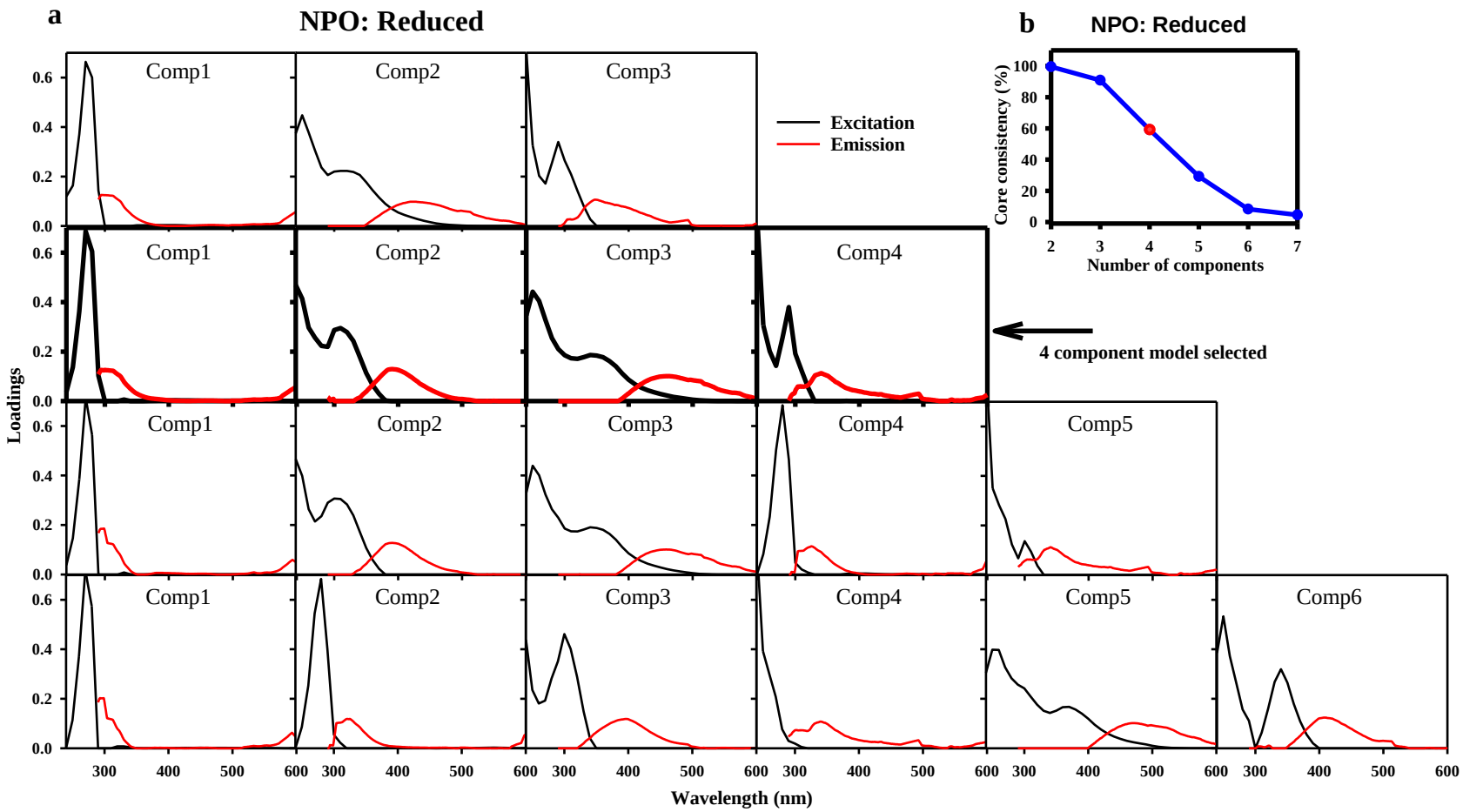

Figure S6.25: (**a**) Loadings generated by PARAFAC for models with increasing numbers of components for the NPO reduced dataset. The components chosen for the ideal model are bolded. (**b**) The core consistency with increasing numbers of components with the red point indicating the number of components chosen for the ideal model

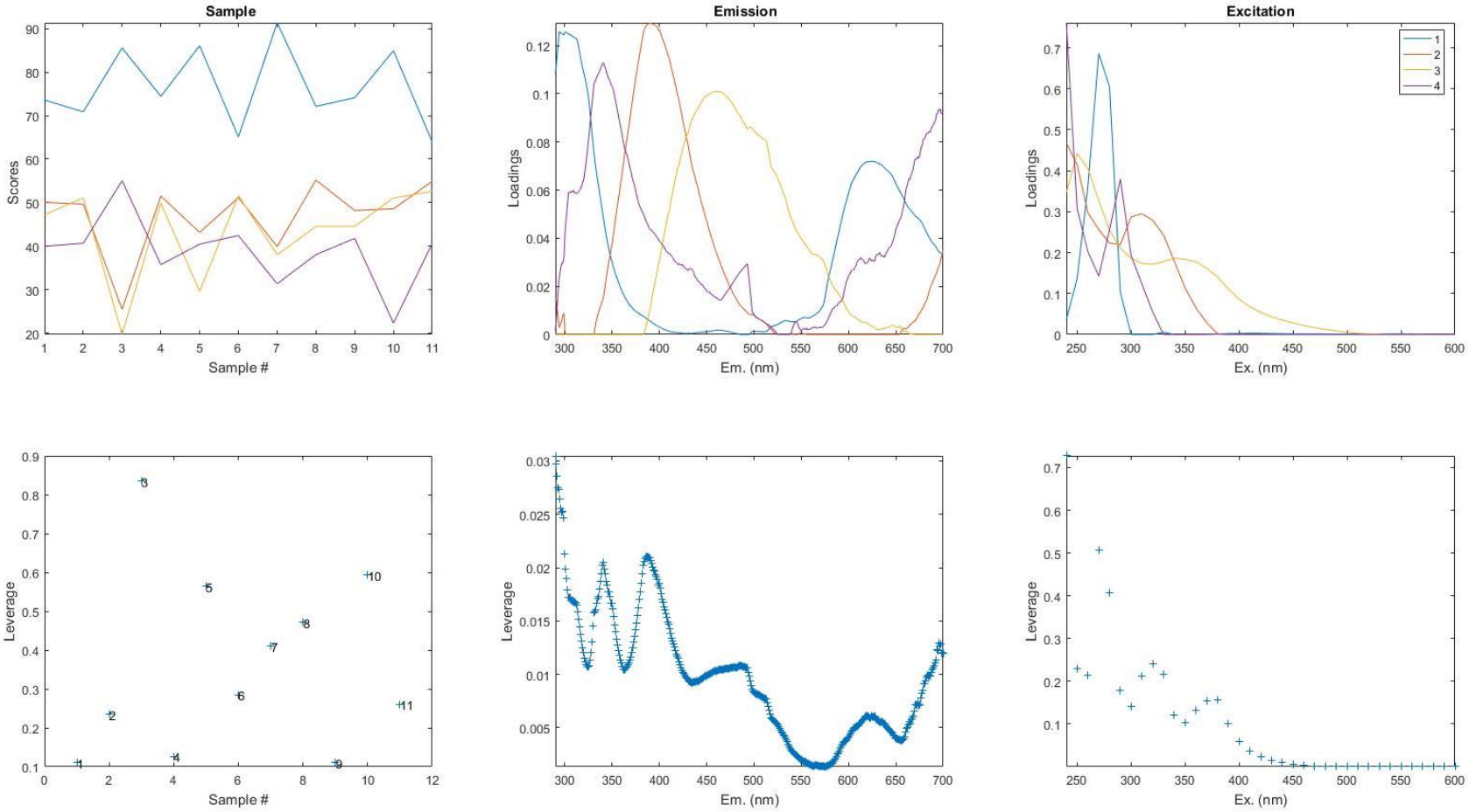

Figure S6.26: NPO reduced dataset, loadings (**top**) and leverages (**bottom**) for the four component model.

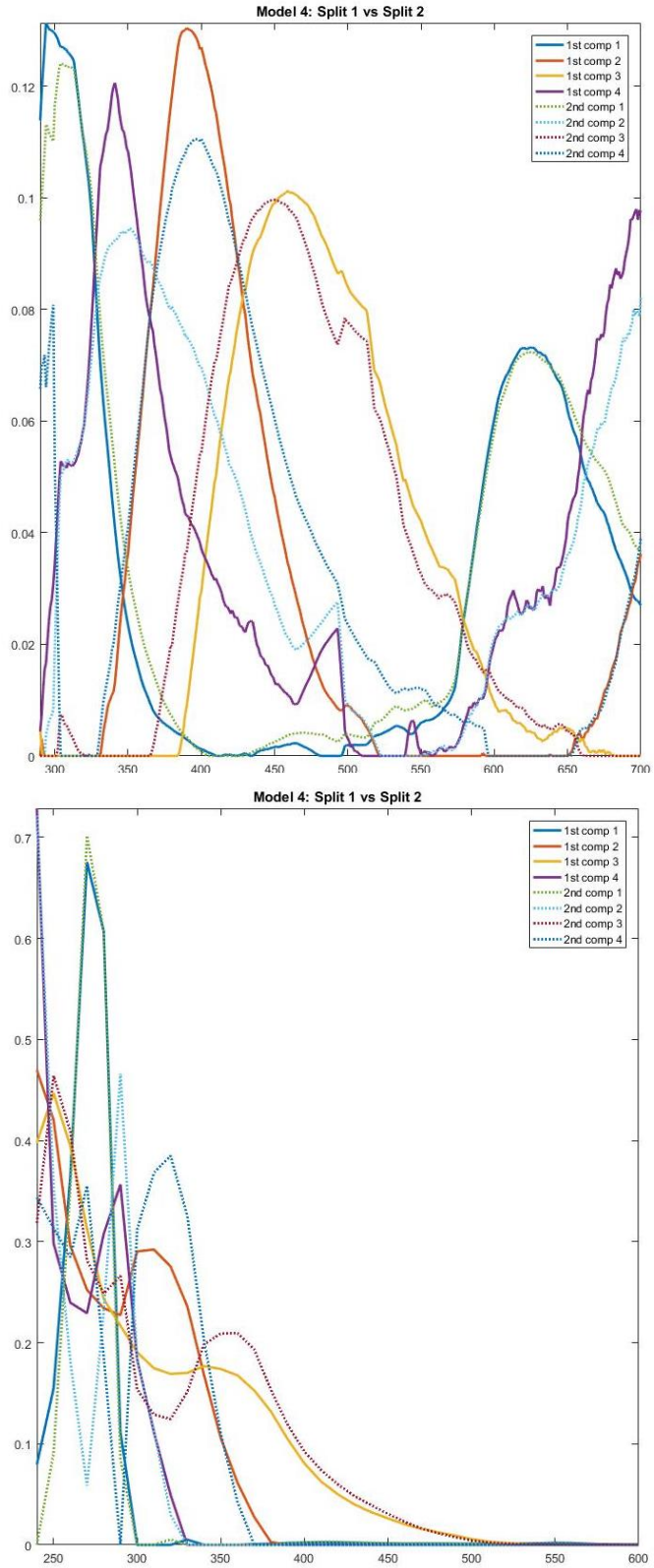

Figure S6.27: NPO reduced dataset, split-half validation; emission spectra (**top**) and excitation spectra (**bottom**) for a four component model.

Table S6.8: Location, station number and date collected for both unfiltered and filtered natural water samples used in the CB samples dataset.

Sample #	Location	Date collected	Station #	Filtered
1	Bodkin Point Shoal	11/13/2018	0	
2	Bodkin Point Shoal	11/13/2018	1	
3	Bodkin Creek	11/13/2018	2	
4	Bodkin Creek	11/13/2018	3	
5	Goose Cove	11/13/2018	4	
6	Goose Cove	11/13/2018	5	
7	Goose Cove	11/13/2018	6	
8	Goose Cove	11/13/2018	7	
9	Goose Cove	11/13/2018	8	
10	Main Creek	11/13/2018	9	
11	Goose Cove	11/13/2018	10	
12	Bodkin Point Shoal	11/13/2018	0	✓
13	Bodkin Point Shoal	11/13/2018	1	✓
14	Bodkin Creek	11/13/2018	2	✓
15	Bodkin Creek	11/13/2018	3	✓
16	Goose Cove	11/13/2018	4	✓
17	Goose Cove	11/13/2018	5	✓
18	Goose Cove	11/13/2018	6	✓
19	Goose Cove	11/13/2018	7	✓
20	Goose Cove	11/13/2018	8	✓
21	Goose Cove	11/13/2018	9	✓
22	Goose Cove	11/13/2018	10	✓
23	Bodkin Point Shoal	10/31/2018	1	✓
24	Bodkin Creek	10/31/2018	2	✓
25	Bodkin Creek	10/31/2018	3	✓
26	Goose Cove	10/31/2018	4	✓
27	Goose Cove	10/31/2018	5	✓
28	Goose Cove	10/31/2018	6	✓
29	Goose Cove	10/31/2018	7	✓
30	Goose Cove	10/31/2018	8	✓
31	Main Creek	10/31/2018	9	✓

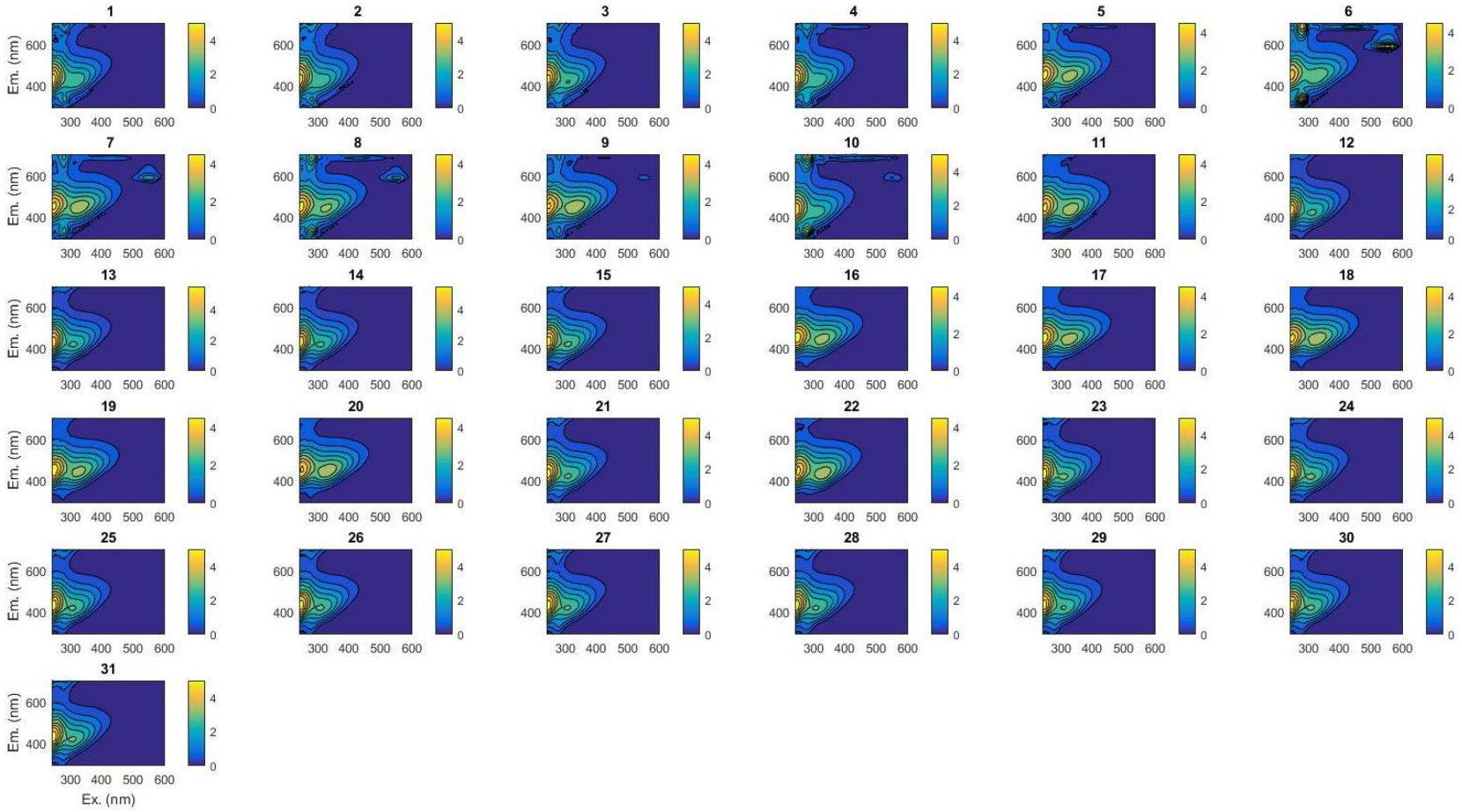

Figure S6.28: EEMs for samples included in the CB samples dataset after normalization

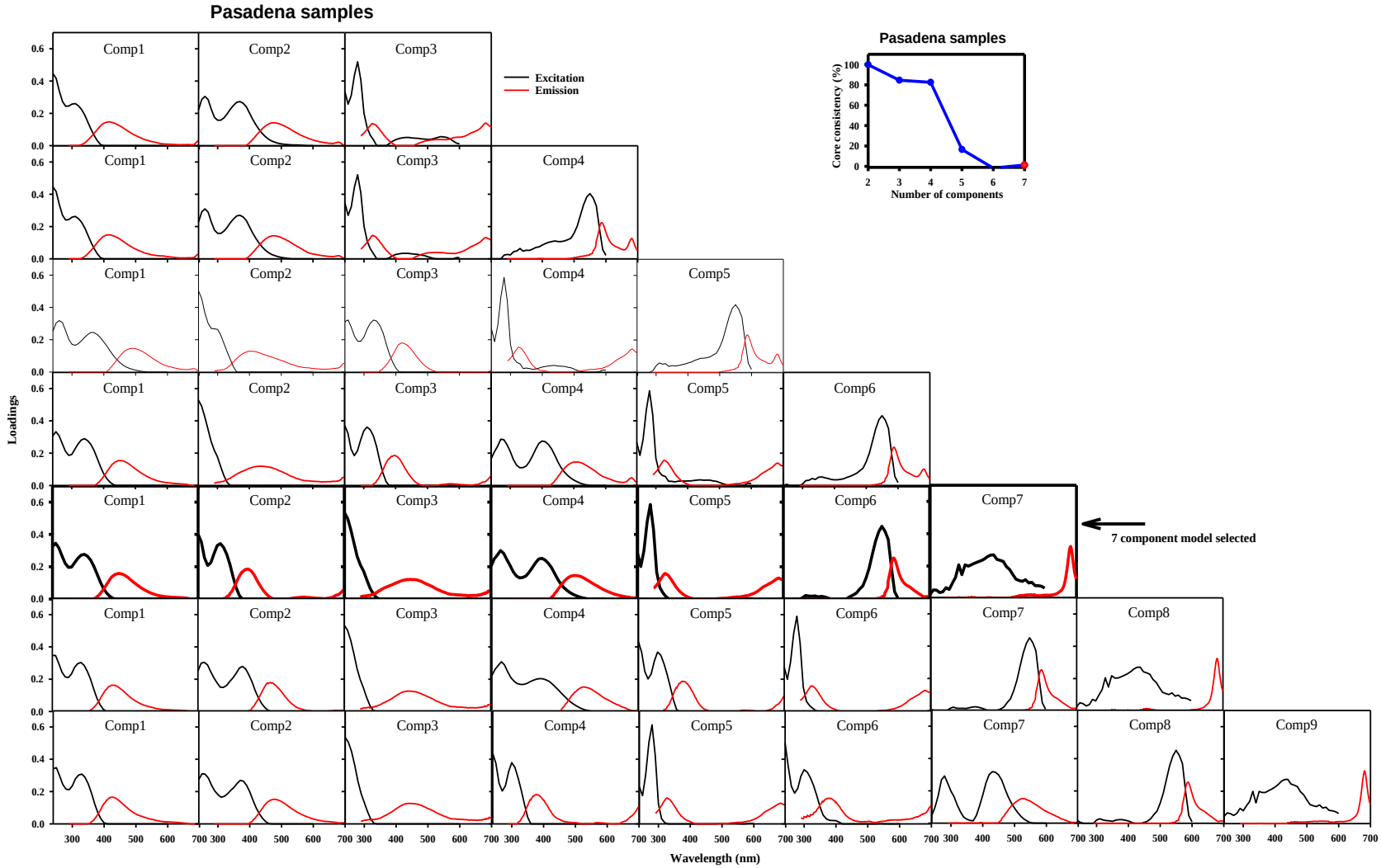

Figure S6.29: (**a**) Loadings generated by PARAFAC for models with increasing numbers of components for the CB samples dataset. The components chosen for the ideal model are bolded. (**b**) The core consistency with increasing numbers of components with the red point indicating the number of components chosen for the ideal model.

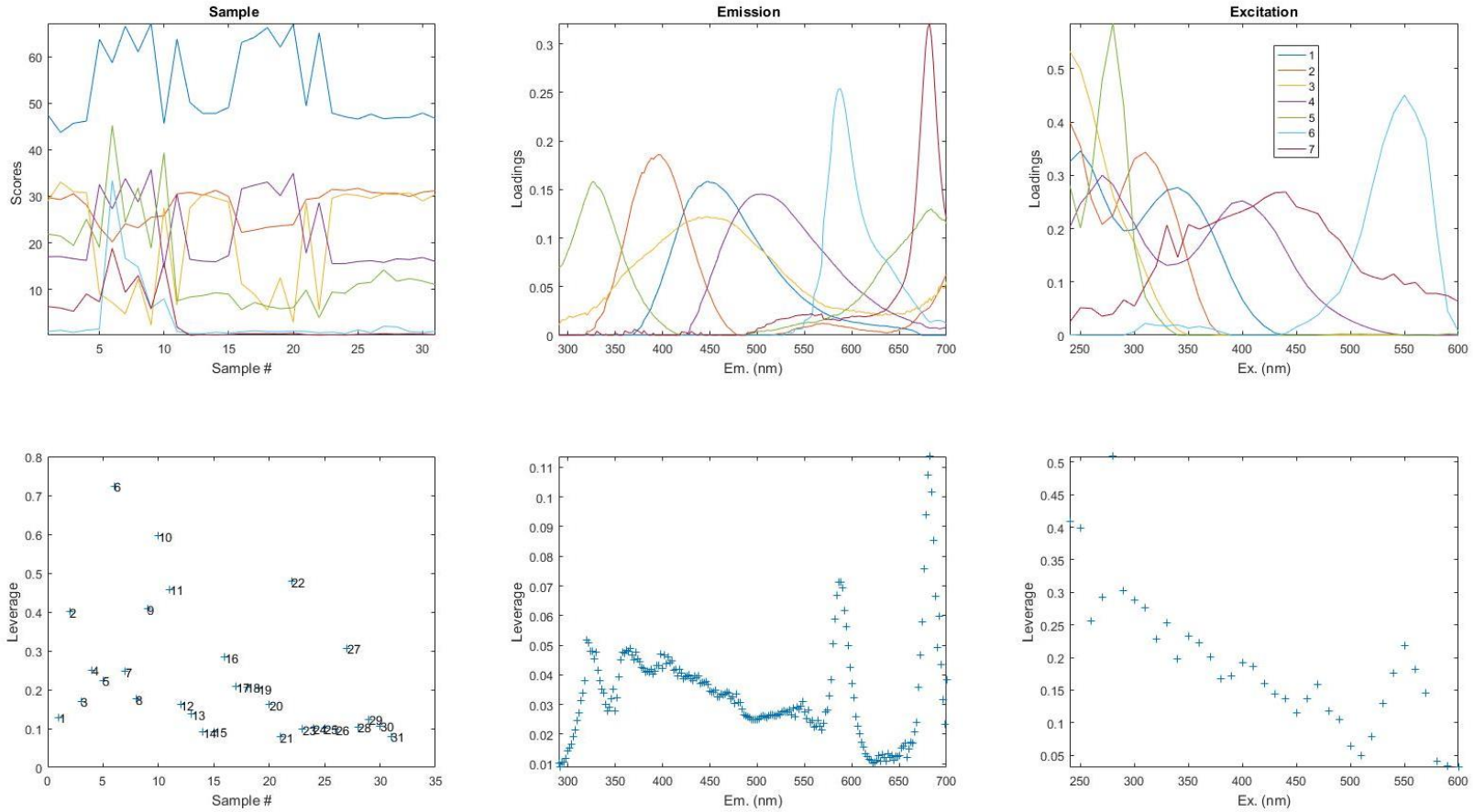

Figure S6.30: CB samples dataset, loadings (**top**) and leverages (**bottom**) for the seven component model.

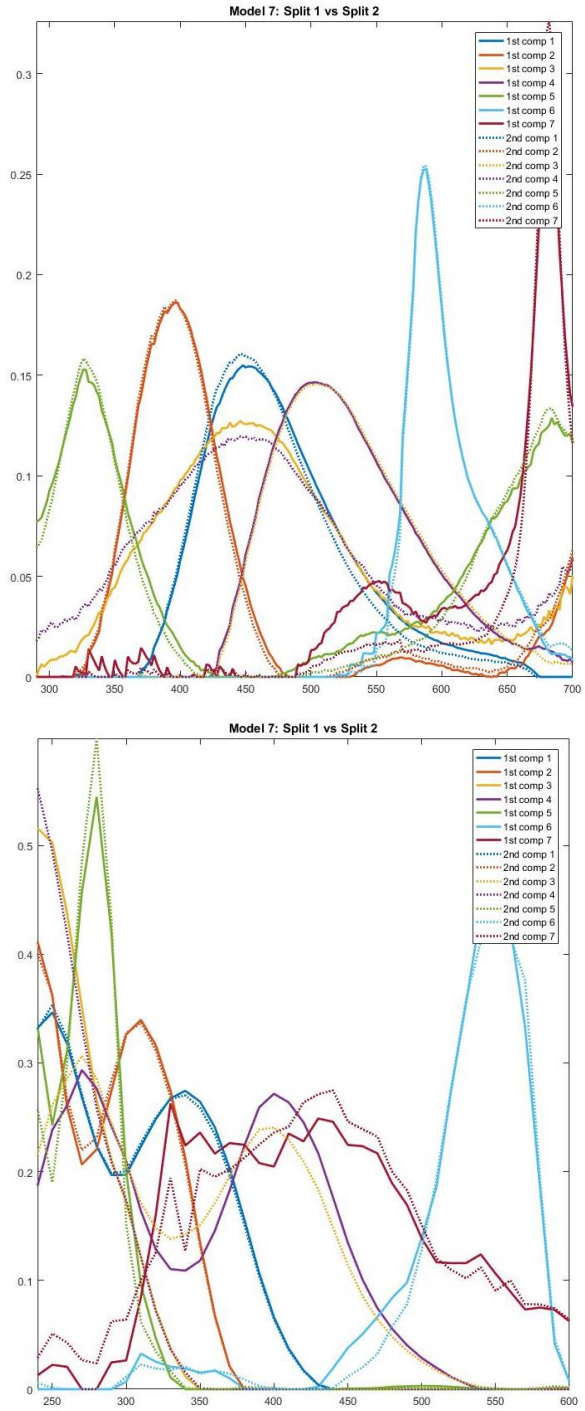

Figure S6.31: CB samples dataset, split-half validation; emission spectra (**top**) and excitation spectra (**bottom**) for a seven component model.

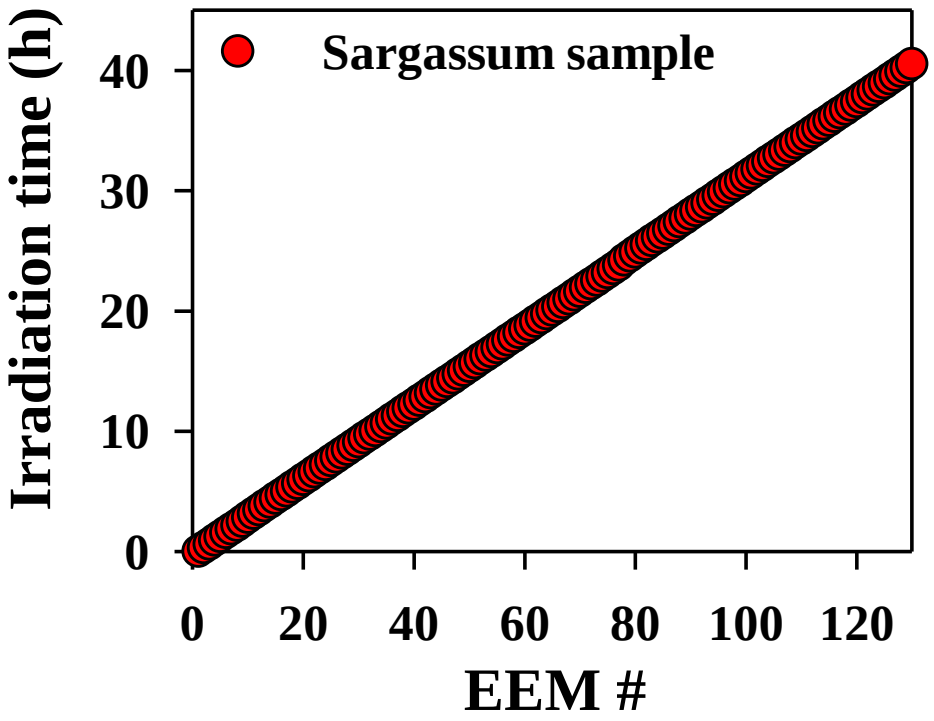

Figure S6.32: Irradiation time of Sargassum sample for each EEM included in the Sargassum dataset.

a

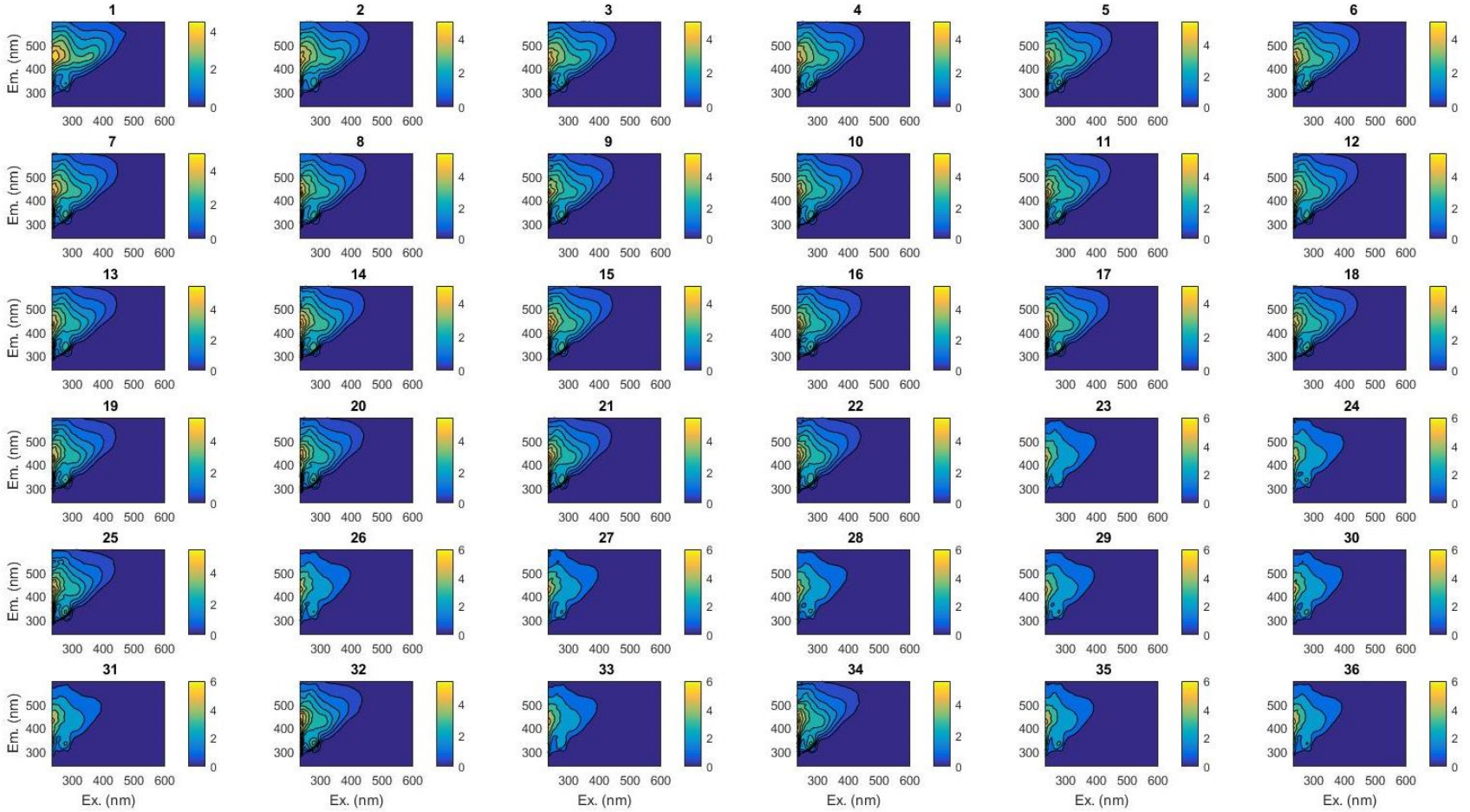
1
2
3
4
5
6
7
8
9
10
11
12
13
14
15
16
17
18
19
20
21
22
23
24
25
26
27
28
29
30
31
32
33
34
35
36
Em. (nm)
Ex. (nm)
300 400 500 600
300 400 500
0 2 4
0 2 4 6

b

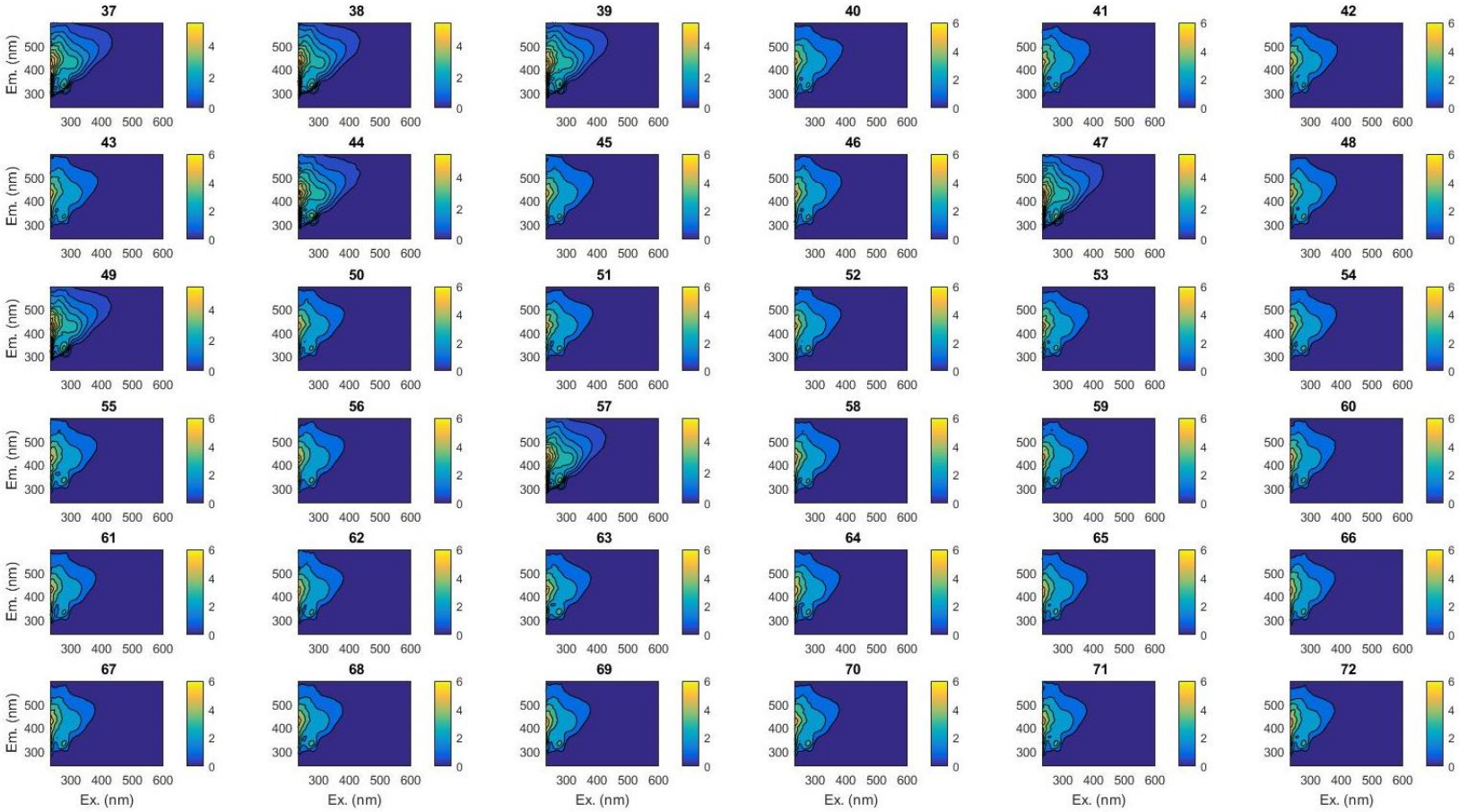
37
38
39
40
41
42
43
44
45
46
47
48
49
50
51
52
53
54
55
56
57
58
59
60
61
62
63
64
65
66
67
68
69
70
71
72
Em. (nm)
Ex. (nm)
300 400 500 600
300 400 500
0 2 4 6

c

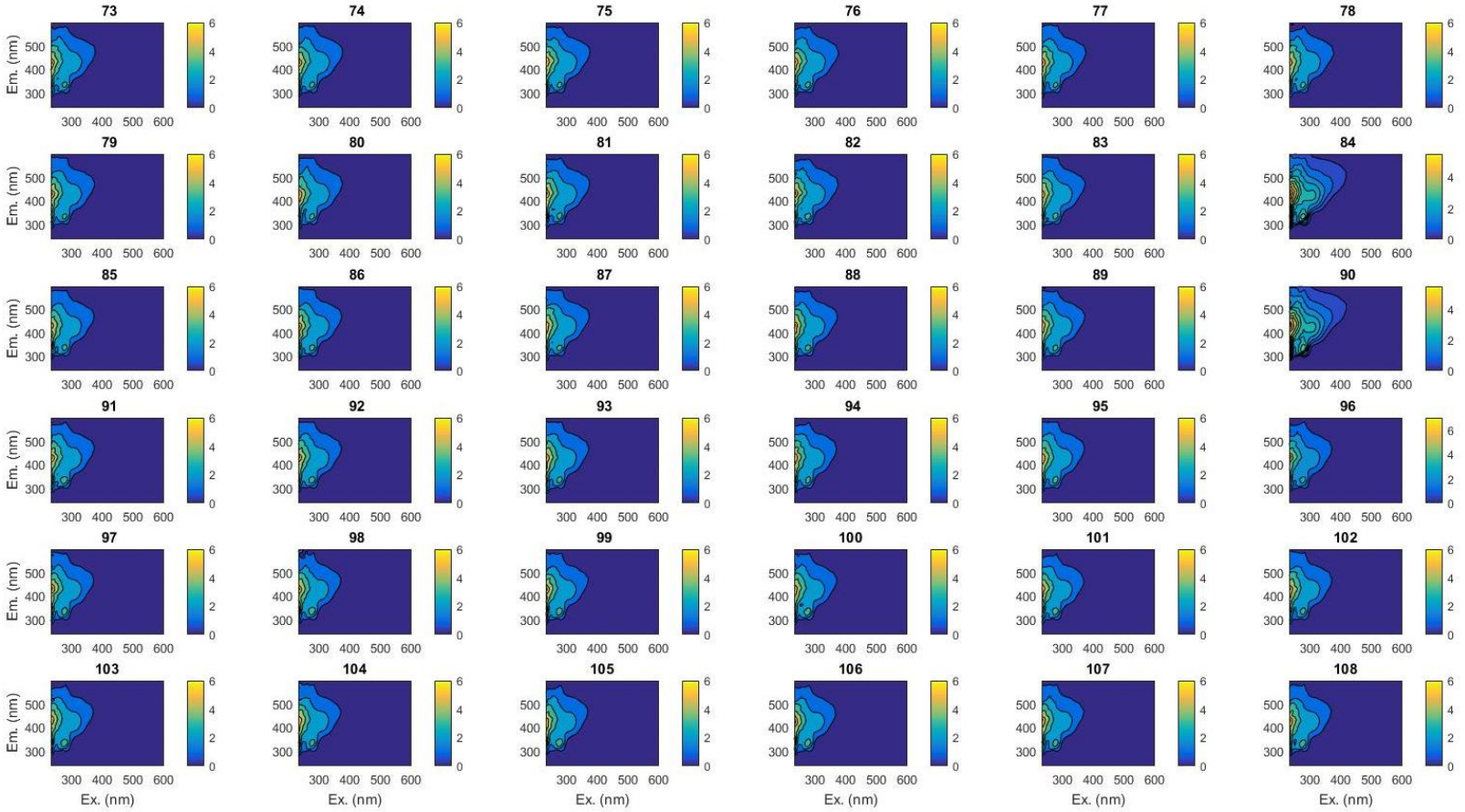
73
74
75
76
77
78
79
80
81
82
83
84
85
86
87
88
89
90
91
92
93
94
95
96
97
98
99
100
101
102
103
104
105
106
107
108
Em. (nm)
Ex. (nm)
300 400 500 600
300 400 500
0 2 4 6

d

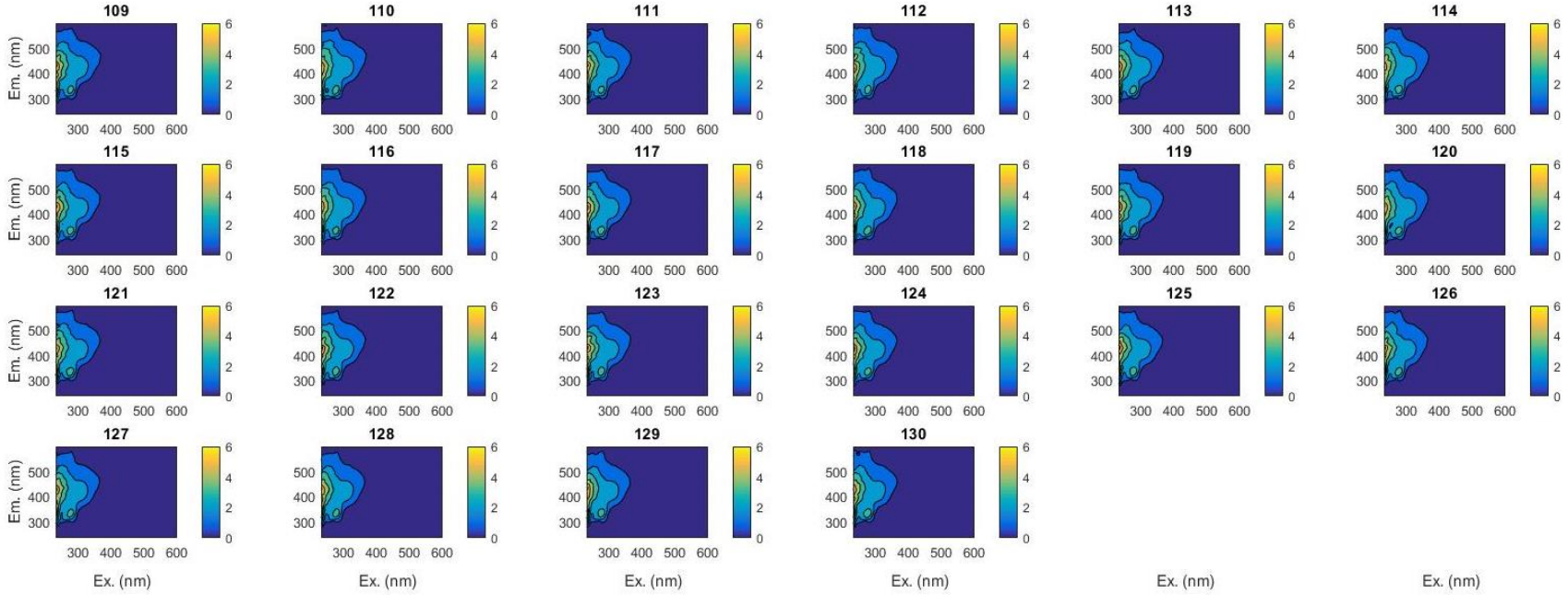

Figure S6.33: EEMs (**a**) 1-36, **b**) 37-72, **c**) 73- 108, and **d**) 109-130) for Sargassum sample at different time point during the irradiation included in the Sargassum dataset after normalization.

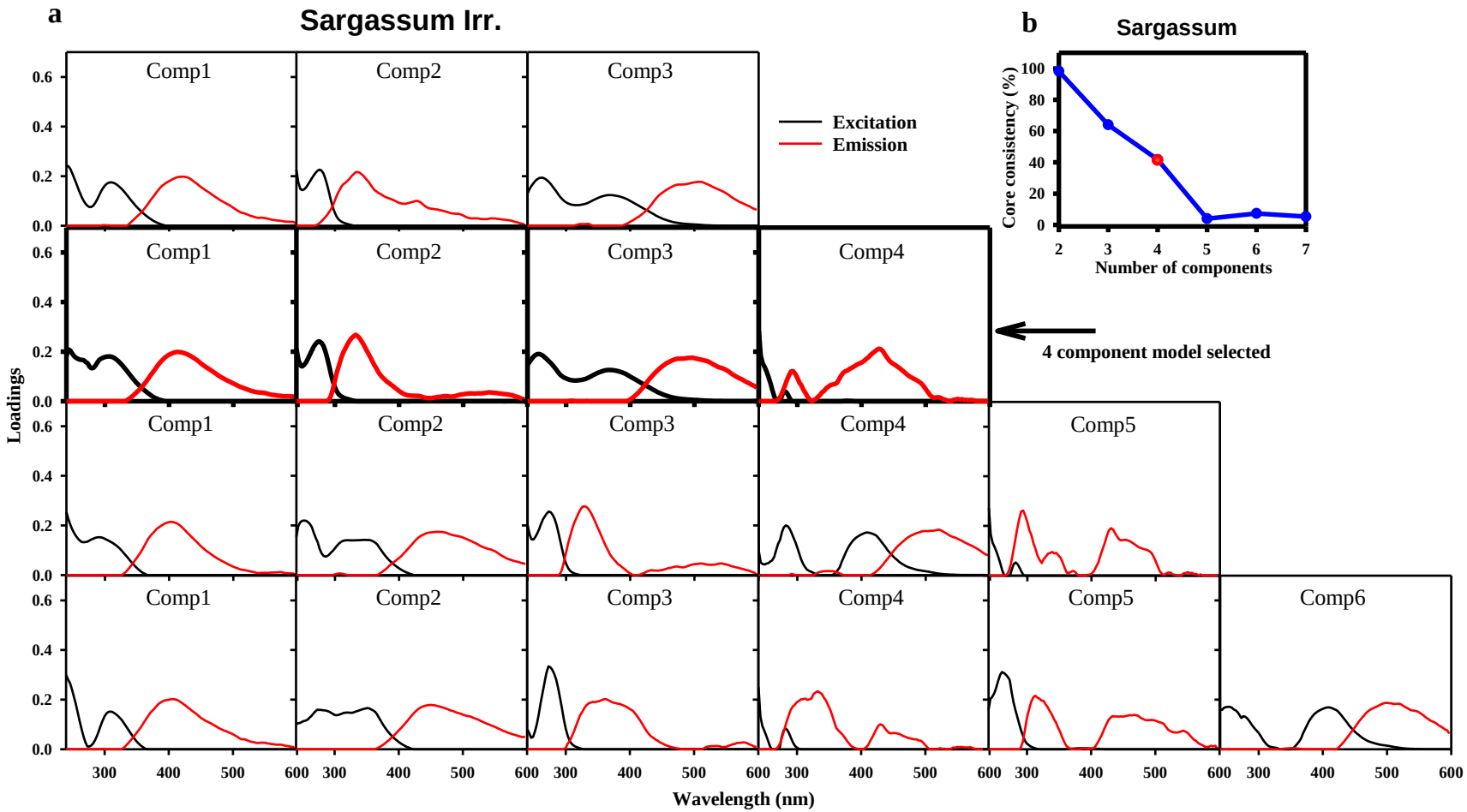

Figure S6.34: (**a**) Loadings generated by PARAFAC for models with increasing numbers of components for the Sargassum dataset. The components chosen for the ideal model are bolded. (**b**) The core consistency with increasing numbers of components with the red point indicating the number of components chosen for the ideal model

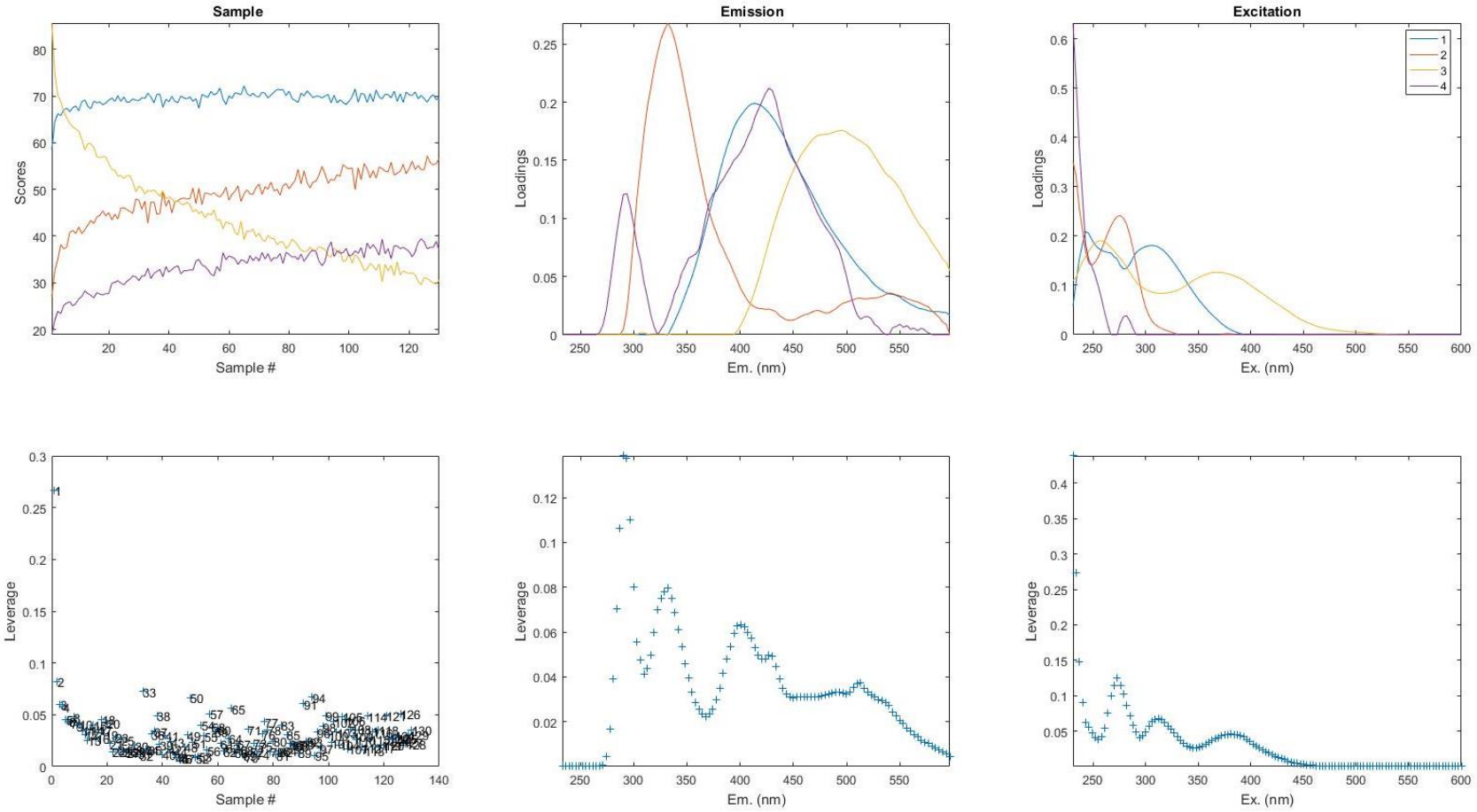

Figure S6.35: Sargassum dataset, loadings (**top**) and leverages (**bottom**) for the four component model.

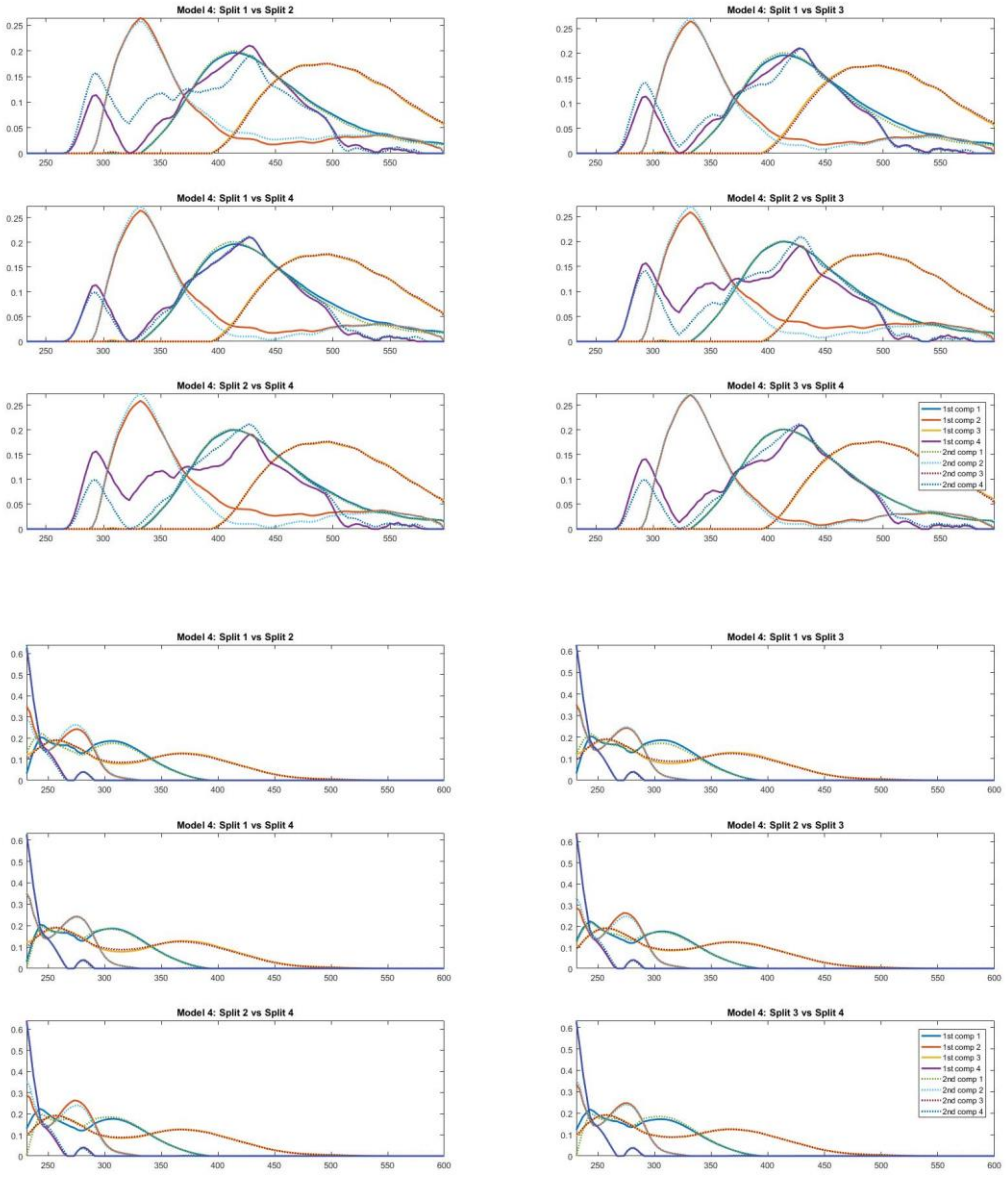

Figure S6.36: Sargassum dataset, split-half validation; emission spectra (**top**) and excitation spectra (**bottom**) for a four component model.

Bibliography

1. Blough, N. V. & Del Vecchio, R. Chromophoric DOM in the Coastal Environment. in *Biogeochemistry of Marine Dissolved Organic Matter* (eds. Hansell, D. A. & Carlson, C. A.) 509–545 (Academic Press, San Diego, California, 2002). doi:10.1016/B978-012323841-2/50012-9
2. Siegel, D. A., Maritorena, S., Nelson, N. B., Hansell, D. A. & Lorenzi-Kayser, M. Global distribution and dynamics of colored dissolved and detrital organic materials. *J. Geophys. Res.* **107**, 3228 (2002).
3. Nelson, N. B. & Siegel, D. A. Chromophoric DOM in the open ocean. in *Biogeochemistry of Marine Dissolved Organic Matter* (eds. Hansell, D. A. & Carlson, C. A.) 547–578 (Academic Press, San Diego, California, 2002).
4. Zepp, R. G., Erickson, D. J., Paul, N. D. & Sulzberger, B. Interactive effects of solar UV radiation and climate change on biogeochemical cycling. *Photochem. Photobiol. Sci.* **6**, 286–300 (2007).
5. Nelson, N. B. & Siegel, D. A. The global distribution and dynamics of chromophoric dissolved organic matter. *Ann. Rev. Mar. Sci.* **5**, 447–76 (2013).
6. Iuculano, F. *et al.* Patterns and Drivers of UV Absorbing Chromophoric Dissolved Organic Matter in the Euphotic Layer of the Open Ocean. *Front. Mar. Sci.* **6**, 1–19 (2019).
7. Andrew, A. A., Del Vecchio, R., Zhang, Y., Subramaniam, A. & Blough, N. V. Are Extracted Materials Truly Representative of Original Samples? Impact of C18 Extraction on CDOM Optical and Chemical Properties. *Front. Chem.* **4**, 1–12 (2016).
8. Dittmar, T., Koch, B., Hertkorn, N. & Kattner, G. A simple and efficient method for the solid-phase extraction of dissolved organic matter (SPE-DOM) from seawater. *Limnol. Oceanogr. Methods* **6**, 230–235 (2008).
9. (IHSS), I. H. S. S. No Title. http://humic-substances.org/source-materials-for-i (2019).
10. Siegenthaler, U. & Sarmiento, J. L. Atmospheric carbon dioxide and the ocean. *Nature* **365**, 119–125 (1993).
11. Weishaar, J. L. *et al.* Evaluation of specific ultraviolet absorbance as an indicator of the chemical composition and reactivity of dissolved organic carbon. *Environ. Sci. Technol.* **37**, 4702–4708 (2003).
12. Helms, J. R. *et al.* Spectroscopic characterization of oceanic dissolved organic matter isolated by reverse osmosis coupled with electrodialysis. *Marine Chemistry* **177**, 278–287 (2015).
13. Abbt-Braun, G., Lankes, U. & Frimmel, F. H. Structural characterization of aquatic humic substances - The need for a multiple method approach. *Aquat. Sci.* **66**, 151–170 (2004).
14. Kellerman, A. M. *et al.* Unifying Concepts Linking Dissolved Organic Matter Composition to Persistence in Aquatic Ecosystems. *Environ. Sci. Technol.* **52**, 2538–2548 (2018).
15. Wetzel, R. G., Hatcher, P. G. & Bianchi, T. S. Natural photolysis by ultraviolet irradiance of recalcitrant dissolved organic matter to simple substrates for rapid

bacterial metabolism. *Limnol. Oceanogr.* **40**, 1369–1380 (1995).
16. Andrew, A. A., Del Vecchio, R., Subramaniam, A. & Blough, N. V. Chromophoric dissolved organic matter (CDOM) in the Equatorial Atlantic Ocean: Optical properties and their relation to CDOM structure and source. *Mar. Chem.* **148**, 33–43 (2013).
17. Vodacek, A., Blough, N. V., Degrandpre, M. D., Peltzer, E. T. & Nelson, R. K. Seasonal variation of CDOM and DOC in the Middle Atlantic Bight: Terrestrial inputs and photooxidation. *Limnol. Oceanogr.* **42**, 674–686 (1997).
18. Golanoski, K. S., Fang, S., Del Vecchio, R. & Blough, N. V. Investigating the mechanism of phenol photooxidation by humic substances. *Environ. Sci. Technol.* **46**, 3912–3920 (2012).
19. Blough, N. V. & Zepp, R. G. *Reactive Oxygen Species in Natural Waters*. *Active Oxygen in Chemistry* (Chapman and Hall, 1995). doi:10.1007/978-94-007-0874-7_8
20. Mopper, K. *et al.* Photochemical degradation of dissolved organic carbon and its impact on the oceanic carbon cycle. *Nature* **353**, 60–62 (1991).
21. Sharpless, C. M. & Blough, N. V. The importance of charge-transfer interactions in determining chromophoric dissolved organic matter (CDOM) optical and photochemical properties. *Environ. Sci. Process. Impacts* **16**, 654–71 (2014).
22. Del Vecchio, R. & Blough, N. V. On the origin of the optical properties of humic substances. *Environ. Sci. Technol.* **38**, 3885–3891 (2004).
23. Coble, P. G. Marine optical biogeochemistry: The chemistry of ocean color. *Chem. Rev.* **107**, 402–418 (2007).
24. Boyle, E. S., Guerriero, N., Thiallet, A., Del Vecchio, R. & Blough, N. V. Optical Properties of Humic Substances and CDOM : Relation to Structure. *Environ. Sci. Technol.* **43**, 2262–2268 (2009).
25. Bricaud, A., Morel, A. & Prieur, L. Absorption by dissolved organic matter of the sea (yellow substance) in the UV and visible domains1. *Limnol. Oceanogr.* **26**, 43–53 (1981).
26. Green, S. a. & Blough, N. V. Optical absorption and fluorescence properties of chromophoric dissolved organic matter in natural waters. *Limonology Oceanogr.* **39**, 1903–1916 (1994).
27. Heighton, L. P. & Schmidt, W. F. Probing the pH Dependent Optical Properties of Aquatic, Terrestrial and Microbial Humic Substances by Sodium Borohydride Reduction. *J. Geogr. Geol.* **6**, 214–227 (2014).
28. Miller, R. L., Belz, M., Del Castillo, C. & Trzaska, R. Determining CDOM absorption spectra in diverse coastal environments using a multiple pathlength, liquid core waveguide system. *Cont. Shelf Res.* **22**, 1301–1310 (2002).
29. Röttgers, R. & Doerffer, R. Measurements of optical absorption by CDOM using a point-source integrating cavity absorption meter. *Limnol. Oceanogr. Methods* **5**, 126–135 (2007).
30. Stedmon, C. A., Markager, S. & Kaas, H. Optical properties and signatures of chromophoric dissolved organic matter (CDOM) in Danish coastal waters. *Estuar. Coast. Shelf Sci.* **51**, 267–278 (2000).
31. Fichot, C. G. & Benner, R. A novel method to estimate DOC concentrations from CDOM absorption coefficients in coastal waters. *Geophys. Res. Lett.* **38**, 1–5

(2011).
32. Morris, D. P. & Hargreaves, B. R. The role of photochemical degradation of dissolved organic carbon in regulating the UV transparency of three lakes on the Pocono Plateau. *Limnol. Oceanogr.* **42**, 239–249 (1997).
33. Helms, J. R. *et al.* Absorption Spectral Slopes and Slope Rations As Indicators of Molecular Weight, Source, and Photobleaching of Chromophoric Dissolved Organic Matter. *Limnol. Oceanogr.* **53**, 955–969 (2008).
34. Fichot, C. G. & Benner, R. The spectral slope coefficient of chromophoric dissolved organic matter ($S_{275\text{-}295}$) as a tracer of terrigenous dissolved organic carbon in river-influenced ocean margins. *Limnol. Oceanogr.* **57**, 1453–1466 (2012).
35. Cartisano, C. M., Del Vecchio, R., Bianca, M. R. & Blough, N. V. Investigating the sources and structure of chromophoric dissolved organic matter (CDOM) in the North Pacific Ocean (NPO) utilizing optical spectroscopy combined with solid phase extraction and borohydride reduction. *Mar. Chem.* **204**, 20–35 (2018).
36. De Haan, H. & De Boer, T. Applicability of light absorbance and fluorescence as measures of concentration and molecular size of dissolved organic carbon in humic Lake Tjeukemeer. *Water Res.* **21**, 731–734 (1987).
37. Peuravuori, J. & Pihlaja, K. Molecular size distribution and spectroscopic properties of aquatic humic substances. *Anal. Chim. Acta* **337**, 133–149 (1997).
38. Mcknight, D. M. *et al.* Spectrofluorometric characterization of dissolved organic matter for indication of precursor organic material and aromaticity. **46**, 38–48 (2001).
39. Cory, R. M. & Mcknight, D. M. Fluorescence Spectroscopy Reveals Ubiquitous Presence of Oxidized and Reduced Quinones in Dissolved Organic Matter Fluorescence Spectroscopy Reveals Ubiquitous Presence of Oxidized and Reduced Quinones in Dissolved Organic Matter. *Environ. Sci. Technol.* **39**, 8142–8149 (2005).
40. Huguet, A. *et al.* Properties of fluorescent dissolved organic matter in the Gironde Estuary. *Org. Geochem.* **40**, 706–719 (2009).
41. Zsolnay, A., Baigar, E., Jimenez, M., Steinweg, B. & Saccomandi, F. Differentiating with fluorescence spectroscopy the sources of dissolved organic matter in soils subjected to drying. *Chemosphere* **38**, 45–50 (1999).
42. Shank, G. C., Zepp, R. G., Vähätalo, A., Lee, R. & Bartels, E. Photobleaching kinetics of chromophoric dissolved organic matter derived from mangrove leaf litter and floating Sargassum colonies. *Mar. Chem.* **119**, 162–171 (2010).
43. Fichot, C. G. *et al.* Predicting Dissolved Lignin Phenol Concentrations in the Coastal Ocean from Chromophoric Dissolved Organic Matter (CDOM) Absorption Coefficients. *Front. Mar. Sci.* **3**, 1–15 (2016).
44. Moran, M. A. & Zepp, R. G. Role of Photoreactions in the Formation of Biologically Labile Compounds from Dissolved Organic Matter. *Limnol. Oceanogr.* **42**, 1307–1316 (1997).
45. Del Vecchio, R. & Blough, N. V. Spatial and seasonal distribution of chromophoric dissolved organic matter and dissolved organic carbon in the Middle Atlantic Bight. *Mar. Chem.* **89**, 169–187 (2004).
46. Ma, J., Del Vecchio, R., Golanoski, K. S., Boyle, E. S. & Blough, N. V. Optical

properties of humic substances and CDOM: Effects of borohydride reduction. *Environ. Sci. Technol.* **44**, 5395–5402 (2010).
47. Phillips, S. M. & Smith, G. D. Further evidence for charge transfer complexes in brown carbon aerosols from excitation-emission matrix fluorescence spectroscopy. *J. Phys. Chem. A* **119**, 4545–4551 (2015).
48. Sharpless, C. M. Lifetimes of triplet dissolved natural organic matter (DOM) and the effect of NaBH 4 reduction on singlet oxygen quantum yields: Implications for DOM photophysics. *Environ. Sci. Technol.* **46**, 4466–4473 (2012).
49. Zhang, Y., Del Vecchio, R. & Blough, N. V. Investigating the mechanism of hydrogen peroxide photoproduction by humic substances. *Environ. Sci. Technol.* **46**, 11836–11843 (2012).
50. Stubbins, A. *et al.* Illuminated darkness: Molecular signatures of Congo River dissolved organic matter and its photochemical alteration as revealed by ultrahigh precision mass spectrometry. *Limnol. Oceanogr.* **55**, 1467–1477 (2010).
51. Spencer, R. G. M. *et al.* Photochemical degradation of dissolved organic matter and dissolved lignin phenols from the Congo River. *J. Geophys. Res. Biogeosciences* **114**, 1–12 (2009).
52. Stenson, A. C., Marshall, A. G. & Cooper, W. T. Exact masses and chemical formulas of individual Suwannee River fulvic acids from ultrahigh resolution electrospray ionization Fourier transform ion cyclotron resonance mass spectra. *Anal. Chem.* **75**, 1275–1284 (2003).
53. Maie, N., Pisani, O. & Jaffe, R. Mangrove tannins in aquatic ecosystems: Their fate and possible influence on dissolved organic carbon and nitrogen cycling. *Limnol. Oceanogr.* **53**, 160–171 (2008).
54. Sleighter, R. L. & Hatcher, P. G. Molecular characterization of dissolved organic matter (DOM) along a river to ocean transect of the lower Chesapeake Bay by ultrahigh resolution electrospray ionization Fourier transform ion cyclotron resonance mass spectrometry. *Mar. Chem.* **110**, 140–152 (2008).
55. Derkacheva, O. & Sukhov, D. Investigation of lignins by FTIR spectroscopy. *Macromol. Symp.* **265**, 61–68 (2008).
56. Schendorf, T. M. Effect of Borohydride Reduction and pH on the Optical Properties of Humic Substances. M.S. Thesis. (2014).
57. Schendorf, T. M., Del Vecchio, R., Koech, K. & Blough, N. V. A standard protocol for NaBH4 reduction of CDOM and HS. *Limnol. Oceanogr. Methods* **14**, **2016**, 414–423 (2016).
58. Schendorf, T. M., Vecchio, R. Del, Bianca, M. & Blough, N. V. Combined Effects of pH and Borohydride Reduction on Optical Properties of Humic Substances (HS): A Comparison of Optical Models. *Environ. Sci. Technol.* (2019). doi:10.1021/acs.est.9b01516
59. Janot, N., Reiller, P. E., Korshin, G. V. & Benedetti, M. F. Using Spectrophotometric Titrations to Characterize Humic Acid Reactivity at Environmental Concentrations. *Environ. Sci. Technol.* **44**, 6782–6788 (2010).
60. Johnson, M. R. & Rickborn, B. Sodium Borohydride Reduction of Conjugated Aldehydes and Ketones. *J. Org. Chem.* **35**, 1041–1045 (1970).
61. Yan, M. *et al.* Effects of Charging on the Chromophores of Dissolved Organic Matter from the Rio Negro Basin. *Water Res.* **59**, 154–164 (2014).

62. Dryer, D. J., Korshin, G. V. & Fabbricino, M. In situ examination of the protonation behavior of fulvic acids using differential absorbance spectroscopy. *Environ. Sci. Technol.* **42**, 6644–6649 (2008).
63. McKay, G. *et al.* The Case Against Charge Transfer Interactions in Dissolved Organic Matter Photophysics. *Environ. Sci. Technol.* **52**, 406–414 (2018).
64. Grandbois, M., Latch, D. E. & Mcneill, K. Microheterogeneous concentrations of singlet oxygen in natural organic matter isolate solutions. *Environ. Sci. Technol.* **42**, 9184–9190 (2008).
65. Chu, C., Lundeen, R. A., Remucal, C. K., Sander, M. & McNeill, K. Enhanced indirect photochemical transformation of histidine and histamine through association with chromophoric dissolved organic matter. *Environ. Sci. Technol.* **49**, 5511–5519 (2015).
66. Blough, N. V. Electron Paramagnetic Resonance Measurements of Photochemical Radical Production in Humic Substances. 1. Effects of O2 and Charge on Radical Scavenging by Nitroxides. *Environ. Sci. Technol.* **22**, 77–82 (1988).
67. Green, S. A., Morel, F. M. M. & Blough, N. V. Investigation of the Electrostatic Properties of Humic Substances by Fluorescence Quenching. *Environ. Sci. Technol.* **26**, 294–302 (1992).
68. Del Vecchio, R., Schendorf, T. M. & Blough, N. V. Contribution of Quinones and Ketones/Aldehydes to the Optical Properties of Humic Substances (HS) and Chromophoric Dissolved Organic Matter (CDOM). *Environ. Sci. Technol.* **51**, 13624–13632 (2017).
69. Blough, N. V. & Del Vecchio, R. Comment on The Case Against Charge Transfer Interactions in Dissolved Organic Matter Photophysics. *Environ. Sci. Technol.* **52**, 5512–5513 (2018).
70. Swan, C. M., Siegel, D. A., Nelson, N. B., Carlson, C. A. & Nasir, E. Biogeochemical and hydrographic controls on chromophoric dissolved organic matter distribution in the Pacific Ocean. *Deep Sea Res. Part I Oceanogr. Res. Pap.* **56**, 2175–2192 (2009).
71. Yamashita, Y., Tsukasaki, A., Nishida, T. & Tanoue, E. Vertical and horizontal distribution of fluorescent dissolved organic matter in the Southern Ocean. *Mar. Chem.* **106**, 498–509 (2007).
72. Yamashita, Y. & Tanoue, E. Production of bio-refractory fluorescent dissolved organic matter in the ocean interior. *Nat. Geosci.* **1**, 579–582 (2008).
73. Yamashita, Y. & Tanoue, E. Basin scale distribution of chromophoric dissolved organic matter in the Pacific Ocean. *Limnol. Oceanogr.* **54**, 598–609 (2009).
74. Nelson, N. B. & Gauglitz, J. M. Optical Signatures of Dissolved Organic Matter Transformation in the Global Ocean. **2**, 1–15 (2016).
75. Murphy, K. R., Stedmon, C. a., Waite, T. D. & Ruiz, G. M. Distinguishing between terrestrial and autochthonous organic matter sources in marine environments using fluorescence spectroscopy. *Mar. Chem.* **108**, 40–58 (2008).
76. Hernes, P. J. & Benner, R. Transport and diagenesis of dissolved and particulate terrigenous organic matter in the North Pacific Ocean. *Deep. Res. Part I Oceanogr. Res. Pap.* **49**, 2119–2132 (2002).
77. Medeiros, P. M. *et al.* A novel molecular approach for tracing terrigenous dissolved organic matter into the deep ocean. *Global Biogeochem. Cycles* **30**, 689–

699 (2016).
78. Koch, B. P., Witt, M., Engbrodt, R., Dittmar, T. & Kattner, G. Molecular formulae of marine and terrigenous dissolved organic matter detected by electrospray ionization Fourier transform ion cyclotron resonance mass spectrometry. *Geochim. Cosmochim. Acta* **69**, 3299–3308 (2005).
79. Hansman, R. L., Dittmar, T. & Herndl, G. J. Conservation of dissolved organic matter molecular composition during mixing of the deep water masses of the northeast Atlantic Ocean. *Mar. Chem.* **177**, 288–297 (2015).
80. Bauer, J. E. Carbon isotopic composition of DOM. in *Biogeochemistry of Marine Dissolved Organic Matter* (eds. Hansell, D. A. & Carlson, C. A.) 405–455 (Academic Press, San Diego, California, 2002).
81. Zigah, P. K. *et al.* Allochthonous sources and dynamic cycling of ocean dissolved organic carbon revealed by carbon isotopes. *Geophys. Res. Lett.* **44**, 2407–2415 (2017).
82. Nelson, N. B. *et al.* Hydrography of chromophoric dissolved organic matter in the North Atlantic. *Deep Sea Res. Part I Oceanogr. Res. Pap.* **54**, 710–731 (2007).
83. Röttgers, R. & Koch, B. P. Spectroscopic detection of a ubiquitous dissolved pigment degradation product in subsurface waters of the global ocean. *Biogeosciences* **9**, 2585–2596 (2012).
84. D'Sa, E. J., Steward, R. G., Vodacek, A., Blough, N. V. & Phinney, D. Determining optical absorption of colored dissolved organic matter in seawater with a liquid capillary waveguide. *Limnol. Oceanogr.* **44**, 1142–1148 (1999).
85. Yao, W., Byrne, R. H. & Waterbury, R. D. Determination of nanomolar concentrations of nitrite and nitrate in natural waters using long path length absorbance spectroscopy. *Environ. Sci. Technol.* **32**, 2646–2649 (1998).
86. Wang, Z. A., Cai, W.-J., Wang, Y. & Upchurch, B. L. A long pathlength liquid-core waveguide sensor for real-time pCO2 measurements at sea. *Mar. Chem.* **84**, 73–84 (2003).
87. Naik, P. & D'Sa, E. J. Phytoplankton light absorption of cultures and natural samples: comparisons using two spectrophotometers. *Opt. Express* **20**, 4871 (2012).
88. Gimbert, L. J. & Worsfold, P. J. Environmental applications of liquid-waveguide-capillary cells coupled with spectroscopic detection. *TrAC - Trends Anal. Chem.* **26**, 914–930 (2007).
89. Mopper, K. & Kieber, D. J. Photochemistry and the cycling of carbon, sulfur, nitrogen and phosphorous. in *Biogeochemistry of Marine Dissolved Organic Matter* (eds. Hansell, D. A. & Carlson, C. A.) 455–507 (Academic Press, San Diego, California, 2002).
90. Belz, M., Larsen, K. & Klein, K.-F. Fiber optic sample cell for polychromatic detection of dissolved and particulate matter in natural waters. *Prog. Biomed. Opt. Imaging Adv. Environ. , Chem. Biol. Sens. Technol. IV SPIE* **6377**, 1–10 (2006).
91. Werdell, P. J. *et al.* An overview of approaches and challenges for retrieving marine inherent optical properties from ocean color remote sensing. *Prog. Oceanogr.* **160**, 186–212 (2018).
92. Grunert, B. K., Mouw, C. B. & Ciochetto, A. B. Characterizing CDOM Spectral Variability Across Diverse Regions and Spectral Ranges. *Global Biogeochem.*

Cycles **32**, 57–77 (2018).
93. Floge, S. A., Hardy, K. R., Boss, E. & Wells, M. L. Analytical intercomparison between type I and type II long- pathlength liquid core waveguides for the measurement of chromophoric dissolved organic matter. *Limnol. Oceanogr. Methods* **7**, 260–268 (2009).
94. Belz, M., Dress, P., Sukhitskiy, A. & Liu, S. Linearity and effective optical pathlength of liquid waveguide capillary cells. *Conf. Intern. Stand. Calibration Archit. Chem. Sensors* **Boston MA**, Vol. 3856, 271-281 (1999).
95. Lefering, I., Röttgers, R., Utschig, C. & McKee, D. Uncertainty budgets for liquid waveguide CDOM absorption measurements. *Appl. Opt.* **56**, (2017).
96. Novak, M. *et al.* Measurements of CDOM absorption spectra using different Instruments and techniques: A round robin exercise and extensive field data set. *Ocean Opt. XXII Conf. Portland, Maine, 2014* 1–16 (2013).
97. Burke, R. W. & Mavrodineanu, R. Standard Reference Materials : Certification and use of acidic potassium dichromate solutions as an ultraviolet absorbance standard - SRM 935. *NBS Spec. Publ. 260-54* **U.S. Gover**, 157 (1977).
98. May, W. E. & Trahey, N. M. NIST Certificate of Analysis: Standard Reference Material 935a. *Natl. Inst. Stand. Technol.* **SRM 935a**, 1–5 (2000).
99. World Precision Instruments, I. *UltraPath System guide: for visible (UPVIS) and ultraviolet (UPUV) systems*. (2007).
100. Langford, V. S., McKinley, A. J. & Quickenden, T. I. Temperature dependence of the visible-near-infrared absorption spectrum of liquid water. *J. Phys. Chem. A* **105**, 8916–8921 (2001).
101. Röttgers, R., McKee, D. & Utschig, C. Temperature and salinity correction coefficients for light absorption by water in the visible to infrared spectral region. *Opt. Express* **22**, 25093–25108 (2014).
102. Burke, R. W. & Mavrodineanu, R. Acidic Potassium Dichromate Solutions as Ultraviolet Absorbance Standards *. *J. Res. Natl. Bur. Stand. (1934).* **80A (Phys.**, 631–636 (1976).
103. Lai, C.-Z. *et al.* Spectrophotometric measurement of freshwater pH with purified meta-cresol purple and phenol red. *Limnol. Oceanogr. Methods* **14**, 864–873 (2016).
104. Miller, W. L. & Zepp, R. G. Photochemical production of dissolved inorganic carbon from terrestrial organic matter: Significance to the oceanic organic carbon cycle. *Geophys. Res. Lett.* **22**, 417–420 (1995).
105. Stedmon, C. A. & Nelson, N. B. The Optical Properties of DOM in the Ocean. in *Biogeochemistry of Marine Dissolved Organic Matter* (eds. Hansell, D. A. & Carlson, C. A.) 481–508 (Academic Press, San Diego, California, 2015). doi:10.1016/B978-0-12-405940-5.00010-8
106. Fellman, J. B., Hood, E. & Spencer, R. G. M. Fluorescence spectroscopy opens new windows into dissolved organic matter dynamics in freshwater ecosystems: A review. *Limnol. Oceanogr.* **55**, 2452–2462 (2010).
107. Osburn, C. L. *et al.* Optical Proxies for Terrestrial Dissolved Organic Matter in Estuaries and Coastal Waters. *Front. Mar. Sci.* **2**, (2016).
108. Helms, J. R. *et al.* Photochemical bleaching of oceanic dissolved organic matter and its effect on absorption spectral slope and fluorescence. *Mar. Chem.* **155**, 81–

91 (2013).
109. Nelson, N. B., Siegel, D. A. & Michaels, A. F. Seasonal dynamics of colored dissolved material in the Sargasso Sea. *Deep Sea Res. Part I Oceanogr. Res. Pap.* **45**, 931–957 (1998).
110. Nelson, N. B., Siegel, D. A., Carlson, C. A. & Swan, C. M. Tracing global biogeochemical cycles and meridional overturning circulation using chromophoric dissolved organic matter. *Geophys. Res.* **37**, 1–5 (2010).
111. Nelson, N. B., Carlson, C. A. & Steinberg, D. K. Production of chromophoric dissolved organic matter by Sargasso Sea microbes. *Mar. Chem.* **89**, 273–287 (2004).
112. Steinberg, D. K., Nelson, N. B., Carlson, C. A. & Prusak, A. C. Production of chromophoric dissolved organic matter (CDOM) in the open ocean by zooplankton and the colonial cyanobacterium Trichodesmium spp. *Mar. Ecol. Prog. Ser.* **267**, 45–56 (2004).
113. Kinsey, J. D., Corradino, G., Ziervogel, K., Schnetzer, A. & Osburn, C. L. Formation of Chromophoric Dissolved Organic Matter by Bacterial Degradation of Phytoplankton-Derived Aggregates. *Front. Mar. Sci.* **4**, 1–16 (2018).
114. Jorgensen, L., Stedmon, C. A., Granskog, M. A. & Middelboe, M. Tracing the long-term microbial production of recalcitrant fluorescent dissolved organic matter in seawater. *Geophys. Res. Lett.* **41**, 5074–5081 (2014).
115. Romera-Castillo, C., Sarmento, H., Alvarez-Salgado, X. A., Gasol, J. M. & Marrase, C. Production of chromophoric dissolved organic matter by marine phytoplankton. *Limnol. Oceanogr.* **55**, 446–454 (2010).
116. Zhao, Z. *et al.* Picocyanobacteria and deep-ocean fluorescent dissolved organic matter share similar optical properties. *Nat. Commun.* **8**, 1–10 (2017).
117. Vernet, M. & Whitehead, K. Release of ultraviolet-absorbing compounds by the red-tide dinoflagellateLingulodinium polyedra. *Mar. Biol.* **127**, 35–44 (1996).
118. Cannon, G. A. Tropical waters in the western Pacific Ocean, August-September 1957. *Deep. Res.* **13**, 1139–1148 (1966).
119. Masuzawa, J. Water characteristics of the North Pacific central region. In: Stommel. *Kuroshio-Its Phys. Asp. Univ. Tokyo Press* 95–127 (1973).
120. McCartney, M. S. The subtropical recirculation of mode waters. *J. Mar. Res.* **40**, 427–464 (1982).
121. Sverdrup, H. U., Johnson, M. W. & Fleming, R. H. *The Oceans Their Physics, Chemistry, and General Biology*. (Prentice-Hall, Inc., 1942).
122. Reid Jr, J. L. Intermediate waters of the Pacific Ocean. *Johns Hopkins Oceanogr. Stud.* **5**, 96 (1965).
123. Talley, L. D. Distribution and formation of North Pacific Intermediate Water. *Journal of Physical Oceanography* **23**, 517–537 (1993).
124. Talley, L. D. & Joyce, T. M. The Double Silica Maximum in the North Pacific. *J. Geophys. Res.* **97**, 5465–5480 (1992).
125. Johnson, G. C. & Toole, J. M. Flow of deep and bottom waters in the Pacific at 10°N. *Deep. Res. Part I* **40**, 371–394 (1993).
126. Louchouarn, P., Opsahl, S. & Benner, R. Isolation and quantification of dissolved lignin from natural waters using solid-phase extraction and GC/MS. *Anal. Chem.* **72**, 2780–2787 (2000).

127. Cartisano, C. M., Del Vecchio, R. & Blough, N. V. A calibration/validation protocol for long/multi-pathlength capillary waveguide spectrometers. *Limnol. Oceanogr. Methods* **16**, 773–786 (2018).
128. Murphy, K. R., Stedmon, C. A., Graeber, D. & Bro, R. Fluorescence spectroscopy and multi-way techniques. PARAFAC. *Anal. Methods* **5**, 6557 (2013).
129. Ohno, T. Fluorescence inner-filtering correction for determining the humification index of dissolved organic matter. *Environ. Sci. Technol.* **36**, 742–746 (2002).
130. Talley, L. D. *et al.* North Pacific Intermediate Water in the Kuroshio/Oyashio Mixed Water Region. *Journal of Physical Oceanography* **25**, 475–501 (1995).
131. Swan, C. M., Nelson, N. B., Siegel, D. A. & Kostadinov, T. S. Deep-Sea Research I The effect of surface irradiance on the absorption spectrum of chromophoric dissolved organic matter in the global ocean. *Deep. Res. Part I* **63**, 52–64 (2012).
132. Blough, N. V., Zafiriou, O. C. & Bonilla, J. Optical absorption spectra of waters from the Orinoco River outflow: Terrestrial input of colored organic matter to the Caribbean. *J. Geophys. Res.* **98**, 2271 (1993).
133. Benner, R. Chemical Composition and Reactivity. in *Biogeochemistry of Marine Dissolved Organic Matter* (eds. Hansell, D. A. & Carlson, C. A.) 59–90 (Academic Press, San Diego, California, 2002). doi:10.1016/B978-012323841-2/50005-1
134. Catalá, T. S. *et al.* Chromophoric signatures of microbial by-products in the dark ocean. *Geophys. Res. Lett.* 7639–7648 (2016). doi:10.1002/2016GL069878.Received
135. Blough, N. V. & Green, S. A. The Role of Nonliving Organic Matter in the Earth's Carbon Cycle. in (eds. Zepp, R. G. & Sonntag, C.) 23–37 (John Wiley and Sons Ltd, 1995).
136. Yan, M., Korshin, G. V., Wang, D. & Cai, Z. Characterization of dissolved organic matter using high-performance liquid chromatography (HPLC)-size exclusion chromatography (SEC) with a multiple wavelength absorbance detector. *Chemosphere* **87**, 879–85 (2012).
137. Hernes, P. J. & Benner, R. Terrigenous organic matter sources and reactivity in the North Atlantic Ocean and a comparison to the Arctic and Pacific oceans. *Mar. Chem.* **100**, 66–79 (2006).
138. Hernes, P. J. & Benner, R. Photochemical and microbial degradation of dissolved lignin phenols: Implications for the fate of terrigenous dissolved organic matter in marine environments. *J. Geophys. Res.* **108**, 3291 (2003).
139. Baluha, D. R., Blough, N. V. & Del Vecchio, R. Selective mass labeling for linking the optical properties of chromophoric dissolved organic matter to structure and composition via ultrahigh resolution electrospray ionization mass spectrometry. *Environ. Sci. Technol.* **47**, 9891–9897 (2013).
140. Ritchie, J. D. & Michael Perdue, E. Proton-binding study of standard and reference fulvic acids, humic acids, and natural organic matter. *Geochim. Cosmochim. Acta* **67**, 85–93 (2003).
141. Nebbioso, A. & Piccolo, A. Molecular characterization of dissolved organic matter (DOM): A critical review. *Anal. Bioanal. Chem.* **405**, 109–124 (2013).
142. Hertkorn, N., Harir, M., Koch, B. P., Michalke, B. & Schmitt-Kopplin, P. High-field NMR spectroscopy and FTICR mass spectrometry: Powerful discovery tools

for the molecular level characterization of marine dissolved organic matter. *Biogeosciences* **10**, 1583–1624 (2013).
143. Leenheer, J. A., Wershaw, R. L. & Reddy, M. M. Strong-Acid, Carboxyl-Group Structures in Fulvic Acid from the Suwannee River, Georgia. 1. Minor Structures. *Environ. Sci. Technol.* **29**, 393–398 (1995).
144. Tinnacher, R. M. & Honeyman, B. D. A new method to radiolabel natural organic matter by chemical reduction with tritiated sodium borohydride. *Environ. Sci. Technol.* **41**, 6776–6782 (2007).
145. Lemon, H. W. The effect of Alkali on the ultraviolet absorption spectra of hydroxyaldehydes, hydroxyketones and other phenilic compounds. *J. Am. Chem. Soc.* **69**, 2998–3000 (1947).
146. Cram, D. J. & Cranz, F. W. Mold Metabolites. IV. The Ultraviolet absorption spectra of certain aromatic hydroxyketones. *J. Am. Chem. Soc.* **72**, 595–600 (1950).
147. Abdulla, H. a N., Minor, E. C., Dias, R. F. & Hatcher, P. G. Changes in the compound classes of dissolved organic matter along an estuarine transect: A study using FTIR and 13C NMR. *Geochim. Cosmochim. Acta* **74**, 3815–3838 (2010).
148. Opsahl, S. & Benner, R. Photochemical reactivity of dissolved lignin in river and ocean waters. *Limnol. Oceanogr.* **43**, 1297–1304 (1998).
149. Canonica, S., Jans, U., Stemmler, K. & Hoigné, J. Transformation Kinetics of Phenols in Water: Photosensitization by Dissolved Natural Organic Material and Aromatic Ketones. *Environ. Sci. Technol.* **29**, 1822–1831 (1995).
150. Canonica, S., Hellrung, B. & Wirz, J. Oxidation of phenols by triplet aromatic ketones in aqueous solution. *J. Phys. Chem. A* **104**, 1226–1232 (2000).
151. Sharpless, C. M. *et al.* Photooxidation-induced changes in optical, electrochemical, and photochemical properties of humic substances. *Environ. Sci. Technol.* **48**, 2688–2696 (2014).
152. Kieber, D. J. & Mopper, K. Photochemical formation of glyoxylic and pyruvic acids in seawater. *Mar. Chem.* **21**, 135–149 (1987).
153. Chen, Y., Khan, S. U. & Schnitzer, M. Ultraviolet Irradiation of Dilute Fulvic Acid Solutions. *Soil Sci. Soc. Am. J.* **42**, 292–296 (1978).
154. Scully, N. M. *et al.* Early diagenesis of plant-derived dissolved organic matter along a wetland, mangrove, estuary ecotone. *Limnol. Oceanogr.* **49**, 1667–1678 (2004).
155. (IHSS), I. H. S. S. Acidic Functional Groups of IHSS Samples. *School of Earth & Atmospheric Sciences, Georgia Institute of Technology, Atlanta, GA, U.S.A.* (2019). Available at: http://humic-substances.org/acidic-functional-groups-of-ihss-samples/.
156. Ritchie, J. D. & Perdue, E. M. *Advances in the Physicochemical Characterization of Dissolved Organic Matter: Impact on Natural and Engineered Systems*. *Geochimica et Cosmochimica Acta* **67**, (2003).
157. Brinkmann, T., Sartorius, D. & Frimmel, F. H. Photobleaching of humic rich dissolved organic matter. *Aquat. Sci.* **65**, 415–424 (2003).
158. Landry, C. & Tremblay, L. Compositional differences between size classes of dissolved organic matter from freshwater and seawater revealed by an HPLC-FTIR system. *Environ. Sci. Technol.* **46**, 1700–1707 (2012).

159. Timko, S. A., Gonsior, M. & Cooper, W. J. Influence of pH on fluorescent dissolved organic matter photo-degradation. *Water Res.* (2015). doi:10.1016/j.watres.2015.08.047
160. Twilley, R. R., Chen, R. H. & Hargis, T. Carbon sinks in mangroves and their implications to carbon budget of tropical coastal ecosystems. *Water. Air. Soil Pollut.* **64**, 265–288 (1992).
161. Shank, G. C., Lee, R., Vähätalo, A., Zepp, R. G. & Bartels, E. Production of chromophoric dissolved organic matter from mangrove leaf litter and floating Sargassum colonies. *Mar. Chem.* **119**, 172–181 (2010).
162. Dittmar, T., Hertkorn, N., Kattner, G. & Lara, R. J. Mangroves, a major source of dissolved organic carbon to the oceans. *Global Biogeochem. Cycles* **20**, 1–7 (2006).
163. Benner, R., Weliky, K. & Hedges, J. I. Early diagenesis of mangrove leaves in a tropical estuary : Molecular-level analyses of neutral sugars and lignin-derived phenols. *Geochim. Cosmochim. Acta* **54**, 1991–2001 (1990).
164. Hernes, P. J. *et al.* Tannin diagenesis in mangrove leaves from a tropical estuary: A novel molecular approach. *Geochim. Cosmochim. Acta* **65**, 3109–3122 (2001).